Experiments in the Ultracold Lithium - Ytterbium System

Alexander Khramov

A dissertation submitted in partial fulfillment

of the requirements for the degree of

Doctor of Philosophy

University of Washington

2013

Reading commmittee:

Subhadeep Gupta, Chair

Anton Andreev

Boris Blinov

Program Authorized to Offer Degree: Physics

University of Washington

Abstract

Experiments in the Ultracold Lithium - Ytterbium System

Alexander Khramov

Chair of the Supervisory Committee: Subhadeep Gupta, Associate professor, Physics

I detail the construction of an experimental apparatus created for performing ultracold atomic experiments with fermionic lithium-6 (Li) and several isotopes of ytterbium (Yb), and several of the first experiments performed using this apparatus. The apparatus consists of a vacuum chamber, laser and auxiliary systems, which together are used to produce the first instance of trapped ultracold mixtures of lithium and ytterbium. We show that the system is stable and obtain the s-wave scattering properties of Li-Yb collisions. By using Yb to sympathetically cool Li, double quantum degeneracy is achieved. I demonstrate the versatility of the new system with several experiments. In the first, we investigate the behvaiour of Li near a broad Feshbach resonance, and modify it with Yb. In the second, we produce Yb in the metastable state, and trap it in a 1064 nm optical dipole trap, which allows for a technically simple spin polarization procedure. We then characterize the dynamics of a Li - metastable Yb mixture.

The work described in this thesis provides a pathway to future extensions such as the magentic tuning of Li-Yb interactions and the production of LiYb molecules by either photo- or magnetoassociation. The potential interest of this specific system lies in the combination of alkali and spin-singlet atom, leading to a potential paramagnetic ground state molecule, and experimental realizations of systems which cannot be accessed with bialkali experiments.

TABLE OF CONTENTS

LIST OF FIGURES

LIST OF TABLES

ACKNOWLEDGMENTS

I want to begin the acknowledgements section with a confession. Whenever I read a thesis, I almost always start with the acknowledgements. I have always considered this behaviour of mine as somewhat shameful and unprofessional. Nevertheless, it has not catastrophically impacted my ability to pursue a physics doctorate or write a thesis of my own. So I wish to reassure you that if you find yourself reading this section, my opinion is that you shouldn't despair for your competence as a scientist or anything like that. It will probably all turn out okay. I would humbly suggest that you read some other parts of the thesis, too, though. That said, I want to thank the people I have been fortunate to know in my time at the University of Washington and in Deep Gupta's lab. Without them, neither would the completion of this thesis be possible, nor the last several years of my life as good.

I have been deeply fortunate in having Deep Gupta as advisor. Deep's combination of broad vision and relentless enthusiasm has made working in his lab tremendously exciting. Deep constantly has ideas for new projects and questions to study for the lab, and this is genuinely a lot of fun, despite the panics in the lab whenever we fear he will suddenly initiate a cesium experiment or construct a green slower. Of course I have also greatly benefited from Deep's profound understanding of atomic physics, experimental skill and nearly legendary patience. When I was a first year, I noticed my lack of contribution to the lab and told Deep that I was quitting since I wasn't being helpful. To which Deep told me not to worry about it, since he was employing me for the lab, and not out of some personal favour. I am greatly thankful to him for that answer, and for all the support in the intervening years. I am also lucky to know and work with the other members of Deep's lab, who have become my friends as well as my colleagues.

Firstly I thank Anders Hansen, with whom I have worked for the entirety of my time at UW. Anders' specialty is knowledge of the arcane and difficult parts of what's necessary for running the lab. If there is anyone in the lab for whom the "bus number" is 1, it is Anders. Working on any kind of physics with Anders is also a great pleasure because whenever he says he will think about a problem, you can be sure that he will and that he will have an original way of looking at it. Outside the lab, I have enjoyed his game nights, his beer connoisseurship and brewing skills and his genuine helpfulness. Ever since he graduated, I can also feel my Georgian-Indonesian patois slipping.

I thank Alan Jamison for explanations in various branches of physics and his ability to wrest the blue laser into submission. It is a great experience to interact with someone with whom you can talk about any of your extraneous interests, who will introduce you to new music, and who also knows about an order of magnitude more physics. I heartily recommend it. Although it must be said that Alan's ideas in the lab are often refreshing but always strange (or possibly the other way around?) [51, 103], for instance the time he took a hacksaw to our vacuum chamber.

I thank Will Dowd for very enjoyable experimental runs - Will is a master of running the experiment. This stems from his (initial, although now somewhat tempered by experience) lab optimism combined with a practical eye as to what needs to be done in the lab and what shouldn't be done, which has saved us many hours of goose chasing. I have also come to support his more outlandish ideas, from global warming arbitrage as a business venture to sandwiches sensu lato.

I thank Vlad Ivanov for his good-natured cynicism and his clear, easily-explained ideas in atomic physics. I must mention that I am graduating roughly 5 years ahead of his guess at the schedule. Although I haven't worked closely with Ben Plotkin-Swing in the lab, I thank him for tips on every sort of outdoor plan, and for confusing me to great effect by putting a tree up another tree. I thank Ricky Roy for a desire to understand everything (that I look up to) and hockey fandom (that I share). Luckily for the lab, Ricky is still relatively new, so the mixture experiment will be in good hands for years to come.

In addition, I am thankful to others whose contributions to the construction of the apparatus form a part of this thesis. By the time I joined, Lee Willcockson was already a wily lab veteran, and many vacuum chamber decisions as well as the schematics in Chapter 2 are made by him. Ryan Weh implemented the data acquisition setup, built the red PA laser, a lot of electronics, and came up with the great idea of the lab bios. Frank Münchow worked with me on the photoassociation setup (I am also grateful for his hospitality in Düsseldorf). Nolan Maloney built the magnetic coils discussed in Section 2.5.2. Carson Teale built the 404 laser in Fig. 3.13 (though we didn't know it at the time). Without their hard work, I wouldn't be writing this thesis.

Stepping (briefly) outside the door of B063, I want to acknowledge the calming presence of Prof. Steve Sharpe, and the help of Jen Lehner and Catherine Provost at UW. I want to also thank those people who steered me towards academics and an atomic physics PhD in one way or another: John Currie, Grenfell Patey (who has supported me in both chemistry-physics and theory-experiment switches which were both against his inclinations), Masaaki Tsubouchi, Taka Momose, Wim Ubachs, Edcel Salumbides. I should also take this opportunity to get Greg Lakatos' name correctly in an acknowledgements section, although in this case he didn't really do anything.

Finally I wish to thank my friends for their steadfast support and the good times we have shared. And my family, whose love for me I feel every day and am hoping that they feel mine. I dedicate this thesis to them.

To Mila, Yuri and Vera

Chapter 1

INTRODUCTION

Experiments with ultracold atoms offer some of the most direct examples of the quantum nature of our world. They naturally attract those of us who find quantum phenomena fascinating. Although fermionic and bosonic statistics underlie many everyday phenomena, there is something very satisfying about directly observing these statistical distributions in clouds of fermionic or bosonic atoms. To compound the strangeness of the situation, this is usually achieved by using photons from a laser, which itself is a manifestation of the quantum nature of night. The invention of the laser in 1960 [75] underpins a lot of the progress in atomic physics since then, including in the field of ultracold atoms. A further impetus for the significant growth and branching-out of ultracold atomic experiments has been the seminal achievement of Bose-Einstein condensation (BEC) in 1995 [3, 23, 11] and the first Fermi degenerate gases (DFG) of atoms in 1999 [27]. Since then, the clean environment offered by the system of ultracold atoms, and the ability to tune interactions has led to advances such as the simulation of condensed matter Hamiltonians as well as that of brand new Hamiltonians not otherwise encountered in nature (See [8] and references therein). Isolation from the environment and low energies have also made ultracold atoms attractive for precision measurements [20] and quantum information [98].

Along with the alkali metal atoms most frequently used for ultracold atomic experiments, the investigation of spin singlet atoms has also progressed apace. The first such BECs and DFGs were produced in ytterbium by the Takahashi group in Kyoto [116, 37]. This was followed by BEC in calcium [72] and strontium [111, 77]. The atomic techniques developed for studying two valence electron atoms are also continually improving, leading to, for example, the recent record-breaking speeds for Bose-Einstein condensation in strontium [110]. The motivation has been the possibility of extending the power of ultracold atomic simulations beyond what is possible with alkali metal atoms *e.g.* [34, 41]. Central to this promise has been the complexity of internal states in such atoms, and in particular the existence of metastable states. It is the metastable states that make two valence elctron atoms particularly useful for atomic clocks, *e.g.* [55]. These atoms are also thought to be useful for some other precision measurement applications *e.g.* [71].

One possible avenue of pushing these boundaries is to extend the system of study from simple systems composed of one type of atom to mixtures and molecules. In particular, mixtures of one- and two-valence electron atoms offer a great versatility in terms of available states for the system. This is the direction that is explored in this dissertation, using quantum mixtures of lithium and ytterbium atoms.

1.1 Ultracold Atomic Mixtures and Ultracold Molecules

Experiments with mixtures were at the heart of ultracold atomic experiments almost from the beginning. Because of the Pauli exclusion principle, a mixture is indispensable to cooling fermions below the p-wave threshold. Mixtures consisting of two different atomic species were first created with K and Rb [83], and with Li and Na [46]. The initial use of mixtures was to sympathetically cool species with interesting atomic properties that could not be cooled to the quantum regime on their own. This continues to be a widely used application. However, mixtures have since then developed other uses, including the study of many-body physics, *e.g. [93]* and formation of diatomic heteronuclear molecules, *e.g.* [88].

One potential reason to study molecules in ultracold atomic physics is very simple: the rest of the world is full of them. If atomic physics is to be used as a tool to model the physics of more complex systems, then having the building blocks to make such complex systems could be important. More precisely, molecules offer additional degrees of freedom unavailable to atoms: they can have vibrational and rotational excitations, as well as having external structure, unlike (usually, approximately) 0-dimensional atoms. Information can be stored in these new degrees of freedom, and new interactions are available for study. Particularly exciting is the possibility of tunable anisotropic long-range interactions due to the permanent electric dipole in heteronuclear molecules. Molecules also offer some perhaps less appreciated benefits, such as the close spacing of rotational levels making polarization of molecules much less technologically challenging than that of atoms.

Broadly, there are two routes towards experiments with ultracold molecules. One is to begin with ensembles of molecules, and cool them to the ultracold regime. In this case, obtaining molecules can be a trivial step, depending on the particular molecule of interest. However, reaching cold temperatures and high densities while retaining the molecules in a gas phase is often very challenging. Buffer gas cooling, as well as Stark deceleration, molecular synchrotrons and fountains are some of the techniques developed to tackle this problem. Laser cooling methods have recently had some success as well [4, 58], but they remain limited to a very narrow class of molecules. The advantage of these "molecule-first" techniques is that, except for laser cooling and evaporative cooling, they often are very broadly applicable. They are of greater utility if the aim is to find information that is specific to a given molecular system, or to compare properties among an ensemble of molecular species. In addition, atomic methods have so far been confined to creating diatomic molecules, and ones that are relatively loosely bound. If two- or three-dimensional molecular geometry or strong binding is essential (*e.g.* in some collision or cold chemistry studies), direct cooling methods look to be the better choice.

The other approach to ultracold molecules is to start with an ultracold system and then make molecules. This is the path we have chosen. The advantage to this approach is that laser and evaporative cooling methods for atoms are well-developed, and thus getting to low temperatures and high densities is the "easy" part. The disadvantage is the limitations placed on which molecules to study. For instance, lithium-ytterbium is not a molecule that is particularly relevant, or that a chemist would even classify as a molecule at all. However, if you are trying to model something universal, the particulars of any given molecule may not matter all that much. In addition, the tunability of atomic systems helps retain some versatility. One method that has been used with great success that falls under this atoms-first approach is magnetoassociation using a Feshbach resonance. Tuning across a Feshbach resonance adiabatically transfers pairs of atoms to loosely bound diatomic molecules. The first ultracold molecules using ^{40}K [99] and ^{6}Li [113, 21] were produced in this way. An alternative is to couple using laser light. This method, called photoassociation, has been used to produce a wide range of ultracold molecules, such as, for example, LiCs [26] and Sr_2 [76].

1.2 Dissertation Organization Information

This dissertation concerns a new double species experiment of ytterbium and lithium at the University of Washington, and the apparatus created and used for this experiment. The list of systems available to ultracold atomic and molecular experiment is ever expanding. Still, these systems are hard to come by, and the addition of a new system with sufficiently unique properties remains worthwhile. Thus, the introduction of the lithium-ytterbium system is the main result of this dissertation. I cover the characterization of this new system and the achievement of sympathetic cooling and double quantum degeneracy for the two species. In particular, we determine the magnitude of the interspecies s-wave scattering length $|a_{^{174}\mathrm{Yb}-^{6}\mathrm{Li}}| = (13 \pm 3)\ a_0$, where a_0 is the Bohr radius. We achieve the coexistence of a DFG of ^{6}Li with a BEC of ^{174}Yb. We also demonstrate the use of sympathetic cooling by ^{174}Yb to reach temperatures $\lesssim 0.1\, T_F$, where T_F is the Fermi temperature. The versatility of the new system and its potential usefulness for ultracold experiment is demonstrated in a pair of studies that forms most of the rest of the dissertation. In the first, we study the effect of ^{174}Yb on molecule formation and reactions near a broad Feshbach resonance in ^{6}Li. We show the usefulness of our system to study three-component mixtures with resonant interactions, and our ability to use ^{174}Yb to probe or even drive lithium behaviour. In the second, we produce ytterbium in the metastable $^{3}P_{2}$ state, and observe its interactions with lithium. This is the first achievement of an ultracold system consisting of a heteronuclear mixture of electronically ground and electronically excited state atoms. In addition to providing a check on *ab initio* atomic physics calculations, such a system can be used to explore strong interactions or for magnetoassociation of electronically excited molecules.

The rest of the dissertation is organized as follows. Chapters 2 and 3 introduce our experimental apparatus as well as recounting the tale of its construction. Chapter 2 is concerned with the vacuum system and magnetic coils, while Chapter 3 focuses on the system of lasers. Chapter 4 describes the first experiments with the system, including proof of co-existence, sympathetic cooling and double quantum degeneracy. Chapter 5 discusses Feshbach resonances. There is an introduction to the concept, followed by a more thorough description of our experimental study of the broad Feshbach resonance in lithium-6. I then briefly mention several other directions of using Feshbach resonances explored in our lab. In Chapter 6, I discuss a little bit of the theory of diatomic molecules, as a segue to photoassociation, both generally and in our system. Chapter 7 is about the production of, and experiments with, metastable ytterbium. This is the most recent set of experiments in the mixture group.

Chapter 2

CONSTRUCTION OF EXPERIMENTAL APPARATUS

> 'Tis vain to be angered with things
> They care not a rap for our wrath
>
> Plutarch

We began an effort to construct an apparatus for a combined lithium-ytterbium experiment right as I joined the ultracold atoms group in October of 2007. At first, Anders Hansen, Lee Willcockson and I were the grad students working on the project, with the undergrad students Ryan Weh and Billy English. Soon afterwards another grad student, Kalista Smith, joined us. Most of the specific choices about the chamber construction were made by Deep Gupta. The CAD modeling of the chamber was done by Lee. The computer control system was implemented by Ryan. The water system was designed and built by Anders, etc. The building and setup of the experimental apparatus was a collaborative project throughout. The aim of this chapter is not to detail the specifics of the work done by me exclusively. Instead, it is to provide a guide for the construction of a chamber for double-species experiments, and to document the specific choices made by our group. Some of the particulars of our apparatus are detailed in [50]. For more information, including details of the magnetic field electronics and water system, refer to Anders' thesis [51].

One important choice to make immediately in apparatus design is whether to have separate beamlines for the two species. Initially, we considered a single beamline design, with the ovens positioned sequentially. This design is well-suited to the lithium-sodium system [107] and has the potential for leading to a more compact and simple apparatus, but requires a reduction in vapour pressure along the beam to prevent flow backwards into the first oven. Alternatively, for species which require similar vapour pressures, a design with two closely-located ovens to make two nearly-parallel beamlines may be appropriate [108]. However, because of concerns about potential chemical reactions, and the very different optimal Zeeman slower lengths, we ended up with a double line design. This choice has had the great advantage of allowing us to easily continue working with our machine on one-species experiments while breaking vacuum in the other line. It also makes separate optimization of slowing and trapping possible, as well as shuttering of individual beamlines during operation.We also occasionally use the independent magnetic slowers to provide corrective fields for horizontal positioning of our trapped atoms. A disadvantage is the reduction of optical access to the atoms.

2.1 Vacuum System Overview

Our apparatus is designed for performing atomic experiments with ultracold lithium and ytterbium. For this purpose, we need to generate atomic beams of lithium and ytterbium, which is done by heating up samples of metal until a sufficient vapour pressure is achieved and then using a nozzle and collimating tube to select atoms within a certain velocity range. Typical evaporative cooling and experimentation timescales are on the order of seconds to 10's of seconds. Thus the experimental challenge consists of two related problems: we need a trapping apparatus with good optical access on one hand and total isolation from the environment on the other; we also need the apparatus to have a zone with high vapour pressure for our metallic species, and another zone with ultra high vacuum (UHV) to ensure long potential experimental timescales.

Our vacuum system consists of a main chamber fed by two separate lines connected to two separate ovens. A top down schematic view is presented in Fig. 2.1, whereas an isometric render and the corresponding (rather obstructed) real-life view are shown in Fig. 2.2. The main chamber is a custom part constructed to our specifications

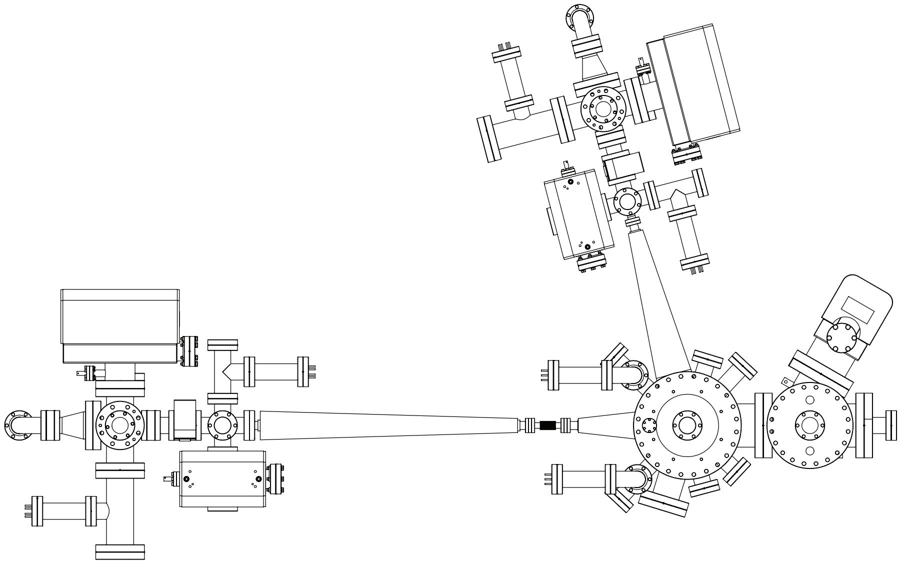

Figure 2.1: Top down view of experimental apparatus. This figure and other SolidWorks figures in this chapter courtesy of Lee Willcockson

by Sharon Vacuum. It is pumped by a 75 L/s ion pump (Gamma vacuum), and a titanium sublimation (Ti-sub) pump (Thermionics) is attached, which was fired after an initial bake to reach ultra high vacuum, but has only been used once in four years since then. Both of these pumps are connected to the chamber via a custom 4-way cross (Sharon). An ion gauge (Varian) at the side of the main chamber opposite the ion pump gives a pressure of $< 1 \times 10^{-10}$ Torr during experimental operation[1], whereas the gauge of the ion pump gives a pressure of 5×10^{-9} Torr. We are able to obtain background limited lifetimes of $\gtrsim 30$ s with this vacuum. From the main chamber, two Zeeman slower tubes extend in the direction of the ovens, at an angle of 80° with respect to each other. Both lines consist of a Zeeman tube, followed by an intermediate chamber with a 45 L/s ion pump, ion gauge and four viewports to be used for diagnostics. This is followed by a gate valve (MDC), and then a differential pumping tube. On the other side of the tube is an oven chamber with two viewports

---

[1] Using SRS Ion gauge controllers with N_2 sense factor 25, emission current 4 mA

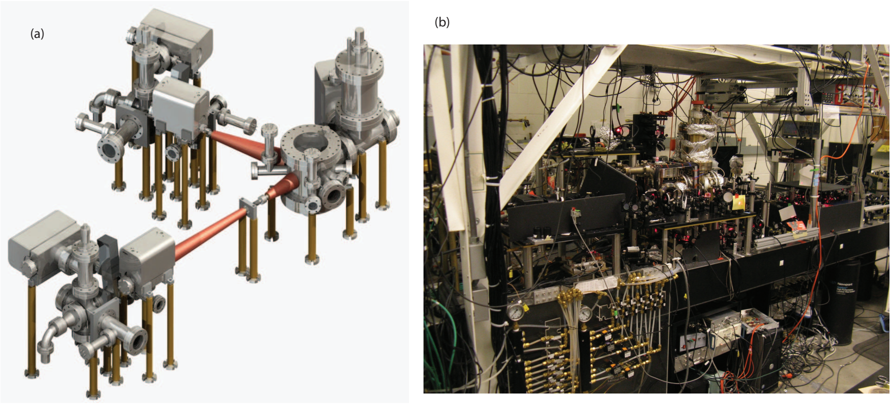

Figure 2.2: (a) isometric view of experimental apparatus (b) the real-life version

for diagnostics, a copper cold finger for adsorption of stray sample atoms, and an atomic beam shutter. This chamber is likewise pumped by a 45 L/s ion pump and the pressure is monitored with an ion gauge. At the far end of the chamber is a nozzle leading to the oven itself. The oven consists of a cup filled with metal sample, separated from the beam line by a 90° elbow and the nozzle. The nozzle is constantly kept at 450°C to prevent blockage by atoms recondensing. During operation, the lithium oven cup is kept at 400°C, corresponding to a lithium vapour pressure of 9×10^{-5} Torr. The corresponding total pressure after the nozzle is $\sim 2 \times 10^{-8}$ Torr at the ion gauge, and $\sim 1 \times 10^{-8}$ Torr according to the ion pump. The ytterbium oven cup is operated at 375°C, corresponding to a vapour pressure of $\sim 3 \times 10^{-4}$ Torr. The corresponding total pressure after the nozzle is $\sim 1 \times 10^{-7}$ Torr at the ion gauge, and $\sim 5 \times 10^{-9}$ Torr according to the ion pump. There are three angle valves (VAT) - one at each oven and one connected to the main chamber ion pump - for attaching external pumps during the bake-out procedure, or during sample replacement in the ovens. All vacuum components are connected to each other with conflats, using copper for the vacuum gaskets between knife edges (except in the lithium oven), and silver-plated vacuum bolts. We do not use any vacuum grease. The entire chamber assembly is

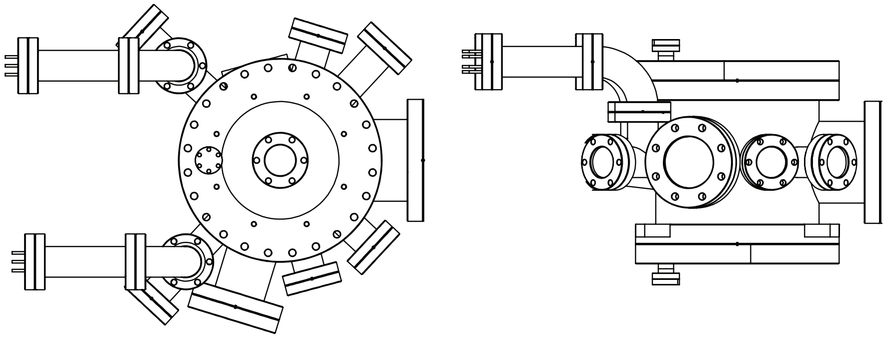

Figure 2.3: Main chamber schematic

held at an average height of 13 in. above the optical table by $1\frac{1}{4}$ in. thick brass supports clamped to the optical table. Any sort of attempt to nudge or move these supports or their clamps is to be very strongly discouraged.

2.2 Main Chamber

Our main chamber is the location of the MOT, ODT, evaporative cooling, and all of our further experimentation. The chamber design was in part inspired by the chamber used in the MIT BEC-III experiment [15]. Atoms are to be trapped in the centre of the chamber. Recessed "buckets" at the top and bottom allow for the placement of magnetic coils close to the atoms, see the side view in Fig. 2.3. The chamber contains 12 ports. One port is on the top of the chamber, one on the bottom, and the rest are horizontally arranged around the centre of the chamber, see the top-down view in fig. 2.3 . Of these 12, one each is connected to the lithium and ytterbium lines, and the rest are viewports (Larson). Viewports opposite the atomic beam lines are uncoated sapphire glass to be robust against heating, while the rest are BK7 glass, AR coated for the visible and 1064 nm IR light. The glass in the viewports is rated to vacuum below 1×10^{-11} Torr. The bottom viewport location suffers from a difficulty of access. In recent years, this has become even more difficult due to an accretion of optical components, and we generally align top-down MOT optics by retro-reflection exclusively. The viewports opposite to the slower arms suffer from a deposition of untrapped lithium and ytterbium atoms on the glass. This adsorption happens at exactly the location where we would want to point the slowing laser beams, and ruins the transmissivity, which is already lower for the sapphire glass. Yamaguchi [125] reports "cleaning" the viewports by applying focused 532 nm from their Verdi laser to heat up the glass and desorb the metal. While we have considered such steps, so far simply heating the viewports has been sufficient. The ytterbium viewport is kept at 250°C. The lithium viewport is at 200°C. This latter is likely to be close to an upper limit, however. Stan [107] reports adverse effects for a lithium-coated viewport at 300°C. At the bottom of the chamber is a BNC feedthrough for the radio-frequency (RF) magnetic coils located in the chamber (see Section 2.5.4).

2.3 Beamlines

Each of our atomic beamlines consists of an oven followed by an oven chamber, gate valve and intermediate chamber leading to a Zeeman slower along which the atomic beams feed into the main chamber. Our oven systems consist of three parts: a "cup" for loading atomic sample; a 90° angled "elbow" for connecting the cup to the beamline; a "nozzle" consisting of a diameter= 4 mm hole drilled in a conflat blank for converting the vapour pressure in the oven into a directed atomic beam. The assembly is shown in Fig. 2.4. We fill the ytterbium oven with 25g of natural Yb, obtained from Alfa Aesar, at a time. We have not yet run out of sample, but we did replenish the oven with 50 g of Yb in May of 2010 when last opening the ytterbium oven to deal with a vacuum leak. We fill the lithium oven with 5g of isotopically enriched ^{6}Li at a time[2]. So far one load has been sufficient for all experimentation since early 2009. The ovens

---

[2] At least we think we do. The first time we attempted to load the oven, we were instead mistakenly given natural lithium (or even, potentially, enriched ^{7}Li) by Icon Isotopes. Our further isotope purchases have been from Sigma Aldrich, cleaned and prepared by Ames.

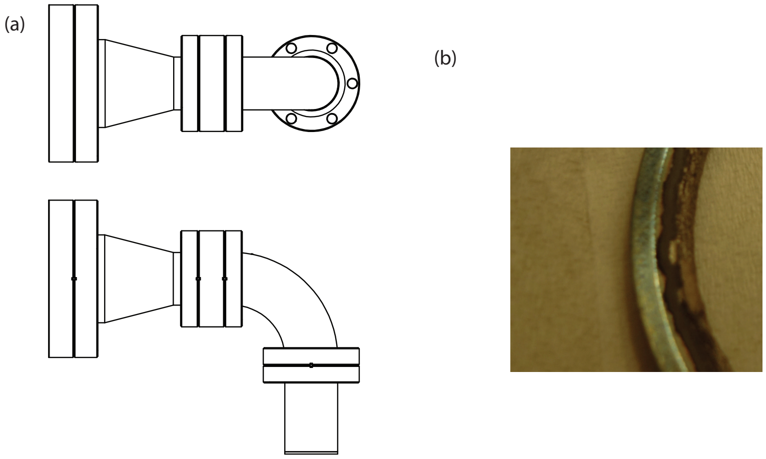

Figure 2.4: (a) Oven assembly schematics.(b) closeup of nickel gasket showing reaction with ytterbium

were the location of highest temperature during the bake[3], and the ovens continue to be kept at temperatures $375 - 450°\text{C}$ during operation, which presents a challenge for vacuum technology. Copper, used for vacuum gaskets elsewhere in the vacuum assembly, has a tendency to seize at these high temperatures in the presence of lithium [106]. Thus, we initially used nickel gaskets on both ovens. However, we soon saw vacuum leaks at the nickel gaskets that were placed in proximity to hot ytterbium. The porous, whitish substance that we found is both gummy and somewhat brittle (see photo in Fig. 2.4). We could easily chip off flakes of gasket, but it proved hard to separate from the steel entirely. The knife edges had to be re-machined during the gasket replacement. Although we do not know if there is an issue with seizing in the ytterbium oven, we at least have avoided the vacuum problems we experienced with nickel. We are therefore now using exclusively copper gaskets for the ytterbium oven setup and exclusively nickel gaskets for the lithium oven setup. This incompatibility would be another potential problem for a single-line design. The temperatures also

---

[3] Including a section of the lithium oven which was unintentionally heated to 550°C due to a malfunctioning PID controller photodiode

proved troublesome for the silver-plated vacuum bolts in the ytterbium setup. So far we have eventually dealt with all seized bolts, using technologies as inappropriate for ultra-high-vacuum work as a hacksaw[4] and a handdrill, but this is a source for potential future problems, as well.

The chamber immediately after the oven nozzle contains a copper cold finger and an atomic beam shutter. The cold finger consists of a copper bar with a "skimmer" hole for the atomic beam. The plate is fed through to outside the chamber, where it is thermally connected to a square plate, which in turn forms a sandwich of two such plates with thermoelectric coolers (TECs) in between creating a temperature differential. Both the lithium and ytterbium cold finger assemblies contain 4 TECs (Melcor), which should draw 3 A for a total of 24 at the normal operating voltage of 12 V. However, over time the TEC degrades, and we are currently down to 19.2 A, with all 8 TECs seemingly still working. The hot side is water cooled, while the cold condenses water vapour into water and ice from the air in the room. Thus shutting off the TEC power supply for when the water line needs to be closed leads to water drips at the cold fingers. This may be non-ideal (especially if there are any electronics nearby), but isn't a leak in the water system, and so far we have not seen any adverse consequences. Conversely, operating without the cold fingers altogether doesn't seem to have a disastrous effect on oven pressures, either. The atomic beam shutter likewise consists of a copper bar, this one connected to a rotary feedthrough (Thermionics). The beam shutter can either be rotated by hand, or electronically, using a pair of solenoids which can be activated and pull the feedthrough in either direction[5]. Because of the excellent differential pumping provided by the collimating tube and slowers, the fast timescale of our experiments, and the tendency of the shutter snapping closed to disturb the lithium laser lock, we usually don't use atomic

---

[4] It is very sad that there is no photographic documentation of this

[5] the solenoids overheat when they are on for too long, and in any case are only needed to rotate the beam shutter, not to keep it in place. Therefore it is not recommended to keep either the "opening" or "closing" solenoid on for more than 500 ms at a time.

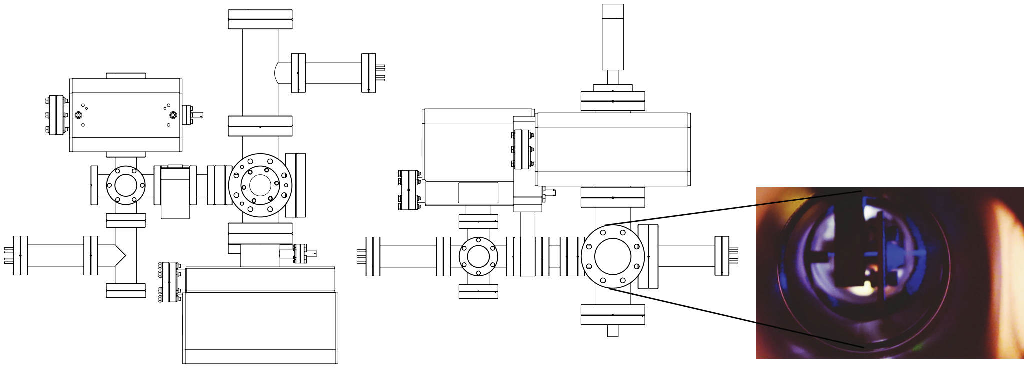

Figure 2.5: Schematic for oven chamber and intermediate chamber. Inset: view through Yb oven nchamber viewport

beam shutters. However, use of the ytterbium atomic shutters seems to increase background lifetimes on the order of 50% in ytterbium-only experiments. In addition, the first chamber is connected to a 45L/s ion pump on one side, and an ion gauge on the other, which are both conncted to the chamber via "T"-shaped connectors. Thus there is also space for two viewports, along the "top bar" of the "T". These viewports are useful for ensuring Zeeman slower beam alignment, and also afford the best view of the atomic beam (see inset in Fig. 2.5). In the case of ytterbium, we have a video-camera monitoring the chamber to aid in slower diagnostics.

.

The oven chamber is followed by a narrow collimating tube ($l = 11\,\mathrm{cm}$, diameter= $5\,\mathrm{mm}$) that ensures beam collimation and helps provide differential pumping between the relatively high-pressure oven and the low pressure of the main chamber. This is followed by a $1\frac{1}{2}$ in. gate valve (MDC GV1500 M with Kalrez gasket). The gate valve ensures we can operate at ultra high vacuum in the main chamber even while one of the oven assemblies is up at atmospheric pressure. Although there is potential concern about chemical reactions between the viton ring and the atomic beam, we have not so far had any indications that such reactions are occurring. After the gate valve, we have an intermediate chamber. Again, we have a 45 L/s ion pump and ion gauge on opposite sides, attached via “T”s. We do not ordinarily operate these ion gauges since we only have three ion gauge controllers[6]. The ion pumps themsleves indicate post-gate valve pressures of 2×10^{-10} Torr and 5×10^{-11} Torr for the Li and Yb lines, respectively, during operation. In addition to the side viewports on the “T”s, there are also viewports above and below. These are useful in case we wish, for example, to lock a laser to the atomic beam line (as we have done for 556 nm). The entire oven+intermediate chamber assembly is shown in Fig. 2.5. The intermediate chambers are connected to the main chamber by long slower tubes (OD= 0.75 in.) made for seating Zeeman slower coils around them. The slower tube for the ytterbium line is 40 cm long, whereas the lithium line consists of a 60 cm tube coming from the oven and a 15 cm tube coming from the main chamber, connected by a flexible bellows.

2.4 Baking and Pumping

I once applied for a job as a baker, but balked at having to wake up at 3 a.m. to do the job. Luckily, I got a second chance as an atomic physics student. In order to achieve ultra-high vacuum, any lingering impurities need to be desorbed from the steel so that there isn’t a slow process of desorption during operation. This is achieved by heating the steel far above the operational temperature while being pumped. It is this procedure is colloquially known as a “bake”. The remaining vapour in the chamber can be analyzed with residual gas analyzer (RGA, Dycor series), which is essentially a miniature mass spectrometer. The aim for a bake is to reduce the partial pressure of high-mass components, leaving light gases to be pumped by the ion pump during operation and H_2 to be pumped by the Ti-sub. In preparation for the bake, the angle valves are connected to turbo pumps, the backs of which are in turn connected to a roughing pump. Our first bake consisted of the main chamber

---

[6] Operating the Yb intermediate ion gauge would actually interfere with currently used optics for ODT beam 2

Component	Temperature Limit(s)
Chamber body	450°C
AR coated BK7 Glass VP	250°C, 10°C/min
Sapphire Glass VP	450°C
Gate Valve	200°C (closed)
Bellows	450°C
Rotary Feedthroughs	200°C
Epoxy for Zeeman Slowers	260°C
Ion Pumps	350°C
Ion Gauge Faces	450°C
Angle Valves	300°C, 60°C/hr
Turbo Pumps	120°C at inlet flange
Kapton tape	260°C

Table 2.1: Temperature limits for apparatus baking

and lithium line. We used 63 separate heating elements - band heaters and heating tape (both obtained from Omega) - powered by Variacs, including some extremely ancient specimens obtained from Bob Van Dyck's lab. Temperature monitoring is an important part of the baking procedure, as different parts of the apparatus can have vastly different temperature limitations (see Table 2.1) . The temperature monitoring during the first bake consisted of taking a temperature probe to specific holes put in the tin foil and waiting for the temperature to equilibrate. This led to a system where the next round of temperature measurements had to be started before the first round was finished, and was unreliable due to temperature gradients, and slow response of temperature probe. We had several iterations to perfect the system. For the third bake and all subsequent ones, thermocouples (Omega) were glued with kapton tape to the chamber itself. Along with being a time-saver, it also helped provide a more accurate reading than reading at holes (which had us measuring at the coldest point of each area and induced unwanted temperature gradients). The sequence of events in a bake then proceeds as follows: heating elements and temperature probes are attached to the area about to be baked. The entire area is covered in aluminum foil and gradually heated, with most areas of the chamber being het up to 250°C. Once the highest temperatures are reached and kept for 24 hours, the degassing of pump filaments is performed. First the ion gauge filaments are degassed for 30 min. periods at 25 W, until further degassing does not have an effect on overall pressure. Then Ti-sub pump filaments are degassed for 30 min. periods at 45 A (the action of the pump is very sensitive to this final current).. There is a certain gentleness that is required in getting the filaments to this high current, and it is a gentleness that we do not quite possess. At this point, only one of the filaments (I believe it is fil. 4 but am unsure) has survived. If the resulting pressure is sufficiently low, ion pump filaments can be degassed by turning on the ion pumps themselves. Then the temperature is gradually reduced back down to room temperature. Ion pumps are kept on whenever the pressure is sufficiently low to do so. In order to reach the lowest pressures, the angle valves are closed and the chamber continues to be pumped only by the ion pumps. Finally, once low pressure and room temperature is reached, everything is defoiled[7]. Our first bakeout resulted in a minimum overall pressure of 5×10^{-8} Torr, which was much worse than our target vacuum. We traced the problem to a leak in one of the main chamber ion gauges, which required the replacement of the ion gauge. This replacement was performed under argon flush of the main chamber. Nevertheless, due to the large volume we would be exposing to atmosphere, we decided to redo the bake. For this second bake, we only took up the steel to a maximum of 150° C. After the second bake, the main chamber came to a pressure of 8×10^{-9} Torr as it cooled and was continuing to come down. However, we soon had another vacuum issue: in removing a clamp for the brass legs of the support structure for the lithium slower, a further leak developed and the entire procedure had to be repeated once more[8]. Finally, by late January 2009, roughly two months after the beginning of the first bake, we had our target pressure of 1×10^{-10} Torr as

---

[7] I've been waiting for an opportunity to write this phrase for some time

[8] Some fun stories relating to this bake can be found in Chapter 5 of [51]

read by the main chamber ion gauge, and could proceed with the lithium portion of the experiment. The ytterbium oven assembly beyond the gate valve was baked at a later date, following the same procedure, and without any serious complications.

2.5 Magnetic Coils

We have constructed electromagnets for producing the bias, gradient and RF magnetic fields necessary for our experiment. The Helmholtz, anti-Helmholtz and Slower coils are constructed of kapton-covered square copper wire (S-W Wire Corporation). The outer length of the wire is 1/8" and the inner length is 1/16". Water flows through the inside of the coils for cooling. Because our ability to change the magnetic fields is much slower than the time it takes to reach the atoms from our magnetic coils at the speed of light, all can be effectively treated using the Biot-Savart law,

$$\mathbf{B} = \frac{\mu_0 I}{4\pi} \oint \frac{d\mathbf{l} \times \mathbf{r}}{r^3}. \tag{2.1}$$

Even for the RF coils, which we run at a maximum frequency of 30 MHz, deviation from magnetostatics is minor [15].

2.5.1 Slower Coils

Going through a nozzle at 450°C, the atoms to be used in experiment are going to be moving very quickly: $\bar{v} = \sqrt{8k_BT/(\pi m)} = 300$ m/s for ytterbium and 1600 m/s for lithium. In order to trap these atoms for experiment, they need to be considerably slowed down, which we do with a Zeeman slower. A Zeeman slower consists of a long solenoid with magnetic field varying along the direction of the atomic beam and a counterpropagating laser beam. The laser frequency $\omega_0 + \delta\omega$ remains on resonance with the atomic transition $\omega_0 - kv + \mu_B g_J B/\hbar$ throughout the length of the slower even as the atoms slow down, as the change in Doppler shift is compensated by a change in bias field. The magnetic field for a maximal slowing profile is

$$B(z) = B_0 \left(1 - \frac{z}{L_0}\right)^{1/2} + B_{bias} \tag{2.2}$$

where L_0 is the length of the Zeeman slower, z is the position along that length and B_0 is the magnetic field to achieve resonance with an atom going at the maximum velocity that will be slowed. If the aim is to have a zero velocity beam at the end of the slower, $B_{bias} = 0$ is ideal. However, there are several reasons why you would want to have a bias field. First, the MOT is not located at the end of the slower, but in the middle of the main chamber, and if the atoms do not have sufficient forwardgoing velocity the beam will "bloom" - spread out too far in the other dimensions to have a reasonable atom flux at the MOT. Additionally, if the slower beam is actually on resonance with 0 velocity atoms, it will cause heating and depletion in the MOT. It is a lot easier to run the experiment if the Zeeman laser beam is well detuned from the atomic transition. Thus, both our slowing arms were engineered to have a large bias field. For ytterbium we constructed an increasing field slower (that is one with 0 field at the entrance, or $B_0 = -B_{bias}$), 45 cm in length. Powered by a 30 A power supply (Sorensen 20-50), it is able to generate up to a $\Delta B_{max} = 480\,\mathrm{G}$. For lithium we used a "spin flip" configuration consisting of two Zeeman slowers separated by a bellows where $B = 0$. The oven is followed by a 60 cm long decreasing field slower, and then after the bellows, a 15 cm long increasing field slower. Such a configuration ensures that we are able to span a large magnetic field range (and thus a high velocity range) without as high a current (or as many coil windings) in any one place. Powered by two 30 A power supplies (Sorensen 20-50), the lithium slower system generates $\Delta B_{max} = 980\,\mathrm{G}$.

The slower coils were hand-wound on a lathe on top of a kapton-covered brass tube from which the completed and epoxied slowers were lifted. In winding, we rotated the lathe shaft (which was in neutral) while feeding from a spool of coil. A special

	MOT (gradient mode)	MOT (bias mode)	Feshbach
Bias (G/A)	NA	2.4	4.2
Gradient (G/cm/A)	1.0	0.3	0.1

Table 2.2: Main chamber coil parameters

wooden "bit" was necessary to ensure the coil would fit snugly. Upon completion of winding, the slower was covered in high temperature epoxy and left to set. Because of the epoxy cover, subsequent baking has converted the slower colour into an uncheery matte black, however, both the epoxy and the kapton tape survived several days of baking at above 200°C.

2.5.2 Helmholtz and anti-Helmholtz coils

The Helmholtz (generates bias field with minimum field gradient and curvature at the atoms) coils are necessary for our experiment in order to provide bias fields. Anti-Helmholtz (generates field gradient with minimum bias field and curvature at atoms) coils are needed to make a MOT and to provide in-trap gradients for species-selective manipulation. Both were designed and built by REU student Nolan Maloney with the help of Lee and Anders. Both coils are kept in place inside the recessed chamber buckets with aluminium brackets.

The anti-Helmholtz coil has been converted by Anders to be switchable, that is, the current direction in one of the two coils can be reversed so that they create a bias rather than gradient field. The switching mechanism, and the control system more generally are well detailed in Chapter 6 of Anders' thesis [51]. The characteristics of the main chamber coils are summarized in Table 2.2. The values obtained there were calibrated using several different methods. One such method used at high fields was narrow p-wave resonance positions in ^{6}Li from [104]. At low fields, the calibration was done using rf transfer between two lowest hyperfine states of lithium.

	Li slower	Yb slower	vertical
#coils	16	20	18
length (cm)	24	32	r =10.5
width (cm)	24	25	
z_{MOT} (cm)	17	14	7
I_{max} (A)	~15	~15	6.25
$B_{max}(z_{MOT})$ (G)	2.7	4.9	3.5
$dB/dz_{max}(z_{MOT})$ (G/cm)	0.3	0.5	0.5

Table 2.3: compensation coil parameters

2.5.3 Compensation coils

There are three sets of compensation coils attached to the chamber, which are wound with HTRG-1CU series wire (Omega), which has an ampacity of 24 A due to an insulation temperature limit of 80°C. Because the compensation coils consist of several strands of wire wound close together and as a result are less air-cooled than one would suppose, the single-wire ampacity is an overestimate, and we can only safely run at about 15 A. This wire has the additional notable feature of causing extreme itchiness. Avoiding skin contact by wearing gloves is advised. The lithium compensation coil is mounted on an aluminium frame that was assembled around the cross separating the main chamber from the ion-pump and Ti:sub pump assembly.and was wound in-situ. It is powered by Xantrex XPD 18-30 power supply, limited to 18 A. The ytterbium slower compensation coil was mounted pre-wound to a similar aluminum frame and put in place between the vacuum chamber and the MOT breadboard. It is powered by Sorensen DLM 20-30 power supply, limited to 30 A. The vertical compensation coil, is wound directly around the vacuum chamber. It is powered by Xantrex XT 7-6 power supply, limited to 6.25 A. The maximum bias field at the atoms is limited by the combination of power supply capabilities and wire ampacity. The current compensation coil parameters are summarized in2.3.

2.5.4 Radio Frequency (RF) Magnetic Field Coils

Although we were not intending to perform RF evaporation in a magnetic trap, we decided to include RF coils for potential use in transfer between Zeeman levels. We followed the design used in Wolfgang Ketterle's group at MIT [15], which consists of two sets of square loops 14 x 2.5 cm of kapton-insulated wire (KAP2 from MDC) separated by 5.4 cm. The current to the wires is delivered through a feedthrough at the bottom of the vacuum chamber. On the exterior, there is a simple BNC plug. The wires themselves are rated to 5.5 A, while the only other limitation is that of the BNC connector. We currently power the coils using a DS345 ssignal generator (SRS), with or without the use of additional RF amplifiers (IntraAction). The currently used signal generator is limited to a maximum RF frequency of 30 MHz.

Chapter 3

LITHIUM, YTTERBIUM, AND LASERS

> Something in that triggered a bunch
> of associations and projections.
> Like, what kind of activities do you
> have to engage in to get to the point
> where you need to bring a laser into
> the equation
>
> Beck

Now that we have our vacuum apparatus all ready, what do we need to conduct our experiment? Lithium, ytterbium, and the lasers to manipulate them. Lasers are integral at every step of our experiment. Initially hot atomic beams are slowed using laser cooling in a Zeeman slower. This is followed by trapping in a laser-derived magneto-optical trap (MOT), and loading into an optical dipole trap (ODT). We evaporatively cool our atoms in the ODT, and then proceed to image our atomic clouds in time of flight with resonant laser light. This section goes over the construction and parameters for the laser systems in use for our mixture experiments. In order to contextualize the laser schemes, I begin with an introduction to the constituent atomic species we use, and their atomic properties.

3.1 Ytterbium

Ytterbium (Yb) is a rare-earth metal with the ground state electronic structure [Xe]$4f^{14}6s^2$. Because the closed f-shell lies below the (also closed) valence s-shell, the low-lying atomic levels have a structure similar to that of alkaline earth metals.

Atomic mass	Natural abundance (%)	Nuclear spin
168	0.13	0
170	3.05	0
171	14.30	1/2
172	21.9	0
173	16.12	5/2
174	31.8	0
176	12.7	0

Table 3.1: Isotopes of ytterbium

An advantage of using Yb for atomic experiments is the existence of several stable bosonic and fermionic isotopes with large natural abundances. This allows for easy switching of atomic statistics, the potential of multi-species Yb experiments, and potentially the ability to vary isotopes to obtain desired scattering parameters. The isotope information is displayed in Table 3.1 . The melting point of ytterbium is 824°C, and at room temperature the vapour pressure is 4.3×10^{-19} Torr. In order to produce a usable atomic beam, we heat our sample to around 375°C, where the vapour pressure becomes 2.6×10^{-4} Torr.

Cold atom experiments in neutral ytterbium are a field of growing interest. The first BECs and DFGs were produced by the Kyoto University group, in ^{174}Yb [116] and ^{173}Yb [37], respectively. Since then, quantum degenerate gases of ^{170}Yb [35], ^{176}Yb [36], ^{171}Yb, ^{172}Yb and, most recently, the rare ^{168}Yb isotope [114] have been reported. The existence of many coolable isotopes which can all be accessed with the same laser setup is of great utility for potential Bose-Fermi, Bose-Bose, Fermi-Fermi mixture studies. Another interesting feature of Yb for us is the existence of accessible metastable states. The $^3\mathrm{P}_0$ state[1] has a theoretical $1/e$ lifetime of at least 16 s for the odd isotopes, and infinite lifetime for the even isotopes [82] and is the so-called "clock state". Because of the long lifetime and lack of magnetic sensitivity, it has been

---

[1] The atomic term symbol nomenclature is given by $^{2\mathrm{S}+1}\mathrm{L}_\mathrm{J}$ for spin, orbital and total angular momenta S, L and J, respectively.

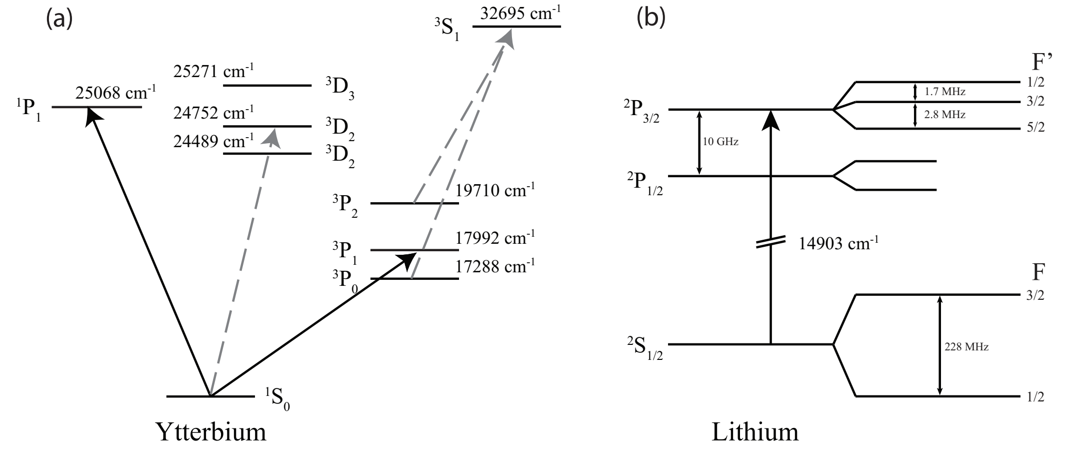

Figure 3.1: (a) Some low-lying levels of ytterbium atom relevant for our experiment. Transitions with arrows are those which we excite in our lab. The black arrows are the cooling, imaging and trapping transitions relevant for the ground state atom, whereas the grey dashed arrows are transitions relevant for metastable state experiments. (b) The D1 and D2 lines in 6-lithium, showing the hyperfine structure.

Property	Symbol	$^1S_0 \rightarrow {}^1P_1$	$^1S_0 \rightarrow {}^3P_1$
Transition wavelength (vacuum)	λ_{vac}	398.911 nm	555.803 nm
Linewidth	$\Gamma/2\pi$	27.9 MHz	182 kHz
Recoil temperature	T_{rec}	172 nK	88 nK
Doppler temperature	T_{Dop}	$670\,\mu$K	$4.35\,\mu$K
Saturation intensity	I_{sat}	57 mW/cm^2	0.14 mW/cm^2

Table 3.2: Properties of ytterbium lines relevant for trapping and cooling

used for state-of-the-art atomic clocks, and is a promising candidate for the optical standard. The $^3P_2$ state is likewise very long-lived ($1/e$ lifetimes of at least 8 s for the fermions and 14.7 s for the bosons [82]) and as a result, these states have been used for extremely precise spectroscopy [127], and have been suggested as a system for simulation of several Hamiltonians of theoretical interest [41, 34]. This has led to experimental interest in ytterbium in the $^3P_2$ state in our lab, an area we will revisit in Chapter **??**.

For our experiment, we primarily use the bosonic ^{174}Yb isotope, although we have

Property	$^1S_0 \rightarrow {}^3D_2$	$^1S_0 \rightarrow {}^3P_2$	$^3P_2 \rightarrow {}^3S_1$	$^3P_0 \rightarrow {}^3S_1$
λ_{vac} (nm)	404.009	507.347	770.161	649.087
$\Gamma/2\pi$	350 kHz	10 mHz	12 MHz	12 MHz
T_{rec}(nK)	168	107	46	65
T_{Dop}	$8.4\,\mu$K	$0.2\,$pK	$288\,\mu$K	$288\,\mu$K
I_{sat}(mW/cm^2)	NA	1×10^{-8}	3.4	5.7

Table 3.3: Properties of ytterbium transitions relevant for the metastable experiment

also worked with others, achieving quantum degeneracy in ^{173}Yb and making MOTs of ^{172}Yb and ^{176}Yb. Some of the low-lying atomic levels of ytterbium are presented in Fig. 3.1 (a). For manipulation of the ground state ytterbium atom, we use the transitions denoted by black solid arrows. The properties of these transitions are given in Table 3.2. Zeeman slowing and imaging proceeds on the $^1S_0 \rightarrow {}^1P_1$ transition. The first ytterbium MOTs were also achieved using this transition, both globally [56] and in our lab. However, due to a Doppler temperature of $670\,\mu$K, the MOT is quite hard to transfer to an optical trap. In addition, the transition is not quite closed, with ~1 in 10^7 atoms decaying to the $^3D_2$ level. Thus we use the $^1S_0 \rightarrow {}^3P_1$ transition. This so-called “intercombination” transition involves a spin flip, and thus is much narrower. The transitions involved in our metastable state work are shown in Fig. 3.1 (a) as grey dashed lines. The properties of these transitions, as well as the direct transition to the $^3P_2$ state are given in Table 3.3.

3.2 Lithium

Lithium (Li) is the lightest alkali-metal atom, with a ground state electron configuration of $1s^2 2s^1$ and a standard atomic weight of 6.94 a.m.u. There are two stable isotopes, bosonic lithium-7 and fermionic lithium-6, with natural abundances of 92.5% and 7.5%, respectively. At room temperature, lithium is a soft white-grey metal, which, like all alkali metals, is readily and quickly oxidized by water vapour in the atmosphere. For everything about lithium from an atomic physicist's perspective, an invaluable resource is Michael Gehm's thesis [38] and "All you need to know about lithium" document, and all numbers presented in this section should be taken to reference these documents unless they specifically refer to our experiment. Despite its low melting point (180°C), lithium's boiling point is quite high (1340°C) and vapour pressure at room temperature is basically nonexistent ($< 10^{-20}$ Torr). Thus, like ytterbium, in order to produce an atomic beam of lithium for experiment, a lithium sample needs to be heated up to around 400°C.

Lithium was one of the first atoms to be successfully laser cooled and trapped during the initial push for the experimental realisation of Bose-Einstein Condensates (BEC). After the initial evidence of BEC in ^{7}Li 1995 [11], a larger, stable ^{7}Li BEC was achieved in 1997 [10]. The first all-optical trapping of ^{6}Li occurred in 1999 [90], followed by a degenerate Fermi gas (DFG) of magnetically trapped ^{6}Li in 2001 [117]. Today, lithium continues to be central to a lot of research in ultracold atomic physics. This is at least partly due to how amenable a lithium system is to studying magnetically tunable interactions. A broad Feshbach resonance between the two lowest magnetic sublevels of ^{6}Li was first discovered in 2002 [91]. Since then, the remarkable stability of this system, as well as the discovery and exploration of other Feshbach resonances in Li [104, 5] has led to a great deal of activity. This has included molecule production [113, 21] the study of molecular BECs [63, 134], the BEC-BCS crossover [6], superfluidity [133], solitons [22, 128], p-wave resonances and exploration of Efimov states. Alternative cooling and trapping schemes are also a hotbed for new research [44, 32].

In our experiment, we use the fermionic lithium-6 isotope. Like other alkali-metal atoms, lithium is straightforward to laser cool, because for all alkalis there is a transition in the visible or near infra-red for which the atom is well approximated as a two-level sytem. In the case of lithium-6, this transition is the $^2S_{1/2} \rightarrow ^2 P_{3/2}$ transition at 671 nm, a $2\pi \times 6$ MHz broad transition which is named the D2 transition in analogy to other alkali atoms and for historical reasons. The relevant information

Property	Value
λ_{vac}	670.997 nm
$\Gamma/2\pi$	5.87 MHz
T_{rec}	3.54 μK
T_{Dop}	140 μK
I_{sat}	2.54 mW/cm^2

Table 3.4: The D2 transition in lithium

on the transition is displayed in Table 3.4. In the ground nuclear state, ^{6}Li has a nuclear spin of $I = 1$. This leads to total spin $F = I + J = \frac{1}{2}, \frac{3}{2}$ in the ground electronic state, and $F = \frac{5}{2}, \frac{3}{2}, \frac{1}{2}$ in the $^2\mathrm{P}_{3/2}$ state. However, the overall hyperfine manifold in the latter is only $2\pi \times 4.5$ MHz broad, and thus individual hyperfine levels are not resolved. As a result, in the presence of imperfect polarization there is strong coupling to other excited hyperfine states. Thus the transition is far from closed and large amounts of light for repumping from the other ground hyperfine state are required. The level structure is shown in Fig. 3.1 (b). The hyperfine splitting between the $F = \frac{1}{2}$ and $F = \frac{3}{2}$ ground electronic states is 228 MHz, which can be easily spanned by an acousto-optical modulator (AOM).

3.3 Light for the Yb 399 nm Transition

Violet light for slowing and imaging is derived from a commercial solid state-diode - tapered amplifier - second-harmonic-generation cavity combination system (TOPtica SHG). About 1.2 W of light at 798 nm is generated. The light is then doubled in a hermetically sealed bowtie cavity containing a LBO doubling crystal, generating anywhere up to 350 mW of 399 nm light. The output power seems to degrade on the weeks timescale due to fatigue in the crystal, and can usually be brought back by moving to a different crystal position. Our standard operating power is around 250 mW, but we have proceeded to experiment with as little as 100 mW. The laser is stabilized via a saturated absorption lock to the $^1\mathrm{S}_0 \rightarrow {}^1\mathrm{P}_1$ line. The power budget

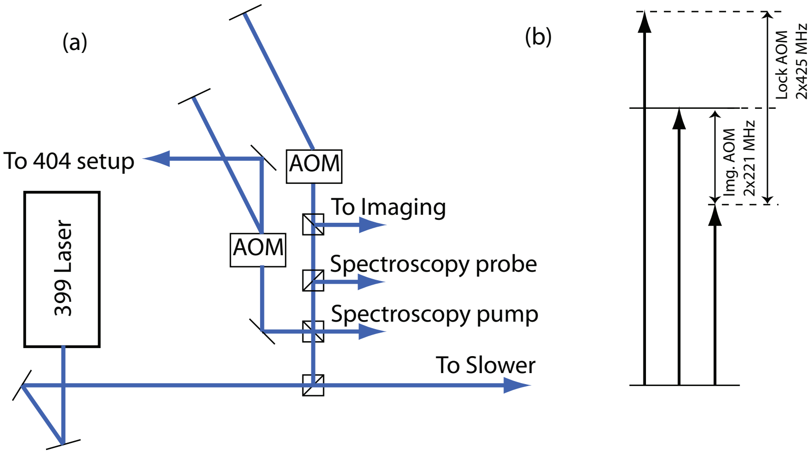

Figure 3.2: (a) Splitting for 399 nm light. (b) frequency schematic for 399 nm light for operation with ^{174}Yb

is roughly as follows: 13 mW for the saturated absorption lock, of which 3 mW is diverted to the metastable lock system, about 10 mW for imaging, and the rest for the Zeeman slower. This typically translates to 100 mW at the slower viewport. The arrangement for the splitting is shown in Fig. 3.2 (a). For operation with ^{174}Yb, the laser is locked 425 MHz to the red of the $^1S_0 \rightarrow {}^1P_1$ transition, corresponding, since the increasing field slower starts at almost 0 G, to a maximum capturing velocity for the slower of 170 m/s. The frequencies bridged by the AOMs are shown in Fig. 3.2 (b). Although in principle, the slower requires σ_+ light, we find that the polarization of the beam does not have an impact on slower performance fo ^{174}Yb (in the case of ^{173}Yb, the correct circular polarization does seem to help). This, and the low maximum slower capturing velocity compared to the average velocity of the Yb beam (300 m/s) implies that the slower parameters could be further optimized by running the slower with higher current and the beam with larger detuning.

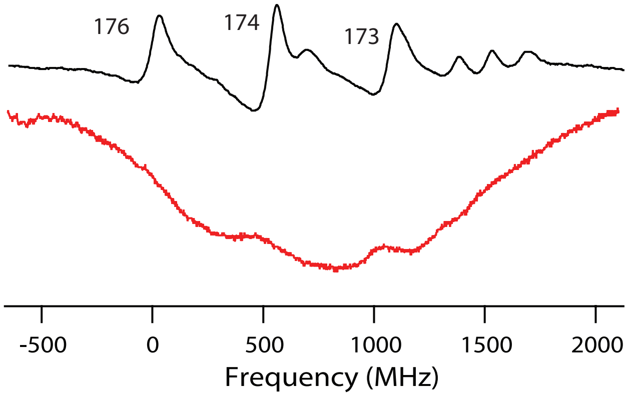

Figure 3.3: Saturated absorption spectroscopy signal for 399 nm laser. The photodiode signal (red) shows the broad Doppler peak and narrow Doppler-free features. Taking the error signal (black) accentuates the Doppler-free features and enables locking to the centre of a Doppler-free feature, which has a large slope in the error signal as opposed to in the photodiode signal itself.

3.3.1 399 nm Lock System

The 399 nm laser is locked to the ytterbium transition by saturated absorption spectroscopy. To obtain the ytterbium gas for spectroscopy we use a hollow cathode lamp (HCL) from Hamamatsu (L2783-70NE-YB)[2]. The principle of saturated absorption spectroscopy is well-described in Chapter 8 of [33]. Our setup consists of a frequency modulated pump overlapped through the HCL with a counterpropagating unmodulated probe beam, which latter is then picked off with a polarizing beamsplitter cube amd imaged on a photodiode. The frequency modulation is dithered at a frequency of about 150 kHz, and the dithering frequency is de-mixed from the resulting photodiode signal in order to obtain an error signal. The photodiode signal we observe and the resulting error signal that we use to lock are shown in 3.3. The compilation of isotope shifts for this transition can be seen in Table 2.2 of [125]. A large enhancement in

---

[2] This is not really relevant, but our Hamamatsu contact at the time of purchase of the HCL had the rather poetic name Dieu Quan, which is no doubt what many French people exclaim after having ordered Hamamatsu products, while waiting for delivery.

signal to noise for the error signal was obtained by switching the modulation from the probe beam to the pump. Modulating the pump ensures that any difference in photodiode signal is due to absorption in the HCL, rather than due to different AO efficiency at different frequencies, etc. This change is achieved at the expense of a greater power requirement (due to low AOM efficiency at 399 nm). We typically run with at least 1 mW of power in the pump beam and 200 μW in the probe. In order to remove the Doppler-broadened features from the background, we have several times attempted to use a second HCL, and difference the saturated signal from a simple Doppler absorption profile. However, we have found tuning the probe power levels and aborption to achieve equal signals on two photodiodes to be quite tricky, and any gains in signal to noise were small and impermanent. Therefore the use of the second HCL has been deprecated, and it has now passed over into the metastable detection laser lock setup[3].

3.3.2 Alternate Schemes

The scheme for generating light at 399 nm has gone through several iterations. At the very beginning, we were using a system inherited from Norval Fortson's laboratory. This consisted of an argon ion (Ar^+) laser pumping a Coherent 899 titanium sapphire (Ti:Sa) laser at 798 nm, which was then doubled in a homeuilt doubling cavity which used a LBO crystal. However, the Ar^+ laser soon began to malfunction, and was replaced by a Coherent V18 Verdi laser at 532 nm. We achieved our first ytterbium MOTs and ODT trapping with this system. However, the weak point here was the Ti:Sa, which had great day-to-day instability and took several hours of tuning most mornings to reach the desired 1.1 W output at 798 nm. Our current 399 nm source arrived amid much fanfare in January 2011, and was instrumental in letting us achieve

---

[3] Subtracting out the Doppler-broadened features may be more useful if we attempt to lock to one of the features at the edge of the spectroscopy signal, which is an overlap of several displaced Doppler peaks, and thus relatively flat close to the middle of the distribution, where both the ^{174}Yb and ^{173}Yb are found.

double degeneracy (see Section 4.3.2). The TA was replaced in the Fall of 2012, boosting the 798 nm power up to 1.2 W, and temporarily boosted our 399 nm power to over 350 mW. Due to greater power and much better medium-scale (day-to-day) power stability of the commercial system, it is that system that is exclusively being used now, and has been used for most of the work described herein.

3.4 Light for the Yb 556 nm Transition

The ytterbium MOT uses the $^1\mathrm{S}_0 \leftrightarrow {}^3\mathrm{P}_1$ intercombination transition at 556 nm as its narrow width ($\Gamma = 2\pi * 182$ kHz) ensures a colder MOT, which simplifies loading into the ODT. The light is derived from a commercial solid-state diode - fibre amplifier - second-harmonic-generation cavity system (TOPtica DL-FA-SHG). Although we have had as much as 400 mW of green light generated by the laser, the current standard is about 260 mW. The laser is locked 392 MHz to the red of the transition. The power splitting is obtained by sending the minimum amount of light possible through a cube to the lock AOM, and the rest to the MOT AOM. We typically have about 70 mW of light before the MOT light is split into three paths.

3.4.1 556 nm Lock System

For the 556 lock, we again (as in Section 3.3.1) use saturated absorption spectroscopy. Due to the narrowness of the transition, the HCL does not provide sufficient absorption at a reasonable temperature. Therefore, we use an evacuated stainless steel pipe with a cup. The construction and testing of the pipe is due to Jason Grad. The cup is typically heated to 420°C. In a previous iteration of the heat pipe, the pipe viewports suffered from an extreme level of ytterbium deposition, becoming indistinguishable from a silver mirror. We got around this issue by extending the heat pipe length, while reducing the pipe inner diameter far away from the Yb sample. In this way, the cup in the center of the pipe is heated as are the viewports (to desorb any ytterbium gas) while in the intermediate region, the pipe dips to near room-temperature, and conduction between the two areas is low. The usual power splitting is about 50 μW for the probe to 450 μW for the pump beams. Because the bulky heat pipe is located on a different table from the laser setup and light needs to be transferred via a single mode fibre that is not polarization maintaining, we are unable to have the pump and probe be at different frequencies, as they are for the 399 nm lock. It also means we can't modulate just the pump, and our signal quality suffers as a result. By far the largest cause of noise is movement of the fibre that carries the light from the laser table to the spectroscopy table. This movement strongly affects the polarization of light output from the fibre, which in turn changes the pump-probe power splitting. A secondary, but also important, source of noise is drifting of alignment into the photodiode.

3.4.2 Alternate Schemes

Initially, green light in our lab was generated by doubling 1112 nm light generated by a Koheras Boostik fibre laser that was inherited from Norval Fortson's lab. The doubling was initially done in a homebuilt doubling cavity that was worked on by Kalista Smith and then Jiawen Pi. Later, we used a single-pass PPLN crystal (HC Photonics). The crystal was heated up to 43.5°C. This system produced up to 30 mW of green light, and was used for the work described in Chapter **??**. However, the low overall power was a limitation to MOT size. The Koheras fibre laser unexpectedly broke in May 2011[4] and took a long enough time to fix[5] that we were forced to look for an alternative green source. Since obtaining the TOPtica commercial system in August 2011, we have repurposed the system for Li-Yb photoassociation, but so far have only used it to perform photoassociation in Yb_2 (see Section 6.3.2).

---

[4] By sheer coincidence, this occurred during an INT conference on degenerate Fermi gases, thereby disappointing several visiting ultracold atomic experimentalists who had come down for a lab tour

[5] due to seemingly silly-sounding issues such as a new hire in Koheras' receiving department, the fact that this department was located in a different building from the engineering department, etc. etc.

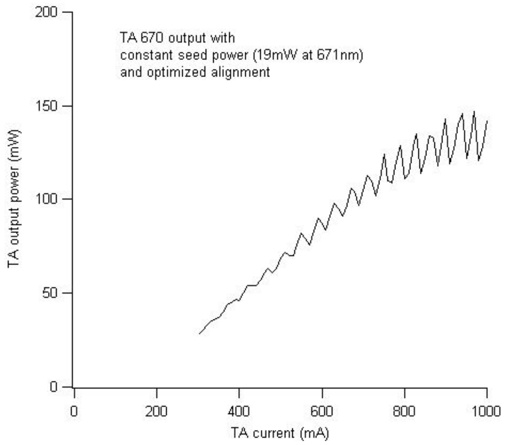

Figure 3.4: Behaviour of broken 670 nm TA

3.5 Light for the Li 671 nm Transition

In contrast to the ytterbium system, for lithium we use one transition for slowing, imaging and the MOT. The light is generated by a TOptica DL-100 laser that was one of the first purchases for the lab. The laser consists of a single mode diode in an ECDL (20 mW after the isolator) that feeds a tapered amplifier (TA). Over the last six years this laser has been somewhat reliable, staying in the 300-350 mW range for the majority of the time. However, it has not been entirely without issues. First, within a year of purchase, the TA had to be replaced due to oscillatory behaviour of seeded TA power with increased current (see Fig. 3.4). At the same time, one of the two isolators in the system was also found to be faulty. The TA problem reoccurred about half a year later. We have also replaced the ECDL piezo several times (until a new piezo model was developed by Toptica) as well as the master diode (we now use an Eagleyard ridge waveguide diode). In October 2011, the laser began to exhibit a strange behaviour where the running TA current would suddenly drop by about 20 mA (from around 920 mA). The feedback circuit would attempt to recover the current by increasing voltage, tripping the TA voltage limit. Then, about a minute

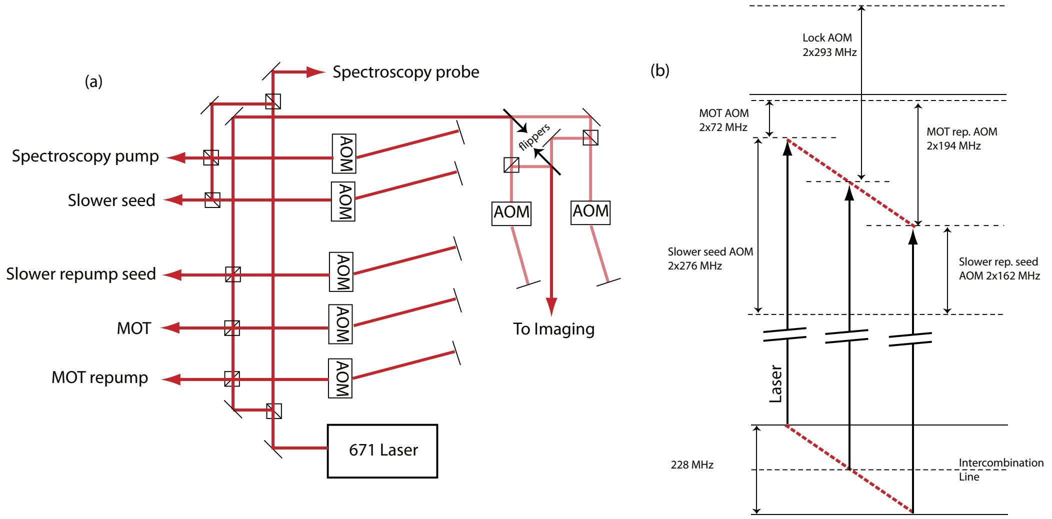

Figure 3.5: (a) Splitting arrangement for 671 nm light (b) Schematic of various laser frequencies obtained

later, the current would bounce back to normal. This issue lasted about a week, but then disappeared only to reoccur about a year later. Luckily, we were somewhat removed from the absolute maximum TA voltage and so could increase the setpoint for TA voltage limit. However, it is unclear what is causing these sporadic dips in TA current. The problem is transient in nature, and it is hard to tell whether it has been dealt with. Additionally, the mode of the DL-100 remains a problem. It is especially evident in the profiles of the MOT and MOT repumper light beams, which go through an AOM each, but are not thereby cleaned. A potential near future upgrade could be the coupling of MOT and repumper light into a fibre. The schematic for power splitting is shown in Fig 3.5 (a). Our typical minimum values for the AO branches are 110 mW for the MOT, 40 mW for the MOT repumper, 16 mW for the slower injection, 7mW for the slower repumper injection, 30 mW for the lock and 20 mW for imaging. The frequencies obtained by AOMs are shown in Fig. 3.5 (b).

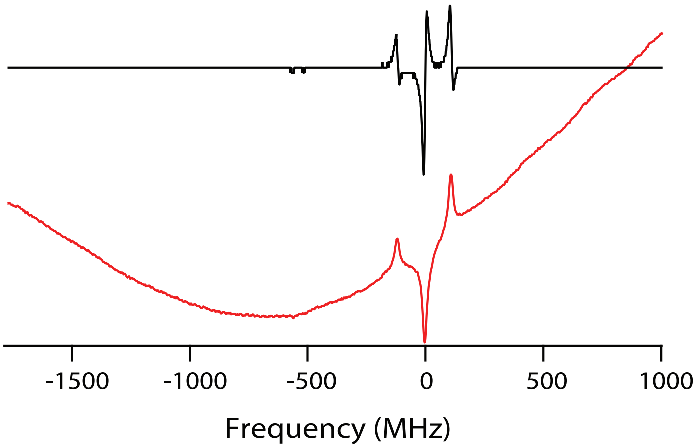

Figure 3.6: Lithium spectroscopy signal on the photodiode (red) and the resulting error signal (black). The residual signal from 7-lithium remaining in the can be seen on the error signal detuned by roughly 500 MHz to the red of the crossover peak.

3.5.1 671 Lock System

Once again, we use saturated absorption spectroscopy, modulating only the pump beam, using the same arrangement as in Section 3.3.1. The absorption signal, obtained by passing the beams through a heat pipe with the cup heated to 360°C, is shown in Fig. 3.6. We lock to the crossover peak. The heat pipe was originally filled with 5g of 7-lithium, then with 5g of enriched 6-lithium. Thus we have mostly worked with a 50-50 mixture, which is useful for telling the 6-lithium D2 and D1 lines apart. Recently we had issues with transmissivity of the heatpipe viewports due to lithium deposition. Attempting to deal with this by heating the viewports beyond 200°C have led to requiring viewport replacement. When the pipe was opened to make this replacement, we decided to put in an additional 5g of 6-lithium, so the overall isotope ratios have changed. We also noticed the extreme gumminess of the walls of the heatpipe, even well away from the cup. Thus we conclude that a large amount of lithium has travelled far away from the cup and condensed there, where it can't be easily heated back up.

3.5.2 Injection Locked Diode System for the Slower

In Section 2.5.1, I gave the average velocity of the lithium beam as 1600 m/s, which corresponds to a Doppler shift of 2.4 GHz. This explains the spin-flip slower arrangement, but we are still saddled with a large frequency shift. Low maximum efficiency of the AOMs required to span frequency differences of this magnitude contrasted with the large amount of power we want for the slower led us to using an injection locked diode as an amplifier. The diode is placed in a Thorlabs TCLDM9 diode mount. One thing to note about the diode mount is that when the specifications say that 70°C is the damage threshold for this mount, they really mean it. Our first diode mount broke immediately upon being taken to 72°C. The success of injection can be measured using a metric jocularly called "The Booth Factor," after a member of Kirk Madison's group at UBC [120]. This is defined as

$$f_B \equiv \frac{(P_{seeded} - P_{unseeded})\Big|_{threshold}}{P_{reflected\,seed}}, \tag{3.1}$$

that is, it compares the maximum power of the seeding light reflected by the diode when it is off to the difference in diode power when the seed light is on. Generally, the diode will remain reliably seeded at operating current whenever near threshold you can find a location with$f_B \gtrsim 10$. After a relatively extensive diode search, we currently use LD1779 diodes (PowerTech) run at 69.3°C with 200 mA of current at operation. This diode gives a $f_B \gtrsim 25$ and we obtain up to 35 mW of seeded light at the slower viewport. We can also achieve similar results using ML101J27 diodes (Mitsubishi) at a comparable temperature and overclocked to 370 mA. Typically we have the overall seeding power at about 2 mW before the isolator, with about 80% of the power for the $|F = 3/2\rangle \rightarrow |F' = 5/2\rangle$ transition and 20% for repumping from the other ground hyperfine state on the $|F = 1/2\rangle \rightarrow |F' = 3/2\rangle$ transition. This leads to a diode output with the carrier frequency given by the main injection signal

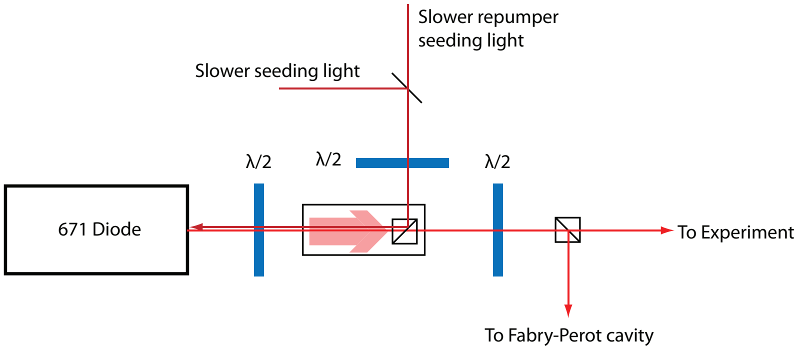

Figure 3.7: Seeding scheme for slower diode

and sidebands on either side offset by the beatnote between the two injection signals. Optimal MOT load speed is achieved with a carrier : sideband ratio of roughly 10 : 1. We verify the seeding by sending a portion of the diode light into a Fabry-Perot cavity (Thorlabs; 1 GHz FSR, 750 nm centre). The seeding scheme is shown in Fig. 3.7 .

3.6 Optical Dipole Trap

The cooling in a MOT is limited by the recoil momentum imparted by each photon, and, more crucially in the case of ytterbium and lithium, neither of which are well-suited to sub-Doppler cooling[6], by the Doppler temperature of the cooling transition. Thus, in order to cool to high phase space densities, a different cooling method is required. We use evaporative cooling, which is normally performed in an optical or magnetic conservative trap. Since ground state ytterbium is magnetically insensitive, an optical trap (ODT) is the clear choice.

The optical dipole trap works on the principle of the dipole force, $F = -\nabla U_{dipole}$, due to the interaction of the trap light with the induced dipole of an atom, causing a force in the direction of sharpest intensity gradient. By treating each transition as

---

[6] Although there has now been some very recent success in sub-Doppler cooling of lithium [44, 48], the schemes to do so are quite complex

a 2-level system, we can obtain the contribution of each individual transition to the trap depth

$$U_{dipole} = \frac{\hbar\Gamma^2}{8}\frac{I}{I_{sat}}\left(\frac{1}{\omega-\omega_0}+\frac{1}{\omega+\omega_0}\right), \tag{3.2}$$

where Γ, ω_0 and $I_{sat} = \omega_0^3 h\Gamma/(24\pi^2c^2)$ are the linewidth, frequency and saturation intensity of the transition, and ω and I are the ODT frequency and intensity, and the trap depth is further scaled by the Clebsch-Gordan coefficient for the transition given the ODT polarization. Meanwhile, the scattering rate from the same transition is

$$\Gamma_{scatt} = \frac{U_{dipole}\Gamma}{\hbar}\left(\frac{1}{\omega-\omega_0}+\frac{1}{\omega+\omega_0}\right), \tag{3.3}$$

which implies that to get a large dipole force while reducing scattering requires a high power beam at a large detuning. The total trap depth can then be obtained by summing the individual contributions from each relevant transition and the atomic polarizability α is given as $\alpha = 2U_{dipole}/\mathcal{E}^2$ where $\mathcal{E}$ is electric field strength. A simple approximation for the $^2\mathrm{S}_{1/2}$ state of lithium is that only transitions to $^2\mathrm{P}_{1/2}$ and $^2\mathrm{P}_{3/2}$ are relevant, giving a polarizability of $8.35 \times 10^{-37}\,\mathrm{m^2s}$. Similarly, for the $^1\mathrm{S}_0$ state in ytterbium, only transitions to $^1\mathrm{P}_1$ and $^3\mathrm{P}_1$ need be considered, and give a polarizability of $3.58 \times 10^{-37}\,\mathrm{m^2s}$. For metastable ytterbium, the situation is more complicated, as approximating transitions as 2-level systems is clearly wrong. In addition the allowed transitions, and thus the scattering rate, are magnetic substate dependent. Keeping in mind that our ODT is π-polarized, the $m_J = 0$ state should be most closely linked with $^3\mathrm{S}_1$, $^3\mathrm{D}_1$ and $^3\mathrm{D}_3$ states; the $m_J = \pm 2$ states with $^3\mathrm{D}_1$, $^3\mathrm{D}_2$, $^3\mathrm{D}_3$ and $^1\mathrm{D}_2$; the $m_J = \pm 1$ states with all of the above. For a more complete picture, including polarizability values calculated at a wide range of wavelengths by the Kotochigova group at Temple University, and experimentally obtained for three substates for our trap, see Section 7.3.

3.6.1 Trap Characterization

Our optical trap is derived from a 100W single transverse-, multi longitudinal-mode fibre laser (IPG Photonics YLR-100-1064-LP). The laser power can in principle be controlled externally, but this requires extreme caution (we broke the laser by doing so, as the laser is not stable at a total output below 20 W). Instead, we use a high power AOM (IntraAction). The various ODT trap geometries we have used in our lab are shown in Fig. 3.8. Initially, we adopted a scheme of almost-retro reflection. However, we saw a polarization dependent loss for lithium atoms in the trap. This loss limited our trap lifetimes to a maximum of 5 s (in the perpendicular polarization arrangement). The source of this loss remains a mystery, however, it is possible that stimulated Raman transitions with absorption from one beam and emission into the other were occurring at sufficiently high rates to heat the atomic cloud significantly and cause evaporative loss. We then moved to a scheme where the first pass beam was recycled by being recollimated and passed over the lithium and ytterbium slowers at glancing angles. This scheme solved the lithium lifetime issues, but was problematic for alignment as it consisted of using several optics that were not vibrationally coupled to each other, but, standing on extremely long posts, were quite vibrationally unstable. Although we performed some of the experiments detailed in Chapter **??** with this arrangement, it required too much day-to-day maintenance. Additionally, we found the alignment of the first pass and second pass beams would be dependent on overall beam power. We currently believe this to be due to thermal lensing in the AOM crystal and chamber viewports, which shifts the focus of the first pass beam closer to the laser source at higher powers, affecting alignment downstream. Finally, we settled on splitting the intial beam into two beams using a waveplate-beamsplitter combination immediately after the AOM. This arrangement has the additional advantage of making the two beams independently controllable and the power splitting tunable. A disadvantage is that the overall power at the atoms is half of what we

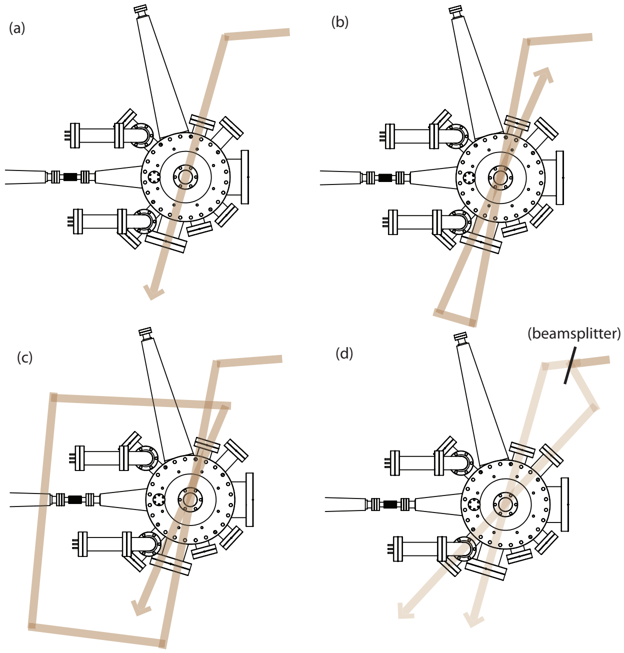

Figure 3.8: ODT geometries in top-down view. (a) Single beam setup (b) “almost-retro” setup (c) “beam recycle” setup (d) Split-beam setup

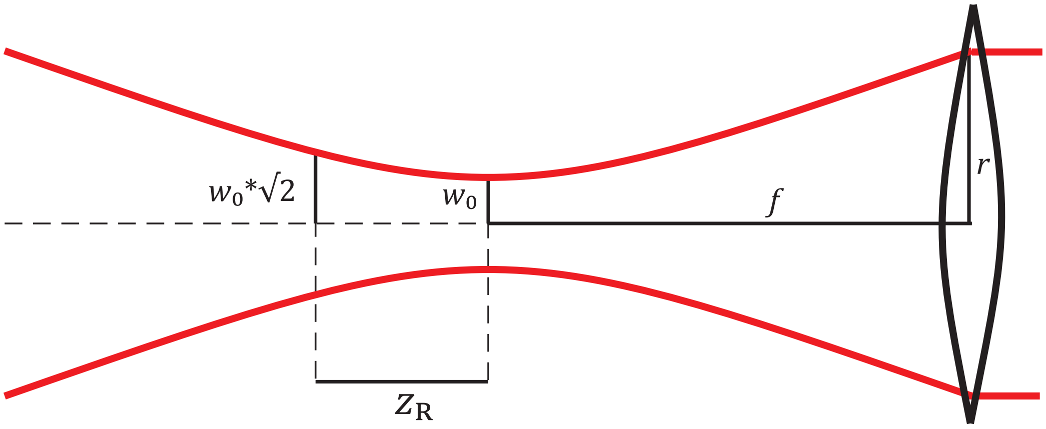

Figure 3.9: Geometry of a Gaussian beam

would get with a recycled beam. In principle, this can be mitigated by running the ODT laser at higher power, but here again we run into the thermal lensing issue. Currently, we run the IPG laser at 30-32 W, which allows us to reach the optimal trap depth for loading the ytterbium MOT, but is below the power needed to achieve the optimal lithium MOT load. However, this low laser power improves the stability and reproducibility of the trap. We keep the ODT AOM turned off for nearly the entirety of the ytterbium MOT load step to further reduce thermal effects.

In the absence of strong thermal lensing effects and other aberrations, we can treat, a single ODT beam as a Gaussian beam, where intensity is given as

$$I(r,z) = \frac{2P}{\pi w(z)^2} \exp\left(-\frac{2r^2}{w(z)^2}\right) \tag{3.4}$$

where P is the power and r and z are the radial and axial displacement from the focus of the beam. The definition of the waist $w(z)$ is then the radial distance from centre at which the intensity is $1/e^2$ that at the centre of the beam at a given z value. The waist at $z = 0$, usually denoted w_0 is a useful parameter. An analogous length parameter in the axial direction is the Rayleigh length

$$z_R = \frac{\pi w_0^2}{\lambda} \qquad w(z) = w_0\sqrt{1+\left(\frac{z}{z_R}\right)^2}. \tag{3.5}$$

The Rayleigh length gives the axial distance at which the $1/e^2$ spot size is double that at $z = 0$, and approximates the range over which the trap can be thought of as harmonic. The beam focus parameters can be related to the optics used to form the focus as

$$\frac{r}{f} = \frac{\lambda}{\pi w_0} = \frac{z_R}{w_0} \tag{3.6}$$

where f is the focal length of a lens, and r the radius of a collimated beam impinging upon the lens, limited by its size. The relevant distances are shown in Fig. 3.9. In order to obtain these trap characteristics experimentally, we treat the ODT as a harmonic trap. The trap frequencies in the radial direction is given by the familiar $U = \frac{1}{2}m\omega_r^2 r^2$, and similarly for z in the axial direction. Making the identification $I(0,0) = U_{dipole}/\alpha$ and Taylor-expanding about $r = 0$ in Eq. 3.4, we get

$$\frac{2r^2}{w^2}U_{dipole} = \frac{1}{2}m\omega_r^2 r^2 \;\rightarrow\; \omega_r = \sqrt{\frac{4U}{mw_0^2}} \tag{3.7}$$

where m is the mass of the atomic species, and ω_r is the frequency of radial oscillation. Experimental input for ω_r in conjunction with Eqs. 3.7 and 3.2 can be used to determine the waist of our beam. An analogous procedure can be used for the Rayleigh length. We obtain this experimental input by perturbing the trap in one of two ways. In the first, we amplitude modulate the trap depth around a certain value, which deposits energy into the system if the modulation frequency is around the parametric resonance frequency (double the natural frequency of the trap) and its harmonics. An example scan showcasing two frequencies is shown in Fig. 3.10 (c). Although we obtain resonance signatures in both cloud size and atom number, the cloud size signature is the more reliable of the two. In order to leave the trap, an atom would have to traverse anharmonic regions of the trap, where it will be parametrically excited at a different (lower) frequency. Thus in general, we find the loss maxima to be located at lower frequencies than maxima obtained from cloud size measurements. The second way to determine trap frequencies is to disturb the trapped cloud and monitor oscillation frequencies in the trap. Our preferred method is to suddenly squeeze from a shallow trap to the desired trap depth and monitor cloud size as a function of time, which oscillates at double the natural frequency of the trap due to quadrupolar breathing modes. An example is shown in Fig. 3.10 (b). An additional advantage of this method is that unlike parametric excitation it can distinguish between the two radial directions. Other methods of disturbing the trap, such as turning the trap off and then back on to displace the cloud centre vertically from its equilibrium position, are also possible.

In the absence of gravitational effects, the ratio of trap depths for the same trap will be $U_{Li}/U_{Yb} = \alpha_{Li}/\alpha_{Yb} \approx 2.2$, and the ratio of trap diameters at the same temperature, and well away from quantum degeneracy are $x_{Li}/x_{Yb} = \sqrt{U_{Yb}/U_{Li}} \approx 0.7$ (see Fig. 3.10 (a)). This determines the method of cooling used in combined experiments, as the shallower trap for ytterbium means that with clouds thermally equilibrated, ytterbium will evaporatively cool much more readily, and then will sympathetically cool lithium.

The extension of trap characterization to elliptical waists (separation of w_0 into w_{0x} and w_{0y}) and two beams (addition of frequencies in a rotated frame) are straightforward as long as the foci are collocated. The most recent work done in our lab has been done in a single beam trap using the vertically polarized ODT beam ("beam 1"), with radial trap frequencies determined by excitation of quadrupolar breathing modes and the axial trap frequency determined by parametric excitation. From trap frequency ratios and beam power we deduce an elliptical waist of $17\,\mu$m in the vertical and $32\,\mu$m in the horizontal direction, and high-depth trap depths for our species

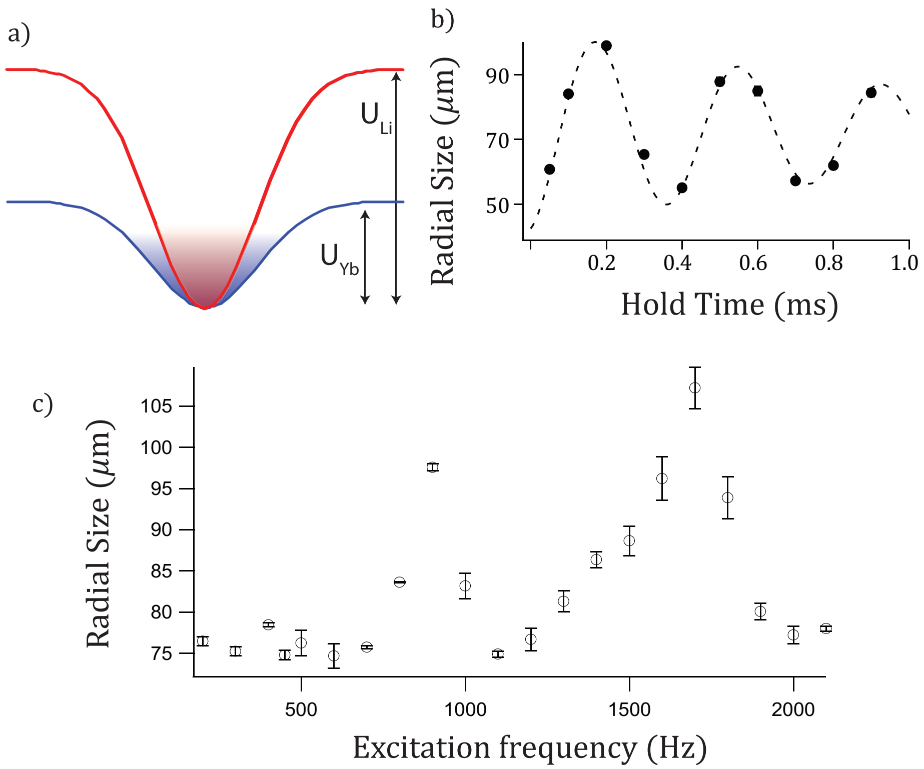

Figure 3.10: Our optical trap. (a) Ratio of trap depths and diameters at large trap depth. (b) Sample trap frequency obtained by measuring of cloud size after exciting a quadrupolar breathing mode (c) A frequency scan showing parametric excitation resonances.

of $U_{Yb\,(Li)} = 30\,(70)\,\mu\mathrm{K/W}$. Gravitational sag complicates the situation by adding a vertical gradient to the trap profile. The sag, which leads to a separation of ytterbium and lithium clouds at low trap depths, as well as a method for cancelling the separation through species-selective manipulation are treated in-depth elsewhere [50, 51].

3.7 Absorption Imaging System

The vast majority of data collection in our lab proceeds through the technique of absorption imaging in time of flight. Beer's Law dictates the absorption of light by a gas:

$$I = I_0 e^{-\sigma \int n dz}, \tag{3.8}$$

where I_0 is the ingoing intensity, I is the outgoing intensity, n is the number density of the gas, which is integrated along the direction of light propagation, and σ is the cross-section for absorption of light by an atom of the gas. Thus, we can obtain column density information about our cloud of atoms, and integrating along the two dimensional image, can extract atom number. Rather than an intensity value, each pixel of the camera reports photon counts, which includes dark counts as well as background light. Three images - the image of the atoms (I), the light without the atoms (I_0), and a background shot with neither light nor atoms (B), need to be taken. Thus the number of atoms pictured can be calculated as

$$N_{atoms} = -\frac{MA}{\sigma} \sum_{x,y} \ln \frac{I_{x,y} - B_{x,y}}{I_{0x,y} - B_{x,y}}, \tag{3.9}$$

where x, y are for the indices for a given pixel, M is the magnification value, A is the area of each pixel. In the case of imaging two collocated clouds of different species, the

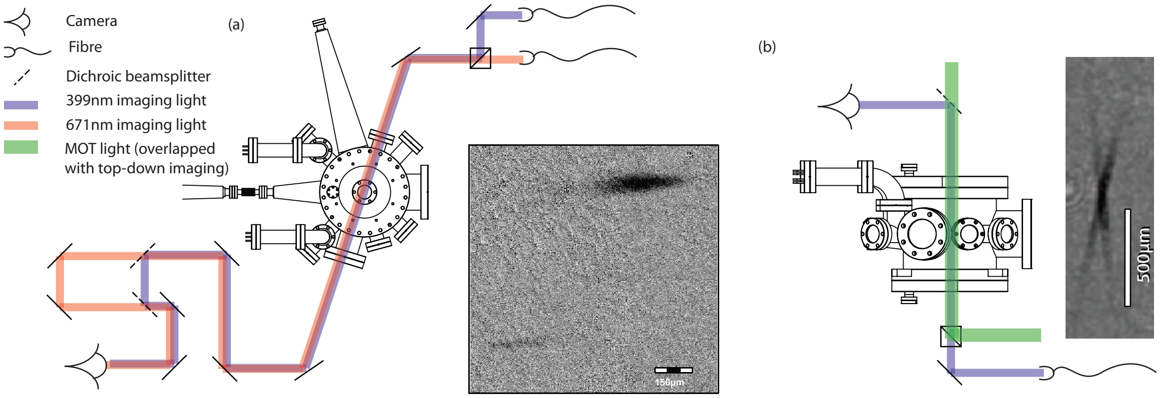

Figure 3.11: (a) current scheme for "side imaging". Inset shows a simultaneous picture of collocated ytterbium (top right) and lithium (wispy cloud at bottom left). (b) "Top-down imaging". Inset shows a picture of Yb in an XODT

above method can be modified to give simultaneous atomnumbers for both species:

$$N_{Yb} = -\frac{MA}{\sigma_{Yb}}\sum_{x,y}\ln\frac{I_{x,y}-L_{x,y}}{Y_{x,y}-B_{x,y}} \tag{3.10}$$

$$N_{Li} = -\frac{MA}{\sigma_{Li}}\sum_{x,y}\ln\frac{I_{x,y}-Y_{x,y}}{L_{x,y}-B_{x,y}} \tag{3.11}$$

where L and Y are images with just the lithium-resonant, and just the ytterbium-resonant imaging light, respectively. The above equations clearly fail for a pixel that contains both species of atoms (because there is no way to differentiate absorption from one beam from absorption by another). Thus it requires clouds that are well-separated on the camera. In order to achieve this, we require separate paths for the two imaging beams. This is achieved by first combining the two imaging beam paths at a polarizing cube before the chamber, splitting them after the chamber using a long-wave-pass beamplate (CVI model LWP-45-RS400-TP670), and then nearly combining them again at a second such beamplate. The entire arrangement is shown schematically in Fig. 3.11 (a), while an inset shows an example of a single image containing both an ytterbium cloud and a lithium cloud, which are collocated in reality but displaced on-screen.. In order to obtain absolute rather than proportional number information, we must know the absorption cross-section, σ, which strictly speaking depends on detuning, saturation parameter, polarization of the light, and the resonant dipole absorption cross-section given by $3\lambda^2/2\pi$. In terms of imaging beam intensity, a balance needs to be struck between sufficient signal-to-noise on the camera from absorption, and being far away from the saturation regime. We routinely use about 200 (150) μW of 399 (671) nm light, collimated and at an average intensity of ~3 (1.5) mW/cm^2. An additional complication for lithium imaging is the need to repump atoms from the other ground hyperfine state during the duration of imaging.

3.7.1 High-field imaging for lithium

We ordinarily trap both the $|F, m_F\rangle = |1/2, 1/2\rangle$ and $|1/2, -1/2\rangle$ states of Li, which are degenerate at zero magnetic field. We need a means of discriminating those two states as a diagnostic and the ability to selectively populate the states for some applications (*e.g.* looking for specific Feshbach resonances). We achieve this by using a bias magnetic field, which splits the two states, one of which can then be imaged or cleared out. The behaviour of substates of ^{6}Li as a function of magnetic field are shown in Fig. 3.12. Currently, our setup consists of using an alternative AOM for high-field imaging, This corresponds to 528 G for state $|1\rangle$, and 475 G for state $|2\rangle$[7]. These values are chosen somewhat arbitrarily, but their proximity to a zero-crossing of the s-wave scattering length for $|1\rangle + |2\rangle$ (527 G) ensures there are unlikely to be any collisions between states $|1\rangle$ and $|2\rangle$ during a clearing step. An additional advantage of high-field imaging is that it does not rely on repumping during the imaging step, and thus the atom numbers are potentially more reliable. We use the same AOM driver as for the zero-field imaging AOM and control the light path using flipper mirrors. However, the lack of ability to do *both* high-field clearing and zero-field imaging in

---

[7] The ordering, which is counterintuitive if you consider Fig. 3.12, is due to the magnetic field dependence of the excited state

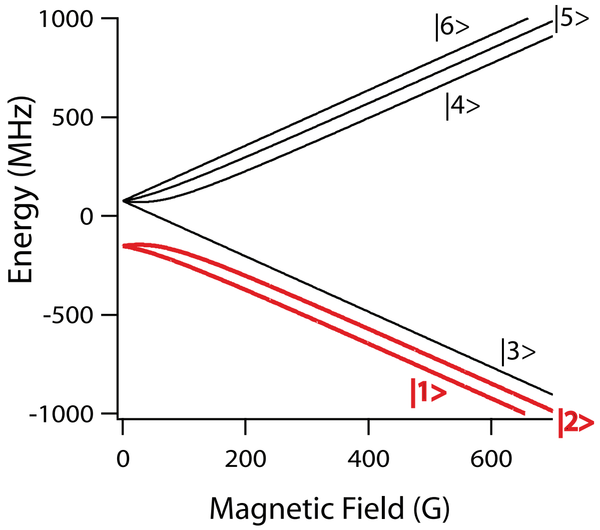

Figure 3.12: Breit-Rabi diagram for lithium-6.

one sequence is somewhat limiting, and may need to be addressed in the future.

3.7.2 Magnification calibration

Although in principle the magnification is easily calculated from the optics used in the imaging path, the reality is slightly more complicated. The achromatic optics used for the imaging path are not exactly achromatic, neither are the viewports. There may be some slight error in optics placement, and in any case the atomic clouds can have varying position and extent, and the paths for ytterbium and lithium images are slightly different. This all means that the magnification of the imaging system needs to be calibrated, which is done in one of several ways. The first of these is by the use of a test pattern (Edmund) which gives us both the magnification and resolution of a path, and which we use to calibrate using a path we believe to be equivalent to the imaging path. However, placing the test pattern at the exact location of our

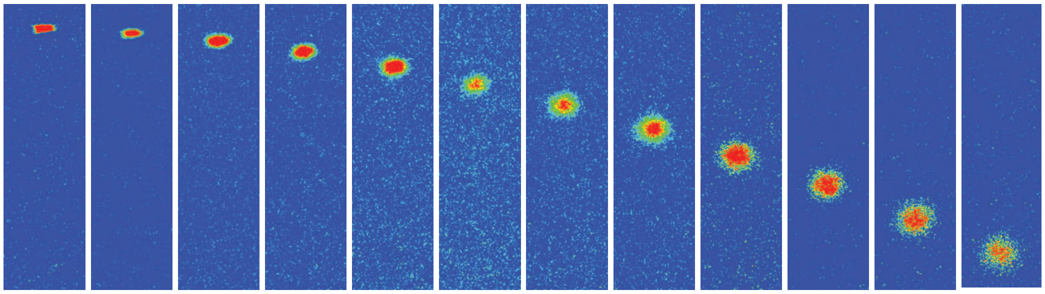

Figure 3.13: Ytterbium clouds falling under influence of gravity

atomic trap, i.e. inside the vacuum chamber, is neither possible nor desirable. To calibrate the images of atoms more directly, we initially use gravity measurements, since we know g relatively well. A complication arises if the atoms have some residual centre-of-mass motion at the time they leave the trap, but if we image from an ODT rather than from a MOT, this is unlikely, and can, in any case, be corrected for. A sequence of images of a thermal cloud of ytterbium falling under the influence of gravity is shown in Fig. 3.13. Due to its smaller mass, clouds of lithium typically expand too fast to make gravity measurements reliable. Instead, we use temperature measurements. Over several seconds within the trap (just how long this takes will be discussed in Chapter **??**), lithium and ytterbium clouds thermally equilibrate with one another as long as they remain in thermal contact. Thus the long-time temperature ratio can be used to recalibrate the lithium mganification if ytterbium magnification is known.

3.7.3 Alternate Schemes

Throughout the years, a wide variety of imaging schemes have been used. The primary difference has been in the camera and software used. We began by using a PI Acton inherited from Norval Fortson's group, with a 24 μm pixel size, and with WinView as the image acquisition software. Although this system was sufficient for our needs, we faced a slow deterioration in the mechanical shutter separating the CCD plane from the lab. Initially we were forced to use "dummy images" during data collection in order to warm up the shutter mechanism, and a liquid crystal shutter to prevent stray light depositing on the CCD. However, the mechanical shutter was becoming progressively less reliable, requiring multiple "dummy" images or several runthroughs of the experiment to obtain usable data. The imaging surface also developed Airy ring patterns which added noise to our data. Thus in January of 2012, we switched to the currently used system of Andor camera and acquisition software. The Andor camera has a pixel size of $8\,\mu$m, allowing for finer resolution, and a fast internal shutter which removes the need for both the liquid crystal shutter and for sdummy images.

One thing to note about our most common imaging setup ("side imaging") is that we are not imaging along a primary axis of the trap. In the crossed ODT case with equal beam powers, the imaging beam is at an angle of 17° to the trap's longitudinal axis, and in the case of a single-beam ODT using beam 1, the angle is 8°. We do not align our imaging beam to the ODT axis because that would be problematic from a setup perspective, but also because the longitudinal axis is "special" and we want some ability to obtain information about that axis, even if we get it in foreshortened perspective. Nevertheless, the difference from on-axis imaging provides a complication when dealing with excitations in the trap (e.g. for frequency measurements) or quantum degeneracy. At the same time, the angle is often too small to get the necessary information about the longitudinal axis. One attempted solution is to perform imaging along the vertical axis ("top down imaging"). The scheme, and an example image of a crossed ODT, are shown in Fig. 3.11 (b). Reduced numerical aperture and smaller experimental atom numbers due to interference between imaging and MOT optics have so far prevented us from using top-down imaging on a more frequent basis.

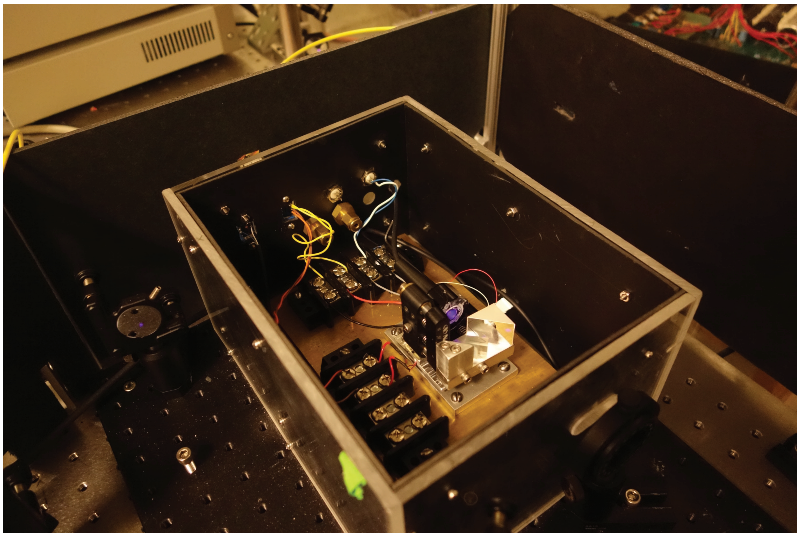

Figure 3.14: Homebuilt grating-stabilized diode laser

3.8 Laser for the Yb 404 nm transition

The 404 nm transition is an electric quadrupole transition centred at 24751.948 cm^{-1}. We derive light for the transition from a ML320G2-11 diode (Mitsubishi) in an ECDL in the Littrow configuration. The homebuilt ECDL was made by REU student Carson Teale. The diode centre frequency is 403 nm, but with a combination of temperature and grating tuning, it can easily span several nm in either direction. A photo of our laser is shown in Fig. 3.14. The isotope shifts are given in Fig. 2.15 of [125]. We find the ^{174}Yb transition around 24751.924 cm^{-1}. In order to retain single mode operation of the diode, we generally have to run well away from the operating current (120 mA), running insteard at about 70 mA. This corresponds to about 6 mW of power at the diode. We typically have a total of 1 mW power at the atoms, split roughly evenly between two counter-propagating beams, and focussed to an intensity of $5 \times 10^4\,\mathrm{mW/cm^2}$.

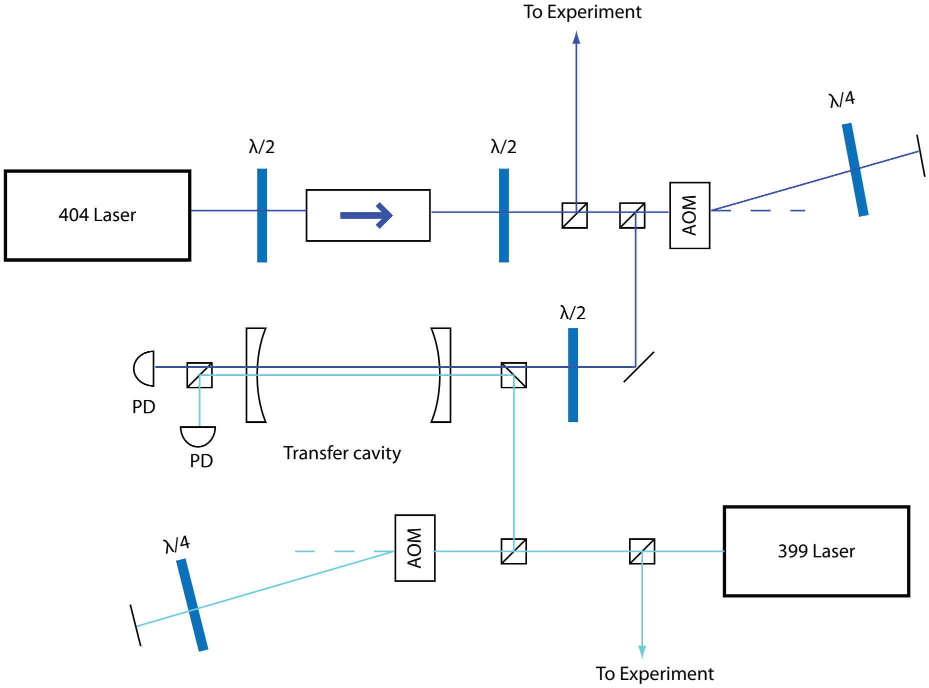

Figure 3.15: Optical scheme for 404 nm laser lock

3.8.1 Transfer lock

Stabilizing the 404 nm ECDL in the same manner as other lasers in our lab is not possible, because the weakness of the transition makes it difficult to use standard saturated absorption spectroscopy methods. We have attempted to use the saturated absorption spectroscopy cell for the 556 nm lock (see Section 3.4.1), but have not seen a signal. Instead, we follow the long-term stabilization scheme detailed in [119]. We use the 399 nm light to lock the length of a transfer cavity, and then lock the wavelength of the 404 nm, in principle transferring the width of the source laser to that of the target laser. The optical arrangement is shown in Fig. 3.15. We use a Thorlabs confocal Fabry-Pérot cavity (SA200-3B). The lock scheme is shown in Fig 3.16. We test the width of the lock by resonance scans on the $^1S_0 \to {}^3D_2$ transition. Our best values for lock width are about 3 MHz.

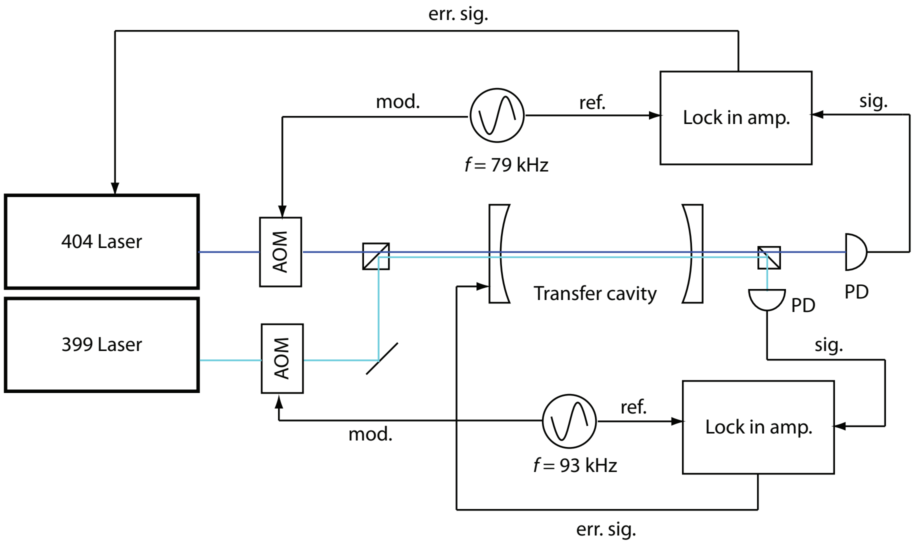

Figure 3.16: Electronic scheme for 404 nm laser lock

The nature of the lock means that noise from the 399 nm lock is transferred to the 404 nm laser, and so signal-to-noise of the 399 nm lock is important for 404 lock consideration. The lock point determination requires the use of a wavemeter in addition to the 399 nm light. The cavity free spectral range (FSR) is 1.5 GHz, which is much greater than the drift of the 404 laser; however, because the cavity length itself can be tuned through several FSRs, there is an additional source of ambiguity. The transfer lock relies on matching the number of wavelengths of 404 and 399 nm light in the cavity. There are several ways to achieve such a match, meaning that depending on how the cavity is locked to the 399 nm light, the lock point for 404 nm will dirft by

$$N_{399} = \frac{2L}{\lambda_{399}} \approx 250682; \quad N_{404} = \left\lfloor \frac{2L}{\lambda_{404}} \right\rfloor \approx 247519; \tag{3.12}$$

$$\Delta\nu_{404} = \frac{c}{2\lambda_{399}} \left(\frac{N_{399}}{N_{404}} - \frac{N_{399}-1}{N_{404}-1} \right) \approx 18.9\, MHz \tag{3.13}$$

which is well within the frequency range for laser drift. This is further complicated by environmental conditions, which have an effect on the differential index of refraction. There is considerable variability in room conditions in our lab. We do not monitor the pressure, but anecdoatal observation of occasional strong pressure gradients between our lab and the corridor, the corridor and our neighbouring building (Kincaid Hall) (in each case causing winds and slamming doors) that seem to happen without any notable change in the weather or atmospheric pressure, leads me to believe that pressure changes within our lab could also be occurring. The refractive index of air for specific wavelengths can be calculated using the modified Edlén equation, a phenomenological tool to calculate indices of refraction where

$$n = 1 + \frac{P}{D}\frac{(1 + (E - FT)P)}{1 + GT}, \tag{3.14}$$

where P is pressure, T is temperature, and $A - K$ are specific constants. In addition there is a corrective term for relative humidity. For the values of the constants and explication of the equation, see [112, 7]. For a reasonable range of lab temperatures and pressures, we can expect frequency drifts of the scale of 3 MHz. A further complication is the not-quite confocal-nature of our confocal cavity.

3.9 Lasers for the Yb 649 and 770 nm transitions

In order to monitor the number and temperature of metastable ytterbium clouds, we need to pump them back into the ground state where we can use 399 nm imaging. We perform the pump on the $^3\mathrm{P}_2 \rightarrow {}^3\mathrm{S}_1$ transition at 770 nm, from which the atoms decay back into the ^{3}P manifold[8]. Those atoms which fall into $^3\mathrm{P}_1$ decay with a lifetime of 850 ns into the ground state and can be imaged, but those that decay into $^3\mathrm{P}_0$ remain dark unless they are pumped out of this state, which we achieve

---

[8] Mostly. 0.4 % of the atoms decay to the ground state via $^1\mathrm{P}_1$, which still allows us to image these atoms.

with a second pump on the $^3\mathrm{P}_0 \to {}^3\mathrm{S}_1$ transition at 649 nm. We use commercial diode lasers for generating 649 nm and 770 nm light (Toptica DL100). The beams are conveyed to the machine table using a multi-mode fibre, and combined with the lithium slower light in a polarizing beamsplitter. We can obtain about 4 (0.25) mW of 770 (649) nm light at the chamber viewport, which allows us to perform the pump step in under $200\,\mu$s, enabling transfer in time of flight, which is crucial for obtaining accurate temperature information and for the Stern-Gerlach experiments performed in Section 7.3. We typically only use the 770 nm laser.

Using the dipole matrix elements $\langle a, J\| \, D \, \|a', J'\rangle$ from [97] we can calculate transition probabilities as

$$W_{aJ,a'J'} = \frac{4}{3c^3}\frac{\omega^3_{aJ,a'J'}}{2J+1}\left|\langle a, J\| \, D \, \|a', J'\rangle\right|^2, \tag{3.15}$$

where J is the total electronic angular momentum of the initial state, a are all other quantum numbers associated with that state, a' and J' are analogues for the final state, c is the speed of light and ω is the transition frequency. We determine that we should recover 74% of the total atom number when not repumping out of $^3\mathrm{P}_0$. Experimental comparison of atomic clouds recovered with and without the 649 nm laser gives reasonable agreement of $76 \pm 1\%$. The lasers are locked to atomic lines in an HCL identical to the one used inth 399 nm laser setup using saturated absorption spectroscopy. However, due to the “ground’ state of the spectroscopy being a metastable level, and the possibility to decay to the absolute ground level via the “excited” state of the spectroscopy, the standard saturated absorption scheme is only partially applicable in this case. For details of the optics and the locking scheme for these lasers, see Section 9.2.2 of [51].

Chapter 4

TRAPPING, COOLING AND DEGENERACY IN THE LITHIUM-YTTERBIUM MIXTURE

> Uttering a peculiar but scientific warcry...
>
> J.G. Farrell

By now, the use of heteronuclear mixtures is well-established in ultracold atomic physics. Initially, the use of these mixtures was for sympathetic cooling new species to degeneracy [83, 46]. Since then, the repertoire of heteronuclear mixture experiments has expanded to include 3-species cooling procedures [124], studies of many-body physics [70], simulation in optical lattices [54], impurity probes of superfluid physics [105, 121], and the production of heteronuclear polar molecules [102, 88, 26]. However, the specific mixture of lithium and ytterbium is new and presents several new opportunities. The large mass mismatch is of potential interest in few-body physics, leading to new and favourable Efimov state scalings. It is also interesting from the point of view of many-body physics with fermions, with the predictions of FFLO states, etc. The most salient difference, however, is that between the more common bialkali mixtures and alkali-alkaline-earth(-like) mixtures. A diatomic heteronuclear molecule made in this mixture would be paramagnetic as well as polar. That gives the opportunity to use such molecules for lattice spin models [80] and novel quantum computation schemes. The initial hope of greater electric dipole moments for the molecules have not been theoretically borne out [130], but studies in mixtures of alkali and alkaline earth (or alkaline earth-like) atoms have begun to explore some of these other advantages. It is an as yet small but rapidly growing field, with, to my knowledge, experiments in mixtures of rubidium and ytterbium (Duesseldorf, NIST groups), cesium and ytterbium (Durham/Imperial College group), and rubidium and strontium (Innsbruck, Tokyo groups). The lithium-ytterbium combination itself seems to be experiencing a growing experimental [92, 53] and theoretical [130, 13, 39] interest. Thus a somewhat detailed description of the properties of this system could be useful, and it is with this hope that I am writing this chapter. For an introduction to the constituent atoms, see the previous chapter. In this chapter I cover thermalization and sympathetic cooling in the mixture and cooling the mixture to double degeneracy. New achievements described include co-trapping of the two atomic species, sympathetic cooling using a spin singlet atom as a coolant, quantum degeneracy in both bosonic and fermionic ytterbium in a 1064 nm optical trap, and double quantum degeneracy in the $^6\mathrm{Li} - {}^{174}\mathrm{Yb}$ fermi-bose mixture. Portions of this chapter, and the work discussed herein, has appeared in:

- V.V. Ivanov, A. Khramov, A.H. Hansen, W.H. Dowd. F. Münchow, A.O. Jamison and S. Gupta, “Sympathetic cooling in an optically trapped mixture of alkali and spin-singlet atoms” Phys. Rev. Lett. 106, 153201 (2011)

- A.H. Hansen, A. Khramov, W.H. Dowd, A.O. Jamison, V.V. Ivanov and S. Gupta, “Quantum Degenerate Mixtures of Ytterbium and Lithium Atoms” Phys. Rev. A 84, 011606(R) (2011)

- A.H. Hansen, A.Y. Khramov, W.H. Dowd, A.O. Jamison, B. Plotkin-Swing, R.J. Roy and S. Gupta, “Production of quantum degenerate mixtures of ytterbium and lithium with controllable inter-species overlap” Phys. Rev. A 87, 013615 (2013)

4.1 MOTs for Lithium and Ytterbium

We begin all of our experiments by trapping in magneto-optical traps (MOTs). The physics of MOTs will not be covered here, see [79] for a thorough treatment. Our MOT loading is done sequentially, with a longer ytterbium MOT loading step followed by loading the ODT with ytterbium, and then a shorter lithium MOT load step. Photos of the MOTs are shown in Fig. 4.1. We have also attempted to load the two MOTs simultaneously. This was quickly abandoned because of inelastic losses and sub-optimal loading parameters for both. But it did lead to a video of MOT loading, and a picture of simultaneous MOTs (Fig. 4.1 (d)) that was used by our lab with frustrating frequency, considering it was not the actual method of ODT loading. Will has several times succeeded in convincing the lab to attempt to reverse the sequence to load lithium first. The potential advantage of this method stems from the ytterbium MOT being colder than lithium in both the MOT and immediately upon capture in the ODT. Because of its colder temperature, the ytterbium MOT loads optimally into a shallower trap. Thus, rather than loading into a deeper trap than necessary or recompressing after ytterbium ODT load, either of which leads to heating of the ytterbium cloud and, due to weak magnetic confinement and our particular alignement, well-displaced from the ODT load. However, so far the ytterbium-first version of sequential load has been much more successful.

After loading a MOT at settings which are optimized for quickest number growth, both MOTs are compressed (cMOTs) to reduce temperature and increase density for loading into the ODT. The MOT and cMOT parameters for both lithium and ytterbium are presented in Table 4.1.

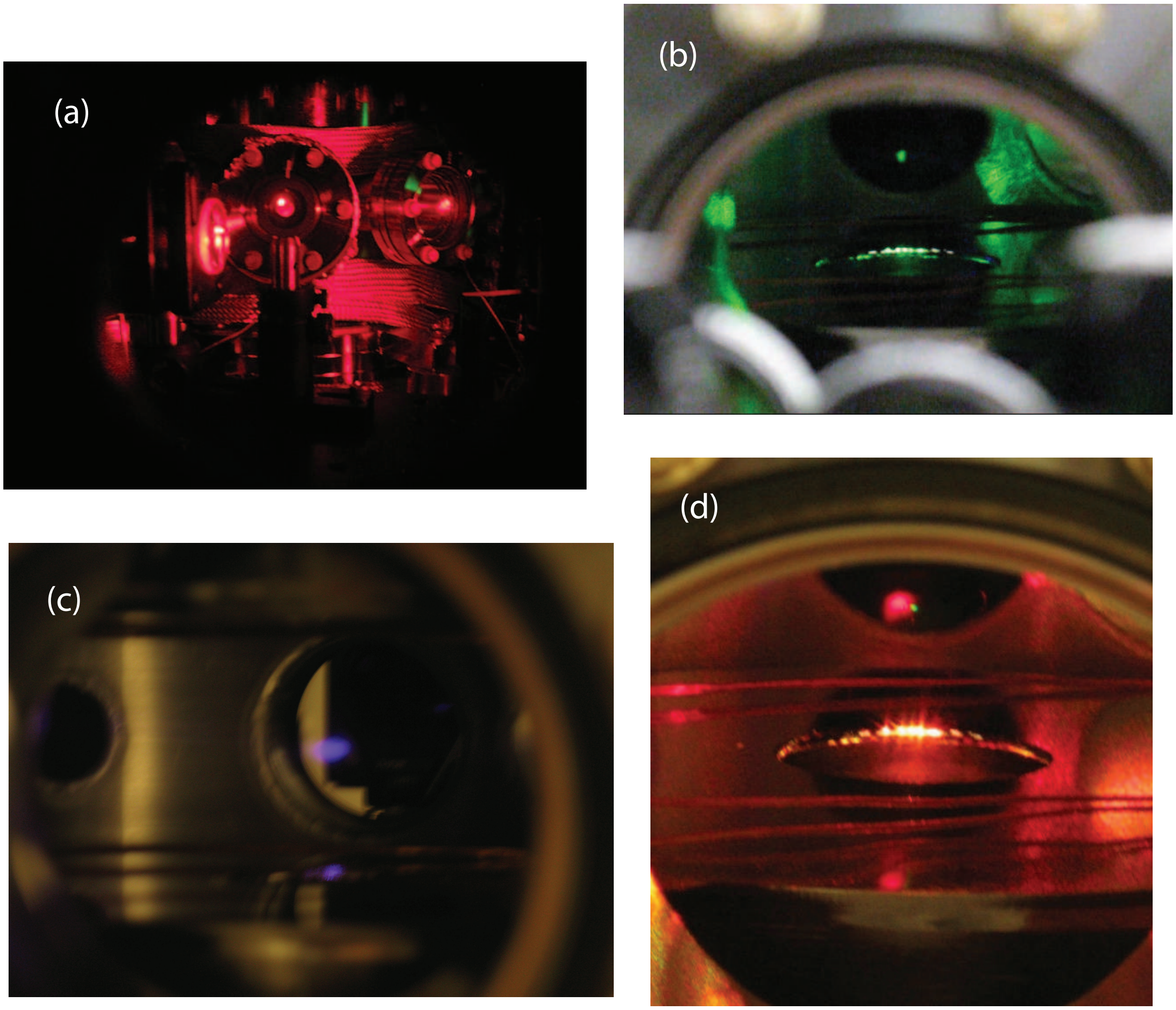

Figure 4.1: Magneto-optical traps in our lab. (a) Li MOT (b) Yb intercombination-line MOT. These are the two MOTs that are the stepping stone for all further experiments. (c) Yb broad-line MOT in 2009 (d) Simultaneous Li-Yb MOT

		^{6}Li F $={}^{3}/_{2}$	^{6}Li F $={}^{1}/_{2}$	^{174}Yb	^{173}Yb
Load	Time (s)	2		15	30
	I/I_{Sat}	60	55	750	750
	Detuning δ/Γ	6	3.5	55±20	40±20
	B'(G/cm)	20		3	3
	T (μK)	1000		100	100
Compression	Time (s)	0.05		0.2	0.2
	$(I/I_{Sat})_{Final}$	0.07	0.08	0.8	2
	$(\delta/\Gamma)_{Final}$	1.5	3	2	4
	B'_{Final}(G/cm)	60		18	25
	T (μK)	350		15	10

Table 4.1: Typical parameters for MOT loading and compression

4.2 Optical Trapping of Li-Yb Mixture and Determination of Scattering Length

For thermalization measurements, we loaded an ytterbium MOT into a single beam optical trap of 13 W corresponding to a trap depth $U_{Yb} = 220\,\mu$K, followed by recompression during lithium MOT load to 27 W ($U_{Yb} = 500\,\mu$K). The measured trap frequencies for ytterbium at this trap depth are $2\pi \times 1600$ Hz radially and $2\pi \times 13$ Hz axially, measured by trap loss from parametric heating. The starting conditions for the following thermalization measurements are $N_{0,Yb(Li)} = 1.1 \times 10^6 (1.4 \times 10^5)$ atoms at $T_{0,Yb(Li)} = 35(110)\,\mu$K. The results are plotted in Fig. 4.2.A single-beam trap is used to simplify modeling of the trap to extract scattering properties.

For analysis of thermalization measurements, we assume that elastic interactions are purely s-wave in nature. We are justified in this assumption because our measured temperatures ($\leq 110\,\mu$K) are much smaller than the p-wave threshold given by $\frac{2}{\sqrt{C_6}}\left(\frac{2\hbar^2}{6\mu}\right)^{3/2} \simeq 2.5\,\mathrm{mK}$. Here μ is the reduced mass and the C_6 coefficient used is that obtained by Zhang *et al.* [130]. In the s-wave limit, scattering is parametrized by only one scale factor, called the s-wave scattering length, or a. The collisional cross-section is given by $\sigma_{Li-Yb} = 4\pi a^2$. The amount of collisions in our system is

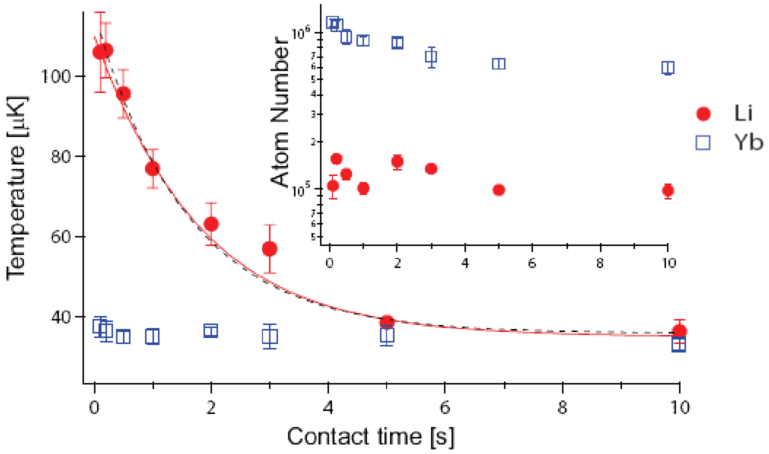

Figure 4.2: Single-beam thermalization

$\bar{n}\sigma\bar{v}$, where $\bar{n}$ is the density overlap

$$\bar{n} = \left(\frac{1}{N_{Yb}} + \frac{1}{N_{Li}}\right) \int n_{Yb} n_{Li} dV \tag{4.1}$$

and $\bar{v}$ the mean relative velocity

$$\bar{v} = \sqrt{\frac{8k_B}{\pi}\left(\frac{T_{Yb}}{m_{Yb}} + \frac{T_{Li}}{m_{Li}}\right)}. \tag{4.2}$$

Thermalization does not happen in a single collision, however. The average number of collisions to thermalize is $\alpha = 2.7$ for equal-mass species, and an additionall inefficiency factor $\xi \equiv \frac{4m_1m_2}{(m_1+m_2)^2}$for different-mass species [85]. In our case, the ξ/α prefactor gives an average of 21 collisions to thermalize. The thermalization timescale for a given starting temperature difference $\Delta T = T_{Li} - T_{Yb}$ is then given as

$$-\Delta T \frac{dT}{dt} = \frac{\xi}{\alpha}\bar{n}\sigma\bar{v}. \tag{4.3}$$

The temperatures and densities of the atomic clouds change during hold. Thus the interaction cross-section can be extracted either by numerically propagating with trial values for a and then picking the best fit, or more simply by fitting the initial slope $\left.\frac{dT}{dt}\right|_0$. Both approaches give the value $|a|_{^{174}\mathrm{Yb}-^{6}\mathrm{Li}} = 13 \pm 3\,a_0$, where $a_0 = 0.53\,$Åis the Bohr radius. The primary source of uncertainty is the determination of cloud densities. This value is useful to constrain long-range behaviour of the ground state Li-Yb potential curve. The Kyoto group later corroborated these results, finding a similar value of $|a|_{^{174}\mathrm{Yb}-^{6}\mathrm{Li}} = 1.0 \pm 0.2\,\mathrm{nm}$ and determining $|a|_{^{173}\mathrm{Yb}-^{6}\mathrm{Li}} = 0.9 \pm 0.2\,\mathrm{nm}$, consistent with mass scaling[1] [53]. Since we only have information about a^2, we are unable to determine the sign of the scattering length. This information could be greatly useful especially in predicting ground state Feshbach resonances [13]. One possible method for determining is to observe thermalization once out of the s-wave regime. However, trapping atoms at such high temperatures is experimentally challenging for us with the current setup. Another potential method is to observe the effect of the mean field shift on cloud size. However, the very small magnitude of the scattering length makes such an experiment challenging as well.

In order to perform sympathetic cooling of lithium by ytterbium, we moved to a crossed trap geometry in which. O'Hara *et al.* found [89] a highly efficient evaporation

---

[1] The s-wave scattering length can be given as [43]

$$a = \bar{a}\left(1 - \tan\left(\Phi - \frac{\pi}{8}\right)\right). \tag{4.4}$$

The definition of $\bar{a}$ is given in Eq. 5.10, where the scaling is as $\mu^{1/4}$, with μ the reduced mass. Φ is the semiclassical phase given by

$$\Phi = \frac{\sqrt{2\mu}}{\hbar} \int_{r_0}^{\infty} \sqrt{-V(r)}dr, \tag{4.5}$$

where r_0 is the inner turning point of the potential energy curve $V(r)$ at 0 energy. Thus the actual mass scaling of a is generally weak, but depends on the details of the potential, since the scaling of $\tan\Phi$ with Φ depends on the value of Φ itself. For the LiYb potential, Φ is about 80 rad [40, 131, 53]. Quite apart from these considerations, we generally do not expect strong mass dependence here as the reduced mass of the Bose-Fermi and Fermi-Fermi systems is nearly identical.

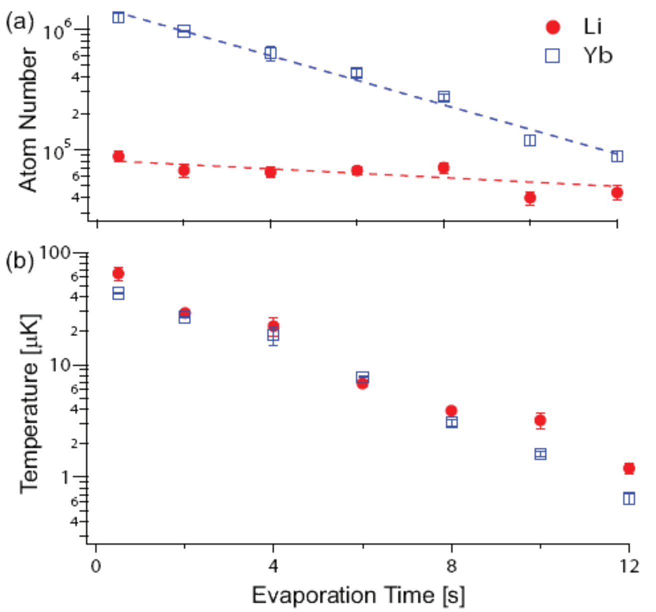

Figure 4.3: Evaporation ramp from Ivanov *et al.* [59]

curve to be

$$U(t) = \frac{U_0}{(1 + \frac{t}{\tau})^{2(\eta' - 3)/\eta'}} \tag{4.6}$$

where η' and τ are parameters defined in terms of the ratio of trap depth to temperature $\eta = U/k_B T$ and scattering rate. We initially attempted to replicate this curve, but found nearly exponential or even linear evaporation ramps to be comparable in efficiency. The result of the evaporation reported in our first experimental paper is shown in 4.3. We reach a lithium temperature of $T/T_F \approx 0.7$. However, this temperature is still above degeneracy.

4.3 Double Quantum Degeneracy

Some potential lithium-ytterbium experiments require quantum degeneracy, and so we wanted to show that we are able to achieve this condition in our system. Moreover, highly degenerate clouds of lithium are necessary for investigating many-body physics effects including superfluidity and the BEC-BCS crossover region. Even in the absence of quantum degeneracy, high phase space densities are desirable for molecule production. We also wish to show versatility and efficiency in our cooling scheme. For all these reasons, double quantum degeneracy was an important early goal for the lab. At the time we were nearing double degeneracy in our system, the Takahashi group in Kyoto achieved it [53].

4.3.1 Signatures of degeneracy

In order to show quantum degeneracy of atomic clouds, we need to understand how those clouds would behave according to the laws of bosonic and fermionic statistics. This is a topic that has been discussed many times, and so a bare minimum, as it relates to our experimental studies, will be presented here. For more, I have found the discussion of quantum statistics in [42] to be very useful. Throughout, we assume a non-interacting gas.

At high temperatures, the Maxwell-Boltzmann distribution is sufficient to describe the number distribution function of a gas

$$f_{MB} = \frac{1}{e^{(\varepsilon-\mu)/k_B T}}. \tag{4.7}$$

At lower temperatures, the symmetry nature of the particles starts to play a role and the distribution function becomes

$$f = \frac{1}{e^{(\varepsilon-\mu)/k_B T} \mp 1} \tag{4.8}$$

where the top sign is for bosons and the bottom for fermions. In principle this means that we should be able to observe signatures of the importance of quantum statistics in a snapshot of the kinetic energy of our cloud, such as the time of flight absorption pictures provide. This brings up two questions: when do we expect to see such a signature and what will it look like. The answer to the first is that quantum statistics becomes important when the assumption of microscopic filling of all quantum states begins to break down. Thus the useful metric by which to define the onset of degeneracy is density in phase space. A heuristic is that the gas is well-described classically as long as the wavefunctions of the individual atoms do not overlap, giving a rough idea that degeneracy occurs in the neighbourhood of

$$n\lambda_{dB}^3 \approx 1, \qquad \lambda_{dB} = \sqrt{\frac{2\pi\hbar}{mk_BT}}, \tag{4.9}$$

where n is the number density. Very naively, the answer to the second question should be that a Bose distribution should be more highly peaked than a Maxwell-Boltzmann distribution at the same temperature, while a Fermi distribution should be flatter and broader. More quantitatively, using the distribution functions in Eq. 4.8 and integrating over phase space[2], we calculate

$$n = \frac{g}{2\pi^2\hbar^3}\int_0^\infty \frac{p^2 dp}{e^{(\varepsilon-\mu)/k_BT} \mp 1} \tag{4.10}$$

All of our experiments are done in the harmonic trap created by the ODT, where the energy states available are

$$\varepsilon = \sum_{i=x,y,z}\left(\frac{p_i^2}{2m} + \frac{1}{2}m\omega_i^2 r_i^2\right) \tag{4.11}$$

which means we can solve eq. 4.10 to get

$$n = \pm\frac{1}{\lambda_{dB}}\mathrm{Li}_{3/2}\left(\pm\exp(\mu/k_BT)\exp(-\frac{1}{2}m\sum_{i=x,y,z}\omega_i^2 r_i^2/k_BT)\right), \tag{4.12}$$

where $\mathrm{Li}_n(x)$ is the n-th order polylogarithm function. Integrating over one spatial

---

[2] the conversion from a sum over quantum states to a phase space integral relies on the local density approximation

dimension at a time, we can recover the density profiles that we would expect to see from projecting a cloud's image onto fewer dimensions, which allows us to compare to the images we obtain in experiment. Note however, that in writing the integral in Eq. 4.10, we have ignored the absolute ground state, which has macroscopic occupation in a BEC. Thus in addition to the Bose thermal distribution given by Eq. 4.12, we may expect to see the $\varepsilon = 0$ fraction, that is the condensed atoms themselves, which should reproduce the shape of the trap[3]. Thus we expect to see a two-part distribution of thermal and condensed bosons.

To return to the first question and determine where the onset of degeneracy takes place more quantitatively, it is more useful to represent the energy levels in a 3D harmonic trap as

$$\varepsilon = \hbar\omega(n_x + n_y + n_z + \frac{3}{2}). \tag{4.13}$$

Then, we observe that to avoid negative occupation values in Eq. 4.8 for bosons, the chemical potential must never become positive. The $\mu = 0$ limit corresponds to a limit, N_{max}, on the number of atoms with non-zero energy in the system that depends on ε/k_BT and the symmetry of the system. It follows that whenever the total number exceeds N_{max}, all the excess atoms are in the condensate. Assuming an isotropic trap and $\hbar\omega \ll k_BT$, we can show (see [19], Section 21.3) that in a 3D harmonic trap, the onset of degeneracy happens at

$$T_C = \left(\frac{N}{\zeta(3)}\right)^{\frac{1}{3}} \frac{\hbar\omega}{k_B} \tag{4.14}$$

where $\zeta(x)$ is the Riemann zeta-function and $\zeta(3) \approx 1.202$.

For fermions, the Fermi energy corresponds to the largest vibrational quantum number for a fully filled 3D harmonic trap, $(6N)^{1/3}$. This provides the relevant

---

[3] To see why this is, we note that, as will be discussed in the next paragraph, the chemical potential of a BEC is 0. Then we can use the Gross-Pitaevskii equation to see that in the non-interacting case, the momentum distribution will follow the trapping potential.

temperature scale,

$$T_F = (6N)^{\frac{1}{3}} \frac{\hbar\omega}{k_B}. \tag{4.15}$$

Equations 4.14 and 4.15 likewise hold in an anisotropic trap, except that the single trap frequency ω is replaced by the geometric average trap frequency $\bar{\omega} = \sqrt[3]{\omega_x \omega_y \omega_z}$. For bosons, once critical temperature is reached, the condenate number grows quickly as

$$N_c = N(1 - (\frac{T}{T_c})^3) \tag{4.16}$$

and may easily be observed. Another well-known signature of BEC that makes it easy to observe is aspect ratio inversion (See [19], Section 22.7). In contrast, the Fermi temperature is not a threshold of any kind - it is just the temperature at which the average energy of an atom is equal to the Fermi energy, and further cooling is necessary to observe clear the difference of the cloud density as given by 4.12 from the Boltzmann distribution. The Fermi cloud is said to be degenerate at $T/T_F = 0.55$, because that is where the chemical potential $\mu = 0$, in analogy with the onset of BEC. An additional signature of Fermi degeneracy is the clamping of the cloud size at the Fermi radius

$$R_F = \sqrt{\frac{2k_B T_F}{m\bar{\omega}^2}} \tag{4.17}$$

and thus a growth of the cloud upon further evaporation is expected (in the case of an optical trap).

4.3.2 Experimental realization

After the publication of thermalization and evaporation data, we obtained the current 399 nm laser setup, and reconfigured the ODT to the current more stable and tighter focused (though lower power) scheme. We were thus able to pursue double quantum degeneracy. We expected our atom clouds to remain thermalized and

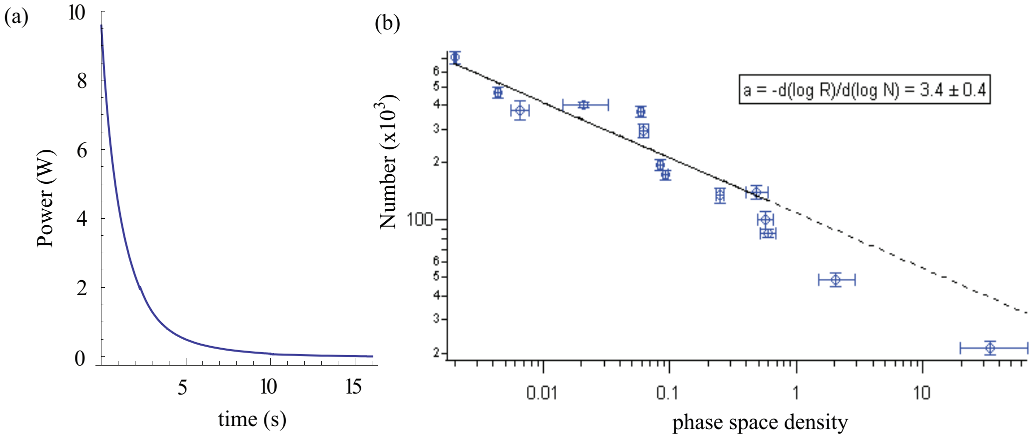

Figure 4.4: Achievement of degneracy for ^{174}Yb in 1064 nm trap (a) Evaporation ramp (b) Evolution of phase space density during evaporation

wanted $T/T_F \leq 0.55$. Thus using Eqs. 4.14 and 4.15 we see that $T_{F,\mathrm{Li}}/T_{C,\mathrm{Yb}} \approx 1.7(N_{\mathrm{Li}}/N_{\mathrm{Yb}})^{\frac{1}{3}}(\bar{\omega}_{\mathrm{Li}}/\bar{\omega}_{\mathrm{Yb}})$, which, for equal atom numbers means we should obtain double degeneracy wher lithium has a temperature ~ 7.5 times higher than that for ytterbium. Therefore conditions which led to a BEC of ^{174}Yb would also be likely to lead to double quantum degeneracy, and we concentrated on achieving BEC in a 1064 nm trap.

Our first condensates were made by loading 1×10^6 atoms into a with a trap depth of $430\,\mu$K and evaporating by a factor of 100 over the course of 14 s in two nearly-exponential stages. The evaporation ramp and its efficiency are shown in Fig. 4.4. We obtain a efficiency metric of $-d(\ln\rho)/d(\ln N) = 3.4 \pm 0.4$, where $\rho \equiv n\lambda_{dB}^3$ is the phase density. We were able to achieve pure condensates of up to 3×10^4 atoms. We first achieved double degeneracy in the Bose-Fermi combination, as seen in Fig. 4.5(a). The values for the experiment displayed in are as follows. $T = 100 \pm 10\,\mu$K, with $T/T_C = 0.8 \pm 0.1$ for ytterbium. The temperature in this case is obtained by fitting the thermal wings of the distribution. Separately, we can obtain T/T_C by fitting to a two-part distribution as discussed in Section4.3.1, and then comparing the numbers condensate fraction to Eq. 4.16. Finally, the two numbers can be compared by obtaining a theoretical T_C for our trap from the trap frequencies and total atom number. The lithium cloud is at $T = 320 \pm 40\,\mu$K, with a $T/T_F = 0.27 \pm 0.03$, well within the degenerate regime. Similarly to the boson case, we can arrive at temperatures both from our knowledge of the trap and cloud temperature or from looking at the shape of the distribution. There are two additional things to note about this result. One is that the temperatures of the two clouds are very different. This is likely due to the separation of the two clouds due to gravitational sag in the case of ytterbium. A more thorough treatment is presented in [51], but briefly the positional displacement of due to gravity goes as g/ω_y^2 where g is the acceleration due to gravity and ω_y the trap frequency in the vertical direction. Because of the greater mass (i.e. smaller ω), the ytterbium cloud is displaced from the lithium cloud, reducing their thermal contact. The other is that despite the above fact, in the presence of lithium, we are unable to achieve a situation with pure condensate of ytterbium. We also have some indication that the lifetime of ytterbium in the doubly degenerate case is much shorter than our vacuum limited lifetime. Similarly, Hara *et al.* [53] found a depletion in ytterbium condensate number in the presence of lithium. We conjecture that this may be due to collisions with highly energetic lithium atoms where, even at $T \ll T_F$ every atom has an average energy no less than $\frac{3}{5}E_F$.

Shortly after the achievement of double degeneracy as detailed in our paper [49], our 556 nm laser system broke down, precipitating a several-month delay in ytterbium trapping. After a further upgrade to the 556 nm power (up from 12 mW to 80 mW at the atoms), we are able to achieve fermi degeneracy in ^{173}Yb (Fig. 4.5(b)) and pure condensates of over 2.5×10^5 atoms. A "waterfall" picture of the evolution of a cloud of ^{174}Yb into a large pure condensate is shown in Fig. 4.5(c). The elliptical shape of the cloud demonstrates aspect ratio inversion. The temperature of the condensate is obtained by fitting the thermal wings of the distribution, and by comparing the condensate fraction to eq. 4.16.

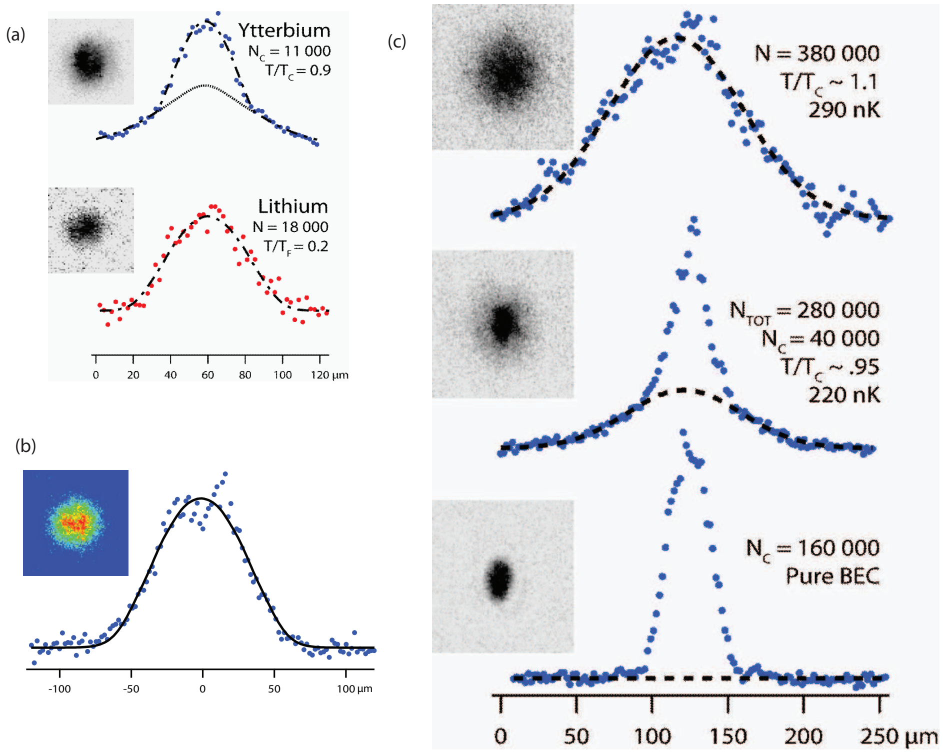

Figure 4.5: (a) Fermi-Bose double degeneracy (b) Fermi-Fermi double degeneracy (c) Evolution of ytterbium cloud into a large BEC

Chapter 5

FESHBACH RESONANCES

Feshbach resonances occur when a bound molecular state is tuned into resonance with respect to the energy of two colliding atoms. In their most common experimental realization, magnetic Feshbach resonances, it is the magnetic field that provides the tuning "knob". This occurs when the molecular state has a different magnetic moment than the incoming atom pair. In that case, even with weak coupling between the two states, the scattering dynamics is strongly affected. Magnetic Feshbach resonances have been a widely used tool in ultracold atomic physics because they provide precise control of the collision properties of the ultracold gas. A key is nearly arbitrary strength of interaction, including access to the so-called unitary regime where the temperature (or, in the case of degenerate fermions the Fermi temperature) provides the only length scale for the system. Additionally, Feshbach resonances can be used to perform magnetoassociation, that is converting pairs of atoms into molecules. In this chapter I go over the basic physics of a Feshbach resonance, introduce the Feshbach resonance of 6-lithium, discuss an experiment where we look at the creation and stability of lithium Feshbach molecules in the presence of ytterbium, and then briefly mention some other avenues of inquiry in our lab where Feshbach resonances come into play. For a more in-depth look at Feshbach resonances, the review by Chin *et al.* [17] is recommended.

Portions of this chapter, and the results discussed herein appear in the following paper

- A.Y. Khramov, A.H. Hansen, A.O. Jamison, W.H. Dowd and S. Gupta, "Dynamics of Feshbach Molecules in an Ultracold Three-Component Mixture", Phys.

Rev. A 86, 032705 (2012)

5.1 *Basic Physics of Feshbach Resonances*

Feshbach resonances are, in general, scattering resonances between a bound state of two colliding atoms and the continuum. However, few bound states are naturally found so close to the continuum to exhibit resonant behaviour. Thus in practice the resonance occurs whenever a bound state can somehow be tuned with respect to the continuum. The Hamiltonian of two colliding atoms 1 and 2 can be given as

$$\mathcal{H} = \frac{-\hbar^2}{2\mu}\left[\frac{1}{r}\frac{\partial^2}{\partial r^2}r - \frac{l(l+1)}{r^2}\right] + \mathcal{H}_1 + \mathcal{H}_2 + V(\mathbf{r}), \tag{5.1}$$

where μ is the reduced mass, $\mathcal{H}_{1,2}$ are the Hamiltonians of the individual atoms, and $V(\mathbf{r})$ is the interaction, which depends on the spatial separation and, in principle, orientation of the two constituents. We can restrict ourselves to atoms without internal electronic orbital angular momentum, which in our case is reasonable since we are dealing with lithium atoms in $^2\mathrm{S}_{1/2}$ and ytterbium atoms in $^1\mathrm{S}_0$. In that case, the Hamiltonians for each individual atom become, for example, for atom 1,

$$\mathcal{H}_1 = a_{HF}\mathbf{i}_1 \cdot \mathbf{s}_1 + (\mu_B g_J \mathbf{s}_1 + \mu_N g_F \mathbf{i}_1) \cdot \mathbf{B}. \tag{5.2}$$

Also, then, the interaction potential depends primarily on the magnitude of internuclear separation and the total spin of the system

$$V(\mathbf{r}) \approx \sum_{\mathbf{S}=\mathbf{s}_1+\mathbf{s}_2} |S\rangle\langle S|V(r)|S\rangle\langle S| \tag{5.3}$$

where V_0 denotes this term for $\mathbf{S} = 0$ and so on. In the $\mathbf{s}_1 = \mathbf{s}_2 = 1/2$ case, if we consider a basis where the individual atomic Hamiltonians are diagonalized, we see that there is a coupling term $V_1 - V_0$, corresponding to change in the total spin.

Alternatively, we can consider a molecular basis where the potential energy curves V_0 and V_1 are a good description of the potential, that is, our basis states are eigenstates of total spin $\mathbf{S} = \mathbf{s}_1 + \mathbf{s}_2$. In that case, we see that, for instance, the hyperfine interaction,

$$\begin{aligned} V_{HF} &= a_{HF}(\mathbf{i}_1 \cdot \mathbf{s}_1 + \mathbf{i}_2 \cdot \mathbf{s}_2) && (5.4) \\ &= a_{HF}\left(\mathbf{I} \cdot \mathbf{S} - \mathbf{i}_1 \cdot \mathbf{s}_2 - \mathbf{i}_2 \cdot \mathbf{s}_1\right) && (5.5) \end{aligned}$$

for two identical atoms, or its analogue for different atoms, is not diagonal in the total spin, and thus provides a coupling between the two states. This isn't the only such possible coupling, but it is the most commonly used. The upshot of this coupling, no matter which basis it's considered in, is that atoms coming together in a scattering state can spend a portion of the collision time in the nearby molecular state, thereby altering the collision dynamics significantly.

More quantitatively, the effect of a Feshbach resonance on the scattering properties of a system is given as

$$a - ib = a_{bg} + \frac{a_{bg}\Gamma}{-E_0 + i(\gamma/2)} \tag{5.6}$$

where the real coefficient a describes elastic scattering and the imaginary coefficient b describes inelastic loss. Γ is a parameter describing the strength of the resonance, E_0 the location of the resonance, and γ the resonant loss rate. For a magnetically tuned resonance in the absence of decay channels, such as in the scattering between two ground state atoms, the resonance energy depends, on the initial energy difference between two states, and the differential magnetic moment $\delta\mu$; we can also define$\Delta \equiv \Gamma/\delta\mu$ which is convenient because Δ then defines the distance between $a = \infty$ and $a = 0$. Thus s-wave scattering length near a Feshbach resonance can be re-parametrized as [84]

$$a(B) = a_{bg}\left(1 - \frac{\Delta}{B - B_0}\right). \tag{5.7}$$

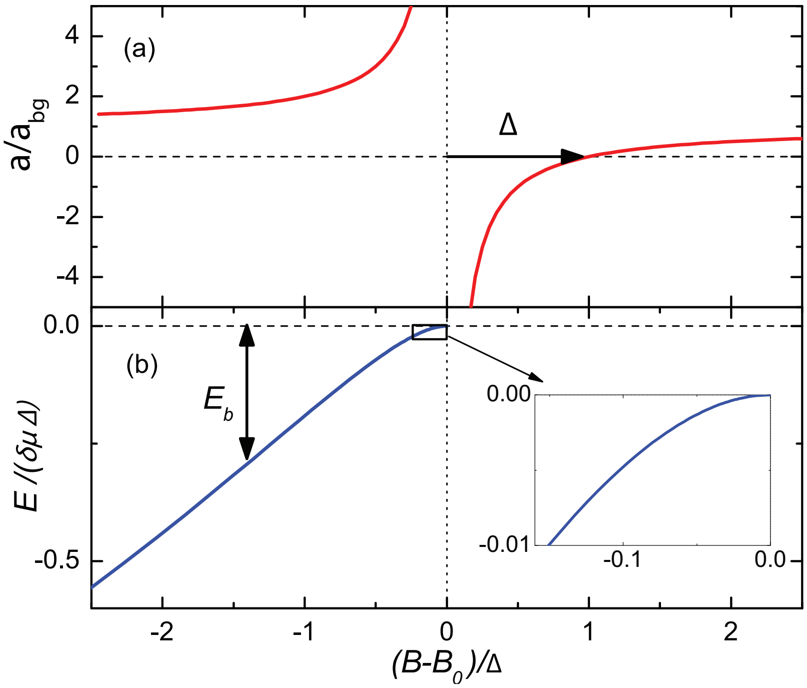

Figure 5.1: The s-wave scattering length (red) and binding energy (blue) behaviour in the vicinity of a Feshbach resonance. The geometric interpretation of the values Δ and B_0, which parametrize the resonance, is indicated. Figure from [17]

The typical behaviour of a as a function of magnetic field is shown in Fig. 5.1 .

5.1.1 Unitarity and broad vs. narrow Feshbach resonances

Away from resonance, the s-wave scattering properties are well described by a. However, when a becomes comparable to either the interparticle spacing $n^{1/3}$ or size of the atomic wavefunctions $\lambda_{dB} \sim 1/k$, it no longer makes sense to assume all collisions are two-body (even less so to treat the situation as collisions of hard spheres of size $|a|$, which is a picture used when talking about scattering phase shifts), and so s-wave scattering properties are no longer determined by the scale of a. This regime is called the “unitary” or “universal” regime, as scattering is parametrized only by the wavenumber k or Fermi wavenumber k_F, and so is completely independent of specifics of the atomic system.

In the unitary regime, the bound molecular state becomes "dressed" by the nearby scattering state, resulting in a molecule that is very large in extent and loosely bound. Such states are called "Feshbach molecules" or halo dimers. The constituent atoms have properties, including spin, qualitatively similar to their free atom values. The binding energy is no longer linearly dependent on B but follows

$$E_b = \frac{\hbar^2}{2ma^2}. \tag{5.8}$$

Feshbach resonances can be parametrized by whether a large portion of their width Δ is found in this regime. Although in principle this depends on the temperature of the system, often a dimensionless resonance strength parameter

$$s \approx \frac{a_{bg}}{\bar{a}} \frac{\Gamma}{\bar{E}} \tag{5.9}$$

is used. Here $\Gamma = \Delta\delta\mu$ as before, and $\bar{a}$ and $\bar{E}$ are length and energy scales defined by the van der Waals potential (see eq. 6.13)[1]. Reconances with $s \gg 1$ usually have the unitary behaviour over a large portion of their width, and are termed "broad" resonances, whereas resonances with $s \ll 1$ are "narrow". Although the correspondence is not strict, it is usually the case that "broad" resonances are those with $\Delta \gtrsim 1\,\mathrm{G}$ and "narrow" ones have $\Delta < 1\,\mathrm{G}$, so that is sometimes taken to be the operational definition. In general, "broad" resonances are more useful than "narrow" ones, because they allow a more precise control of scattering behaviour, and can be used to investigate

---

[1] Strictly speaking,

$$\bar{a} \equiv \frac{2\pi}{\Gamma(1/4)^2} \left(\frac{2\mu C_6}{\hbar^2} \right)^{\frac{1}{4}} \tag{5.10}$$

where Γ is the Gamma function, μ is the reduced mass and C_6 the van der Waals coefficient, and

$$\bar{E} \equiv \frac{\hbar^2}{2\mu\bar{a}^2} \tag{5.11}$$

the unitary regime with less constraints on experimental parameters.

5.2 Feshbach Resonances in Lithium

We now discuss the instances of Feshbach resonances relevant in our experiments. The list of known Feshbach resonances in ^{6}Li, along with their positions and widths, is given in Table 5.1. I first showed the hyperfine energy levels in the ground electronic state of ^{6}Li as a function of magnetic field in Fig. 3.12. Because we load our ODT at a bias magnetic field level close to 0, and pump into the lower hyperfine manifold, the states most relevant to us experimentally are the two lowest hyperfine states, $|1\rangle$ and $|2\rangle$, and so we are best positioned to use the broad Feshbach resonance around 834 G. The first observation of this resonance was made in [91]. To explain why this resonance is so uncommonly broad, we note that the background scattering length of the system, $a_{bg} = -2160\,a_0$is anomalously high. This scattering length is due to perturbation from a virtual bound state just above threshold in the triplet potential. As mentioned in [135], the breadth of the 834 G resonance can then be qualitatively explained by the virtual bound state mediating interactions between the open and closed channel. Interestingly, the 0-crossing of this resonance at 527 G occurs in the vicinity of the other, much narrower, s-wave resonance at 543 G. These resonances are actually due to the interaction of the incoming scattering state with the same bound molecular state, just with or without the mediation of the virtual state. The s-wave scattering length between states $|1\rangle$ and $|2\rangle$ is shown in Fig. 5.2. There are also several more narrow resonances, including p-wave resonances that we use to calibrate magnetic fields in our system.

One notable feature of the broad 834 G resonance is the location of the loss maximum well away from the resonance centre. This location has been studied and can be explained in terms of the creation and subsequent decay of Feshbach molecules.

substates	l_c	$B_0(G)$	$\Delta(G)$	ref
$\|1\rangle$, $\|2\rangle$	s	834.1	-300	[5]
$\|1\rangle$, $\|3\rangle$	s	690.4	-122.3	[5]
$\|2\rangle$, $\|3\rangle$	s	811.2	-222.3	[5]
$\|1\rangle$, $\|2\rangle$	s	543.25	0.1	[113]
$\|1\rangle$, $\|1\rangle$	p	159.14	na	[104]
$\|1\rangle$, $\|2\rangle$	p	185.09	na	[104]
$\|2\rangle$, $\|2\rangle$	p	214.94	na	[104]

Table 5.1: Properties of known Feshbach resonances in ^{6}Li

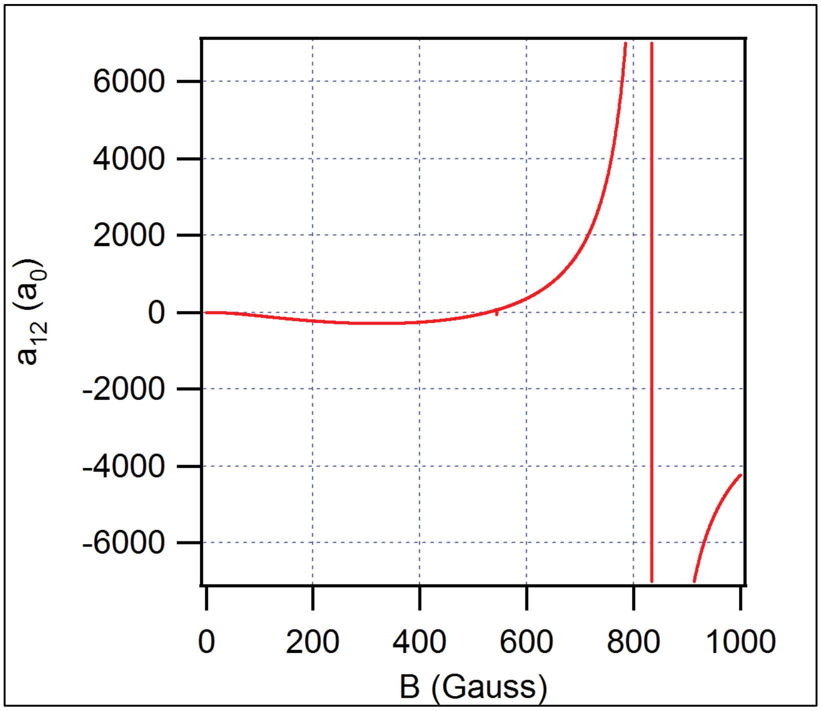

Figure 5.2: Scattering length between the two bottom hyperfine states of ^{6}Li as a function of magnetic field. Note the broad resonance centred at 834 G, and the narrow one at 543 G.

The contributing chemical processes can be written as:

$$\mathrm{Li}|1\rangle + \mathrm{Li}|2\rangle + \mathrm{Li} \quad \rightleftharpoons \quad \mathrm{Li}_2^s + \mathrm{Li} \quad (+\epsilon_\mathrm{B}) \tag{I}$$

$$\mathrm{Li}_2^s + \mathrm{Li} \quad \rightarrow \quad \mathrm{Li}_2^d + \mathrm{Li} \quad (+\epsilon_\mathrm{D}) \tag{II}$$

Here $\mathrm{Li}|1\rangle$ denotes an atom in the lowest hyperfine state, $\mathrm{Li}|2\rangle$ an atom in the second hyperfine state, Li an atom in either of the two states, Li_2^d a deeply bound molecule with large binding energy ϵ_D and finally Li_2^s a shallow Feshbach molecule with binding energy $\epsilon_B = \frac{\hbar^2}{2m_\mathrm{Li}a^2}$. Process (I) can proceed in either direction, either two atoms coming together to form a loosely bound molecule or a loosely bound molecule breaking apart into atoms (with a third constituent to ensure conservation of energy and momentum in both cases). In the absence of losses, this process produces an equilibrium ratio of atoms and Feshbach molecules given by

$$\frac{2N_m}{N_\mathrm{Li} + 2N_m} = \left(1 + \frac{e^{-\epsilon_B/k_B T}}{\phi_\mathrm{Li}}\right)^{-1}, \tag{5.12}$$

where N_m is the molecule number and ϕ_Li is the phase space density for each spin component in the ground state of the trap [16, 131]. Process (II) disrupts that equilibrium. Theoretically, the rates of the two processes (I) and (II) are $\propto a^6$ and $\propto a^{-3.3}$ [96, 30]. The displacement of the loss maximum from resonance can thus be qualitatively explained by noting that the dimer formation rate increases with magnetic field while equilibrium dimer fraction and molecule decay rate decrease. Considering the problem as a chemical kinetics problem, the rate-limiting step determining the system evolution is the molecule formation rate at low fields and decay rate at high fields. The loss spectrum shape is also affected by trap depth and overall hold time. Additional complications arise once fermionic statistics begin to play a role. Zhang and Ho [131] have presented a model based on rates of processes in and out of the fermi-degenerate regime which reproduces the displacement of the loss maximum for broad Feshbach resonances between fermions. They numerically verified their model by comparing with several loss curves already present in the literature. We initially sought to explore this behaviour somewhat quantitatively by obtaining loss spectra at identical trap conditions and with the same consituents, but at different temperatures and T/T_F values. Our initial results seemed to suggest a broadening of the loss maximum with temperature reduction, consistent with the Zhang and Ho model. However, we quickly realized that just looking at atom loss would give an incomplete picture, and were also curious to investigate the potential effect of Yb. Thus, this avenue was abandoned in favour of studies of Feshbach resonances in the Li$|1\rangle$+Li$|2\rangle$+Yb mixture.

5.3 Feshbach Resonances in a Three Component Mixture

As detailed in Section 5.2, the 834 G broad Feshbach resonance between states $|1\rangle$ and $|2\rangle$ has been remarkably fruitful for the study of two-component Fermi gases near a Feshbach resonance. These studies are possible due to the stability of the atom-molecule system on the positive scattering length side of the resonance. This stability had largely been attributed to Fermi statistics. For instance, in the case of ^{7}Li, it is noticeably absent, making the study of bosons at unitarity a very difficult task [100]. Collisional stability of Feshbach molecules in a three-component mixtures thus becomes a crucial question, since Fermi statistics is no longer enough to prevent three-body interactions even below the p-wave threshold. A recent theoretical analysis of such mixtures suggests a possibility for enhanced molecule formation rates with good collisional stability [31]. Studying three-component mixtures in which only two are interacting also offers the possibility of modifying or probing the pairing dynamics by selective control of the third component. A third component may also be used as a coolant bath for exothermic molecule-formation processes, provided that inelastic processes with the bath are negligible. In the context of many-body physics, a third non-resonant component can be useful as a microscopic probe of superfluid

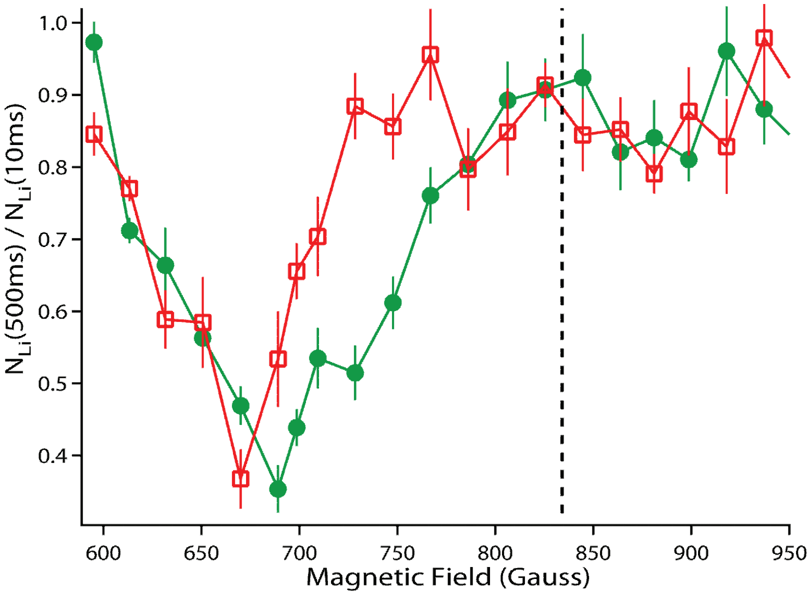

Figure 5.3: Lithium atom loss around the broad Feshbach resonance in the presence (green) and absence (red) of ytterbium bath

properties, as a stable bath for studies of non-equilibrium phenomena, or for accurate thermometry of deeply degenerate fermions.

Previous experimental studies of three-component mixtures included observation of increased atom loss at a ^{6}Li p-wave resonance in the presence of a ^{87}Rb bath [25], while a small sample of the probe species ^{40}K was found to be stable within a larger strongly interacting ^{6}Li sample [105]. We investigated the Li$|1\rangle$+Li$|2\rangle$+Yb mixture, where the Li$|1\rangle$+Li$|2\rangle$interaction is strongly magnetic-field dependent, and Yb-Li interactions remain weak throughout. We observed the number and temperature dynamics of the atoms, and also the number dynamics of the molecules.

We performed our experiments in a crossed ODT at a trap depth $U_{\mathrm{Yb(Li)}} = 15(55)\,\mu$K and mean trap frequency $\bar{\omega}_{\mathrm{Yb(Li)}} = 2\pi \times 0.30(2.4)\,$kHz. Following evaporation, the mixture is held at constant trap depth to allow inter-species thermalization. With a time constant of 1 s the system acquires a common temperature $T_{\mathrm{Yb}} = T_{\mathrm{Li}} = 2\,\mu$K with atom number $N_{\mathrm{Yb(Li)}} = 2 \times 10^5(3 \times 10^4)$. This corresponds

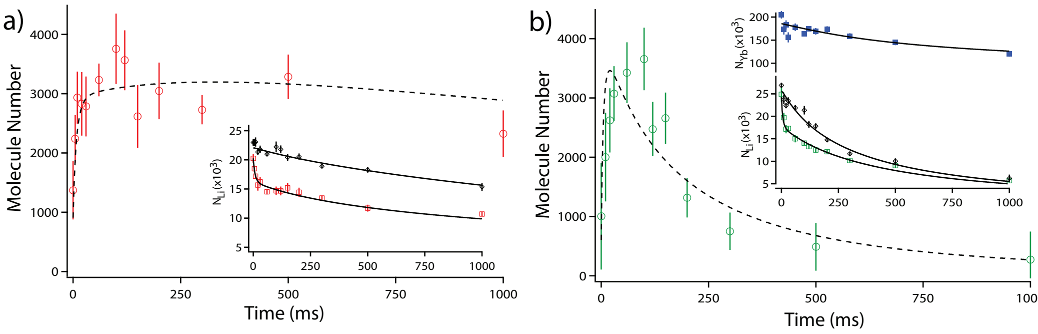

Figure 5.4: Evolution of Li Feshbach molecule number at 709 G without (a) and with (b) an Yb bath. The numbers are obtained by comparing Li atom numbers (insets) ramped across resonance (diamonds) or not (open squares) as described in the text. Lower inset also shows Yb number (filled squares). The curves are fits with a rate equations-based model.

to $T_{\rm Li}/T_F \simeq 0.4$, and $T_{\rm Yb}/T_C \simeq 2.5$, where T_F is the Li Fermi temperature and T_C is the Yb Bose-Einstein condensation temperature.

After the initial preparation, we ramp up the magnetic field to a desired value and observe the system after a variable hold time. For fields in the vicinity of the Feshbach resonance, there is a field-dependent number loss and heating for the Li cloud during the 20 ms ramp time, resulting in $T_{\rm Li}$ rising to as high as $4.5\,\mu$K. At this point, the average density $\langle n_{\rm Yb(Li)} \rangle$ is $2.6(0.35)\times10^{13}\,{\rm cm}^{-3}$. Ytterbium may be removed from the trap with a 1 ms clearing pulse resonant with the ${}^1{\rm S}_0 \rightarrow {}^1{\rm P}_1$ transition. This clearing pulse was sometimes performed after the magnetic field ramp, and sometimes before. However, this did not seem to impact the evolution of the lithium cloud, and so we used both sets of data interchangeably. The experimental runs with ytterbium present could then be compared to those where ytterbium is absent. The shape of the atom loss curve is shown in Fig. 5.3). The atom-loss maximum obtained in the absence of Yb has been observed previously [29] and can be explained as a result of the formation and subsequent decay of shallow lithium Feshbach dimers [62, 21, 16, 131]. In the presence of the Yb bath, the loss feature is shifted and broadened. The behaviour of our system can then be described using the two chemical processes given in Section 5.2, with the addition of new processes involving ytterbium. Altogether, the potential chemical processes are:

$$\begin{aligned}
\mathrm{Li}|1\rangle + \mathrm{Li}|2\rangle + \mathrm{Li} &\rightleftharpoons \mathrm{Li}_2^s + \mathrm{Li} \quad (+\epsilon_\mathrm{B}) && \text{(I)}\\
\mathrm{Li}_2^s + \mathrm{Li} &\rightarrow \mathrm{Li}_2^d + \mathrm{Li} \quad (+\epsilon_\mathrm{D}) && \text{(II)}\\
\mathrm{Li}|1\rangle + \mathrm{Li}|2\rangle + \mathrm{Yb} &\rightleftharpoons \mathrm{Li}_2^s + \mathrm{Yb} \quad (+\epsilon_\mathrm{B}) && \text{(III)}\\
\mathrm{Li}_2^s + \mathrm{Yb} &\rightarrow \mathrm{Li}_2^d + \mathrm{Yb} \quad (+\epsilon_\mathrm{D}) && \text{(IV)}\\
\mathrm{Li}|1\rangle + \mathrm{Li}|2\rangle + \mathrm{Yb} &\rightarrow \mathrm{Li}_2^d + \mathrm{Yb} \quad (+\epsilon_\mathrm{D}) && \text{(V)}
\end{aligned}$$

Processes (III) and (IV) are similar to (I) and (II) with the spectator atom being Yb rather than Li. Process (V) corresponds to direct three-body loss to a deeply-bound molecule. Processes (II, IV, V) always result in particle loss from the trap since $\epsilon_D \gg U_{\mathrm{Li}}$. We denote the density independent rate coefficients for the above processes, respectively, as L_3, L_2, L_3', L_2' and $L_3'^d$. This is not a fully exhaustive list of available processes. Vibrational relaxation due to collisions between Li_2^s Feshbach molecules may contribute at the lowest fields, but has a negligible rate for the fields at which we perform our analysis [62, 131]. We have experimentally checked that direct three-body loss processes to deeply-bound states involving three Li atoms as well as those involving one Li atom and two Yb atoms are negligible for this work. Three-body losses involving Yb atoms alone have a small effect [116] and are taken into account. Analogues of process (IV) and (V) with a deeply bound LiYb molecule as one of the products are possible, but since we are unable to distinguish them from processes (IV) and (V), their rates are subsumed within L_2' and $L_3'^d$, respectively.

In the presence of Yb, the additional dimer formation (III), dimer decay (IV), and 3-body loss (V) processes contribute, altering the lithium loss spectrum. The observed loss spectrum is broadened on the higher field side (where loss is limited by molecule decay rate), suggesting that for our parameters, processes (IV) and/or (V) play an important role while process (III) does not. The rate constants L_3', L_2', and L_3^d, for processes (III), (IV) and (V), have theoretical scalings a^4, a^{-1}, and a^2, respectively [31, 96]. Overall, we see two regimes of behavior - a lossy one where molecule formation is energetically favored ($\epsilon_B > k_B T_{\mathrm{Li}}$) and a stable one closer to resonance ($\epsilon_B < k_B T_{\mathrm{Li}}$). The criterion $\epsilon_B = k_B T$ separating these two regimes is equivalent to $ka = 1$ where $\frac{\hbar^2 k^2}{2m_{\mathrm{Li}}} = k_B T_{\mathrm{Li}}$, i.e., the unitarity criterion. In order to expand upon this qualitative picture, we study the time evolution of the three-component mixture at representative magnetic fields in the above two regimes. We are then able to extract quantitative information for the above processes from a rate-equations model of the system.

Fig. 5.4 shows the Li atom and molecule number evolution at 709 G ($\epsilon_B = k_B \times 8.3\,\mu\mathrm{K}$) where modifications due to the Yb bath are apparent in Fig. 5.3. The number of Feshbach molecules at a particular field is determined by using a procedure similar to earlier works [62, 21]. After variable evolution time, we ramp the magnetic field with a speed of 40 G/ms either up to 950 G, which dissociates the molecules back into atoms that remain in the trap, or to 506 G, which does not. We then rapidly switch off the magnetic field and image the atomic cloud. The molecule number is obtained from the number difference in the two images (see insets in Fig. 5.4).

We see that the presence of Yb alters the molecule decay rate while the formation rate is unchanged. The Feshbach molecules appear to coexist for a long time ($>$ 100 ms) with the Yb bath, even in the absence of Pauli blocking [31]. We adapt Zhang and Ho's rate-equations analysis of Feshbach losses in a Fermi-Fermi mixture [131] to incorporate a third component, temperature evolution, and trap inhomogeneity. $T_{\mathrm{Li}}/T_F > 0.5$ is satisfied throughout the measurement range, allowing a classical treatment of the Li cloud. We model the density evolutions due to processes (I-V) using:

$$\begin{aligned}\dot{n}_m &= R_m + R'_m - L_2 n_m n_{\rm Li} - L'_2 n_m n_{\rm Yb} &(5.13)\\ \dot{n}_{\rm Li} &= -2R_m - 2R'_m - L_2 n_m n_{\rm Li} - 2L_3^d n_{\rm Li}^2 n_{\rm Yb} &(5.14)\\ \dot{n}_{\rm Yb} &= -L'_2 n_m n_{\rm Yb} - L_3^d n_{\rm Li}^2 n_{\rm Yb}. &(5.15)\end{aligned}$$

Here n_m, $n_{\rm Li}$ and $n_{\rm Yb}$ are the densities of shallow dimers Li_2^s, Li atoms and Yb atoms, respectively. $R_m(R'_m) = \frac{3}{4}L_3(L'_3)n_{\rm Li}^2 n_{\rm Li(Yb)} - qL_3(L'_3)n_m n_{\rm Li(Yb)}$ is the net-rate for molecule production via process (I)((III)). We determine q through the constraints on the molecule fraction at equilibrium ($R_m(R'_m) = 0$). We obtain an upper bound for $L_3'^d$ by observations at large negative a (by going to 935 G) which indicates a negligible effect for the data in Fig. 5.4, allowing us to set $L_3'^d = 0$ for the analysis at 709 G.

The time evolution of temperature based only on the energy deposition of the above chemical processes would be

$$\begin{aligned}\dot{T}_{Li} &= \frac{\epsilon_B}{3k_B N_{tot}}\left(R_m + R'_m\right) &(5.16)\\ \dot{T}_{Yb} &= 0 &(5.17)\end{aligned}$$

since only processes (I) and (III) deposit energy in trapped particles. However, we also need to include anti-evaporation from the density-dependent loss processes (II), (IV) and (V) [122]. Briefly, since collisions occur most frequently at highest densities, and highest densities are found at the bottom of the trap where the coldest atoms are, on average inelastic collisions preferentially take away the coldest atoms, leading, after rethermaliztion, to an effect opposite to that of evaporative cooling. In addition, our model also takes into account the effects of evaporative cooling [89], inter-species thermalization [59], one-body losses from background gas collisions, and Yb three-body losses [116, 122]. The Li scattering length at 709 G is $a = 1860\,a_0$,

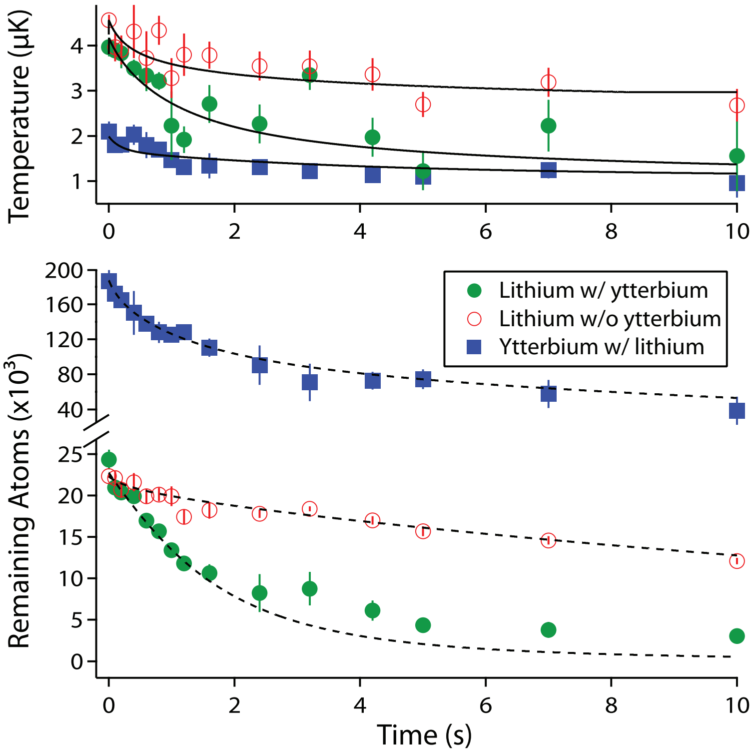

Figure 5.5: The evolution of temperature and number at 810 G for Li atomic cloud with Yb (filled circles) and without (empty circles) and also for Yb in the presence of Li (filled squares). The curves are fits with a rate equations-based model.

ensuring rapid thermalization ($< 1\,\mathrm{ms}$) in the lithium atom-Feshbach molecule mixture [96]. This allows the assumption of equal temperature T_{Li} to lithium atoms and Feshbach molecules. The heating from molecule-formation at 709 G dominates over inter-species thermalization, maintaining $T_{\mathrm{Li}} \simeq 4.5\,\mu\mathrm{K}$ and $T_{\mathrm{Yb}} \simeq 2\,\mu\mathrm{K}$, as observed in both experiment and model.

The best-fit rate coefficients extracted from the atom data (shown in the insets in Fig. 5.4) are $L_3 = (1.4 \pm 0.3) \times 10^{-24}\,\mathrm{cm}^6/\mathrm{s}$, $L_2 = (1.3 \pm 0.3) \times 10^{-13}\,\mathrm{cm}^3/\mathrm{s}$, and $L_2' = (2.3 \pm 0.2) \times 10^{-13}\,\mathrm{cm}^3/\mathrm{s}$. L_3' is consistent with 0. All reported uncertainties are statistical. The L_3 value is consistent with that obtained in [62], after accounting for the slight differences in experimental parameters. Using $L_2'\langle n_{\mathrm{Yb}}\rangle$ as a measure of the dimer decay rate, we get 170 ms as the lifetime of a Li Feshbach molecule in the Yb bath.

We now turn to the unitary regime, where we choose 810 G ($ka = +6$, $\epsilon_B = k_B \times 0.11\,\mu\mathrm{K}$) as our representative field to study the mixture properties. It is difficult to reliably observe the molecule number using our earlier method in this regime, so we only monitor the atoms (see Fig. 5.5). Starting with an inter-species temperature differential as before, we observe a fast drop in T_{Li} in the presence of Yb and clear evidence of inter-species thermalization. The Li number in the three-component mixture exhibits a long $1/e$ lifetime of 2 s, far larger than at 709 G. However this is still an order of magnitude shorter than that obtained in the absence of Yb. The interpretation of the decay is not straightforward as both two-body (process (IV)) and three-body (process (V)) inelastic loss can contribute [105]. The large rate for process (I) in this regime ensures equilibrium molecule fraction at all times. By fitting to data taken at 935 G where $ka = -2$ and process (V) is expected to be the dominant inelastic loss component, we obtain $L_3'^{d} = (4.3 \pm 0.3) \times 10^{-28}\,\mathrm{cm}^6/\mathrm{s}$. This sets a lower bound for L_3^d at 810 G. We fit the first 2.5 s of data in Fig. 5.5 after fixing L_2' to its value scaled from 709 G and find $L_3^d = (9.5 \pm 0.5) \times 10^{-28}\,\mathrm{cm}^6/\mathrm{s}$ at 810 G. The slight disagreement in Li atom number at long times may be due to a small

($< 10\%$) inequality in our spin mixture composition, which the model does not take into account.

The qualitative features of both spectra in Fig. 5.3 can be theoretically reproduced by using field-dependent reaction coefficients scaled from our measured values at 709 and 810 G. This scaling procedure, along with a thorough description of the modeling of the inelastic and elastic processes, including numerical techniques and error analysis can be found in Anders' thesis [51].

By extending the forced evaporative cooling step, lower temperature mixtures can be produced where bosonic ^{174}Yb shrinks to a size smaller than the Fermi diameter of the ^{6}Li cloud. Such experiments at 834 G yield $T_{\mathrm{Li}}/T_F \simeq 0.25$ with $N_{\mathrm{Yb}} = N_{\mathrm{Li}} = 2.5\times 10^4$. Here, the estimated volume of the Yb sample is $\simeq 0.3$ of the Li sample volume, compared to 3.3 in the classical regime. The mixture is thus also capable of achieving the opposite regime of a second species being immersed inside a strongly interacting quantum degenerate Fermi gas, similar to earlier studies in the K-Li mixture [105]. Our demonstrated stability of the mixture near the unitary regime of the resonance opens various possibilities of studying strongly interacting fermions immersed in a bath species or being interrogated by a small probe species. Attempts to cool further to below the critical temperature for superfluidity ($T_C/T_F \approx 0.16$ close to unitarity) were made but were not successful. While we were able to cool to $T_{\mathrm{Li}}/T_F \lesssim 0.1$ at 0 G, the magnetic field ramp to unitarity heated the system to above $T_{\mathrm{Li}}/T_F = 0.25$. We attributed this heating to passing through the atom loss maximum for the broad resonance. To avoid this problem, we attempted to perform evaporation on only one spin state, or to evaporate at unitarity. Both of these methods resulted in lower atom numbers at a given temperature, and we were unable to reach the superfluid regime. However, with the improved ytterbium numbers available in our current setup, it may be a future possibility.

5.4 Other Feshbach Resonance Matters

As is evident from a lack of electronic spin in ground state ytterbium, the hyperfine coupling term as given in 5.4 remains diagonal in total spin in a collision between lithium and ytterbium. This means that there is no hyperfine coupling-mediated Feshbach resonance between Li and Yb in the ground state. However, this has not deterred the group from considering the possibilities of Feshbach resonances in our system. In fact, not a day goes by that we don't think of Feshbach resonances in one way or another. Here are some of those ways.

5.4.1 Narrow Feshbach Resonances in the Lithium-Ytterbium System

In 5.1 we claimed that V_0 and V_1 are the two potential curves to consider. Equivalently, we highlighted the hyperfine interaction as being the coupling term. This is a good enough approximation when looking at bi-alkali systems, but is not, strictly speaking, the whole story. Recently, Zuchowski and co-workers [132] showed that other interactions are also expected to produce Feshbach resonances, albeit much narrower ones. They have identified several such mechanisms, however, the most important one seems to be the modification of the hyperfine coupling constant of the atom with spin depending on the proximity of a second atom. An extension of this phenomenon, to where the proximity of the alkali atom polarizes the spin density of the spin singlet atom, is supposed to be the strongest effect in the lithium ytterbium system [13]. The coupling is then between the nuclear magnetic moment of ytterbium and electronic spin, thus creating a hyperfine coupling term $\Delta a_{HF(Yb)}(r)\mathbf{i}_{Yb}\cdot\mathbf{S}$. The uncertainty in s-wave scattering length for the system limited the precision with which Brue and Hutson were able to predict the location of the Feshbach resonances. Nevertheless, we have made several attempts to observe these narrow resonances by magnetic field sweeps. An example scan is shown in Fig. 5.6. The main and inset scans were performed with different trapping conditions, but as an example, the main

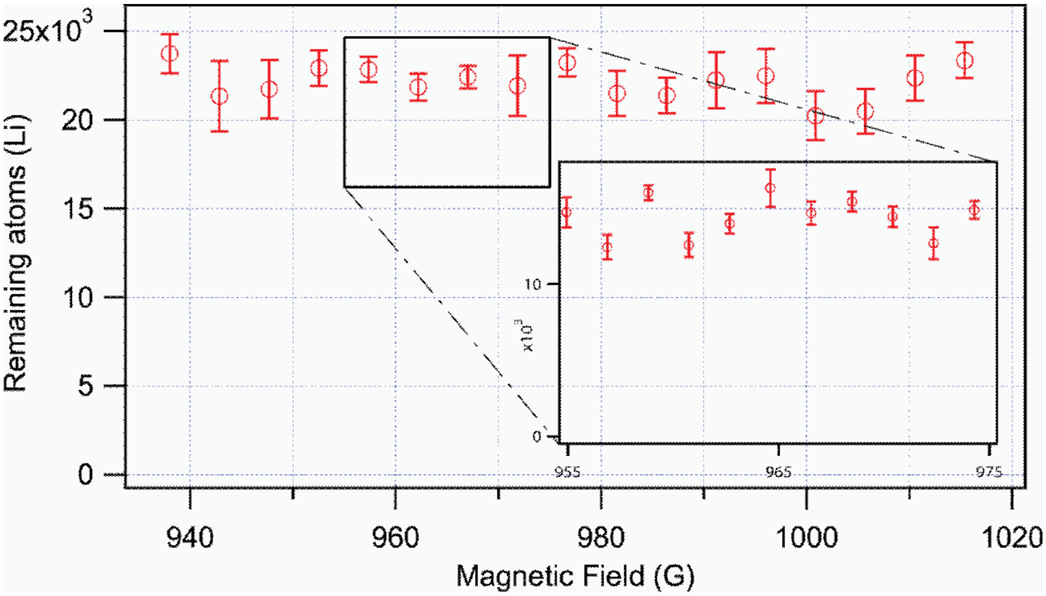

Figure 5.6: Atoms remaining after 5G (inset: 2G) sweeps over 5 s for a range of starting magnetic fields, constituting an example narrow Feshbach scan

scan represents a ramp of 1 mG/ms, with trap densities $\langle n_{\mathrm{Yb\,(Li)}}\rangle \approx 1(2) \times 10^{13}/\mathrm{cm}^3$. Thus, taking the overlap integral due to our trap shape into account, in the case of a 1 mG wide reonance, we would only be sensitive to two-body inelastic loss coefficients of the order of several times $10^{-10}\mathrm{cm}^6/\mathrm{s}$. We have performed scans in the vicinity of both 960 and 1600 G. At the higher field, our standard water flow is not enough to keep the Feshbach coils safely below water evaporation temperature, which creates a safety hazard. Therefore we use an additional water pump (WebTrol) to increase the water pressure five-fold. The use of the WebTrol introduces a large amount of acoustic noise into our system, which somehow translates to reduced atom numbers and lifetimes (and is also quite annoying apart from that). Additionally, even with the increased waterflow, the Feshbach coils experience significant heating during scans, so we are limited to relatively short scan times of $\lesssim 5\,\mathrm{s}$. Finally, the highest magnetic field we can safely reach is 1660 G, which is well within the potential region of interest. Thus our scans of the 960 G region can perhaps be better believed than those at 1660

G. Nevertheless, the precision of our search in both regions is probably limited by the stability of the magnetic fields.

5.4.2 Anisotropic Feshbachs in the Lithium-Ytterbium System*

Another simplification in the introduction presented in Section 5.1 was that we neglected to consider the electronic orbital angular momentum of the constituent atoms. However, this turns out to also lead to a rich world of anisotropic couplings [73, 95]. The coupling is between a bound state in a collision channel with a given Zeeman level M_J and a scattering state in a lower Zeeman level. The multichannel nature of these collisions couples levels with $\Delta l = \pm 2, \pm 4 \pm 6 \ldots$ These were considered of the dysprosium system [95] and observed in the Yb-Yb* system [66]. It is possible that at least some of the magnetically tuned resonances recently found in erbium [2] are also of this type. They are also a potential source of resonances in the Li-Yb* system, although not the only such source [39].

Chapter 6

PHOTOASSOCIATION AND DIATOMIC MOLECULES

Compared to atoms, molecules have many more degrees of freedom, which is a large part of the reason we are interested in them. However, this is also what makes them complicated. In addition to the electronic orbital and spin, and nuclear spin angular momenta for each atom, molecules can have the angular momentum possessed by the entire molecule (rotation), vibrational excitations, and various ways for these degrees of freedom to couple to one another. Within this jungle of complexity, diatomic molecules are the simplest form of molecule to consider as there is only one interatomic axis. This does not mean that there is only one axis to consider overall, however, because the electronic angular momenta need not point along it. The addition of angular momenta will be covered more in-depth in the section on Hund's cases (6.2.1). Additionally, the laboratory frame needs to be considered in the case of application of external fields. However, the reward for this complexity is the ability to study long-range anisotropic interactions and potential usefulness in quantum information protocols [28, 80] or precision measurement, *e.g.* [57].

For experimenters starting from mixtures of ultracold atoms such as ours, diatomic molecules first have to be created before they can be studied. The method of magnetoassociation using Feshbach resonances has been discussed in the previous chapter. The other option is photoassociation, which will be discussed in Section 6.3. Overall, the purpose of this chapter is to convey the basic analytical tools of studying diatomic molecules, and then discuss photoassociation, and the steps taken in our lab to perform photoassociation of the Li-Yb molecule.

6.1 The Born-Oppenheimer Approximation

For all their purported simplicity, the exact Hamiltonian for a diatomic molecule is difficult to derive and impossible to solve. The problem becomes easier if we decouple the motion of electrons and nuclei. To a first approximation, this is justified because the motions of nuclei are much slower than those of electrons. This is typically discussed in terms of "clamping" the positions of the nuclei, considering the electronic wavefunctions as if the electrons were moving in a static field created by nuclei, and then coming back and treating the nuclear movement as if they are moving in a potential that includes "smeared" electrons. If we ignore any relativistic coupling terms, we can translate this language into the Hamiltonian

$$\mathcal{H}_{tot} = \mathbf{T}_N + \mathbf{T}_e + V_{ee} + V_{Ne} + V_{NN}, \tag{6.1}$$

where the nuclear kinetic energy term $\mathbf{T}_N$ includes the rotational and vibrational nuclear kinetic energies. The potential energy terms are just the Coulombic electron-electron, electron-nucleus and nucleus-nucleus interactions, which are all (somewhat confusingly) convenient to treat as part of the electronic Hamiltonian. If we further suppose that the rotational and vibrational terms in $\mathbf{T}_N$ are independent, this allows us to write the total energy eigenvalue as a sum of eigenvalues of three separate Hamiltonians:

$$E_{tot} = E_{el} + E_{vib}(\nu) + E_{rot}(J) \tag{6.2}$$

which are here arranged in order of decreasing importance to the overall energy. This separation is never strictly correct, but it is almost always used when discussing molecular energy levels. The total wavefunction is more convenient to split into two functions:

$$\psi_{BO} = \Phi_{el}\chi_{\nu,R} \tag{6.3}$$

with Φ_{el} being the electronic wavefunction and $\chi_{\nu,R}$ being the nuclear vibrational-rotational wavefunction. This is called the Born-Oppenheimer Approximation and the solution to the Schroedinger equation thus obtained the Born-Oppenheimer product function. Using the assumption of clamped nucleons, we first obtain a trial electronic wavefunction

$$\mathcal{H}_{el}\Phi_i = E_{el}\Phi_i. \tag{6.4}$$

We then plug in our trial function Φ_i into the Schroedinger equation where the total wavefunction is given by Eq. 6.3 and the total Hamiltonian by Eq. 6.1

$$\left[\mathbf{T}_N + \mathbf{T}_e + V\right]\Phi_i\chi_{\nu,R} \quad = \quad E_{tot}\Phi_i\chi_{\nu,R}. \tag{6.5}$$

Unity-normalizing Φ_i and treating it as a spatial probability distribution, we can integrate:

$$\begin{aligned} \langle\Phi_i|\mathbf{T}_N + \mathcal{H}_{el}|\Phi_i\rangle\chi_{\nu,R} &= E_{tot}\langle\Phi_i|\Phi_i\rangle\chi_{\nu,R} && (6.6)\\ \left[\mathbf{T}_N + E_{el}(r)\right]\chi_{\nu,R} &= E_{tot}\chi_{\nu,R}. && (6.7) \end{aligned}$$

This invites the interpretation of $E_{el}(r)$ as the potential within which the nuclei move. $E_{el}(r)$ is termed a potential energy curve or surface (PES). It is important to keep in mind that the potential energy curve is just an approximation to the potential felt by the nuclei and doesn't correspond to a real observable. We have ignored any relativistic effects, such as spin-orbit coupling of the electrons. We also by design omitted coupling of the nuclear and electronic motions, *i.e.* rotational coupling ... However, the BO approximation and the PES's generated by using it are a starting point for talking about diatomic molecules.

Ang. mom. term	Symbol and formation	Projection onto z
total electron orbital ang. mom.	$\mathbf{L}$	Λ
total electron spin	$\mathbf{S}$	Σ
total electron ang. mom.	$\mathbf{J}_a = \mathbf{L} + \mathbf{S}$	$\Omega = \Lambda + \Sigma$
molecular rotation ang. mom.	$\mathbf{R}$	0
total ang. mom.	$\mathbf{J} = \mathbf{R} + \mathbf{L} + \mathbf{S}$	Ω
total ang. mom. excluding spin	$\mathbf{N} = \mathbf{R} + \mathbf{L}$	Λ

Table 6.1: Angular momenta in the diatomic molecule exclusive of nuclear spin, and their projections onto the internuclear axis, z. The nomenclature convention follows [74].

6.2 Talking Diatomic Molecules

In general, the calculation of $E_{el}(r)$ or a PES is a difficult *ab initio* quantum chemistry problem. In our case, several groups have performed the calculations for the Li-Yb molecule [40, 130]. The other parts of Eq. 6.2 are much more straightforward to understand. The vibrational energies are just eigenfunctions of a particular harmonic oscillator

$$\mathcal{H}_{vib} = A(\nu + \frac{1}{2}), \quad \nu = 0, 1, 2, \ldots \tag{6.8}$$

The rotational energies approximate the energy levels of a rigid rotor

$$\mathcal{H}_{rot} = B_J J(J+1), \quad B_J \simeq \frac{\hbar^2}{2\mu r^2}, \quad J = 0, 1, 2, \ldots \tag{6.9}$$

Typical energies of a single electronic excitation are on the scale of 5000 K, that of a vibrational excitation 50 K, and a rotational excitation 0.5 K.

In order to connect these values with the behaviour of actual molecules and determine which molecules we can make, however, we need to put back in the couplings we ignored in making the BO approximation: the nuclear-electronic rotational coupling, electronic spin-orbit coupling, etc. The angular momenta and projections to consider, and the notation ordinarily used for them in the literature are given in Table 6.1. In

System	Production method	Term Symbol
$({}^2\mathrm{S\,Li} + {}^1\mathrm{S\,Yb})$	Magnetoassociation, 2-photon PA	${}^2\Sigma$
$({}^2\mathrm{P\,Li} + {}^1\mathrm{S\,Yb})$	671 nm PA	${}^2\Sigma,\ {}^2\Pi$
$({}^2\mathrm{S\,Li} + {}^3\mathrm{P\,Yb})$	556 nm PA	${}^{2,4}\Sigma,\ {}^{2,4}\Pi$
$({}^2\mathrm{S\,Li} + {}^3\mathrm{D\,Yb})$	404 nm PA	${}^{2,4}\Sigma,\ {}^{2,4}\Pi,\ {}^{2,4}\Delta$
$({}^2\mathrm{S\,Li} + {}^1\mathrm{P\,Yb})$	399 nm PA	${}^2\Sigma,\ {}^2\Pi$

Table 6.2: Term symbols for potential photoassociation products in our experiment. Since PES calculations assume BO approximation, we can give Λ values corresponding to a given electronic manifold, but these would not necessarily be good quantum numbers for an actual physical molecule in this manifold which we would create.

order to aid inclassification of molecular states, the equivalent of the term symbols for atoms, ${}^{2S+1}L_J$ becomes for molecules

$$ {}^{2S+1}\Lambda_{\Omega} \tag{6.10} $$

with S, $\Lambda$and Ω defined as above. As is the case for atoms, the situation occasionally arises where molecules do not have these as good quantum numbers. However, for most molecules binding between nuclei is strong, and so the coupling of angular momentum to the internuclear axis is large and Λ and Ω are useful. Since PES's are calculated using the BO approximation that necessarily has these as good numbers, they are labelled using this system anyway. The term symbols for molecular states potentially available with single photoassociation excitations or in the ground state in our lab are given in Table 6.2. For most molecules we can make, these labels are somewhat misleading since the assumption of strong internuclear binding doesn't hold. Note also that there are about a dozen low-lying PES's, and since these potentials perturb each other, sometimes in the manner of avoided crossings, there is a frightening amount of complexity.

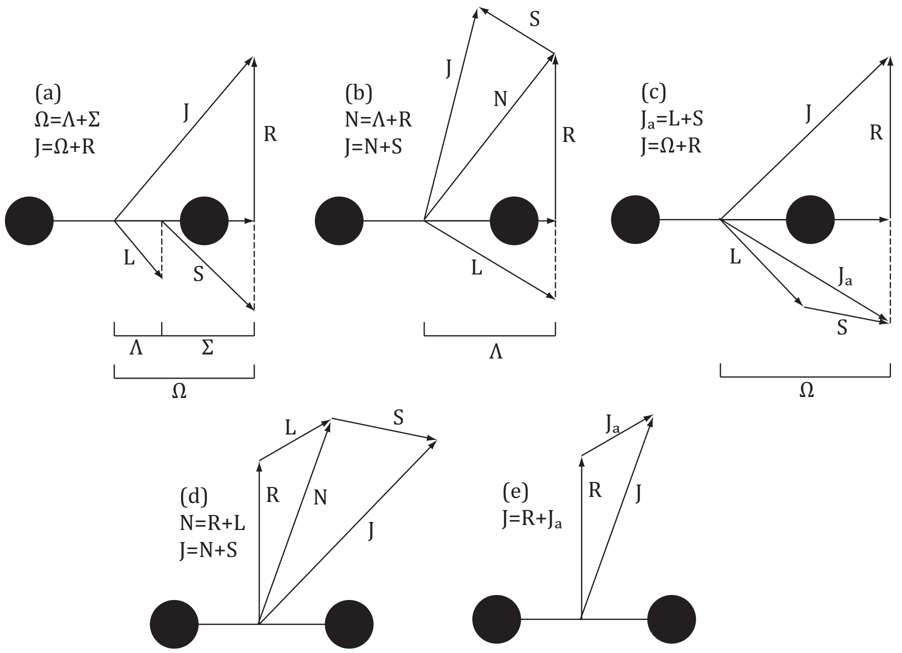

Figure 6.1: Hund's Cases

6.2.1 *Hund's Cases*

Hund's cases are a means of classifying the profusion of angular momenta discussed in Table 6.1. They specify the most convenient basis for analysis of the molecule, which part of the molecular Hamiltonian is convenient to diagonalize, and which to treat as a perturbation. They are covered in any book on molecular spectroscopy [74, 12, 129]. The angular momentum diagrams for the five cases are given in Fig. 6.1. Altogether, Hund's cases are differentiated by the ranking of three energy scales: the energy difference between two PES's in the same manifold (electrostatic coupling), the spin orbit coupling, and the rotational coupling between (some component of) electronic angular momentum and molecular rotation. Only in the case that the first energy is strongest, is Λ a good quantum number and does it make sense to analyze a molecule in terms of PES's. This is the case for the overwhelming majority of molecules. However, the ultracold atomic physicist is potentially dealing with a molecule that a molecular spectroscopist would consider bizarre: the internuclear bond is very weak, therefore even the labelling introduced in Eq. 6.10 is no longer a good means of classifying the molecules. However, because of the ultracold temperatures, the average number of molecular rotational excitations is small and so the effect of the rotational coupling may also be weak. In particular, in terms of application to our experiment, the Li_2 Feshbach molecules discussed in Section 5.2 would probably fall under case (d), as there is no spin-orbit coupling at all, but the coupling to the internuclear axis is very weak [64]. An eventual ground state LiYb molecule is more likely to be an example of case (b), due to somewhat stronger electrostatic coupling and a lack of spin-orbit interaction. A 1-photon photoassociated LiYb molecule, however, were it to have a molecular rotational excitation as well as non-zero electronic orbital angular momentum, would probably fall into the very obscure case (e). This case was ignored by Hund himself, and it was not until about 20 years ago that the first experimental observation was made of a molecule [14] which it made sense to treat in this basis. For that reason it is sometimes skipped in molecular spectroscopy texts. Case (e) occurs where the energy difference between two different PES's is smaller than either the rotational or spin-orbit coupling. This is often true near the dissociation limit, where molecules created through 1-photon photoassociation typically are found. In this case, the strongest coupling may be that between L and S to give a total electronic angular momentum, J_a, which then couples with the nuclear rotation R to give a total J. Alternatively, the rotational-electronic coupling may be stronger than the spin-orbit coupling, but this doesn't change the picture. In both cases, it is J_a, R and J that are the only good angular momentum quantum numbers.

6.2.2 Long Range Behaviour

For deeply bound states, the PES for a collision of two atoms is well approximated by a Morse potential,

$$V(r) = D\left(\left(1 - e^{a(r-r_0)}\right)^2 - 1\right), \tag{6.11}$$

which is just a phenomenological fit without any physical basis. At greater distances. however, we can distinguish several possibilities for leading-order interactions, each with its power-law dependence. In the simplest case of neutral atoms without the possibility of spin exchange collisions, the induced dipole-induced dipole interaction is described by a van der Waals potential[1] together with the angular momentum term

$$V(r) = -\frac{C_6}{r^6} + \frac{\hbar^2 l(l+1)}{2\mu r^2} \tag{6.13}$$

For s-wave collisions, $l = 0$ and so the C_6 coefficient is the one parameter governing behaviour outside the deeply bound region. However, as long as $\int V(r) 4\pi r^2 dr$ converges, the potential is too weak to lead to long range order. In order to observe long-range behaviour, we need a potential that scales at least $\propto 1/r^3$. One way to achieve this scaling is through resonant dipole-dipole interactions [69]. This occurs in collisions between homonuclear atoms where one is in the excited, and one in the ground state, because the two atoms can effectively "share" the excitation, and thus each atom can be thought of as being in a superposition of ground and excited state, which gives it a real oscillating dipole moment [64]. However, the use of these interactions is limited, as they are shortlived. A potential way to harness resonant dipole-dipole interactions is to use heteronuclear molecules. Heteronuclear molecules have a permanent dipole moment, and so, in the presence of an electric field, the potential between two molecules has the form

$$V(\mathbf{r}) = \frac{\mathbf{d}_1 \cdot \mathbf{d}_2 - 3(\mathbf{d}_1 \cdot \hat{\mathbf{r}})(\mathbf{d}_2 \cdot \hat{\mathbf{r}})}{4\pi\varepsilon_0 r^3} \tag{6.14}$$

---

[1] In order to replicate a reasonable-looking PES, for simulation purposes usually a Lennard-Jones potential,

$$V(r) = \frac{\sigma_{12}}{r^{12}} - \frac{\sigma_6}{r^6} \tag{6.12}$$

is used, but, as far as I know, the r^{12} term has no physical significance.

where $\mathbf{d}$ are the dipole operators for the given molecule, r the separation between two molecules and $\hat{\mathbf{r}}$ a unit vector in the direction of that internuclear axis. This potential is inherently anisotropic as well as being long-range, which leads to interesting consequences in polarized samples. We see that the potential is attractive in the $\mathbf{d} \parallel \mathbf{r}$ case, and repulsive if $\mathbf{d} \perp \mathbf{r}$. Thus "head-to-tail" collisions between molecules are strongly favoured over "side-to-side" collisions. This means that by putting in a 1-D optical lattice and polarizing the molecules perpendicular to the lattice planes, for example, collisions between molecules can be suppressed [24]. Conceptually, this kind of phenomenon can also be used to control chemical reaction mechanisms. Further afield, interactions mediated by the resonant dipole-dipole interaction in a 3-D optical lattice can be used to model exotic Hamiltonians and perform quantum information protocols.

6.3 Photoassociation

The next step in studying diatomic molecules is to have actual diatomic molecules to study. Photoassociation (PA) is the process of bringing a scattering state of two atoms in resonance with a bound state of the molecule by using light. PA spectroscopy has a long history [64] and has been used to create ultracold homonuclear [1] and heteronuclear [47] bialkali molecules, as well as molecules involving alkaline earth or alkaline earth-like atoms [87, 115, 76]. 1-photon PA couples a scattering state of two atoms to a (usually) weakly-bound vibrational state in an electronically excited manifold (see Fig. 6.2). Ground state molecules may then be populated by spontaneous emission [26], but usually the amount of available states for decay is very large, and so absolute ground state molecule density is small. To deal with this, 2-photon PA can be used to convert atoms into a bound molecular state, and then stimulate emission into the rovibrational ground state, *e.g.* [109]. As well as creating ground state molecules, 2-photon PA can be used to probe the least-bound levels of the ground electronic state, which in turn allows for a more accurate determination of the PES. In general,

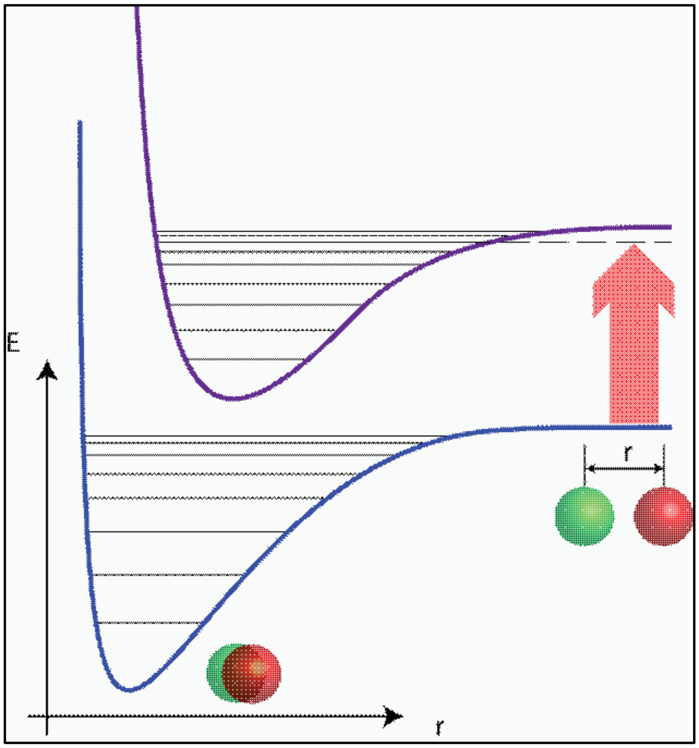

Figure 6.2: Photoassociation schematic. The laser (red arrow) couples the scattering state of the ground PES (blue) with a bound state in another PES (purple).

PA spectroscopy can give valuable information about atomic collisions, and molecular properties in several ways, which are well summarized in the review by Jones *et al.* [64]. However, for us the primary motivation is molecule production, and so we should examine how effective PA could be at producing molecules.

The rate of molecule production from atoms 1 and 2 can be written as

$$\dot{N}_{mol} = \int K_{12} n_1 n_2 dV, \tag{6.15}$$

where n is the cloud density and K_{12} is a constant subsuming all the other factors including laser intensity and depends on the stimulated width of the transition, given by

$$\Gamma_{stim} = \Gamma_A \frac{3}{4\pi} \frac{I\lambda_A^3}{c} f_{rot} f_{FC}, \tag{6.16}$$

where the subscript A indicates values for the atomic transition, Γ is the natural decay width, λ the transition wavelength, c the speed of light and f_{rot} a rotational line strength factor of order one. That leaves f_{FC}, known as the Franck-Condon (FC) factor. The FC factor is straightforward to calculate

$$f_{FC} = |\langle \psi_g | \psi_e \rangle|^2 \tag{6.17}$$

provided both wavefunctions are well-known. In the case of a transition between a scattering and a bound state, unity normalization is no longer appropriate, and usually some approximation for the scattering state is required. One approach [9, 18] is to use the asymptotic form

$$\psi(k,r) = \sqrt{\frac{2\mu}{\pi \hbar^2 k}} \sin\left[k\left(r - a_{bg}\right)\right] \tag{6.18}$$

at large internuclear separation r. Here $k = \sqrt{2\mu\varepsilon}/\hbar$, μ is the reduced mass, ε is the energy above threshold of the incoming channel and a_{bg} is the background scattering length. This is often sufficient in situations where the outer turning point of the target excited state is past that of the least bound ground state, i.e. past the point where the ground state potential strongly affects the scatttering wavefunction. This is the case where the ground state PES scales at long range as $1/r^6$, and the excited state as the much longer-range $1/r^3$as occurs in homonuclear systems. Otherwise, the wavefunction may need to be connected to the scattering wavefunction in the deeply bound region and a FC-like overlap integral calculated. This connection is dependent on relatively precise knowledge of the PES in the intermediate region between the asymptotic and deeply bound regions. Since the form of the long range ground state scattering wavefunction depends on the scattering length a_{bg}, this represents another method to determine the sign and amplitude of the scattering length. Practically, the transition amplitude to the excited state vanishes wherever eq. 6.18 has a node, so by comparing transition amplitudes to different excited states (or, potentially, at different temperatures), we may get at a_{bg}.

An alternative method for determining the FC overlap [9, 67] is to use the reflection approximation. Although I will omit going through the approximation here[2], the idea is to notice that the (as was already implicitly assumed in the other method to obtain a_{bg}), the excited state wavefunction would oscillate rapidly everywhere except near the Condon point, R_C, which is the outer turning point of the molecular wavefunction, or alternatively the point where the potential curves $V_g(r) + \hbar\omega$ and $V_e(r)$ intersect. Thus, it is only around R_C that we need to calculate the overlap. Then, rather than calculating an integral, the f_{FC} can be approximated as

$$f_{FC} \approx \sqrt{2\pi}\hbar \frac{\Gamma(7/6)}{\Gamma(2/3)} \left(\frac{R_C^6}{\mu C_6^*} \right)^{1/2} |\chi(R_C)|^2 \tag{6.19}$$

where Γ is the gamma function, μ the reduced mass, C_6^* is the van der Waals coefficient of the excited state, and $\chi(R_C)$ is the value of the ground state scattering wavefunction at R_C.

6.3.1 Photoassociation in the $({}^2\mathrm{P\,Li} + {}^1\mathrm{S\,Yb})$ *manifold*

The intensity required to saturate a PA transition to a very weakly bound molecular state is given as

$$I_{sat,PA} \approx \frac{I_{sat,A}}{\pi\hbar\Gamma_A f_{FC}} \tag{6.20}$$

where the subscript A once again refers to the atomic values. Using Eq. 6.19 to estimate the FC factor and the C_6^* from [130], we obtain an estimate for $I_{sat,PA} \simeq 7\,\mathrm{W/cm^2}$. Without amplification by TA, we can expect roughly 20 mW of power

---

[2] A derivation and explanation can be found in [65]

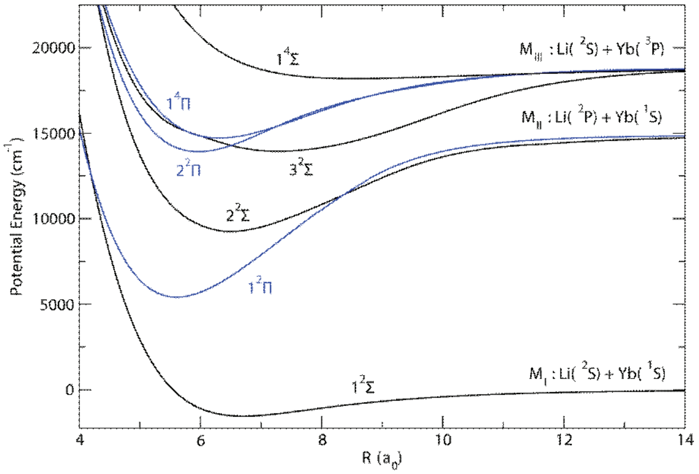

Figure 6.3: Potential energy curves for the LiYb system. Figure taken from [130]

from our red PA diode, and after isolation, filtering, locking and potentially beam profile cleaning through the use of a fibre, a conservative estimate of 5 mW to use in experiment. Thus, in order to saturate a PA transition, we expect to require an average beam diameter of 300 μm at the atoms.

To get a qualitative idea of the landscape of vibrational states in the ground state and our target $^2\Pi$, we can simply solve the radial part of the Schroedinger equation with a potential $V(r)$ given by the PES for each electronic manifold. We use potential curves from [130] (see Fig. 6.3) to obtain the potentials at short range, and extend the potentials to long range by fitting the last 5 a_0 to a C_6/r^6 potential. To solve the Schroedinger equation, we convert it to the form

$$\left(\frac{\partial^2}{\partial r^2} + \frac{2\mu}{\hbar^2}\left(E - V(r)\right)\right) u(r) = 0 \tag{6.21}$$

and solve using the Numerov-Cooley algorithm[3] to obtain electronic wavefunctions (see Fig. for examples) and energy eigenvalues. We thus see that the ground electronic

---

[3] For an equation of the form $\left(\frac{\partial^2}{\partial r^2} + f(r)\right) u(r) = 0$ this consists of starting from beyond the outer and inner turning points, where the values of the wavefunction are expected to be really

state manifold supports about 25 vibrational levels, (a value closely matching the 24 levels obtained in [13]), whereas the $1^2\Pi$ manifold supports 44. Furthermore, we calculate that the least bound state in the $^2\Pi$ excited electronic manifold is red-detuned $8\,\mathrm{cm}^{-1}$ from the atomic resonance, and the spacing of the first few bound levels starts out at $\simeq 10\,\mathrm{cm}^{-1}$, roughly doubling with every bound state. These specific values should not be believed too readily as the potentials from Zhang *et al.* are accurate to only within a few percent, and furthermore our method of constructing the long-range potential is very unsophisticated, and does not quantitatively match the C_6 coefficients derived in [130]. A more thorough investigation would consist of using those C_6 coefficients to construct the long-range potential, and then joining the short- and long-range parts, for example with the use of switching functions [60]. In any case, although a few percent error in trap depth makes very little difference for deeply bound states, the number and character of the least-bound states can be very strongly affected. Nevertheless, these results are enough to suggest that we should be able to access the first several bound states with a laser system that is tuneable between the $^2\mathrm{S}_{1/2} \rightarrow {}^2\mathrm{P}_{3/2}$ transition in ^{6}Li, and somewhere 7-8 nm to the red of the transition. We note that the spacing of weakly bound LiYb vibrational lines is expected to be much less dense than the comparable excitation in the Li_2 system [1], a finding that can be explained by the $1/r^3$ scaling of the long-range potential in the latter case as opposed to $1/r^6$ in our case.

In order to perform photoassociation, we have built two Littrow-configuration ECDLs, of the same design as mentioned for the 404 nm laser in Section 3.8 (Ryan

---

small; propagating towards the region of interest in steps of size h as

$$u_{n+1} \equiv u(r_{n+1}) = \frac{\left(2 - \frac{5h^2}{6} f_n\right) u_n - \left(1 + \frac{h^2}{12} f_{n-1}\right) u_{n-1}}{1 + \frac{h^2}{12} f_{n+1}}, \tag{6.22}$$

and rescaling to match the amplitudes where the solutions meet. The trial energy that forms a constant offset to $f(r)$ can then be moved in the direction that would lead the slopes to match at the meeting point, and a solution can iteratviely be found.

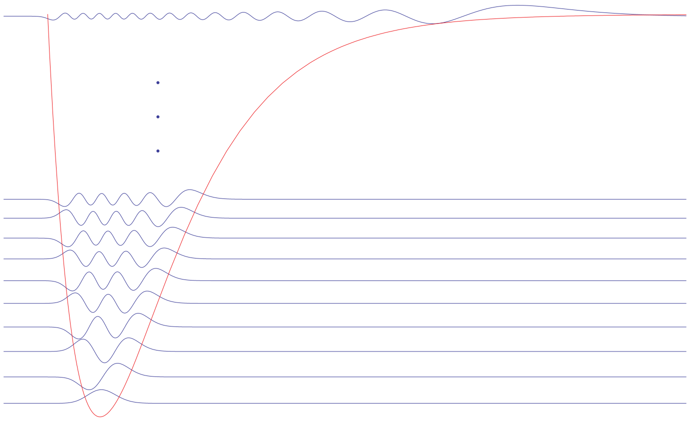

Figure 6.4: Examples of wavefunctions obtained for different vibrational levels in the LiYb ground state electronic potential. The PES is shown in red, and the 10 most deeply bound and one least bound wavefunction are shown in blue (and are arbitrarily placed with respect to the PES)

Weh built the first red PA laser, and a similar laser was built by REU student Ryne Saxe). We use an Eagleyard ridge waveguide diode, which provides up to 23 mW of light tunable between 665 and 678 nm using the external grating. We are able to achieve 8 GHz of mode hop-free tuning, allowing for relatively large scans to be performed electronically. Although our PA laser appears to be single-mode by Fabry-Perot spectroscopy, we initially found large, almost frequency independent trap losses in the presence of a PA beam even well away from atomic resonance. We are able to reduce these losses by filtering the PA beam to remove any remaining light around the atomic resonance. We do this by passing the beam through the lithium saturated absorption spectroscopy cell. With the beam thus filtered, we are able to locate and strongly broaden Li_2 PA resonances, *e.g.* Fig. 6.5 (a), showing that it is realistic to use this setup to search for LiYb PA resonances. However, currently the red PA laser setup, the beam filtering through the saturated absorption spectroscopy cell and the path to the atoms have been dismantled in favour of performing PA close to the ytterbium green intercombination line. The main advantage of the green line

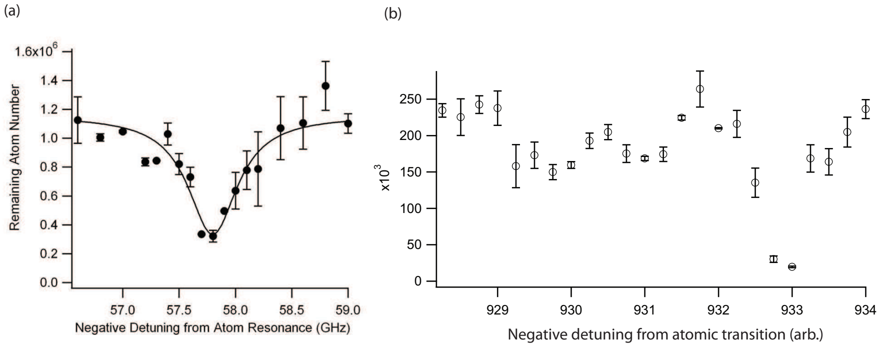

Figure 6.5: (a) Example of a PA resonance scan in Li_2 (b) Example of a PA resonance scan in Yb_2

is that we would now be able to search for the PA signal in lithium rather than ytterbium atom loss. Since we are technically able to create mixtures with large numbers and densities of ytterbium and small numbers of lithium but not vice versa, this simplifies the search process. Additionally, the narrow atomic transition makes it a possible avenue for studying optical Feshbach resonances. These last are analogues of magnetic Feshbach resonances, as described by Eq. 5.6 where the b coefficient now describes PA loss, and γ represents the breadth of the atomic transition. However, the advantage of PA near the red lithium line is the greater tunability of our available laser, the potentially increased ease of finding resonances due to a broader atomic transition, and the existence of two lasers in case 2-photon PA is ever contemplated.

6.3.2 Photoassociation in the $(^2\mathrm{S}\,\mathrm{Li} + {}^3\mathrm{P}\,\mathrm{Yb})$ *manifold*

We repeat the calculations of Section 6.3.1, this time for the $2^2\Pi$ excited state manifold that asymptotically approaches the 556 nm atomic excitation at large distances. Making the same choice for C_6^* as in [39], we find $I_{sat,PA} = 1.4\,\mathrm{W/cm^2}$, and that the potential supports 30 vibrational states. The initial separation is calculated as $1\,\mathrm{cm^{-1}}$, again roughly doubling for each lower bound state. Once again, these values' utility is not in the specifics, which are unreliable, but for estimating the potential usefulness of the laser sources available to us. We once more note that the spacing of LiYb lines is predicted to be much less dense than that ofYb_2 photoassociation lines [115]. In this case, in addition to the $1/r^3$ scaling, a compounding issue is the reduced mass factor μ scaling the kinetic and potential energies for the Schroedinger equation.

For performing PA on the "green" line, we use the Koheras laser at 1112 nm followed by a single-pass PPLN doubler that has previously been used for our Yb MOT (see Section 3.4.2). We couple the PPLN output into a fibre, resulting in about 8 mW at the atoms. We are able to locate Yb_2 PA resonances with relative ease (see Fig. 6.5 (b)). This provides a proof of concept for a search in the LiYb manifold. However, we note that we do not expect to find many lines using this method. The Koheras laser is tunable by temperature between 20° and 40°C with a tunability of 11 pm/°C. The atomic transition is found at 33.7°C, which, when coupled with the 17 pm tunability of the grating piezo, and halved to account for the frequency doubling, corresponds to ~$1.4\,\mathrm{cm}^{-1}$ of frequency tunability. Given our level spacing calculations, this is at best enough for locating only one vibrational level. Therefore, in order to pursue PA spectroscopy to gain information about LiYb collisions and the PES's of the ground and excited states, a more widely tunable laser is required. We are considering alternatives, including a homebuilt design for an 1112 diode that would be grating-tunable, or a commercial system.

Chapter 7

PRODUCTION AND EXPERIMENTS WITH METASTABLE YTTERBIUM

During the past year, most of the mixture group's efforts have been directed to producing, and performing experiments with, metastable ytterbium in the ^{3}P$_2$ state. Our main motivation has been to use metastable ytterbium as a stepping stone for molecule production in the mixture, although metastable ytterbium also possesses other nice properties including a high magnetic dipole moment. We have been drawing on the experience of the Takahashi group with metastable ytterbium [119, 118, 126, 66]. The new achievements are as follows: we have obtained Yb in ^{3}P$_2$ in a 1064 nm optical dipole trap; we have used the relative polarizations of the optical trap, excitation beam and magnetic field, as well as magnetic-field-gradient based spilling to obtain a pure magnetic substate. We have used RF transfer to show that we can obtain an arbitrary spin substate composition. Finally, we have put the electronically excited ytterbium together with a ground state into one ultracold system. This constitutes the first instance of an ultracold heteronuclear mixture of excited and ground state atoms. Our experimental technique consists of excitation of ytterbium atoms on the ^{1}S$_0$ → ^{3}D$_2$ transition, and trapping the ^{3}P$_2$ atoms resulting from spontaneous decay. These atoms are detected by excitation on the ^{3}P$_2$ → ^{3}S$_1$ transition, after which the atoms decay back to the ground state and can be imaged using the standard technique.

Portions of this chapter, and the results discussed herein appear in the following paper

- A. Khramov, A. Hansen, W. Dowd, R.J. Roy, C. Makrides, A. Petrov, S. Kotochigova and S. Gupta, "Ultracold heteronuclear mixture of ground and excited state atoms", arXiv:1309.7926 (2013)

7.1 Background

Metastable atoms have a relatively long history in ultracold atomic physics experiments. Bose condensation of metastable ^{4}He* in the ^{3}S$_1$ state was achieved in 2001 [101, 94]. In the case of He* species, the primary advantage was the very high energy of the metastable state, and thus the ability to use multichannel plates to obtain three dimensional positional information for individual atoms with great spatial resolution. This was used, for example, to show the Hanbury-Brown and Twiss effect for bosonic and fermionic cold atoms [61]. Additionally, the internal simplicity of the atom promised easy comparison between experiment and theory, and the high s-wave scattering length of ^{4}He* gave a means of accessing the hydrodynamic regime in the absence of a Feshbach resonance. Metastable states of ultracold alkaline earth and alkaline earth-like atoms were initially created as byproducts of MOTs on the broad ^{1}S$_0$ → ^{1}P$_1$ transitions. The ^{3}P$_2$ states in Ca, Mg, and Sr were magnetically trapped and explored in the context of attempts to cool alkaline earth (like) atoms to degeneracy *e.g.* [86]. A MOT on the ^{3}P$_2$ $\rightarrow^3$ D$_3$ transition was made for Ca [45], but cooling ^{3}P$_2$ atoms has been very difficult due to a high level of inelastic collisions. However, the inelastic collisions themselves turned out to be an avenue for further study [52, 66]. The Kyoto group has pioneered production of ultracold Yb in the ^{3}P$_2$ state, both via excitation to ^{3}D$_2$ [119], and via direct excitation of the ultra-narrow line [118]. The direct excitation route has the advantage of allowing selective state population, and extremely low temperatures, but is technically difficult and produces limited numbers.

The primary motivation for production of Yb in the ^{3}P$_2$ state (hereafter referred to as Yb*) in our group is the potential for the existence of magnetically tunable interactions with lithium [39]. Such resonances may occur either due to anisotropic multichannel coupling, as discussed in Section 5.4.2 or through more conventional coupling methods. If found, such resonances could be useful for making LiYb* molecules and finding novel Efimov states, among other potential experiments.

*7.2 Production of Yb**

For production, we drive to the intermediate $^3D_2$ state with the 404 nm laser described in Section 3.8. The $^1S_0 \rightarrow {}^3D_2$ transition is an electric quadrupole (E2) transition, and so the selection rules are

$$\Delta J = 2 \quad \Delta M = 0, \pm 1, \pm 2 \tag{7.1}$$

but the ability to drive the transition is dependent on the specific transition matrix element. Instead of figuring these out directly, we use the vector spherical harmonics[1]

---

[1] Vector spherical harmonics are related to spherical harmonics as

$$\mathbf{Y}_{J,L,M}(\theta,\phi) = (-1)^{1-L-M}\sqrt{2J+1}\sum_{q=-1}^{+1}\begin{pmatrix} L & 1 & J \\ M-q & q & -M \end{pmatrix} Y_{L,M-q}(\theta,\phi)\hat{e}_q \tag{7.2}$$

where $\begin{pmatrix} L & 1 & J \\ M-q & q & -M \end{pmatrix}$ is a Wigner $3-j$ symbol and $q = 0, \pm 1$ correspond to π and $\sigma^{\pm}$ polarized light. in turn the particular spherical harmonics of interest to us for EJ transitions

$$\mathbf{Y}^{(1)}_{J,M}(\theta,\phi) = \sqrt{\frac{J+1}{2J+1}}\mathbf{Y}_{J,J-1,M}(\theta,\phi) + \sqrt{\frac{J}{2J+1}}\mathbf{Y}_{J,J+1,M}(\theta,\phi) \tag{7.3}$$

for E2 transitions [123]

$$\begin{aligned}\mathbf{Y}^{(1)}_{2,\pm2}(\theta_{\mathrm{k}},\phi_{\mathrm{k}}) &= \left(\sqrt{\frac{3}{5}}Y_{1,\pm1}(\theta_k,\phi_k)+\sqrt{\frac{2}{7}}Y_{3,\pm3}(\theta_k,\phi_k)\right)\hat{\mathrm{e}}_{\pm1}\\ &\quad -\sqrt{\frac{2}{21}}Y_{3,\pm2}(\theta_k,\phi_k)\hat{\mathrm{e}}_0+\sqrt{\frac{2}{105}}Y_{3,\pm1}(\theta_k,\phi_k)\hat{\mathrm{e}}_{\mp1}\end{aligned}\tag{7.4}$$

$$\begin{aligned}\mathbf{Y}^{(1)}_{2,\pm1}(\theta_{\mathrm{k}},\phi_{\mathrm{k}}) &= \left(\sqrt{\frac{3}{10}}Y_{1,0}(\theta_k,\phi_k)+\sqrt{\frac{4}{21}}Y_{3,\pm2}(\theta_k,\phi_k)\right)\hat{\mathrm{e}}_{\pm1}\\ &\quad +\left(\sqrt{\frac{3}{10}}Y_{1,\pm1}(\theta_k,\phi_k)+\sqrt{\frac{16}{105}}Y_{3,\pm1}(\theta_k,\phi_k)\right)\hat{\mathrm{e}}_0-\sqrt{\frac{2}{35}}Y_{3,0}(\theta_k,\phi_k)\hat{\mathrm{e}}_{\mp1}\end{aligned}\tag{7.5}$$

$$\begin{aligned}\mathbf{Y}^{(1)}_{2,0}(\theta_{\mathrm{k}},\phi_{\mathrm{k}}) &= \left(\sqrt{\frac{1}{10}}Y_{1,-1}(\theta_k,\phi_k)+\sqrt{\frac{4}{35}}Y_{3,1}(\theta_k,\phi_k)\right)\hat{\mathrm{e}}_{+1}+\left(\sqrt{\frac{2}{5}}Y_{1,0}(\theta_k,\phi_k)+\sqrt{\frac{6}{35}}Y_{3,0}(\theta_k,\phi_k)\right)\hat{\mathrm{e}}_0\\ &\quad +\left(\sqrt{\frac{1}{10}}Y_{1,1}(\theta_k,\phi_k)+\sqrt{\frac{4}{35}}Y_{3,-1}(\theta_k,\phi_k)\right)\hat{\mathrm{e}}_{-1},\end{aligned}\tag{7.6}$$

where $Y_{l,m}(\theta_k,\phi_k)$ are the familiar spherical harmonics. The transition is forbidden whenever $\mathbf{Y}^{(1)}_{J,\Delta M}(\theta_k,\phi_k)\cdot\mathbf{e}_k=0$. Here θ_k and ϕ_k describe the direction of propagation of the excitation laser with respect to the polarization axis for the atoms, which is taken to be z; $\mathbf{e}_k$ is the vector of polarization of the excitatio1n laser, and $\mathrm{e}_{0,\pm1}$ correspond to π and $\sigma^{\pm}$ polarization.

Initially, we used an alignment scheme with the excitation beam aligned top-down. In this case, whenever we had a bias magnetic field,$\mathbf{k}\parallel z$, and the excitation. The vector spherical harmonics thus become

$$\mathrm{Y}^{(1)}_{2,\pm2}(0,\phi_{\mathrm{k}}) = 0\tag{7.7}$$

$$\mathrm{Y}^{(1)}_{2,\pm1}(0,\phi_{\mathrm{k}}) = \frac{3}{\sqrt{40\pi}}\hat{\mathrm{e}}_{\pm1}-\frac{1}{\sqrt{10\pi}}\hat{\mathrm{e}}_{\mp1}\tag{7.8}$$

$$\mathrm{Y}^{(1)}_{2,\pm0}(0,\phi_{\mathrm{k}}) = \sqrt{\frac{6}{5\pi}}\hat{\mathrm{e}}_0,\tag{7.9}$$

however, since it is impossible to have $\mathbf{k},\hat{\mathbf{e}}\parallel z$, only the $M=\pm1$ states could be populated, and, since by our arrangement we had no control over the 404 nm beam polarization, much of the light was wasted. This scheme also suffered from difficulty in alignment and only a small spatial overlap between excitation light and the atomic cloud. Therefore we moved to a scheme with the 404 excitation collinear with the ODT beam. In this case, $\mathbf{k} \perp z$, and

$$\mathrm{Y}^{(1)}_{2,\pm2}(\frac{\pi}{2},\phi_\mathrm{k}) = \mp \left(\sqrt{\frac{5}{32\pi}}e^{\pm3i\phi_k} + \sqrt{\frac{9}{40\pi}}e^{\pm i\phi_k}\right)\hat{\mathrm{e}}_{\pm1} \pm \sqrt{\frac{1}{160\pi}}e^{\pm i\phi_k}\hat{\mathrm{e}}_{\mp1} \quad (7.10)$$

$$\mathrm{Y}^{(1)}_{2,\pm1}(\frac{\pi}{2},\phi_\mathrm{k}) = \mp\frac{e^{\pm i\phi_k}}{\sqrt{80\pi}}\hat{\mathrm{e}}_0 \quad (7.11)$$

$$\mathrm{Y}^{(1)}_{2,0}(\frac{\pi}{2},\phi_\mathrm{k}) = 0. \quad (7.12)$$

Thus we are able to populate $M = \pm1, \pm2$ states in $^3\mathrm{D}_2$. We split the degeneracy of these Zeeman levels by going to a magnetic field of 12 G. We show our ability to access these levels in Fig. 7.1 (a). The much better spatial overlap in this arrangement ensures that we are typically able to deplete the $^1\mathrm{S}_0$ state entirely in 20 ms of pumping. The $^3D_2$ state has a linewidth of $2\pi \times 350$ kHz, with branching ratios of 0.88 and 0.12 to $^3P_1$, and $^3P_2$. Thus each ground state atom is pumped to the $^3P_2$ state after an average of $1/.12 = 8$ excitations. To optimize the pumping efficiency, the available 1 mW of 404 nm light is tightly focussed to an intensity of $5 \times 10^5\ \mathrm{W/m^2}$ at the atomic sample and aligned along the axial direction of the ODT. Two counter-propagating laser beams are used to suppress axial dipole oscillations of the Yb* cloud due to photon recoil. The importance of accounting for photon recoil momentum can be seen in Fig 7.2 (b), which shows initial displacement of the centre of the $^3\mathrm{P}_2$ cloud as a function of the splitting between co- and counter-propagating beams.

Starting from a population in a given $^3\mathrm{D}_2$ substate, the resulting population after spontaneous emission into the $^3\mathrm{P}_2$ state is dictated by the relevant Clebsch-Gordan coefficient. The branching ratios to the different substates of Yb* are shown in Fig.

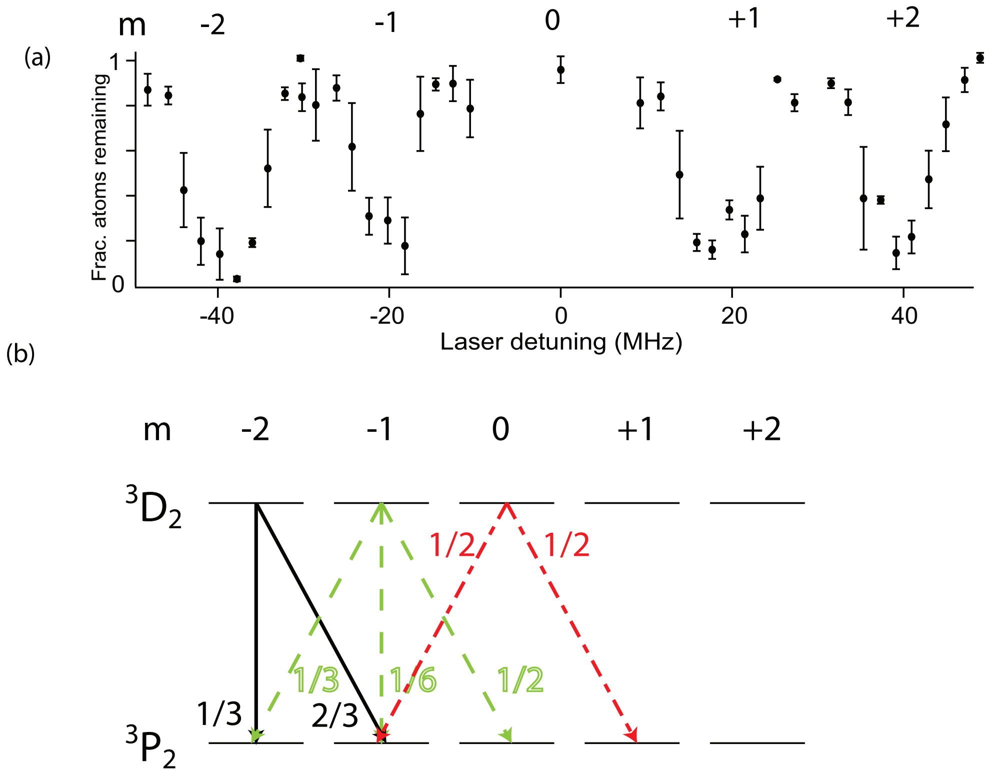

Figure 7.1: (a) Zeeman scan of $^1S_0 \rightarrow {}^3D_2$ transition (b) branching ratios for the $^3D_2 \rightarrow {}^3P_2$ transition. The branching ratios from positive m_J substates of $^3D_2$ are identical to those from negative m_J substates and are omitted from the figure.

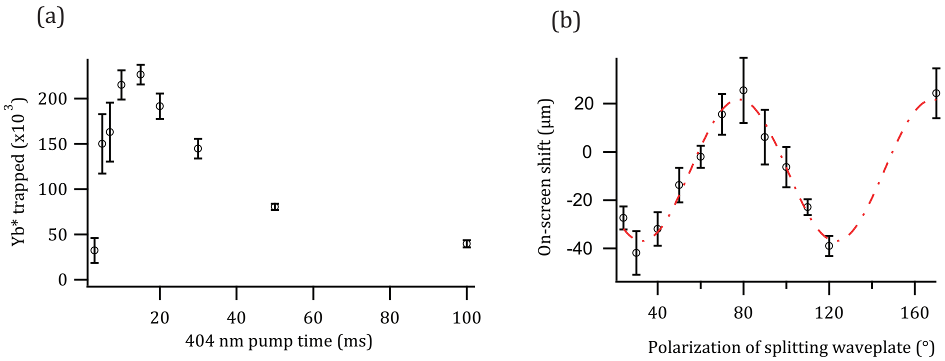

Figure 7.2: ^{3}P$_2$ load. (a) Atoms in $^3P_2$ state versus time of applied 404nm pulse. In this instance, 404nm pulse is unidirectional with an intensity of $5 \times 10^5\,W/m^2$. The initial slope can be fit with a pumping rate of 50 Hz. The reduction in Yb* at larger transfer times is due to inelastic processes (b) Initial displacement of on-screen trap centre as a function of power-splitting beamsplitter position. The maximal positive displacement corresponds to a 2:1 beam power ratio of about 20 to 1. The maximal negative displacement is at about 1 to 10. Because we are observing the trap centre off-axis, the actual trap centre displacement is potentially much greater, by up to a factor of $1/\sin(8°)$

7.1 (b). The Yb* load dependence on 404nm duration is displayed in Fig 7.2 (a). For all the experiments discussed, we remove any remaining $^1S_0$ atoms with a 3 ms light pulse resonant with the $^1S_0 \rightarrow {}^1P_1$ transition.

The transfer of Yb* to the ground state is achieved by applying a 4 mW pulse of 770 nm light resonant with the $^3P_2 \rightarrow {}^3S_1$ transition for 200 μs. The $^3S_1$ state decays via the $^3P_1$ state to $^1S_0$. Atoms which decay to the long-lived $^3P_0$ state can be brought back into the transfer cycle with a simultaneously applied 649 nm pulse resonant with the $^3P_0 \rightarrow {}^3S_1$ transition. We typically used only the 770 nm resonant light, resulting in some atoms getting stuck in $^3P_0$. Averaging collected atom numbers in the presence or absence of 649 nm light (0.25 mW), we obtain the ratio $N_{770+649} : N_{770} = 1.31 \pm 0.05$.

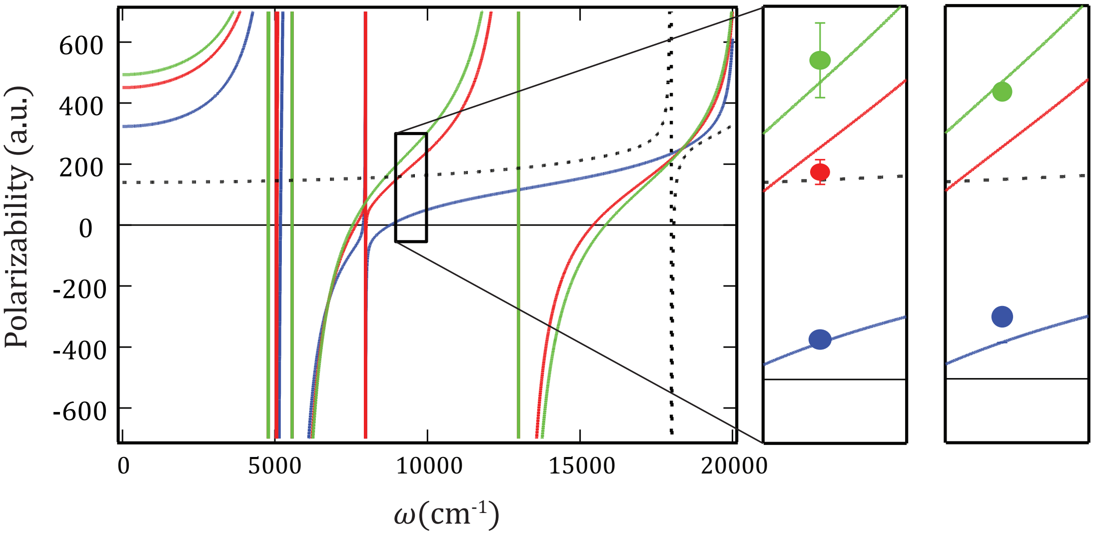

Figure 7.3: Polarizability of as a function of frequency of light linearly polarized parallel to the spin polarization axis. Figure from [68], courtesy of Svetlana Kotochigova. Insets: comparison of theoretical polarizability values to experimentally obtained ratios from trap frequencies (middle) and rf transfer (right).

7.3 Spin Composition and Polarizabilities

As briefly discussed in Section 3.6, the polarizabilities of the spin substates of Yb* are distinct. For the set of experiments I discuss here, the polarization of our ODT beam is parallel to that of the trapped atoms, meaning that the atoms see the ODT as carrying a π polarization. Thus transitions such as $|{}^3\mathrm{P}_2, m_J = -2\rangle \rightarrow |{}^3\mathrm{S}_1\rangle$ or $|{}^3\mathrm{P}_2, m_J = 0\rangle \rightarrow |{}^3\mathrm{D}_2\rangle$ are forbidden by selection rules, resulting in different AC Stark shifts felt by the different substates. A thorough calculation of polarizability for the substates as a function of wavelength of trapping light was performed by our theory collaborators, Constantinos Makrides, Alexander Petrov and Svetlana Kotochigova at Temple University. The result is shown as the curves in Fig. 7.3.

To obtain pure spin states, we rely on these differential polarizabilities in addition to the branching ratios shown in 7.1 (b). The final number trapped in $^3\mathrm{P}_2$ differs from the branching ratios because the magnetic substates are suddenly found in traps of different depth, where they may undergo evaporation or gravitational spilling. For our trap, the $m_J = -2$ stateis very weakly trapped compared to the $m_J = -1$ state, leading to a substantial, ODT beam power-dependent loss of $m_J = -2$ atoms due to gravitational spilling. We can obtain a pure sample of atoms in the $m_J = -1$ substate by evaporating to a $^1S_0$ trap depth of $15\,\mu$K to enhance the effect of gravity gradient spilling. We then transfer via the $m_J = -2$ state in $^3\mathrm{D}_2$ while applying an additional magnetic field gradient of 3 G/cm during transfer. These combine to spill all $m_J = -2$ atoms from the trap, after which we can recompress the trap and turn off the gradient to prevent further loss in $m_J = -1$.

We can get pure samples of other substates by performing RF transfer. We use the RF coils in our chamber, driven at 6 W for $300\,\mu$s to effect a π pulse. The Zeeman shift for each state depends on magnetic field B as $g_J m_J \mu_B B$, where g_J is the Landé factor for the state, which is 1.48 [78], and μ_B is the Bohr magneton. In addition, each state has an AC Stark shift that goes as αI where α is the state's polarizability and I the intensity of the ODT light. Thus the resonance frequency for transfer between two states becomes

$$h\nu = |\Delta m_J| g_J \mu_B B - (\alpha_h - \alpha_l) I, \tag{7.13}$$

where $\alpha_h(\alpha_l)$ is the polarizability of the state with higher (lower) m_J. There is additionally a temperature shift that we do not take into account [125] and a small recoil shift. We can obtain the differential polarizabilities of the states, $\Delta\alpha$, by performing transfer at a range of ODT intensities, as shown in Fig. 7.4 (a). We can recover polarizability ratios by making an assumption about the value of α_{-1}, for which we use the theoretical valueobtained by Kotochigova and co-workers. We obtain $\alpha_0/\alpha_{-1} = 1.23$ and $\alpha_{-2}/\alpha_{-1} = 0.27$. Alternatively, we can derive polarizability ratios by measuring the trap frequencies of the $m_J = 0$, -1 and -2 substates and comparing to an

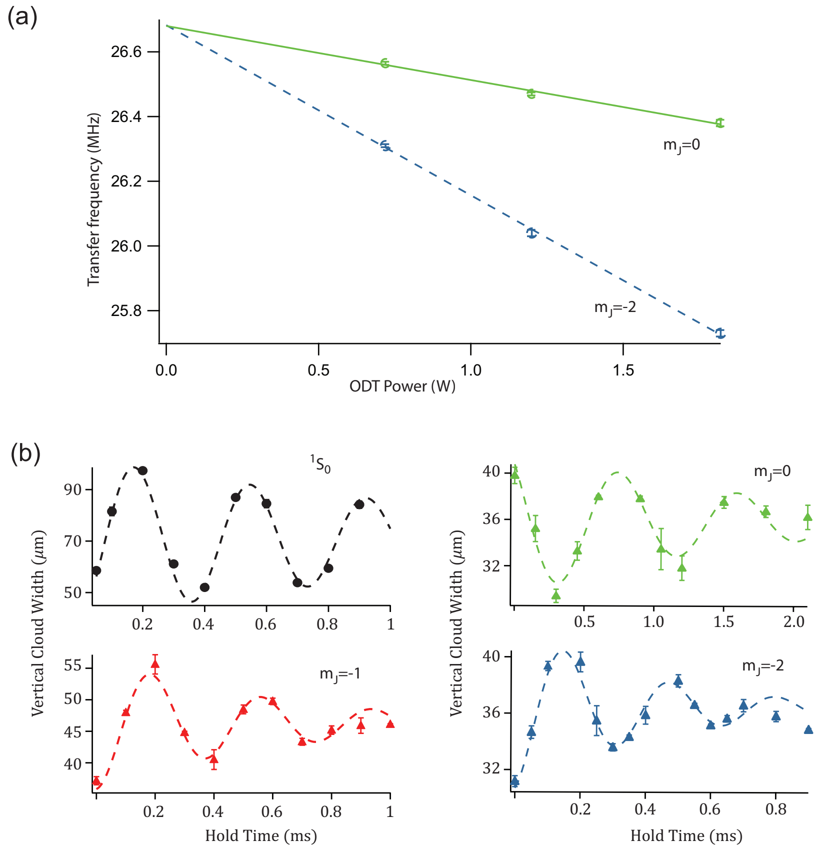

Figure 7.4: Experimental determination of polarizability. (a) AC Stark shift for RF transfer as a function of laser power (b) Trap frequencies for ^{1}S$_0$and the $m_J = 0, -1 - 2$ states of ^{3}P$_2$.

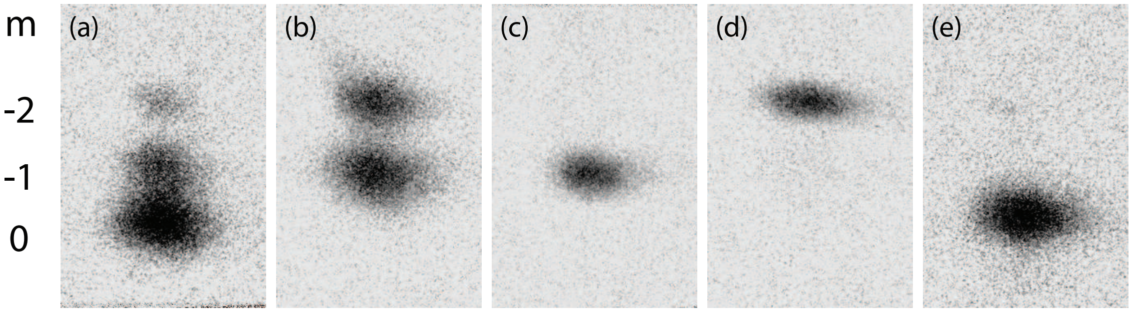

Figure 7.5: 10-image averages of trap spin composition images using Stern-Gerlach technique, showing the $^3\mathrm{P}_2$ magnetic substates displaced vertically. (a) distribution from exciting $^3\mathrm{D}_2$ $m_J = -1$ magnetic state (b) distribution from exciting $^3\mathrm{D}_2$ $m_J = -2$ magnetic state (c) purified $m_J = -1$ from exciting $^3\mathrm{D}_2$ $m_J = -2$ magnetic state and state purification (d) purified $m_J = -2$ from RF transfer of $m_J = -1$ (e) purified $m_J = -0$ from RF transfer of $m_J = -1$

identical measurement for the ground $^1S_0$ state (see Fig. 7.4 (b)). The trap frequencies were measured by observing the oscillation of cloud size (quadrupolar breathing mode) following a diabatic increase in trap depth. These values were also verified by using parametric excitation. The polarizability ratios we obtain in this way are $\alpha_{-1}/\alpha_g = 1.04(6)$, $\alpha_0/\alpha_g = 1.6(2)$, and $\alpha_{-2}/\alpha_g = 0.20(2)$. The comparison of both methods to theoretical prediction are shown in the insets in Fig. 7.3, where we have fixed α_0 for the trap frequency measurements (first inset) and α_{-1} for the RF measurements (second inset). In principle, we can extend the RF transfer technique and use several consecutive pulses to populate the $m = +1$ and $+2$ states as well. Starting at the $m_J = -2$ state, each successive transition is at higher frequency, thus one can even imagine effecting transfer between the two stretached states in a single sweep. It may also be interesting to consider whether can be useful in performing Sysiphus style cooling on an RF transition, similar to [81].

We determine the spin populations of our $^3\mathrm{P}_2$ samples via Stern-Gerlach separation by applying a bias magnetic field and magnetic field gradient in time of flight. At a bias magnetic field of 12 G, we instantaneously turn on a gradient of 50 G/cm, and turn off the ODT within 100 μs. The 770 nm flashback pulse is applied after 2.5 ms in time of flight, after which the clouds continue to propagate for another 0.5 ms. This is done in order to avoid any errors in atom number due to Zeeman shifts in imaging frequency for different cloud positions. The resulting Stern-Gerlach images for several representative experimental situations are shown in Fig. 7.5.

7.4 Co-trapping with Lithium

With the facility to produce, manipulate, and detect Yb* added to our apparatus for studying ground state mixtures of ^{6}Li and ^{174}Yb [59, **?**], we can now investigate the mixture of Yb* and Li. For this work, we focus on a mixture of the lowest hyperfine state of Li and the $m_J = -1$ state of Yb*. The entire experimental sequence is diagrammed in Fig. 7.6. Beginning with an initial ODT depth of $U_{\mathrm{Yb}} = 560\,\mu$K, we evaporatively cool Yb by lowering the trap depth to 15 μK in 3 s. The Yb cloud sympathetically cools an equal mixture of the two lowest hyperfine ground states of Li, which experience a 2.2 times greater optical potential at 1064 nm. We spin-purify the Li component by energetically resolving the two states ($|1\rangle$ and $|2\rangle$) at a high magnetic field (480 G) and removing the upper state ($|2\rangle$) from the trap with resonant light. We then change the magnetic field to a desired value and prepare the $m_J = -1$ state of Yb* as discussed above. We remove any remaining $^1S_0$ atoms with a 3 ms light pulse resonant with the $^1S_0 \rightarrow ^1P_1$ transition, the last 1 ms of which is concurrent with a ramp-up of the trap depth to $U_{\mathrm{Yb}} = 85\,\mu$K, corresponding to a mean trap frequency of $\bar{\omega}_{\mathrm{Yb^*(Li)}} = 2\pi \times 220(1700)$ Hz. We perform this re-compression step in order to suppress atom loss due to evaporation and to improve interspecies spatial overlap against differential gravitational sag. A disadvantage of recompression is that we are forced to do it diabatically due to In the absence of the 404 nm optical pumping step, the Yb and Li temperatures after recompression would be $T_{\mathrm{Yb(Li)}} = 4(8)\,\mu$K at this point. The temperature difference between the species is due to thermal decoupling at

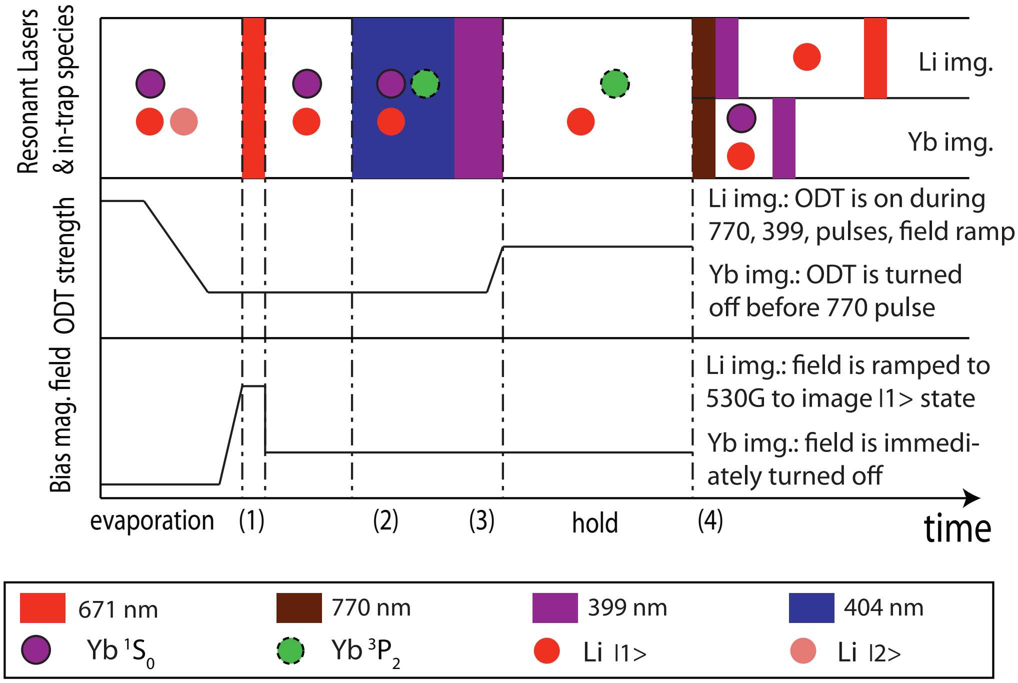

Figure 7.6: Experimental procedure for Yb*-Li co-trapping ecxperiment

the lowest trap depths [59] and is a useful starting point to monitor elastic interspecies interactions.

The evolution of Yb*+Li at an external magnetic field of 12 G is shown in Fig. 7.7 (a). One-body effects from background atoms and off-resonant scattering from ODT photons are negligible on the timescales of the experiment. Since our lithium component is a single state fermion deep in the s-wave regime, the Li-Li interactions are negligible for our parameters. From our calculated values for the $p-$wave threshold for two-body collisions in the Yb*+Yb* and Yb*+Li systems, we infer that all two-body interactions are s-wave dominated. For the starting peak density of $n_{\mathrm{Yb}^*(\mathrm{Li})} = 5.3(1.2) \times 10^{12}\,\mathrm{cm}^{-3}$ and large evaporation parameter $\eta_{\mathrm{Yb}^*(\mathrm{Li})} = U_{\mathrm{Yb}^*(\mathrm{Li})}/k_B T_{\mathrm{Yb}^*(\mathrm{Li})} = 24(20)$, where U is the trap depth, it is reasonable to expect that evaporation is suppressed and all number losses result from two-body inelastic processes. We observe

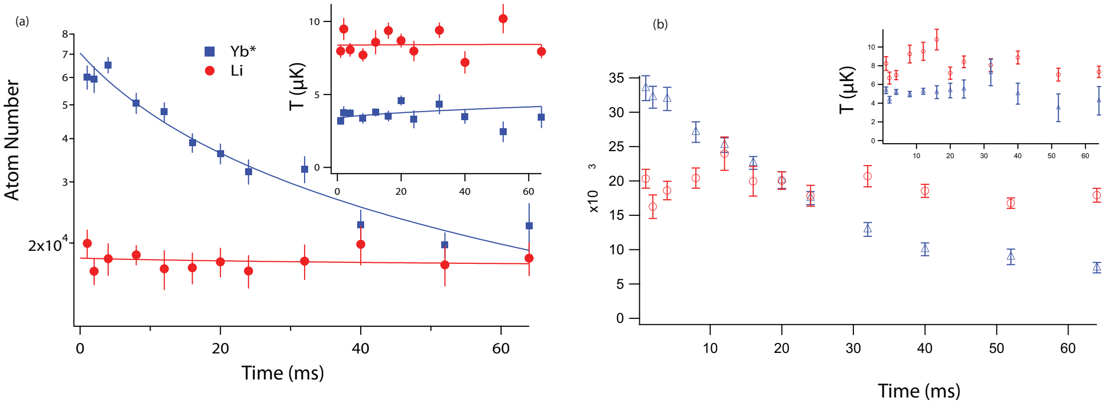

Figure 7.7: Evolution of number and temperature (insets) in a combined Li (red circles) and Yb* in the $m_J = -1$ state(blue) system at (a) 12 G (b) 94 G

that the system retains its initial temperature disparity through the timescale of the experiment. Since 21 collisions per atom are required for Li-Yb* thermalization [59], this indicates an upper bound on the interspecies collision rate of 300 Hz and on the interspecies $s-$wave scattering length magnitude of $300a_0$.

A striking feature of the number evolution is the stability of the Li number on the timescale of Yb* decay, suggesting a dominance of inelastic effects from Yb*+Yb* collisions to Li+Yb* collisions. We model the atomic densities with the coupled differential equations

$$\dot{n}_{\mathrm{Yb}^*} = -K_2' n_{\mathrm{Li}} n_{\mathrm{Yb}^*} - K_2 n_{\mathrm{Yb}^*}^2 \qquad (7.14)$$

$$\dot{n}_{\mathrm{Li}} = -K_2' n_{\mathrm{Li}} n_{\mathrm{Yb}^*}. \qquad (7.15)$$

where $n_{\mathrm{Yb}^*(\mathrm{Li})}$ and $K_2(K_2')$ are the densities of Yb*(Li) and the (volume-independent) two-body decay coefficients of Yb*-Yb*(Yb*-Li). We also incorporate the heating from the density-dependence of the inelastic processes which favor atom loss from near the trap center [122] into our model. Best-fits to this model (see solid lines in Fig. 7.7) yield $K_2 = 2.5 \times 10^{-11}\,\mathrm{cm}^3/\mathrm{s}$, and K_2' consistent with zero. The estimated statistical error provides an upper bound of $K_2' < 3 \times 10^{-12}\mathrm{cm}^3/\mathrm{s}$. By simply fitting the Yb* number according to $\dot{n}_{\mathrm{Yb}^*} = -K_2 n_{\mathrm{Yb}^*}^2$ at the average temperature of $3.6\,\mu\mathrm{K}$, we obtain the value of $K_2 = 2.6 \times 10^{-11}\,\mathrm{cm}^3/\mathrm{s}$, consistent with the earlier estimate.

Our study of interspecies interactions can be extended to arbitrary values of the external magnetic field and also to different magnetic substates of Yb* using the methods described above. As an example, we have performed a similar experiment at 94 G (see Fig. 7.7 (b)). A similarly straightforward treatment of inelastic effects is difficult because the Yb* cloud exhibits quadrupolar oscillations in cloud size. Additionally, the temperature behaviour of the system seems to be different than the 11 G case. Since this data was taken on the same day, back to back without any changes in settings, we find these discrepancies puzzling and as a result making a direct comparison difficult. Nevertheless, a qualitatively similar limit for $K_2' < 1 \times 10^{-11}\mathrm{cm}^3/\mathrm{s}$ at 94 G may still be obtained if we account for the reduction and time variation in cloud overlap due to ytterbium's in-trap breathing mode.

These low values of background interspecies inelastic rates bode well for future searches for the Feshbach resonances in the Yb*+Li system via monitoring the Li population as a function of magnetic field. The Yb* $m_J = -2$ state could exhibit even lower inelastic rates with the Li ground state, since Zeeman state changing collisions will be completely suppressed, and appears to be the best candidate for future studies in this mixture.

Chapter 8

CONCLUSIONS AND OUTLOOK

In this thesis, I have reported on the construction of an apparatus for experiments with ultracold lithium and ytterbium, and have given details of several such experiments. This is by no means the limits of the scope of possible experiments in our chosen system and with the given apparatus. In particular, the construction of the vacuum system as detailed in Chapter 2 should be useful for experiments for many years down the road. We have shown vacuum conditions leading to a vacuum-limited lifetime of $\gtrsim 30\,\mathrm{s}$, which is sufficiently long for any atomic experiment, including potentially precision experiments which require interrogation times on the scale of seconds. Although it took two years of lab construction before the first scientifically relevant results were obtained in the system, at this point the lab is well positioned to make useful contributions to the world of atomic physics in general, and the study of alkali-spin-singlet mixtures in particular. The first result we have shown is that the lithium-ytterbium system is stable and amenable to inter-species sympathetic cooling. This is something that was not at all guaranteed going into the experiment. The lucky finding has led to increased theoretical and experimental interest in the system among other groups worldwide. We found the magnitude of the s-wave scattering length between ^{174}Yb and ^{6}Li to be $|a| = 13 \pm 3a_0$, where a_0 is the Bohr radius. This is sufficiently weak that collapse or phase separation are not observed at coexistence, and Yb-Li scattering can in most situations be treated as background for stronger interactions. Nevertheless, it is not so weak that interspecies thermalization or sympathetic cooling is impossible to achieve. We have shown our ability to use sympathetic cooling to reach double quantum degeneracy in the $^{174}\mathrm{Yb} + {}^{6}\mathrm{Li}$ system.

In the realm of studies of strong interactions, we examined the formation and dynamics of Li_2 Feshbach molecules in a three-component mixture consisting of the two lowest hyperfine states of lithium and the ytterbium ground state. We modeled the chemical dynamics and obtained rate coefficients for these processes. This project was intended to showcase the possibility of using ytterbium as a probe of lithium in the superfluid regime. However, we ran up against experimental limitations, which restricted us to lithium temperatures above the superfluid transition. This is still a potential future area of investigation, but currently our main goal in this direction is inducing strong interactions between lithium and ytterbium. To that end, we have produced and trapped metastable Yb^* in the $^3P_2$ state. Broad Feshbach resonances and thus tunable interactions are predicted in the $Yb^* + Li$ system. This thesis details a substate-selective method of production of Yb^*, and shows co-trapping with Li at different magnetic fields. In the short term, our lab plans to search for Feshbach resonances in the system using loss spectroscopy in Li. The longer-term prospects of this research depend on the nature of resonance(s) that are observed. For broad resonances with only moderate inelastic losses, we can expect to be able to study the production of long-range $LiYb^*$ Feshbach molecules and to search for effects of the mass mismatch leading to new Efimov trimer states in both the Fermi-Fermi and Fermi-Bose systems.

Along with using the $Yb^* + Li$ system to create molecules by magnetoassociation, our lab is also pursuing other potential avenues for molecule creation. Advancements in this direction discussed in this thesis include showing the feasibility of PA spectroscopy, in both the $Li\,^2P + Yb\,^1S$ and $Li\,^2S + Yb\,^3P$ manifolds, with the lasers and apparatus available (or constructed by us), by performing PA spectroscopy in the homonuclear Li_2 and Yb_2 systems, respectively. We plan to pursue “green” PA spectroscopy, and are currently investigating feasibility of performing PA spectroscopy in the MOT or ODT and preparing a more tunable laser source.

At the same time, we are also working on the construction of a 3-D optical lattice for lithium and ytterbium. The high densities achievable in a lattice are crucial for better PA; whereas the ability to reduce collisions between atoms in different lattice sites can help deal with inelastic losses and thus make further investigation of the $\mathrm{Yb}^* + \mathrm{Li}$ system possible. Once ground state molecules are formed, a 3-D lattice is necessary to stabilize them from energetically favourable $2\mathrm{YbLi} \rightarrow \mathrm{Yb}_2{+}\mathrm{Li}_2$ collisions. The existence of a lattice is also a prerequisite for using the long-range anisotropic interactions of molecules for any kind of simulation or quantum information uses. Thus the creation of a lattice is an important short and long term project for the lab. Currently we are beginning with the installation of a 1-D optical lattice in the vertical direction. As well as being a necessary stop towards 3-D, a 1-D lattice would already be an improvement in density for performing PA, and may also be useful to reduce inelastic effects in a polarized sample of Yb^*.

Through any of these several avenues, I believe the production of LiYb molecules is relatively close at hand, and whether or not they are easily converted to the ground state, and whether or not the ground state molecules prove amenable for use in quantum simulations, they will provide an interesting testbed for two-body, few-body and many-body effects. It seems to me that the range of interesting questions available to tackle in the world of ultracold diatomic molecules is much more vast than what can be answered by the comparatively few groups working in the field.

Appendix A

SYMPATHETICALLY COOLING IN AN OPTICALLY TRAPPED MIXTURE OF ALKALI AND SPIN-SINGLET ATOMS

Sympathetic Cooling in an Optically Trapped Mixture of Alkali and Spin-Singlet Atoms

Vladyslav V. Ivanov, Alexander Khramov, Anders H. Hansen, William H. Dowd, Frank Münchow,
Alan O. Jamison, and Subhadeep Gupta
Department of Physics, University of Washington, Seattle, Washington 98195, USA

(Received 26 January 2011; published 11 April 2011)

We report on the realization of a stable mixture of ultracold lithium and ytterbium atoms confined in a far-off-resonance optical dipole trap. We observe sympathetic cooling of ^{6}Li by ^{174}Yb and extract the s-wave scattering length magnitude $|a_{^6\mathrm{Li}\text{-}^{174}\mathrm{Yb}}| = (13 \pm 3)a_0$ from the rate of interspecies thermalization. Using forced evaporative cooling of ^{174}Yb, we achieve reduction of the ^{6}Li temperature to below the Fermi temperature, purely through interspecies sympathetic cooling.

DOI: 10.1103/PhysRevLett.106.153201 PACS numbers: 34.20.Cf, 34.50.Cx, 05.30.Fk, 37.10.De

Ultracold mixtures composed of different atomic species [1–6] offer unique opportunities for probing few- and many-body physics. These include studies of Efimov states with mass-mismatched collision partners [7,8], impurity probes of superfluid properties [6,9], and mass imbalanced regimes of interactions and pairing in Fermi gases [10–12]. Further, the components of the mixture can be linked through field-induced scattering resonances to produce heteronuclear molecules [13–15], which are expected to be valuable tools for the study of dipolar quantum matter, quantum information science, and tests of fundamental physics [16]. An essential requirement for all of these ultracold mixture studies is an understanding of the ground state scattering properties. Favorable collisional properties are needed for mixture production and stability, while knowledge of the underlying potentials allow identification of regimes of tunable interactions.

In this Letter, we report on successful simultaneous optical trapping and measurements of scattering properties for a mixture of alkali ^{6}Li and spin-singlet ^{174}Yb. We observe collisional stability in this mixture and determine the magnitude of the previously unknown ^{6}Li-^{174}Yb s-wave scattering length from the time scale of interspecies thermalization [3,4,17]. Furthermore, we sympathetically cool ^{6}Li to below its Fermi temperature by forced evaporative cooling of ^{174}Yb. Unlike the case for bialkali mixtures [2,3], our method of sympathetic cooling an alkali by a spin-singlet atom has the advantage of being immune to inelastic spin changing collisions.

While studies of ultracold molecule formation from two-species mixtures are dominated by alkali + alkali combinations, molecules created from alkali + spin-singlet mixtures offer the additional advantage of possessing an unpaired electron spin to form a paramagnetic ground state. This is a feature of considerable interest for several proposed applications including quantum simulations of lattice spin models [18], topological quantum computing, and sensitive measurements of the electron electric dipole moment [19]. Prior to this work a dual-species Li-Yb magneto-optical trap (MOT) was demonstrated [20], but with densities too low to observe interspecies effects. First results for alkali + spin-singlet mixtures have been reported for the Rb + Yb combination. These include photoassociation in a dual-species MOT [21], and observations of sympathetic cooling [22] and spatial separation [23] in a combined optical and magnetic trap.

In addition to the pursuit of heteronuclear paramagnetic LiYb molecules, our system forms a starting point for studies of the ^{6}Li Fermi superfluid [24] using Yb as an impurity probe. Furthermore, tunable interspecies interactions may be induced between Li and Yb through magnetic [25] or optical [26] Feshbach resonances. Together with the straightforward availability of fermionic Yb isotopes, this will allow future explorations of few-body collision physics in the highly mass-mismatched regime [7,8] and fermionic interactions and pairing in mass imbalanced mixtures [11,12].

Our dual-species experimental setup consists of ^{174}Yb and ^{6}Li MOTs which are loaded from separate atomic beams, each emerging from a single-species oven and slowed by a single-species Zeeman slower. All laser cooling and absorption imaging of ^{6}Li is performed on the $^2S_{1/2} \rightarrow {}^2P_{3/2}$ line (wavelength $\lambda = 671$ nm, linewidth $\Gamma/2\pi = 6$ MHz). For ^{174}Yb, we use the $^1S_0 \rightarrow {}^1P_1$ line ($\lambda = 399$ nm, $\Gamma/2\pi = 29$ MHz) for Zeeman slowing and absorption imaging, and the $^1S_0 \rightarrow {}^3P_1$ line ($\lambda = 556$ nm, $\Gamma/2\pi = 182$ kHz) for the MOT. The optical dipole trap (ODT) is derived from the linearly polarized output of a 1064 nm fiber laser (IPG Photonics YLR-100-1064-LP) and is operated either in single or crossed beam geometry. The trap depth is controlled by an acousto-optic modulator.

To mitigate the strong inelastic losses in simultaneous two-species MOTs and to allow for different optimum MOT magnetic field gradients [27], we employ a sequential cooling and trapping strategy [see Fig. 1(a)] in which first Yb and then Li is laser cooled and transferred to the ODT. The laser cooling sequence for each species consists of a loading phase with large intensities and detunings of the cooling beams, and a compression phase where these intensities and detunings are reduced and the MOT

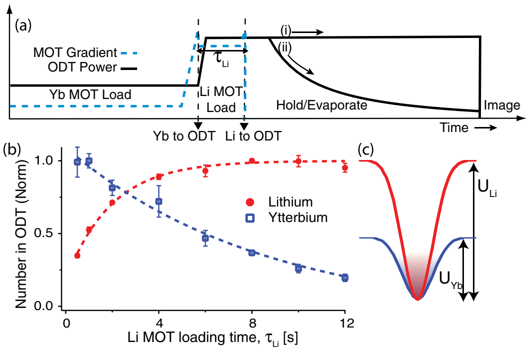

FIG. 1 (color online). Simultaneous optical trapping of ^{6}Li and ^{174}Yb. (a) shows the typical experimental sequence where the laser cooling and ODT loading are performed sequentially for the two species. In addition to the standard procedures for single-species operation, the magnetic field gradients and the initial optical trap depths are adjusted for each species to optimize number and temperature. After both species are in the ODT, either (i) the power is held constant to study interspecies thermalization, or (ii) the power is ramped down to perform forced evaporative cooling. Finally, the optical trap is switched off and the remaining atoms detected with resonant absorption imaging. As displayed in (b), varying the Li MOT loading time τ_{Li} allows us to control the initial ratio of the two species in the optical trap. The peak atom numbers correspond to $N_{\mathrm{Yb(Li)}} = 11(4) \times 10^5$, for trap depth $U_{\mathrm{Yb(Li)}} = 0.5(1.1)$ mK. The dashed lines are exponential fits. The Yb decay time is substantially shorter than the background lifetime because of a partial overlap with the ^{6}Li MOT during τ_{Li}. (c) Optical trapping potentials for Li and Yb for a given ODT power. The shading depicts the distributions at the same temperature.

gradient increased. The compressed Yb MOT contains $\gtrsim 2 \times 10^6$ atoms at a temperature of $\lesssim 30\ \mu$K. The compressed Li MOT contains $\gtrsim 10^8$ atoms at $\lesssim 400\ \mu$K, and is optically pumped into the lower $F = 1/2$ hyperfine state. Each species is transferred to the ODT by using magnetic bias fields to overlap the MOT with the ODT center and then switching off the laser cooling beams. During the Li laser cooling phase, Yb atoms trapped in the ODT are insensitive to the magnetic field manipulations used for the Li MOT. After all cooling beams are switched off, the ODT contains a mixture of Yb and Li atoms [see Fig. 1(b)]. While all the ^{174}Yb atoms are in the single $^1S_0$ ground state, the ^{6}Li atoms are distributed equally between the two $F = 1/2$ Zeeman ground states.

For our ODT wavelength, the relative trap depths and frequencies for the two species are $U_{\mathrm{Li}}/U_{\mathrm{Yb}} = 2.2$ and $\omega_{\mathrm{Li}}/\omega_{\mathrm{Yb}} = \sqrt{\frac{(U_{\mathrm{Li}}/m_{\mathrm{Li}})}{(U_{\mathrm{Yb}}/m_{\mathrm{Yb}})}} = 8$. The relative linear size in the harmonic regime is $x_{\mathrm{Li}}/x_{\mathrm{Yb}} = \sqrt{\frac{(T_{\mathrm{Li}}/U_{\mathrm{Li}})}{(T_{\mathrm{Yb}}/U_{\mathrm{Yb}})}} = 0.7$ for equal temperatures [see Fig. 1(c)]. The parameters are thus well suited for sympathetic cooling of lithium by ytterbium.

To monitor atom number and temperature, we quickly switch off the trap and perform resonant absorption imaging of both species for each experimental iteration. Each species is imaged onto a different part of the same CCD camera with independently adjustable ballistic expansion times. The trapping potential is characterized through measurements of trap frequencies by exciting dipole and breathing oscillations, as well as by parametric heating. The ODT is kept on all the time except during imaging.

We first describe our thermalization measurements, which allow us to determine the magnitude of the interspecies s-wave scattering length. For these measurements, we use a single beam ODT with $1/e^2$ intensity-radius (waist) of 30 μm. Yb is transferred from the MOT into an ODT of calculated depth $U_{\mathrm{Yb}} = 220\ \mu$K (laser power 11 W), after which the depth is increased adiabatically in 0.2 s to $U_{\mathrm{Yb}} = 500\ \mu$K (25 W) while the Li MOT is loaded (see Fig. 1). After $\simeq 0.5$ s MOT loading, Li is transferred into the ODT ($U_{\mathrm{Li}} = 1.1$ mK). We make our thermalization measurements at this point, where the measured trapping frequencies for Yb are $2\pi \times 1600$ Hz radially and $2\pi \times 13$ Hz axially. The initial number, temperature, and peak density of Yb (Li) atoms are $N_{\mathrm{Yb(Li)}} = 1.1 \times 10^6 (1.4 \times 10^5)$, $T_{\mathrm{Yb(Li)}} = 35(110)\ \mu$K, and $n_{0,\mathrm{Yb(Li)}} = 1.1 \times 10^{13} (8.4 \times 10^{11})$ cm^{-3}. All the thermalization measurements are performed at near-zero magnetic field.

We observe the number and temperature evolution of the two atomic species either in separate single-species experiments, or together when in thermal contact with each other. The measured background single-species $1/e$ lifetimes are >30 s for both Li and Yb. The Yb temperature evolution is independent of the presence or absence of Li, equilibrating quickly and staying at 35 μK throughout the measurement. When Yb is not loaded, the two-spin state Li mixture behaves like an ideal gas in the optical trap and remains at its initial temperature of $\simeq 100\ \mu$K without observable changes. This is due to a lack of intrastate collisions from Pauli blocking and a lack of interstate collisions from the negligible zero-field scattering cross section [28]. When both species are loaded, the hotter Li cloud equilibrates to the temperature of the Yb cloud (see Fig. 2). The lack of change in the Yb temperature is mainly due to the large number ratio $N_{\mathrm{Yb}}/N_{\mathrm{Li}}$ [29]. We also observe no change in the Li lifetime from contact with Yb, indicative of negligible inelastic interactions between the two species at these experimental parameters. In similar studies at various loading parameters, we observe additional losses in the Yb number only. We interpret this to be a result of a "sympathetic evaporation" effect [17] where during the thermalization process, Li which is confined by a deeper trap, transfers energy through elastic collisions to Yb, and subsequently ejects it from its shallower confinement [see Fig. 1(c)]. Indeed for larger fractional presence of Li, this effect becomes more pronounced and leads to a substantially reduced lifetime for the Yb cloud.

We analyze the thermalization measurements shown in Fig. 2 by assuming that the elastic interactions are purely s wave in nature. We are justified in this assumption because our measured temperatures ($\leq 110\ \mu$K) are much smaller than the p-wave threshold given by $\frac{2}{\sqrt{C_6}} \times (\frac{\hbar^2 l(l+1)}{6\mu})^{3/2} \simeq 2.5$ mK, where μ is the reduced mass and using the C_6 coefficient for LiYb calculated in [30]. The thermalization rate γ_{th} which characterizes the instantaneous variation of the temperature difference $\Delta T = T_{\mathrm{Li}} - T_{\mathrm{Yb}}$, can then be connected to the s-wave scattering cross section σ_{LiYb} through the relation

$$-\frac{1}{\Delta T}\frac{d(\Delta T)}{dt} = \gamma_{\mathrm{th}} = \frac{\xi}{\alpha}\bar{n}\sigma_{\mathrm{LiYb}}\bar{v}. \tag{1}$$

Here $\alpha = 2.7$ is the average number of collisions needed for thermalization for equal mass partners, $\xi = \frac{4m_{\mathrm{Li}}m_{\mathrm{Yb}}}{(m_{\mathrm{Li}}+m_{\mathrm{Yb}})^2} = 0.13$ is the correction factor for nonequal mass collisions [17], $\bar{v} = \sqrt{\frac{8k_B}{\pi}(\frac{T_{\mathrm{Li}}}{m_{\mathrm{Li}}} + \frac{T_{\mathrm{Yb}}}{m_{\mathrm{Yb}}})}$ is the mean relative velocity, $\bar{n} = (\frac{1}{N_{\mathrm{Li}}} + \frac{1}{N_{\mathrm{Yb}}}) \int n_{\mathrm{Li}} n_{\mathrm{Yb}} d^3r$ is the overlap density, and n, N, and T are the density, number, and temperature of the two species. Since $\bar{v}$ and $\bar{n}$ change with the Li temperature, we use a numerical procedure to model the thermalization process. For a particular value of s-wave scattering length a, we iterate Eq. (1) with a short time step. We also include an energy dependence [31] to the s-wave cross section $\sigma_{\mathrm{LiYb}} = \frac{4\pi a^2}{[1-(1/2)k^2 r_e a]^2 + k^2 a^2}$, where $\hbar k$ is the relative momentum and r_e is the effective range evaluated from C_6 and a. By varying a, we obtain a best fit (see Fig. 2) and infer $|a_{^6\mathrm{Li}\text{-}^{174}\mathrm{Yb}}| = (13 \pm 3)a_0$. The quoted error in our measurement stems mainly from a systematic uncertainty in our trap frequencies ($\pm$ 20%), which limits our knowledge of absolute densities. Variations in σ_{LiYb} from the energy dependent terms are insignificant in comparison.

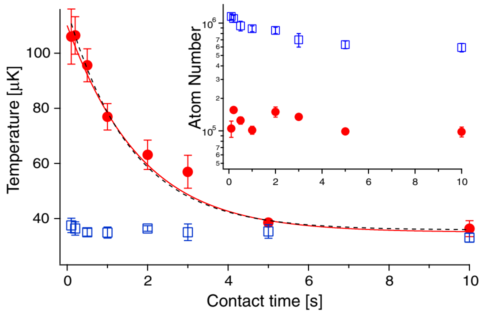

FIG. 2 (color online). Sympathetic cooling of ^{6}Li (red solid circles) by thermalization with a cold ^{174}Yb bath (blue open squares). The temperatures equilibrate with an exponential time constant of (1.7 ± 0.2) s (black dashed line). The red solid line is the result of a numerical model (see text). The inset shows the numbers of the two species which are almost an order of magnitude apart.

Since ^{174}Yb is spinless, we expect that $a_{^6\mathrm{Li}\text{-}^{174}\mathrm{Yb}}$ is the same for all hyperfine ground states of ^{6}Li. By using state selective imaging at magnetic fields near 500 G, we have verified that the two participating ^{6}Li $F = 1/2$ Zeeman states maintain equal population and temperature at an intermediate point during sympathetic cooling.

Since several potential applications of the Li-Yb mixture are at conditions near or below quantum degeneracy, we also assess methods of increasing the phase space density in the mixture. In single-species ^{6}Li experiments in our apparatus, up to $N_{\mathrm{Li}} = 2 \times 10^6$ can be loaded into a high power crossed beam ODT. With subsequent forced evaporation at $B \simeq 330$ G, where the interstate scattering length is $-280a_0$, we are able to enter the Fermi degenerate regime ($T_{\mathrm{Li}}/T_F \lesssim 0.6$) with total number $N_{\mathrm{Li}} = 1.5 \times 10^5$. Applying this approach to the Li-Yb mixture, however, leads to reduced initial N_{Yb} [see Fig. 1(b)] and shorter Yb lifetime from the sympathetic evaporation effect. We therefore restrict ourselves to keeping the initial ratio $N_{\mathrm{Yb}}/N_{\mathrm{Li}}$ large.

We now describe our measurements of sympathetic cooling of ^{6}Li in contact with ^{174}Yb which is undergoing forced evaporative cooling through a continuous lowering of the trap depth. In order to boost the collision rate, the single beam ODT for the thermalization measurement is modified to a crossed beam geometry by adding a second laser beam which intersects the first at a shallow angle of about 10°, and has the same power, orthogonal polarization, and a larger waist of 50 μm. After loading the atoms, we reduce the power in the optical trap following an approximately exponential shape. Figure 3 shows the number and temperature evolution during such an evaporation ramp at near-zero magnetic field.

We observe that Yb decays quickly with an exponential time constant of 4.3 s, while the longer decay constant of 24 s for Li is comparable with the vacuum limited lifetime. This implies that Yb loss is primarily from trap depth reduction while Li loss is primarily from background processes, as desired for efficient sympathetic cooling. During the cooling process, the Li phase space density increases by about 3 orders of magnitude as the gas is brought below the Fermi temperature, to $T_{\mathrm{Li}} = 1.2\ \mu$K with $T_{\mathrm{Li}}/T_F \simeq 0.7$. At this point $T_{\mathrm{Yb}} = 650$ nK, a factor of 4 above the critical temperature for Bose condensation. We are prevented from further sympathetic cooling by the rapidly increasing interspecies thermalization time from the lowered densities and lowered overlap from unequal gravitational sag. We are currently improving our cooling scheme by implementing more tightly focused ODT beams. Substantial improvements are also expected from the introduction of a magnetic field gradient [32] to allow manipulation of the Li trap depth and position, without affecting Yb.

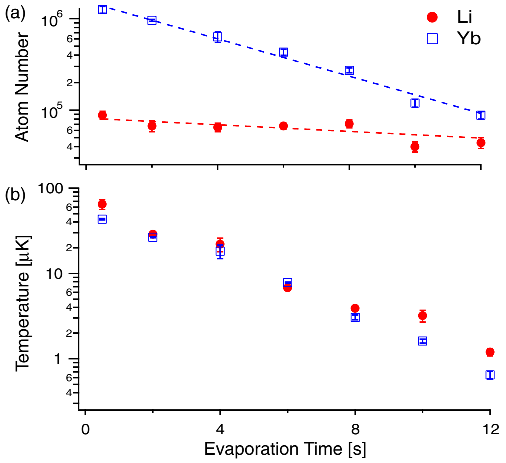

FIG. 3 (color online). Sympathetic cooling of lithium by forced evaporative cooling of ytterbium. (a) Number and (b) temperature evolution for ^{6}Li (solid circles) and ^{174}Yb (open squares) as the power in the crossed optical dipole trap is reduced by a factor of 28 over 12 s, corresponding to an approximately exponential ramp with a time constant of 2.9 s.

Our results establish a stable ultracold alkali + spin singlet mixture and also constitute the first instance of sympathetic cooling of a second atomic species by a spin-singlet atom. Future work includes studies of molecular levels by one- and two-photon photoassociation spectroscopies and searches for magnetically and optically induced Feshbach resonances [25,26], important steps towards production of paramagnetic polar molecules of LiYb. Improving our sympathetic cooling arrangement with magnetic gradients and tighter beams will allow us to reach double quantum degeneracy with various combinations of Li and Yb isotopes, including Fermi-Fermi degenerate mixtures with high mass imbalance. Yb atoms inside a degenerate Li cloud can also serve as an impurity to study superfluidity [33], and for thermometry of a deeply degenerate Fermi gas [6].

We thank W. Willcockson, J. K. Smith, R. Weh, W. English, and N. Maloney, for major technical contributions during the early stages of the experiment, E. N. Fortson for valuable discussions, and A. Görlitz and D. M. Stamper-Kurn for helpful comments. This work was supported by the National Science Foundation, the Alfred P. Sloan Foundation, UW Royalty Research Fund, and NIST. A. K. acknowledges support from the NSERC and F. M. from the DAAD.

[1] G. Modugno *et al.*, Science **294**, 1320 (2001).
[2] Z. Hadzibabic *et al.*, Phys. Rev. Lett. **88**, 160401 (2002).
[3] C. Silber *et al.*, Phys. Rev. Lett. **95**, 170408 (2005).
[4] S. Aubin *et al.*, Nature Phys. **2**, 384 (2006).
[5] M. Taglieber *et al.*, Phys. Rev. Lett. **100**, 010401 (2008).
[6] F. Spiegelhalder *et al.*, Phys. Rev. Lett. **103**, 223203 (2009).
[7] J. P. D'Incao and B. D. Esry, Phys. Rev. A **73**, 030702(R) (2006).
[8] B. Marcelis *et al.*, Phys. Rev. A **77**, 032707 (2008).
[9] E. Vernier *et al.*, Phys. Rev. A **83**, 033619 (2011).
[10] M. Iskin, Phys. Rev. A **78**, 021604(R) (2008).
[11] A. Gezerlis *et al.*, Phys. Rev. Lett. **103**, 060403 (2009).
[12] A. Trenkwalder *et al.*, Phys. Rev. Lett. **106**, 115304 (2011).
[13] J. M. Sage *et al.*, Phys. Rev. Lett. **94**, 203001 (2005).
[14] J. Deiglmayr *et al.*, Phys. Rev. Lett. **101**, 133004 (2008).
[15] K.-K. Ni *et al.*, Science **322**, 231 (2008).
[16] L. D. Carr *et al.*, New J. Phys. **11**, 055049 (2009).
[17] M. Mudrich *et al.*, Phys. Rev. Lett. **88**, 253001 (2002).
[18] A. Micheli *et al.*, Nature Phys. **2**, 341 (2006).
[19] J. J. Hudson *et al.*, Phys. Rev. Lett. **89**, 023003 (2002).
[20] M. Okano *et al.*, Appl. Phys. B **98**, 691 (2009).
[21] N. Nemitz *et al.*, Phys. Rev. A **79**, 061403(R) (2009).
[22] S. Tassy *et al.*, J. Phys. B **43**, 205309 (2010).
[23] F. Baumer *et al.* (to be published).
[24] M. W. Zwierlein *et al.*, Nature (London) **435**, 1047 (2005).
[25] P. S. Zuchowski, J. Aldegunde, and J. M. Hutson, Phys. Rev. Lett. **105**, 153201 (2010).
[26] R. Ciurylo, E. Tiesinga, and P. S. Julienne, Phys. Rev. A **71**, 030701(R) (2005).
[27] We observe significant reduction of Yb MOT number when operating simultaneous Li and Yb MOTs. The optimum MOT gradient for each species is related to the natural linewidth of the cooling transition and for our specific conditions differs empirically by a factor of 7.
[28] M. Houbiers *et al.*, Phys. Rev. A **57**, R1497 (1998).
[29] In the limit of no atom loss, the final temperature after thermalization is defined through the initial parameters as $\frac{N_{\mathrm{Yb}}T_{\mathrm{Yb}}+N_{\mathrm{Li}}T_{\mathrm{Li}}}{N_{\mathrm{Yb}}+N_{\mathrm{Li}}} = 43\ \mu\mathrm{K}$ in our case. This value is reduced by evaporative cooling. Assuming the calculated trap depths given in the text, numerical simulations indicate a Yb temperature rise of $\leq 5\ \mu\mathrm{K}$, comparable to the statistical error bars in our measurement.
[30] P. Zhang, H. R. Sadeghpour, and A. Dalgarno, J. Chem. Phys. **133**, 044306 (2010).
[31] V. V. Flambaum, G. F. Gribakin, and C. Harabati, Phys. Rev. A **59**, 1998 (1999).
[32] C.-L. Hung *et al.*, Phys. Rev. A **78**, 011604(R) (2008).
[33] While the Li cloud is smaller than an equal temperature Yb cloud in the Boltzmann regime, because of Fermi pressure the opposite is true for $T/T_F \lesssim 0.27$ in the unitary regime of strong ^{6}Li interactions.

Appendix B

QUANTUM DEGENERATE MIXTURES OF YTTERBIUM AND LITHIUM ATOMS

RAPID COMMUNICATIONS

PHYSICAL REVIEW A **84**, 011606(R) (2011)

Quantum degenerate mixture of ytterbium and lithium atoms

Anders H. Hansen, Alexander Khramov, William H. Dowd, Alan O. Jamison, Vladyslav V. Ivanov, and Subhadeep Gupta
Department of Physics, University of Washington, Seattle, Washington 98195, USA

(Received 27 May 2011; published 22 July 2011)

We have produced a quantum degenerate mixture of fermionic alkali-metal ^{6}Li and bosonic spin-singlet ^{174}Yb gases. This was achieved using sympathetic cooling of lithium atoms by evaporatively cooled ytterbium atoms in a far-off-resonant optical dipole trap. We observe the coexistence of Bose-condensed ($T/T_c \simeq 0.8$) ^{174}Yb with 2.3×10^4 atoms and Fermi degenerate ($T/T_F \simeq 0.3$) ^{6}Li with 1.2×10^4 atoms. Quasipure Bose-Einstein condensates of up to 3×10^4 ^{174}Yb atoms can be produced in single-species experiments. Our results mark a significant step toward studies of few- and many-body physics with mixtures of alkali-metal and alkaline-earth-metal-like atoms, and for the production of paramagnetic polar molecules in the quantum regime. Our methods also establish a convenient scheme for producing quantum degenerate ytterbium atoms in a 1064 nm optical dipole trap.

DOI: 10.1103/PhysRevA.84.011606 PACS number(s): 67.85.Pq, 37.10.De, 05.30.Fk, 67.10.Db

Quantum degenerate elemental mixtures can be used to study a variety of few- and many-body phenomena and form the starting point for creating quantum degenerate dipolar molecules. While bi-alkali-metal quantum mixtures [1–6] have been produced and studied for about a decade, mixtures of alkali-metal and electron spin-singlet atoms are a more recent development [7–11]. By exploiting the difference in mass of the components, the lithium-ytterbium quantum degenerate mixture may be used to investigate a range of interesting scientific directions including new Efimov states [12,13], impurity probes of the Fermi superfluid [6], and mass imbalanced Cooper pairs [14–16]. Furthermore, unlike the bi-alkali-metal case, mixtures of alkali-metal and alkaline-earth-metal-like atoms can lead to the realization of paramagnetic polar molecules by combining the atoms through field-induced scattering resonances, followed by multiphoton transfer processes to the ground state [17–19]. Such molecules hold great promise for quantum simulation and topological quantum computing applications [20]. They may also be good candidates for sensitive tests of fundamental symmetries, particularly if one of the constituents is a heavy atom, such as Yb [21].

In this paper, we report on simultaneous quantum degeneracy in a mixture of alkali-metal and alkaline-earth-metal-like atoms. In earlier work [11], we reported on collisional stability and sympathetic cooling in the ^{6}Li-^{174}Yb system, together with a measurement of the interspecies s-wave scattering length magnitude. Here we establish a convenient method to produce Bose-Einstein condensates (BECs) of ^{174}Yb. This allows the sympathetic cooling of ^{6}Li to well below its Fermi temperature and the achievement of simultaneous quantum degeneracy in the two species.

The cooling of various isotopes of ytterbium to quantum degeneracy has been pioneered by the group of Y. Takahashi in Kyoto [22–24]. In these studies, the optical dipole trap (ODT) was implemented at the wavelength 532 nm. While suitable for confining ytterbium which has a strong transition at 399 nm, this choice of wavelength will not confine common alkali-metal atoms due to their strong transitions occurring at wavelengths greater than 532 nm. For our ODT, we use 1064 nm light arranged in a straightforward horizontal geometry, and demonstrate efficient evaporative cooling of ^{174}Yb to BEC. This establishes a simple setup for studies with quantum degenerate ytterbium gases, particularly in the context of dual-species experiments.

Our experimental setup (see Fig. 1) is similar to what has been described previously [11]. Briefly, we sequentially load ^{174}Yb and then ^{6}Li from respective magneto-optical traps (MOTs) into the same ODT. We then perform forced evaporative cooling of ^{174}Yb by lowering the power in the ODT. This leads to quantum degeneracy in either single or dual-species experiments. Two improvements to our earlier setup which are crucial for this work are the use of higher power in the Yb Zeeman-slowing beam resulting in larger MOT numbers, and the implementation of a tighter ODT geometry [25] leading to more efficient evaporative cooling.

The ODT is derived from a 1064 nm linearly polarized fiber laser, operated at a power of 45 W. In order to control the trap depth, the output of the laser is sent through an acousto-optic modulator. The first-order output is split into two equal parts with orthogonal linear polarizations which then propagate horizontally toward the atoms. Each beam is focused to a (measured) waist of 26 μm and the foci are overlapped at an angle of 20 degrees. The trapping potential is characterized through measurements of trap frequencies by parametric heating. The relative trap depths and frequencies for the two species are $U_{\rm Li}/U_{\rm Yb} = 2.2$ and $\omega_{\rm Li}/\omega_{\rm Yb} = 8.1$. To monitor atom number and temperature, we quickly switch off the ODT and perform resonant absorption imaging of both species.

In single-species experiments with ^{174}Yb, we load 1.5×10^7 atoms in a MOT in 40 s from a Zeeman-slowed atomic beam. We use 100 mW power in the 399 nm ($^1S_0 \rightarrow {}^1P_1$) slowing beam and a total of 12 mW power in the 556 nm ($^1S_0 \rightarrow {}^3P_1$) MOT beams, operated in retroreflection configuration. A transient cooling and compression scheme then produces an atomic cloud at a temperature of 20 μK containing $\simeq 6 \times 10^6$ atoms.

About 1×10^6 atoms in the $^1S_0$ state are then loaded into the ODT where the background $1/e$ lifetime is 40 s. The initial ODT power at the atoms is 9 W per beam, corresponding to a trap depth of 430 μK. The power is then reduced by a

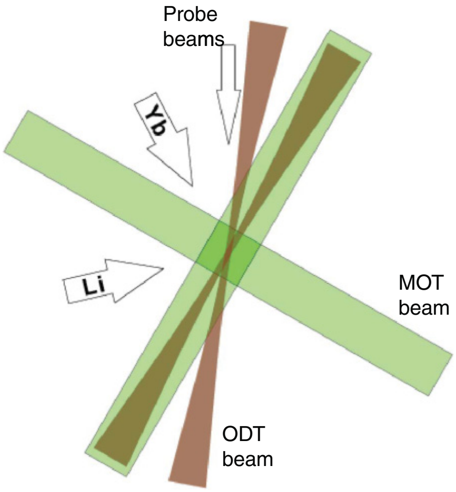

FIG. 1. (Color online) Experimental arrangement (top view) for producing simultaneous quantum degeneracy in lithium and ytterbium. Zeeman-slowed atomic beams of each species propagate along separate axes toward the MOT. The horizontal ODT beams (brown) are crossed at the MOT region at an angle of 20°. MOT beams (green) for both species are overlapped and arranged in a retroreflection configuration. Beams for the vertical MOT axis and Zeeman slowing are omitted from the figure for clarity.

factor of 100 over a time scale of 14 s, utilizing two stages of approximately exponential shape. The first stage lasts for 5 s with a time constant of 1.5 s. The second stage lasts for the remainder of the evaporation period and has a time constant of 3.6 s.

We observe efficient evaporative cooling with this arrangement [see Fig. 2(a)]. The critical temperature for Bose-Einstein condensation is achieved after evaporating for $\simeq$12.5 s. At this point the atom number is $N_{\mathrm{Yb}} = 7 \times 10^4$ and the temperature is $T_{\mathrm{Yb}} = 170$ nK. By fitting to the data prior to condensation, we extract an evaporation efficiency parameter $-d[\ln(\rho_{\mathrm{Yb}})]/d[\ln(N_{\mathrm{Yb}})] = 3.4(4)$ where ρ_{Yb} is the phase space density. Nearly pure condensates of up to 3×10^4 atoms can be prepared by continuing the evaporation process [see Fig. 2(b)].

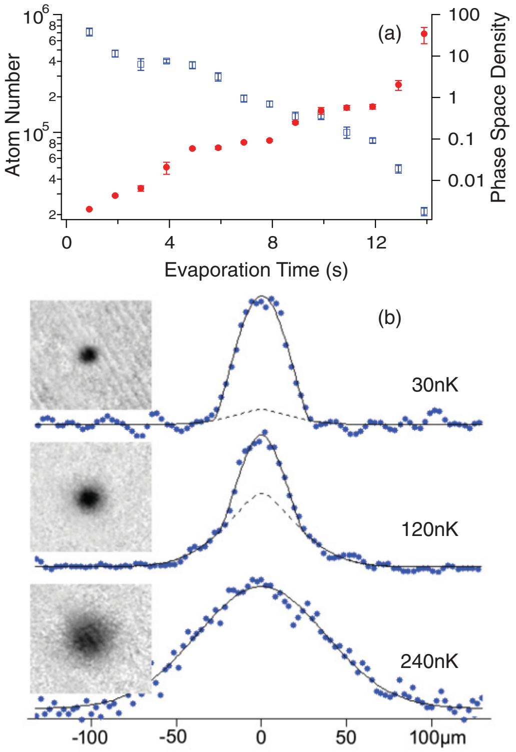

FIG. 2. (Color online) Evaporative cooling of ^{174}Yb to Bose-Einstein condensation in the crossed 1064 nm ODT. Panel (a) shows the evolution of ^{174}Yb number (open squares) and phase space density (filled circles) for a single-species experiment. BEC is achieved after about 12.5 s. Panel (b) shows absorption images and the corresponding atomic density profiles (vertical cross sections of these images) for three different final trap depths, showing the formation of the BEC. The solid line in each plot is a bimodal fit to the distribution with the dashed line showing the thermal component of the fit. The free expansion time after turning off the trap is 8 ms for each image. The total atom numbers and temperatures are 8.0, 5.6, and 2.1 $\times$ 10^4 and 240, 120, and 30 nK, respectively.

For two-species experiments, we add to the optically trapped ^{174}Yb an equal mixture of the two $F = 1/2$ Zeeman states of ^{6}Li with an adjustable total number. After 1 s of interspecies thermalization at constant trap depth, we perform sympathetic cooling of ^{6}Li by ^{174}Yb at near-zero magnetic field by using the same evaporation ramp as described above. Sympathetic cooling works well in this mixture as described in our earlier work [11] where we reported an interspecies s-wave scattering length magnitude of $|a_{^6\mathrm{Li}\text{-}^{174}\mathrm{Yb}}| = (13 \pm 3)a_0$. The ^{6}Li number remains nearly constant due to its greater trap depth. After approximately 14 s of evaporation we observe simultaneous quantum degeneracy in the two species (see Fig. 3). At this point the geometric mean trap frequencies are $\bar{\omega}_{\mathrm{Yb(Li)}} = 2\pi \times 90\ (740)$ Hz, atom numbers are $N_{\mathrm{Yb(Li)}} = 2.3\ (1.2) \times 10^4$, and temperatures are $T_{\mathrm{Yb(Li)}} = 100 \pm 10\ (320 \pm 36)$ nK. Here, N_{Li} is the total lithium atom number distributed equally between the two spin states. T_{Yb} is estimated from the fraction of condensed atoms. T_{Li} is a weighted average of three methods: a best-fit to the shape of the distribution using a Thomas-Fermi model with the fugacity as an independent parameter, and two Fermi-Dirac distribution fits to singly and doubly integrated density profiles.

The difference in temperature between the two species is largely attributable to the relative center-of-mass displacement at the end of the evaporation ramp arising from gravitational sag. Assuming perfect overlap, the estimated interspecies thermalization time at this stage is $\simeq$1 s, which is reasonably short. However, the separation of the two clouds due to unequal

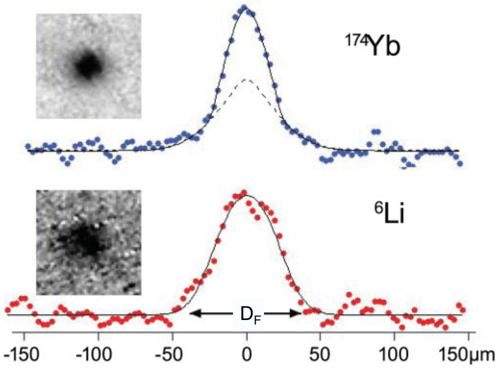

FIG. 3. (Color online) Quantum degenerate mixture of ^{174}Yb and ^{6}Li. The absorption images and density profiles correspond to the same experimental iteration with 14 s of evaporation. The free-expansion times are 8 ms for Yb and 0.7 ms for Li. Here $N_{\mathrm{Yb}} = 2.3 \times 10^4$ and $T_{\mathrm{Yb}} = 100$ nK, corresponding to $T_{\mathrm{Yb}}/T_{\mathrm{C,Yb}} = 0.8$, while $N_{\mathrm{Li}} = 1.2 \times 10^4$ and $T_{\mathrm{Li}} = 320$ nK, corresponding to $T_{\mathrm{Li}}/T_{\mathrm{F,Li}} = 0.3$. For ^{174}Yb, the solid line is a bimodal fit with the dashed line showing the thermal component of the fit. For ^{6}Li, the solid line is a Thomas-Fermi fit. The extent of the momentum-space Fermi diameter D_F, corresponding to the Fermi energy, is also indicated in the figure. The image was taken at near-zero magnetic field and includes both spin components.

effects of gravity is 5.1 μm while the lithium in-trap Fermi radius is 5.8 μm in the vertical direction. A numerical model of the cooling process incorporating this effect predicts a $1/e$ reduction of the interspecies collision rate due to separation when $T_{\mathrm{Yb}} \simeq 300$ nK, suggesting that sympathetic cooling does indeed become inefficient toward the end of evaporation.

Our results establish a new quantum system comprised of simultaneously degenerate one- and two-electron atomic gases. We also demonstrate a new method for achieving Bose-Einstein condensation of ^{174}Yb using a straightforward horizontal optical trapping arrangement with 1064 nm laser beams. Our setup could also be suitable for combining Yb with other alkalis such as Cs and Rb, since the trap depth and relative sizes would be amenable for sympathetic cooling by ytterbium. Further improvements to our cooling scheme include independent control over the powers in the two ODT beams and an additional magnetic field gradient to improve spatial overlap of the two species.

Extending our method to incorporate alternate ytterbium isotopes (such as the fermion ^{173}Yb [23]) appears realistic. This would then realize Fermi degenerate mixtures with a large mass ratio. Finally, our results represent a significant milestone toward the production of quantum gases of paramagnetic polar molecules. Theoretical work on the LiYb molecule has already been initiated by several groups [26–28]. Future experimental work on our system includes photoassociative spectroscopies and searches for Feshbach resonances [29] in this mixture, which are key steps toward forming the molecule.

Note added. Recently, we became aware of similar work [30] in which quantum degenerate mixtures of ^{6}Li-^{174}Yb and ^{6}Li-^{173}Yb were obtained.

This work was supported by the National Science Foundation, the Alfred P. Sloan Foundation, and NIST. A. K. acknowledges support from the NSERC.

[1] G. Modugno, G. Ferrari, G. Roati, R. Brecha, A. Simoni, and M. Inguscio, Science **294**, 1320 (2001).

[2] Z. Hadzibabic, C. A. Stan, K. Dieckmann, S. Gupta, M. W. Zwierlein, A. Görlitz, and W. Ketterle, Phys. Rev. Lett. **88**, 160401 (2002).

[3] C. Silber, S. Gunther, C. Marzok, B. Deh, P. W. Courteille, and C. Zimmermann, Phys. Rev. Lett. **95**, 170408 (2005).

[4] S. Aubin, S. Myrskog, M. H. T. Extavour, L. J. LeBlanc, D. McKay, A. Stummer, and J. Thywissen, Nature Phys. **2**, 384 (2006).

[5] M. Taglieber, A. C. Voigt, T. Aoki, T. W. Hänsch, and K. Dieckmann, Phys. Rev. Lett. **100**, 010401 (2008).

[6] F. M. Spiegelhalder, A. Trenkwalder, D. Naik, G. Hendl, F. Schreck, and R. Grimm, Phys. Rev. Lett. **103**, 223203 (2009).

[7] N. Nemitz, F. Baumer, F. Münchow, S. Tassy, and A. Görlitz, Phys Rev A **79**, 061403(R) (2009).

[8] S. Tassy, N. Nemitz, F. Baumer, C. Höhl, A. Batar, and A. Görlitz, J. Phys. B **43**, 205309 (2010).

[9] M. Okano, H. Hara, M. Muramatsu, K. Doi, S. Uetake, Y. Takasu, and Y. Takahashi, Appl Phys B **98**, 691 (2010).

[10] F. Baumer, F. Münchow, A. Görlitz, S. Maxwell, P. Julienne, and E. Tiesinga, Phys. Rev. A **83**, 040702 (2011).

[11] V. V. Ivanov, A. Khramov, A. H. Hansen, W. H. Dowd, F. Münchow, A. O. Jamison, and S. Gupta, Phys. Rev. Lett. **106**, 153201 (2011).

[12] J. P. D'Incao and B. D. Esry, Phys. Rev. A **73**, 030702 (2006).

[13] B. Marcelis, S. J. J. M. F. Kokkelmans, G. V. Shlyapnikov, and D. S. Petrov, Phys. Rev. A **77**, 032707 (2008).

[14] M. Iskin, Phys. Rev. A **78**, 021604 (2008).

[15] A. Gezerlis, S. Gandolfi, K. E. Schmidt, and J. Carlson, Phys. Rev. Lett. **103**, 060403 (2009).

[16] A. Trenkwalder, C. Kohstall, M. Zaccanti, D. Naik, A. I. Sidorov, F. Schreck, and R. Grimm, Phys. Rev. Lett. **106**, 115304 (2011).

[17] J. M. Sage, S. Sainis, T. Bergeman, and D. DeMille, Phys. Rev. Lett. **94**, 203001 (2005).

[18] J. Deiglmayr, A. Grochola, M. Repp, K. Mortlbauer, C. Gluck, J. Lange, O. Dulieu, R. Wester, and M. Weidemuller, Phys. Rev. Lett. **101**, 133004 (2008).

[19] K.-K. Ni, S. Ospelkaus, M. H. G. de Miranda, A. Peer, B. Neyenhuis, J. J. Zirbel, S. Kotochigova, P. S. Julienne, D. S. Jin, and J. Ye, Science **322**, 231 (2008).

[20] A. Micheli, G. K. Brennen, and P. Zoller, Nature Phys. **2**, 341 (2006).

[21] J. J. Hudson, B. E. Sauer, M. R. Tarbutt, and E. A. Hinds, Phys. Rev. Lett. **89**, 023003 (2002).

[22] Y. Takasu, K. Maki, K. Komori, T. Takano, K. Honda, M. Kumakura, T. Yabuzaki, and Y. Takahashi, Phys. Rev. Lett. **91**, 040404 (2003).

[23] T. Fukuhara, Y. Takasu, M. Kumakura, and Y. Takahashi, Phys. Rev. Lett. **98**, 030401 (2007).

[24] T. Fukuhara, S. Sugawa, Y. Takasu, and Y. Takahashi, Phys. Rev. A **79**, 021601 (2009).

[25] Compared to our earlier work, the power in the slowing beam is about three times larger. For the same ODT laser power, the mean trap frequency is also about three times larger.

[26] P. Zhang, H. R. Sadeghpour, and A. Dalgarno, J. Chem. Phys. **133**, 044306 (2010).

[27] G. Gopakumar, M. Abe, B. P. Das, M. Hada, and K. Hirao, J. Chem. Phys. **133**, 124317 (2010).

[28] Svetlana Kotochigova and Roman Krems (private communication).

[29] P. S. Zuchowski, J. Aldegunde, and J. Hutson, Phys. Rev. Lett. **105**, 153201 (2010).

[30] H. Hara, Y. Takasu, Y. Yamaoka, J. M. Doyle, and Y. Takahashi, Phys. Rev. Lett. **106**, 205304 (2011).

Appendix C

DYNAMICS OF FESHBACH MOLECULES IN AN ULTRACOLD THREE-COMPONENT MIXTURE

PHYSICAL REVIEW A **86**, 032705 (2012)

Dynamics of Feshbach molecules in an ultracold three-component mixture

Alexander Y. Khramov, Anders H. Hansen, Alan O. Jamison, William H. Dowd, and Subhadeep Gupta
Department of Physics, University of Washington, Seattle, Washington 98195, USA

(Received 7 July 2012; published 10 September 2012)

We present investigations of the formation rate and collisional stability of lithium Feshbach molecules in an ultracold three-component mixture composed of two resonantly interacting fermionic ^{6}Li spin states and bosonic ^{174}Yb. We observe long molecule lifetimes (>100 ms) even in the presence of a large ytterbium bath and extract reaction rate coefficients of the system. We find good collisional stability of the mixture in the unitary regime, opening new possibilities for studies and probes of strongly interacting quantum gases in contact with a bath species.

DOI: 10.1103/PhysRevA.86.032705 PACS number(s): 34.50.Lf, 05.30.Fk

Magnetic Feshbach resonances allow precise control of collisional properties, making them a key tool in ultracold atom systems. They have been used extensively to study ultracold molecules, as well as few- and many-body physics [1]. Two-component Fermi gases near a Feshbach resonance provide excellent opportunities to study strongly interacting quantum systems [2]. This is possible due to the remarkable collisional stability of the atom-molecule mixture on the positive scattering length side of the resonance [3,4], attributed largely to Fermi statistics [5,6]. Extending the system to three-component mixtures in which only two are resonantly interacting [7] offers the exciting possibility of modifying or probing pairing dynamics by selective control of the third component. A third component may also be used as a coolant bath for exothermic molecule-formation processes, provided that inelastic processes with the bath are negligible. In the context of many-body physics, a third nonresonant component can be useful as a microscopic probe of superfluid properties [7,8], as a stable bath for studies of nonequilibrium phenomena [9], or for accurate thermometry of deeply degenerate fermions [10].

Collisional stability of Feshbach molecules in the absence of Fermi statistics becomes a crucial question for multicomponent mixtures [7,11,12]. A recent theoretical analysis of such mixtures suggests a possibility for enhanced molecule formation rates with good collisional stability [11]. Enhanced atom loss has been observed near a ^{6}Li p-wave resonance in the presence of a ^{87}Rb bath [13], while a small sample of the probe species ^{40}K has been found to be stable within a larger strongly interacting ^{6}Li sample [7].

In this paper, we investigate a mixture composed of two resonantly interacting spin states of fermionic ^{6}Li immersed in a large sample of bosonic ^{174}Yb atoms. While the Li interstate interactions are arbitrarily tunable by means of an s-wave Feshbach resonance at 834 G [14], the interspecies interactions between Li and Yb are constant and small [15]. We study the formation and evolution of Feshbach molecules in a bath of a second atomic species. In the unitary regime, we observe good collisional stability of the mixture with elastic interactions dominating over inelastic losses. We extract the reaction rate constants from a classical rate equations model of the system.

Our experimental procedure has been described in earlier work [16]. Briefly, 3×10^6 atoms of ^{174}Yb in the $^1S_0$ state and up to 4×10^4 atoms of ^{6}Li, distributed equally between the two $^2S_{1/2}$, $F = \frac{1}{2}$ states (denoted $\text{Li}|1\rangle$, $\text{Li}|2\rangle$), are loaded from magneto-optical traps into a crossed-beam optical dipole trap. We then perform forced evaporative cooling on Yb to a final trap depth $U_{\text{Yb}}(U_{\text{Li}}) = 15(55)\,\mu$K, with mean trap frequency $\bar{\omega}_{\text{Yb}}\,(\bar{\omega}_{\text{Li}}) = 2\pi \times 0.30\,(2.4)$ kHz [17], during which Li is cooled sympathetically by Yb. Following evaporation, the mixture is held at a constant trap depth to allow interspecies thermalization. With a time constant of 1 s, the system acquires a common temperature $T_{\text{Yb}} = T_{\text{Li}} = 2\,\mu$K with atom number $N_{\text{Yb}}\,(N_{\text{Li}}) = 2 \times 10^5\,(3 \times 10^4)$. This corresponds to $T_{\text{Li}}/T_F \simeq 0.4$ and $T_{\text{Yb}}/T_C \simeq 2.5$, where T_F is the Li Fermi temperature and T_C is the Yb Bose-Einstein condensation temperature [18].

After this initial preparation, we ramp up the magnetic field to a desired value and observe the system after a variable hold time. For fields in the vicinity of the Feshbach resonance, there is a field-dependent number loss and heating for the Li cloud during the 20 ms ramp time, resulting in T_{Li} rising to as high as 4.5 μK. At this point, the density-weighted average density $\langle n_{\text{Yb}}\rangle$ ($\langle n_{\text{Li}}\rangle$) is 2.6 (0.35) $\times\, 10^{13}$ cm^{-3}. For interrogation in the absence of the bath, Yb is removed from the trap with a 1 ms light pulse resonant with the $^1S_0 \rightarrow {}^1P_1$ transition [19]. Atom number and temperature are monitored using absorption imaging for both species after switching off the magnetic field.

We first present our results on atom-loss spectroscopy near the Feshbach resonance (see Fig. 1). The atom-loss maximum obtained in the absence of Yb has been observed previously [14] and can be explained as a result of the formation and subsequent decay of shallow lithium Feshbach dimers [3,4,20–22] which form only on the positive a side of the resonance. Here a denotes the $\text{Li}|1\rangle$-$\text{Li}|2\rangle$ scattering length. In the presence of the Yb bath, the loss feature is shifted and broadened. We interpret the behavior of the mixture in terms of five chemical processes:

$$
\begin{array}{rcll}
\text{Li}|1\rangle + \text{Li}|2\rangle + \text{Li} & \rightleftharpoons & \text{Li}_2^s + \text{Li} & (+\epsilon_B) \qquad \text{(I)} \\
\text{Li}_2^s + \text{Li} & \rightarrow & \text{Li}_2^d + \text{Li} & (+\epsilon_D) \qquad \text{(II)} \\
\text{Li}|1\rangle + \text{Li}|2\rangle + \text{Yb} & \rightleftharpoons & \text{Li}_2^s + \text{Yb} & (+\epsilon_B) \qquad \text{(III)} \\
\text{Li}_2^s + \text{Yb} & \rightarrow & \text{Li}_2^d + \text{Yb} & (+\epsilon_D) \qquad \text{(IV)} \\
\text{Li}|1\rangle + \text{Li}|2\rangle + \text{Yb} & \rightarrow & \text{Li}_2^d + \text{Yb} & (+\epsilon_D) \qquad \text{(V)}
\end{array}
$$

Forward process (I) corresponds to a three-body collision event which produces a shallow Feshbach dimer (denoted Li_2^s) accompanied by the release of the dimer binding energy $\epsilon_B = \frac{\hbar^2}{2m_{\text{Li}}a^2}$. Li denotes a ^{6}Li atom in either of the two spin states. Process (II) corresponds to two-body loss to a deeply bound dimer (denoted Li_2^d) with binding energy ϵ_D. Processes

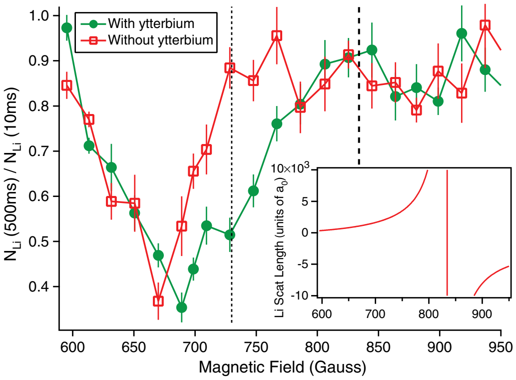

FIG. 1. (Color online) Li atom-loss spectroscopy in the presence (filled circles) and absence (open squares) of a Yb bath near the ^{6}Li 834 G Feshbach resonance (inset). We plot the number of Li atoms after 500 ms of evolution normalized to that at 10 ms. The thick dashed line indicates the resonance center and the thin dashed line indicates the magnetic field at which $\epsilon_B = k_B T_{\rm Li}$ for the initial conditions.

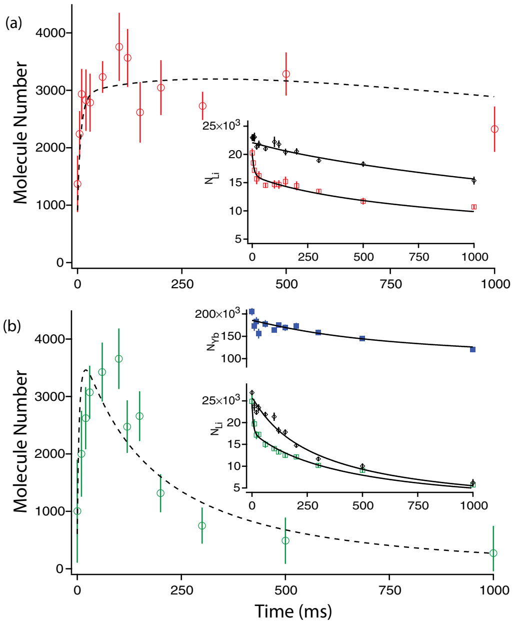

FIG. 2. (Color online) Evolution of Li Feshbach molecule number at 709 G without (a) and with (b) a Yb bath. The numbers are obtained by comparing Li atom numbers (insets) ramped across resonance (diamonds) or not (open squares) as described in the text. The lower inset also shows the Yb number (filled squares). The curves are fits with a rate equations-based model.

(III) and (IV) are similar to (I) and (II) with the spectator atom being Yb rather than Li [23]. Process (V) corresponds to direct three-body loss to a deeply bound molecule. Processes (II), (IV), and (V) always result in particle loss from the trap since $\epsilon_D \gg U_{\rm Li}$. Vibrational relaxation due to collisions between Li_2^s Feshbach molecules may contribute at the lowest fields, but it has a negligible rate for the fields at which we perform our analysis [3,22]. We have experimentally checked that direct three-body loss processes to deeply bound states involving three Li atoms as well as those involving one Li atom and two Yb atoms are negligible for this work [24]. Three-body losses involving Yb atoms alone have a small effect [25] and are taken into account in our analysis.

In the absence of Yb, only processes (I) and (II) contribute. If we neglect loss process (II), the atom-molecule mixture approaches an equilibrium, characterized by an equality of the forward and reverse rates and an equilibrium molecule fraction $\frac{2N_m}{N_{\rm Li}+2N_m} = (1 + \frac{e^{-\epsilon_B/k_B T}}{\phi_{\rm Li}})^{-1}$, where N_m is the molecule number and $\phi_{\rm Li}$ is the phase space density for each spin component in the ground state of the trap [20–22]. The time scale for achieving equilibrium depends on the three-body rate constant L_3 for process (I), which scales with the scattering length as a^6, whereas rate constant L_2 for process (II) scales as $a^{-3.3}$ [26,27]. The shape of the loss spectrum can thus be qualitatively explained by noting that the dimer formation rate increases with magnetic field while the equilibrium dimer fraction and the molecule decay rate decrease. The large rate for process (I) at high fields close to resonance ensures an equilibrium molecule fraction at all times. Broadly speaking, the rate-limiting step determining the system evolution is the molecule formation rate at low fields and the decay rate at high fields. The trap depth also affects the loss spectrum shape, since it determines the magnetic field range over which the formed shallow dimers remain trapped.

In the presence of Yb, the additional dimer formation (III), dimer decay (IV), and three-body loss (V) processes contribute. The observed loss spectrum is broadened on the higher field side, suggesting that for our parameters, processes (IV) and/or (V) play an important role while process (III) does not. The rate constants L_3', L_2', and L_3^d for processes (III), (IV) and (V), have theoretical scalings a^4, a^{-1}, and a^2, respectively [11,26]. Overall, we see two regimes of behavior—a lossy one where molecule formation is energetically favored ($\epsilon_B > k_B T_{\rm Li}$) and a stable one closer to resonance ($\epsilon_B < k_B T_{\rm Li}$). The criterion $\epsilon_B = k_B T$ separating these two regimes is equivalent to $ka = 1$, where $\frac{\hbar^2 k^2}{2m_{\rm Li}} = k_B T_{\rm Li}$, i.e., the unitary criterion.

To expand upon this qualitative picture, we study the time evolution of the three-component mixture at representative magnetic fields in the above two regimes. We are then able to extract quantitative information for the above processes from a rate-equations model of the system.

Figure 2 shows the Li atom and molecule number evolution at 709 G ($\epsilon_B = k_B \times 8.3\,\mu$K), a field value where modifications due to the Yb bath are apparent in Fig. 1. The number of Feshbach molecules at a particular field is determined by using a procedure similar to earlier works [3,4]. After variable evolution time, we ramp the magnetic field with a speed of 40 G/ms either up to 950 G, which dissociates the molecules back into atoms that remain in the trap, or to 506 G, which does not. We then rapidly switch off the magnetic field and image the atomic cloud. The molecule number is obtained from the number difference in the two images (see the insets in Fig. 2).

We see that the presence of Yb alters the molecule decay rate while the formation rate is unchanged. The Feshbach molecules appear to coexist for a long time (>100 ms) with the Yb bath, even in the absence of Pauli blocking [11]. We adapt the recent rate-equations analysis of Feshbach losses in a Fermi-Fermi mixture [22] to incorporate a third component, temperature evolution, and trap inhomogeneity. $T_{\rm Li}/T_F > 0.5$ is satisfied throughout the measurement range, allowing a classical treatment of the Li cloud. We model the density evolutions due to processes (I)–(V) using

$$\dot{n}_m = R_m + R'_m - L_2 n_m n_{\rm Li} - L'_2 n_m n_{\rm Yb}, \tag{1}$$

$$\dot{n}_{\rm Li} = -2R_m - 2R'_m - L_2 n_m n_{\rm Li} - 2L^d_3 n^2_{\rm Li} n_{\rm Yb}, \tag{2}$$

$$\dot{n}_{\rm Yb} = -L'_2 n_m n_{\rm Yb} - L^d_3 n^2_{\rm Li} n_{\rm Yb}. \tag{3}$$

Here n_m, $n_{\rm Li}$, and $n_{\rm Yb}$ are the densities of shallow dimers ${\rm Li}^s_2$, Li atoms, and Yb atoms, respectively. $R_m\,(R'_m) = \frac{3}{4}L_3\,(L'_3)n^2_{\rm Li}n_{\rm Li\,(Yb)} - qL_3\,(L'_3)n_m n_{\rm Li\,(Yb)}$ is the net rate for molecule production via process (I) [(III)]. We determine q through the constraints on the molecule fraction at equilibrium $[R_m\,(R'_m) = 0]$. We obtain an upper bound for L^d_3 by observations at large negative a (described below) which indicates a negligible effect for the data in Fig. 2, allowing us to set $L^d_3 = 0$ for the analysis at 709 G.

The time evolutions of $T_{\rm Li}$ and $T_{\rm Yb}$ are modeled considering the energy deposition from processes (I) and (III) as well as heating from the density-dependent loss processes (II), (IV), and (V) [28]. In addition, our model also takes into account the effects of evaporative cooling [29], interspecies thermalization [15], one-body losses from background gas collisions, and Yb three-body losses [25,28]. The Li scattering length at 709 G is $a = 1860a_0$, ensuring rapid thermalization (<1 ms) in the lithium atom–Feshbach molecule mixture [26]. This allows the assumption of equal temperature $T_{\rm Li}$ for lithium atoms and Feshbach molecules. The heating from molecule formation at 709 G dominates over interspecies thermalization, maintaining $T_{\rm Li} \simeq 4.5\ \mu$K and $T_{\rm Yb} \simeq 2\ \mu$K, as observed in both the experiment and the model.

The best-fit rate coefficients extracted from the atom data (shown in the insets) are $L_3 = (1.4 \pm 0.3) \times 10^{-24}$ cm^6/s, $L_2 = (1.3 \pm 0.3) \times 10^{-13}$ cm^3/s, and $L'_2 = (2.3 \pm 0.2) \times 10^{-13}$ cm^3/s. L'_3 is consistent with 0. All reported uncertainties are statistical. The L_3 value is consistent with that obtained in Ref. [3] after accounting for the slight differences in experimental parameters. Using $L'_2\langle n_{\rm Yb}\rangle$ as a measure of the dimer decay rate, we get 170 ms as the lifetime of a Li Feshbach molecule in the Yb bath.

We now turn to the unitary regime, where we choose 810 G ($ka = +6$, $\epsilon_B = k_B \times 0.11\ \mu$K) as our representative field to study the mixture properties. It is difficult to reliably observe the molecule number using our earlier method in this regime, so we only monitor the atoms (see Fig. 3). Starting with an interspecies temperature differential as before, we observe a fast drop in $T_{\rm Li}$ in the presence of Yb and clear evidence of interspecies thermalization. The Li number in the three-component mixture exhibits a long $1/e$ lifetime of 2 s, far larger than at 709 G. However, this is still an order of magnitude shorter than that obtained in the absence of Yb. The interpretation of the decay is not straightforward as both two-body [process (IV)] and three-body [process (V)] inelastic loss can contribute [7,30]. The large rate for process (I) in this regime ensures equilibrium molecule fraction at all times. By fitting to data taken at 935 G, where $ka = -2$ and process (V) is expected to be the dominant inelastic loss, we obtain $L^d_3 = (4.3 \pm 0.3) \times 10^{-28}$ cm^6/s. This sets a lower bound for L^d_3 at 810 G. We fit the first 2.5 s of data in Fig. 3 after fixing L'_2 to its value scaled from 709 G and find $L^d_3 = (9.5 \pm 0.5) \times 10^{-28}$ cm^6/s at 810 G. The slight disagreement in Li atom number at long times may be due to a small (<10%) inequality in our spin mixture composition, which the model does not take into account.

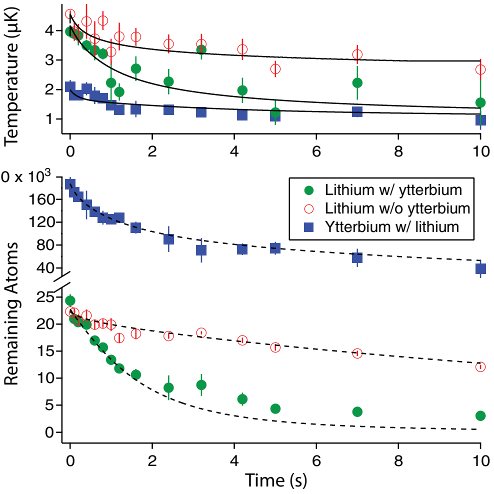

FIG. 3. (Color online) The evolution of temperature and number at 810 G for the Li atomic cloud with Yb (filled circles) and without (empty circles) and also for Yb in the presence of Li (filled squares). The curves are fits with a rate equations-based model.

The qualitative features of both spectra in Fig. 1 can be theoretically reproduced by using field-dependent reaction coefficients scaled from our measured values at 709 and 810 G. However, a full quantitative comparison will need to take into account the theoretical deviations from scaling behavior in the unitary regime as well as experimental variations in the initial temperature, and is open to future investigation.

By extending the forced evaporative cooling step, lower temperature mixtures can be produced where bosonic ^{174}Yb shrinks to a size smaller than the Fermi diameter of the ^{6}Li cloud. Such experiments at 834 G yield $T_{\rm Li}/T_F \simeq 0.25$ with $N_{\rm Yb} = N_{\rm Li} = 2.5 \times 10^4$. Here, the estimated volume of the Yb sample is $\simeq 0.3$ of the Li sample volume, compared to 3.3 in the classical regime. The mixture is thus also capable of achieving the opposite regime of a second species being immersed inside a strongly interacting quantum degenerate Fermi gas, similar to earlier studies in the K-Li mixture [7].

Our experiments with the Yb-Li mixture near a Feshbach resonance demonstrate the effects of an additional species on chemical reaction rates in the micro-Kelvin regime. We observe a long lifetime for Feshbach molecules, even in the absence of Pauli blocking. Our demonstrated stability of the mixture near the unitary regime of the resonance opens various possibilities of studying strongly interacting fermions immersed in a bath species or being interrogated by a small probe species. Future experimental opportunities include realizations of nonequilibrium states and studies of superfluid properties, for instance by controlled relative motion between the two species. Finally, our results constitute an advance in the manipulation of ultracold mixtures of alkali-metal and alkaline-earth-metal-like atoms [16,31,32]. These mixtures may be used to produce quantum gases of paramagnetic polar molecules, which are promising for diverse applications such as quantum simulation of lattice spin models [33], tests of fundamental symmetries [34], and probes of time variations in fundamental constants [35].

We thank Ben Plotkin-Swing for experimental assistance, and J. P. D'Incao, T. -L. Ho, and M. W. Zwierlein for helpful discussions. We gratefully acknowledge support from the National Science Foundation and the Air Force Office of Scientific Research. A.Y.K. thanks the NSERC.

---

[1] C. Chin, R. Grimm, P. S. Julienne, and E. Tiesinga, Rev. Mod. Phys. **82**, 1225 (2010).

[2] S. Giorgini, L. P. Pitaevskii, and S. Stringari, Rev. Mod. Phys. **80**, 1215 (2008).

[3] S. Jochim, M. Bartenstein, A. Altmeyer, G. Hendl, C. Chin, J. H. Denschlag, and R. Grimm, Phys. Rev. Lett. **91**, 240402 (2003).

[4] J. Cubizolles, T. Bourdel, S. J. J. M. F. Kokkelmans, and C. Salomon, Phys. Rev. Lett. **91**, 240401 (2003).

[5] B. D. Esry, C. H. Greene, and H. Suno, Phys. Rev. A **65**, 010705(R) (2001).

[6] D. S. Petrov, C. Salomon, and G. V. Shlyapnikov, Phys. Rev. Lett. **93**, 090404 (2004).

[7] F. M. Spiegelhalder, A. Trenkwalder, D. Naik, G. Hendl, F. Schreck, and R. Grimm, Phys. Rev. Lett. **103**, 223203 (2009).

[8] K. Targonska and K. Sacha, Phys. Rev. A **82**, 033601 (2010).

[9] A. Robertson and V. M. Galitski, Phys. Rev. A **80**, 063609 (2009).

[10] S. Nascimbène, N. Navon, K. J. Jiang, F. Chevy, and C. Salomon, Nature (London) **463**, 1057 (2010).

[11] J. P. D'Incao and B. D. Esry, Phys. Rev. Lett. **100**, 163201 (2008).

[12] J. J. Zirbel, K.-K. Ni, S. Ospelkaus, J. P. D'Incao, C. E. Wieman, J. Ye, and D. S. Jin, Phys. Rev. Lett. **100**, 143201 (2008).

[13] B. Deh, C. Marzok, C. Zimmermann, and P. W. Courteille, Phys. Rev. A **77**, 010701(R) (2008).

[14] K. Dieckmann, C. A. Stan, S. Gupta, Z. Hadzibabic, C. H. Schunck, and W. Ketterle, Phys. Rev. Lett. **89**, 203201 (2002).

[15] V. V. Ivanov, A. Khramov, A. H. Hansen, W. H. Dowd, F. Münchow, A. O. Jamison, and S. Gupta, Phys. Rev. Lett. **106**, 153201 (2011).

[16] A. H. Hansen, A. Khramov, W. H. Dowd, A. O. Jamison, V. V. Ivanov, and S. Gupta, Phys. Rev. A **84**, 011606(R) (2011).

[17] The optical trap wavelength = 1064 nm, initial power = 10 W per beam, waist = 26 μm, crossing angle = 20°. During the evaporative cooling step, the power is reduced by a factor of 16 over 3 s. At the highest optical trap powers, $\bar{\omega}_{\mathrm{Yb}}/\bar{\omega}_{\mathrm{Li}} = 0.12$ and $U_{\mathrm{Yb}}/U_{\mathrm{Li}} = 0.45$. At the lower final power, gravity reduces the effective trap depth of the heavier component more, but has a negligible effect on the frequency ratio.

[18] By continuing the forced evaporation to lower trap depths, we can produce pure Yb BECs with $>2 \times 10^5$ atoms in single-species experiments and deeply Fermi degenerate gases $T_{\mathrm{Li}}/T_F \simeq 0.1$ in two-species experiments.

[19] This step is carried out either immediately before or after the field ramp, with no discernible difference in lithium number or temperature between the two.

[20] C. Chin and R. Grimm, Phys. Rev. A **69**, 033612 (2004).

[21] S. J. J. M. F. Kokkelmans, G. V. Shlyapnikov, and C. Salomon, Phys. Rev. A **69**, 031602(R) (2004).

[22] S. Zhang and T.-L. Ho, New J. Phys. **13**, 055003 (2011).

[23] Since we observe and model process (IV) by its loss signature, we cannot distinguish it from the analogous process resulting in a deeply bound LiYb molecule, $\mathrm{Li}_2^s + \mathrm{Yb} \rightarrow \mathrm{LiYb} + \mathrm{Li}\ (+\epsilon_{\mathrm{D}})$. Thus L_2' is the combined rate constant for both processes.

[24] We obtain an upper limit on the rate of processes involving one Li atom and two Yb atoms from lifetime measurements in mixtures of one spin state of Li with Yb at a magnetic field near the Li-Li Feshbach resonance. We obtain an upper limit on the rate of direct three body decay of Li from lifetime measurements of the Li spin mixture in the absence of Yb, on the negative a side of the resonance.

[25] Y. Takasu, K. Maki, K. Komori, T. Takano, K. Honda, M. Kumakura, T. Yabuzaki, and Y. Takahashi, Phys. Rev. Lett. **91**, 040404 (2003).

[26] D. S. Petrov, Phys. Rev. A **67**, 010703(R) (2003).

[27] J. P. D'Incao and B. D. Esry, Phys. Rev. Lett. **94**, 213201 (2005).

[28] T. Weber, J. Herbig, M. Mark, H.-C. Nägerl, and R. Grimm, Phys. Rev. Lett. **91**, 123201 (2003).

[29] K. M. O'Hara, M. E. Gehm, S. R. Granade, and J. E. Thomas, Phys. Rev. A **64**, 051403(R) (2001).

[30] X. Du, Y. Zhang, and J. E. Thomas, Phys. Rev. Lett. **102**, 250402 (2009).

[31] H. Hara, Y. Takasu, Y. Yamaoka, J. M. Doyle, and Y. Takahashi, Phys. Rev. Lett. **106**, 205304 (2011).

[32] F. Baumer, F. Münchow, A. Görlitz, S. E. Maxwell, P. S. Julienne, and E. Tiesinga, Phys. Rev. A **83**, 040702(R) (2011).

[33] A. Micheli, G. K. Brennen, and P. Zoller, Nat. Phys. **2**, 341 (2006).

[34] J. J. Hudson, D. M. Kara, I. J. Smallman, B. E. Sauer, M. R. Tarbutt, and E. A. Hinds, Nature (London) **473**, 493 (2011).

[35] M. Kajita, G. Gopakumar, M. Abe, and M. Hada, Phys. Rev. A **84**, 022507 (2011).

Appendix D

PRODUCTION OF QUANTUM-DEGENERATE MIXTURES OF YTTERBIUM AND LITHIUM WITH CONTROLLABLE INTERSPECIES OVERLAP

PHYSICAL REVIEW A **87**, 013615 (2013)

Production of quantum-degenerate mixtures of ytterbium and lithium with controllable interspecies overlap

Anders H. Hansen, Alexander Y. Khramov, William H. Dowd, Alan O. Jamison, Benjamin Plotkin-Swing, Richard J. Roy, and Subhadeep Gupta
Department of Physics, University of Washington, Seattle, Washington 98195, USA

(Received 12 November 2012; published 16 January 2013)

Quantum-degenerate mixtures of one-electron and two-electron atoms form the starting point for studying few- and many-body physics of mass-imbalanced pairs as well as the production of paramagnetic polar molecules. We recently reported the achievement of dual-species quantum degeneracy of a mixture of lithium and ytterbium atoms. Here we present details of the key experimental steps for the all-optical preparation of these mixtures. Further, we demonstrate the use of the magnetic field gradient tool to compensate for the differential gravitational sag of the two species and control their spatial overlap.

DOI: 10.1103/PhysRevA.87.013615 PACS number(s): 67.85.Pq, 37.10.De, 34.20.−b, 05.30.Fk

I. INTRODUCTION

Elemental quantum mixtures provide a path toward ultracold diatomic polar molecules [1]. Utilizing a second, distinguishable atomic species, such mixtures may also allow for impurity probing of quantum phenomena in an ultracold gas. Interspecies Feshbach resonances can enable studies of few- and many-body phenomena in mass-imbalanced systems. There has been great progress in the development of ultracold bi-alkali-metal gases, motivated by applications towards sympathetic cooling of Fermi gases [2], studies of strongly interacting mass-mismatched systems [3], and production of ultracold polar molecules [4].

Extending the choice of mixture components to include other parts of the periodic table, new scientific opportunities arise. For instance, the ground state of the diatomic molecule might now have a magnetic moment, leading to *paramagnetic* polar molecules. This has been a key motivation for our pursuit of the lithium-ytterbium combination.

The $^2\Sigma$ ground state of the YbLi molecule makes it a candidate system for simulating lattice spin models with applications in topological quantum computation [5]. Additionally, the Yb-Li mixture possesses a very large mass ratio, and a range of isotopic combinations with Bose and Fermi statistics. Tunable interactions between the components can lead to the creation of novel Efimov states [6]. When confined in an optical lattice, a heavy-light fermion mixture can realize the binary alloy model [7], with applications in simulating exotic condensed matter phases (e.g., studies of pattern formation [8,9]).

In previous work, we assessed the collisional stability of the Yb-Li mixture in weakly interacting regimes, and explored the strengths of various inelastic channels in a three-component mixture with one resonantly interacting pair. In this paper we describe the experimental details of our setup, stressing the areas that have required development beyond typical single-species experiments. We report on the production of large-number Bose- and Fermi-degenerate ytterbium gases and assess the cooling limits of the Yb-Li mixture from interspecies interactions. Finally we report the demonstration of interspecies spatial overlap control over a large temperature range, using a magnetic field gradient.

The remainder of this paper is organized as follows. In Sec. II we describe the salient features of our trapping apparatus. Section III discusses our atom manipulation and cooling techniques. In Sec. IV we summarize the performance of our system for the production of degenerate Yb-Li mixtures in different interaction regimes. Section V describes our interspecies spatial-overlap control scheme. Finally, in Sec. VI we present our conclusions and outlook.

II. TRAPPING APPARATUS

Our trapping apparatus uses standard techniques for single-species experiments, applied to two independent atomic sources, as pictured in Fig. 1. Yb and Li beams emerge from separate effusion ovens, and are directed towards the common "main" chamber through individually optimized Zeeman slower sections. The long slower tubes [lengths 93 cm (Li) and 40 cm (Yb), inner diameter 18 mm] also provide differential pumping. An additional stage of differential pumping is provided by a short tube (length 11 cm, inner diameter 5 mm) separating each oven assembly from an independently pumped "intermediate" chamber. We maintain the vacuum in each subchamber with ion pumps, and augment the main chamber vacuum with a titanium sublimation pump. During standard operation, the pressures are approximately $P_{\mathrm{Li\ oven}} \simeq 3 \times 10^{-8}$ Torr, $P_{\mathrm{Yb\ oven}} \simeq 1 \times 10^{-7}$ Torr, and $P_{\mathrm{main}} < 1 \times 10^{-10}$ Torr, as measured by ion gauges. Each beamline is equipped with a gate valve, positioned between the oven and intermediate chambers. This allows us to perform single-species experiments, even when the other oven is being serviced.

A. Lithium and ytterbium ovens

The effusion ovens each consist of a vertically oriented "cup," connected via a 90° elbow to a nozzle: a 4-mm-diameter aperture in the Conflat (CF) assembly. We stabilize the Yb (Li) cup temperatures to 400 (375) °C during operation. The nozzles are stabilized at 450 °C permanently to prevent deposition and congestion. The areas between each nozzle and gate valve contain mechanical beam shutters mounted on rotary feedthroughs to control the atom flow to the main chamber, and a copper cold plate (−7 °C) to collect the atomic flux not directed towards the main chamber.

All heated oven parts are of type-316 stainless steel, while the rest of the vacuum apparatus is type-304 stainless steel.

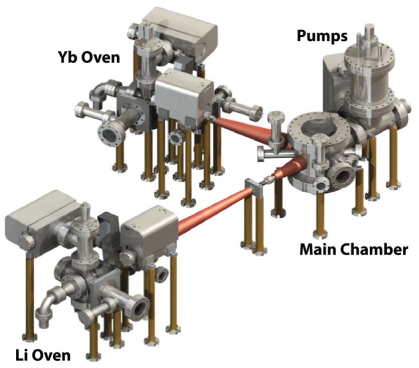

FIG. 1. (Color online) Schematic figure of dual-species apparatus. Ytterbium and lithium are prepared in separate ovens and slowed in individually optimized Zeeman slowers. Each oven is separated from the main chamber by two stages of differential pumping and an independently pumped intermediate chamber. The central part of each intermediate chamber (hidden from view) is a 2.75 in. six-way cross.

For the heated sections of the lithium oven we use nickel CF gaskets, which are more resilient than copper in high-temperature environments in the presence of lithium [10]. We have found, however, that nickel gaskets in the presence of hot Yb vapor undergo corrosive chemical reactions, which compromise the integrity of the vacuum after several months of operation. We now use copper gaskets in the ytterbium oven, which have been trouble-free for two years.

B. Main chamber

Our main chamber has a cylindrical geometry with ten viewports for optical access (Fig. 2). The top and bottom are sealed off by 10 in. CF flanges, into which custom-made re-entrant "buckets" for the electromagnets are recessed. Each bucket also has a 2.75 in. viewport for vertical MOT beams.

We keep the sapphire entry viewports for the Yb (Li) Zeeman slowing laser beams at a permanent 200 (250) °C; otherwise, metallic deposition is clearly evident. All other viewports are BK7 glass antireflection coated at the wavelengths for laser cooling and optical trapping of the two species.

Our experimental setup employs two pairs of electromagnetic coils, shown in Fig. 2. We apply antiparallel currents to the inner pair to generate the quadrupole field for the magneto-optical traps (MOTs), while the outer pair, arranged in parallel (Helmholtz) configuration, provide bias fields to access Feshbach resonances.

The MOT coils produce a vertical gradient of 1.0 G/cm/A, while the bias coils produce 4.2 G/A. We can electronically switch the MOT coils to parallel configuration, in which they yield 2.4 G/A . This allows for larger bias fields and improves the speed of magnetic field ramps.

Each coil is wound from hollow, square copper tubing (outer dimension 1/8 in., inner dimension 1/16 in.). A bias-field upper bound of 1000 G is set by the flow rate of the cooling water through the electromagnets at 100 psi building pressure. In order to reach higher fields (up to 1700 G), we employ a booster pump that raises the water pressure to 400 psi.

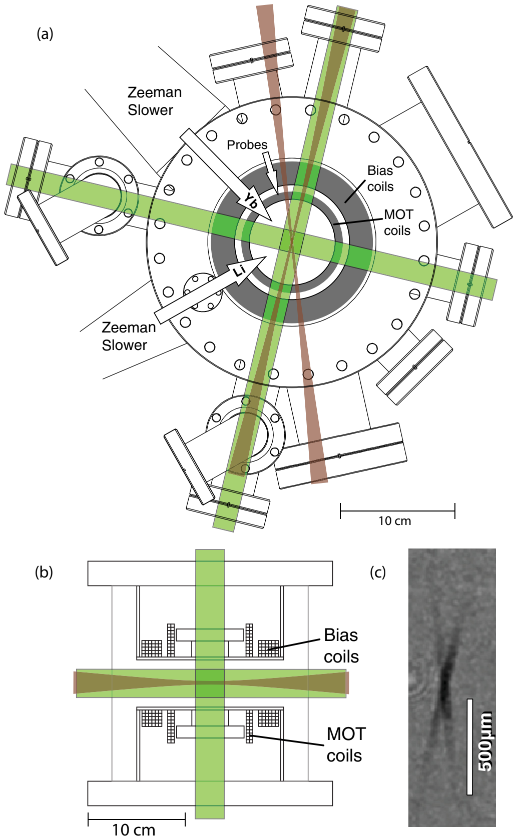

FIG. 2. (Color online) (a) Top view of main chamber, showing the configuration of magneto-optical trap (MOT) beams (green), optical dipole trap (ODT) beams (brown), magnetic coils (gray), and orientation of Yb and Li atomic beams and probe beams (arrows). Vertical MOT beams, vertical probe beams, slowing laser beams, and compensation coils are omitted for clarity. (b) Side view of main chamber, showing vertical and horizontal MOT beams, ODT beams, and recessed buckets with magnetic coils. (c) Sample in-trap absorption image of Yb atoms taken along the vertical axis, immediately after transfer to the ODT. The density distribution clearly shows the crossed-beam geometry. Upon further cooling, the atoms collect in the central crossing point of the two beams.

III. DUAL-SPECIES COOLING AND TRAPPING

We use three laser systems for slowing and laser cooling of lithium and ytterbium: one for ^{6}Li, addressing the $^2S_{1/2} \rightarrow {}^2P_{3/2}$ ($D2$) transition at 671 nm, and two for Yb, addressing the $^1S_0 \rightarrow {}^1P_1$ transition at 399 nm and $^1S_0 \rightarrow {}^3P_1$ (intercombination) transition at 556 nm (Fig. 3). We use acousto-optical modulators (AOMs) to provide all the required

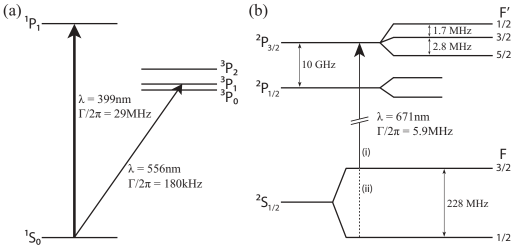

FIG. 3. Relevant energy levels for laser cooling of (a) ^{174}Yb and (b) ^{6}Li. Transitions used for trapping and cooling (see text) are indicated with arrows. In ^{173}Yb, only the excited states acquire hyperfine structure and the cooling lasers are tuned to the appropriate cycling transitions. To address lithium, we require separate frequency components for the cooling (i) and repumping (ii) transitions. The hyperfine splitting of the $^2P_{3/2}$ state is not resolved.

frequency shifts needed for slowing, trapping, repumping, and probing of the atoms.

We derive the 671 nm light from a commercial laser system (Toptica TA100), consisting of an external-cavity diode laser (ECDL) and a tapered amplifier (TA) system. We frequency-stabilize the laser using saturated absorption spectroscopy in a home-built vapor cell, with a lithium sample heated to 420 °C.

We derive the 399 nm light, used for slowing and imaging of Yb, from another commercial system (Toptica TA-SHG pro), consisting of an ECDL at 798 nm, a TA, and a second-harmonic generation (SHG) cavity. We frequency-stabilize this laser using saturated absorption spectroscopy in a commercial hollow-cathode lamp (Hamamatsu Laser Galvatron L2783).

We derive the 556 nm light, used for the Yb MOT, from another commercial system (Toptica FL-SHG pro), consisting of an ECDL, a fiber amplifier, and an SHG cavity. Since the linewidths of the blue and green transitions are different by more than two orders of magnitude, the two lasers require very different Yb column densities for spectroscopy. We frequency-stabilize this laser using saturated absorption spectroscopy in a home-built vapor cell with an ytterbium sample heated to 420 °C. In our setup, to reduce deposition on the cell viewports, we independently heat the viewport flanges while keeping the regions between the atomic sample and the glass at a lower temperature. We have also found it useful to reduce the diameter of the outermost section of the Yb cell on either end to reduce conduction.

A. Zeeman slowers

Each MOT loads from a separate Zeeman-slowed atomic beam. The solenoids for the Zeeman slowers are wound from the same copper wire as the MOT and bias coils. The Li slower uses a "spin-flip" configuration, consisting of a 60-cm-long decreasing-field section followed by a 15-cm-long increasing-field section. We operate each component at 30 A, yielding a net magnetic field variation $|\Delta \mathbf{B}|$ of 980 G. The atoms are slowed by a 40 mW laser beam, 732 MHz red-detuned from the $D2$ transition for the $F = \frac{3}{2}$ state. We derive the slower beam from an injection-locked diode laser. By adding a second injection beam 228 MHz blue-detuned from the first, we obtain light for repumping from the $F = \frac{1}{2}$ ground state within the slower.

The Yb slower consists of a single 40-cm-long increasing-field stage, operated at 15 A to yield $|\Delta \mathbf{B}| = 240$ G. The slowing beam has a power of 100 mW, and a red-detuning of 365 MHz from the $^1S_0 \rightarrow {}^1P_1$ transition.

Compensation coils, mounted opposite to each slower on the main chamber, cancel magnetic fringe fields at the position of the trapped atoms. Together with the vertical bias coils, the slower coils also serve as tools to move the center of the MOT quadrupole along all spatial axes, essential for relative positioning of the traps, as discussed below.

B. Magneto-optical traps

For magneto-optical trapping of the two species we use a standard single-species setup with retroreflected MOT beams [11], modified to accommodate a second atomic species. We combine the beams for the two species using a dichroic mirror, and divide the combined beam into three beams using broadband polarizing beam splitters. The polarizations are controlled by single-wavelength half-wave plates and dual-wavelength quarter-wave plates (Foctek).

Several factors have to be considered in determining the optimum parameters for dual-species laser cooling. Due to the difference in linewidth of the Li $D2$ and Yb intercombination lines (factor of 32) the two MOTs are optimized at very different magnetic gradients (see Table I). Furthermore, the optimal duration of the transitional cooling step (compression) before loading into the ODT differs greatly for the two species. Finally, the two species experience significant losses through inelastic collisions when the magneto-optical traps are spatially overlapped.

We find that the best performance in our setup is achieved using a sequential loading scheme, as described in [12], with typical parameters as listed in Table I. To summarize, we load Yb alone for 10–30 s, depending on experimental requirements. During this time, the detuning of the trapping light is modulated with an amplitude of 20 linewidths, at a frequency of 50 kHz, to increase the phase-space volume of the trapping region. We then compress Yb in 200 ms, and transfer it to the ODT. We subsequently optimize the

TABLE I. Typical experimental parameters for loading of ^{6}Li, ^{174}Yb, and ^{173}Yb: laser intensity I and red-detuning δ, and magnetic axial (vertical) field gradient B'. Two sets of numbers are provided for each isotope, reflecting the parameters for MOT loading and for the end point of compression (see the text) before transfer to the ODT. I refers to the total laser intensity in all three retroreflected beams; the total optical intensity at the atoms is twice the listed value. Γ and I_{sat} for Yb refer to the properties of the intercombination transition.

		^{6}Li $F = 3/2$	^{6}Li $F = 1/2$	^{174}Yb	^{173}Yb
Load	I	$60I_{\text{sat}}$	$55I_{\text{sat}}$	$750I_{\text{sat}}$	$750I_{\text{sat}}$
	δ	6Γ	3.5Γ	$(55 \pm 20)\Gamma$	$(40 \pm 20)\Gamma$
	B'	20 G/cm		3 G/cm	3 G/cm
Final	I	$0.07I_{\text{sat}}$	$0.08I_{\text{sat}}$	$0.8I_{\text{sat}}$	$2I_{\text{sat}}$
	δ	1.5Γ	3Γ	2Γ	4Γ
	B'	60 G/cm		18 G/cm	25 G/cm

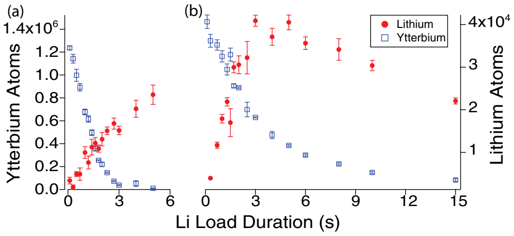

FIG. 4. (Color online) Number of trapped atoms, after a variable Li load time and 1 s hold in the ODT at fixed depth. (a) [(b)] shows results with a vertical bias field of 0 (2) G, corresponding to a 1 mm center-of-mass displacement of the Li MOT. In the favorably displaced case (b), Li numbers are optimized at a finite load time; at longer load times sympathetic cooling becomes inefficient due to low Yb numbers. Each error bar represents statistical fluctuations of four experimental iterations.

quadrupole field for lithium, load the Li MOT for 0.5–4 s (depending on experimental requirements), compress in 50 ms, and transfer to the ODT. A short (100 μs) pulse of light resonant with the Li $F = \frac{3}{2}$ $D2$ transition optically pumps the Li atoms into the ground $F = \frac{1}{2}$ state.

The positioning of the Li MOT during load is crucial for large dual-species samples as can be seen in Fig. 4. The large losses for suboptimal positioning can be interpreted as a consequence of elastic collisions that heat Yb through contact with the Li MOT, and also of inelastic collisions of ground-state Yb with electronically excited Li atoms in which both constituents are lost. The latter process also impedes the rate at which the Li MOT loads, as can be observed in Fig. 4.

We mitigate this effect by applying a bias field during the Li load, which spatially offsets the MOT from the ODT. With a vertical bias field of 2 G the lifetime of Yb atoms is quadrupled. Although this lifetime is less than the vacuum-limited lifetime of ~45 s, this still leads to simultaneous confinement of 10^6 Yb atoms and 10^5 Li atoms in the ODT, immediately after switching off all the laser cooling beams.

Due to the greater abundance of Yb in the ODT, as well as its lower MOT temperature, Yb acts as a coolant for Li. At zero bias field we observe that, in the absence of Yb, most of the Li atoms spill from the trap during the first 1 s after transfer from the MOT. With a large bath of Yb present, these losses are mitigated, as the Li atoms thermalize with the bath.

C. Optical dipole trap

We derive our ODT from an ytterbium fiber laser (IPG Photonics YLR-100-LP) that can provide up to 100 W laser power at 1064 nm. During standard operation, we run the laser at 40 W. We send the laser output through an AOM and split the first-order output into two components of equal power and orthogonal polarization. Each component is focused to a waist of ≈26 μm and crossed at a 20° angle at the atoms. As shown in Fig. 2, both beams are horizontally aligned through the chamber. This configuration provides a straightforward geometry for our crossed ODT.

We perform evaporative cooling by controlling the efficiency of the ODT AOM. The geometry of the trap is thus preserved during evaporation, and trap frequencies may be interpolated between measurements at various depths [13].

D. Evaporative and sympathetic cooling strategies

For a given intensity of the 1064 nm ODT beam, the optical potential for Li is greater than that for Yb by a factor of about 2. Thus, at the same temperature, Yb will evaporate from the trap significantly faster than Li. For this reason, and because the Li (linear) size is smaller by a factor of 0.7 at equal temperature, the most practical cooling strategy involves sympathetically cooling Li in a bath of Yb. We thus optimize the initial conditions to a larger proportion ($\geqslant$90%) of trapped Yb, and set the rate of evaporative cooling to match the interspecies thermalization time, which is of order 1 s throughout. This method works well even in the regime of quantum degeneracy, since the condensation temperature for Yb is an order of magnitude lower than the Li Fermi temperature (for equal Li and Yb numbers). A more detailed discussion of this scheme can be found in [14].

We believe that this method of cooling will readily transfer to other alkali metal + spin-singlet systems, where some performance aspects may be even better than in Yb-Li. The number of interspecies collisions necessary for thermalization between particles of masses m_1 and m_2 is of order $2.7/\xi$, where the dimensionless parameter $1/\xi = (m_1 + m_2)^2/4m_1m_2$ [15]. For ^{6}Li and ^{174}Yb, $2.7/\xi = 21$, which is relatively large. Furthermore, since Li cannot be laser cooled to such low temperatures as Yb, a considerable amount of Yb is lost through evaporation during initial thermalization. Both of these effects will be less severe with other alkali-metal atoms such as Na, K, Rb, and Cs. We also note that a similar mismatch of trap depth in a 1064 nm ODT will exist and a similar immunity to two-body inelastic losses is expected, both advantageous for sympathetic cooling with Yb [16].

E. Simultaneous dual-species imaging

We simultaneously probe the collocated, optically trapped clouds of Li and Yb using absorption imaging. The imaging beams are overlapped before they enter the vacuum chamber, using a broadband polarizing beam splitter. The beams are split after they emerge from the vacuum chamber using dichroic mirrors, and the cloud images are projected onto two different regions of the CCD camera chip. Absorption images for both clouds are obtained for each experimental iteration.

IV. Yb-Li QUANTUM MIXTURES

Our quantum mixture preparation relies on the direct evaporative cooling of Yb which then cools the co-trapped Li sympathetically, as described in Sec. III D. Cooling in the absence of an external magnetic field leads to weakly interacting Bose-Fermi mixtures. By applying external magnetic fields, strongly interacting regimes may then be accessed through available Feshbach resonances. In this section, we first report our current system performance for producing quantum-degenerate gases of single-species Yb isotopes. We then present the production of weakly interacting Yb-Li mixtures through sympathetic cooling. Finally we briefly discuss regimes of strong interactions in Yb-Li mixtures.

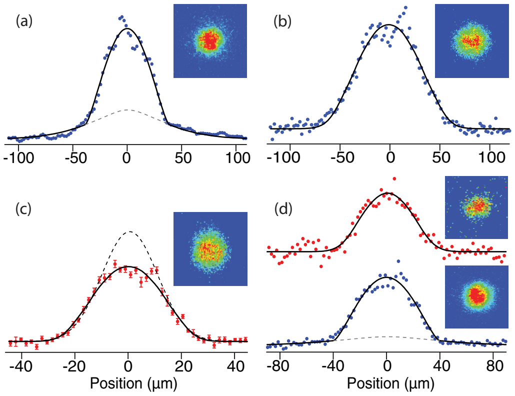

FIG. 5. (Color online) Density cross sections of lithium and ytterbium from absorption images (insets) of degenerate gases. (a) Quantum-degenerate gas of ^{174}Yb atoms with 2.5×10^5 atoms in the condensate imaged at a time of flight (TOF)12 ms. (b) Degenerate Fermi gas of 1×10^5 ^{173}Yb atoms with $T/T_F = 0.3$ and TOF 5 ms. (c) Degenerate Fermi gas of 1.6×10^4 ^{6}Li atoms with $T/T_F \approx 0.06$ and TOF 0.4 ms. (d) Simultaneous quantum degeneracy of ^{6}Li and ^{174}Yb with 2×10^4 (3×10^4) atoms of Li (Yb). $T/T_F \approx 0.2$ for Li and TOF 0.5 (10) ms. Solid lines are least-square fits to local-density-approximation models for Bose and Fermi gases, while dashed lines are classical fits to the wings of the distributions.

A. Quantum-degenerate ytterbium

Our current apparatus has several new features beyond what was reported in [14]. Our Yb laser cooling procedure now employs greater power and frequency sweep range in the MOT beams during load (see Sec. III). The optical trap now features electronic stabilization of depth and adjustable volume through a time-averaged potential generated by frequency modulation of the ODT AOM [18]. This "painting" of the potential increases the volume of the loading trap and allows a much larger load of Yb. Optimization of both loading and evaporation is obtained by continuously reducing the volume and the depth of the trap during evaporative cooling. Loading from 7×10^7 laser-cooled atoms at a temperature of $\simeq 20$ μK, we achieve an optical trap load of up to 5×10^6 atoms and ^{174}Yb condensate numbers of 3×10^5 [Fig. 5(a)]. Applied to fermionic ^{173}Yb, we can achieve up to 1.2×10^5 [Fig. 5(b)] atoms in a mixture of the six spin states at $\frac{T}{T_F} = 0.3$. By reducing the loading and evaporative cooling sequence times, we can improve the repetition rate of Yb condensate production to 10 s, with (5×10^4)-atom Bose-Einstein condensates (BECs). Fast experimental repetition rates are crucial to precision measurements with BECs, which depend on large statistical data samples [19].

B. Weakly interacting quantum-degenerate Yb-Li mixture

For dual-species experiments in which Li is co-trapped and sympathetically cooled by Yb, the time-averaging option is not used as the accompanying reduction in trap depth is too great to efficiently load Li into the optical trap. As noted earlier, the larger polarizability of Li makes Yb a suitable sympathetic coolant. At the lowest temperatures, the large mass difference affects the standard procedure in two significant ways—the degeneracy temperatures for equal numbers are different by an order of magnitude, and the differential gravity-induced trap modification is relatively large.

By controlling the final depth of the evaporation ramp, we achieve simultaneous degeneracy, with similar atom numbers (few $\times 10^4$) of each species. The quantum-degenerate Yb-Li mixture at zero external magnetic field [Fig. 5(d)] is weakly interacting with interspecies scattering length of magnitude $13a_0$ [12,14,20]. In our system, $N_{\rm Li} \approx N_{\rm Yb}$ when the condensation temperature T_C is achieved. By this stage of the cooling the volume of the Li Fermi gas (constrained by Fermi degeneracy) is larger than that of the coolant Yb bosons. The reduction in size and heat capacity of the coolant, and the differential gravitational sag are all effects which can reduce the sympathetic cooling efficiency [14]. Further, we might expect a reduction in condensate number in the presence of Li, due to collisions between energetic Li atoms near the Fermi velocity $v_F \simeq 5$ cm/s and the Yb BEC (peak condensate speed of sound $v_c \simeq 1$ mm/s), which may explain the condensate number reduction reported in [20].

In spite of the aforementioned issues, sympathetic cooling can produce deeply degenerate Fermi gases in our apparatus. By sacrificing all of the coolant Yb through evaporation, temperatures below $0.1T_F$ can be achieved [Fig. 5(c)]. By keeping a small amount of Yb in the trap, we establish a system in which Yb may act as an impurity probe of the ^{6}Li degenerate Fermi gas.

C. Yb-Li mixtures in strongly interacting regimes

Two different regimes of strong interactions in the Yb-Li system are of current scientific interest. The first one is a three-component system of Yb and two resonantly interacting Li spin states, a regime recently explored experimentally by Khramov *et al.* [21]. Here studies of strongly interacting Fermi gases using Yb as a dissipative bath or an impurity probe may be carried out. While the strong interactions induce inelastic loss processes at unitarity, which are unobservable in the weakly interacting regime, the interspecies elastic processes still dominate and we have observed temperatures as low as $0.25T_F$.

The other strongly interacting regime of current interest is a Feshbach resonance between Yb and Li atoms. Theoretical calculations by Brue and Hutson [22], predict narrow magnetically induced Feshbach resonances between ^{173}Yb and ^{6}Li. These have not yet been experimentally observed.

A fundamental limiting factor in preserving interspecies contact in degenerate Yb-Li mixtures is the differential gravitational sag of the two species at low trap depths. In our trap, the Yb atoms, due to their greater mass and weaker optical confinement, become significantly displaced from the Li atoms at temperatures near 300 nK, compromising the efficiency of sympathetic cooling and generally the study of any interspecies interaction effects. A technique for circumventing this limitation is discussed in the following section.

V. CONTROL OF INTERSPECIES SPATIAL OVERLAP

Differences in internal properties between components of an ultracold mixture can result in a differential response to external fields. This sometimes leads to unwanted effects such as the differential vertical displacement due to gravity experienced in mixtures with unequal mass constituents. For the weak optical potentials needed to achieve the highest phase-space densities, this "gravitational sag" leads to reduced spatial overlap and reduced interspecies interactions. The differential gravitational sag is an important limiting factor for the molecule formation efficiency in the K-Rb mixture [23], where the mass ratio is 2.2. In the case of the Yb-Li mixture, where the mass ratio is 29, this effect is even more significant, leading to a nearly complete decoupling of the two species at the lowest temperatures [14]. Here we demonstrate that this differential gravitational sag can be mitigated by the use of a magnetic field gradient which exerts a force on only the lithium component.

In principle, one may use external magnetic fields to achieve independent control of any two atomic species. For instance, in alkali-metal atoms with half-integer nuclear spin there will exist states with magnetic projection $m_F = 0$ in the direction of the magnetic field, allowing one species to be made insensitive to magnetic gradients. However, this insensitivity does not extend to the high magnetic fields often required in experiments (e.g., to address Feshbach resonances) due to hyperfine decoupling. Furthermore, mixtures of high-field- and low-field-seeking atoms are prone to inelastic, internal state-changing collisions, which lead to trap losses.

Mixtures of alkali-metal and alkaline-earth-metal atoms avoid these limitations as the ground-state magnetic moment of the alkaline-earth-metal species is zero or nearly zero for all external fields. Furthermore, in isotopes with zero nuclear moment, spin-exchange collisions are suppressed entirely. This feature has been used to overlap clouds of magnetically trapped rubidium atoms with optically trapped ytterbium atoms [24]. Here we report on manipulating the relative displacement of two species that are confined in the same optical trapping potential, and over a large temperature range down to $<1\ \mu$K.

When atoms in a trap are subjected to a uniform force $F = mg$, the center of mass is displaced by an amount $\Delta z = g/\omega^2$, where ω is the vertical trapping frequency. Due to differences in mass and polarizability, the trap frequencies for Li and Yb differ by a factor of 8, leading to substantial differential gravitational sag at low trap depths.

We demonstrate control of interspecies spatial overlap by applying a magnetic gradient which acts as a "pseudogravitational" force on Li only. We first prepare a mixture of ^{6}Li in its two lowest-energy states and the single ground state of ^{174}Yb at a particular optical trap depth. For experimental simplicity, we ramp the bias field to 530 G, where the two Li spin states have equal magnetic moments $1\mu_B$ and negligible interaction strength. We then turn on our MOT coils to add a magnetic quadrupole field to the vertical bias field, thereby creating a magnetic force in the direction of the bias field. Our system is capable of producing vertical gradients up to 170 G/cm; however, a more modest gradient of 65 G/cm is sufficient to make the atom clouds concentric.

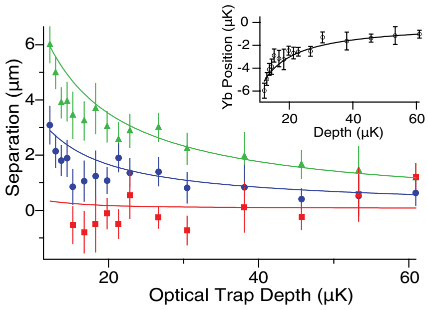

FIG. 6. (Color online) Relative displacement of centers of mass of Li and Yb clouds, versus optical trap depth for Yb atoms, at various magnetic gradients: −13 G/cm (filled triangles), 35 G/cm (filled circles), and 64 G/cm (filled squares). Each data point gives the average center-of-mass position of between 7 and 12 absorption images of lithium, subtracted from the average of 11 ytterbium images. The inset shows the displacement of Yb from the ODT beam center. The solid lines are results of a numerical model.

Figure 6 shows the separation of the cloud centers as a function of optical potential for different magnetic gradients. The gradient strength was determined by releasing the Li atoms and imaging them after a variable time to measure the acceleration $\mu_B B'/m_{\mathrm{Li}} + g$. The analysis also identified and corrected for slight ($<1^\circ$) deviations of the long trap axis from horizontal and the magnetic bias from vertical.

The lowest Yb optical trap depth for the data in Fig. 6 is 12 μK. Due to gravity, this corresponds to an effective trap depth of 4 μK, which goes to zero at an optical trap depth of 6 μK. We observe the onset of BEC at 15 μK optical depth when loading Yb alone.

At the lowest depths, the in-trap $1/e$ height of the ytterbium cloud is approximately 2 μm, whereas the Li cloud size is near the Fermi radius of 6 μm. Thus, in the absence of a magnetic gradient, the spatial overlap of the two clouds is critically reduced at trap depths below 20 μK.

Also shown in Fig. 6 is a set of theoretical curves of relative displacement, derived from a simple numerical model assuming a Gaussian trap profile. The only variable parameter in the model is the ODT (vertical) beam waist, which agrees at the 10% level with measurements of trap frequency via parametric excitation. We find reasonably good agreement between this model and the experimental data, although the calculation slightly overestimates the degree of sag at the lowest trap depths. One plausible explanation for this is a small vertical misalignment of the ODT beams, leading to a deviation from a Gaussian profile.

A side effect of this technique is that the applied gradient, while shifting the center of the trap, also effectively lowers the trap depth. Thus, for deeply degenerate Fermi clouds where the initial trap depth is close to the Fermi temperature, the "tilted" potential leads to spilling of Li atoms near the Fermi energy. This effect appears as a gradient-dependent Li number loss at the lowest depths (when $T \lesssim 0.1T_F$) in our experiment and has been utilized elsewhere to measure interaction strength in Fermi gases [25] and to accelerate evaporative cooling in Bose gases [26].

We also note that the field inhomogeneity introduced by the magnetic gradient can limit its usefulness in experiments that require extremely homogeneous magnetic fields. For instance, a gradient of 65 G/cm corresponds to a magnetic field variation of tens of milligauss across the sample, much larger than the theoretical width of the predicted magnetic Feshbach resonances between ^{173}Yb and ^{6}Li [22].

Species-selective control of atomic samples has also been demonstrated using only optical fields. Bichromatic optical traps exploiting the different ac Stark shifts of atoms have been demonstrated [24]. Our technique has the advantage of requiring no additional lasers or sensitive alignment of optics. The effect is achieved entirely with existing hardware, operating under typical conditions.

In addition to the application described above, the magnetic gradient technique enables experiments involving the use of one atomic species as a local probe of the other. In the ^{6}Li-^{174}Yb system, the Yb acts as a "bath" at temperatures above degeneracy, where its cloud is much larger than that of Li. At low temperatures, Yb can act as a "probe," since the Yb cloud is much smaller than the Li Fermi radius [21]. Under the latter conditions, Yb can be a useful probe for studying the local properties of a Fermi gas in the weakly interacting as well as in the superfluid regime.

Beyond spatial control, one can also use magnetic gradients to achieve selective control of the momentum of the magnetically sensitive species, by changing the gradient nonadiabatically. Such velocity-control techniques may be useful for a range of studies, such as measures of viscosity and tests of superfluidity.

VI. CONCLUSIONS AND OUTLOOK

We have presented a detailed description of our apparatus to produce stable quantum mixtures of lithium and ytterbium atoms. We have also demonstrated a method of controlling the spatial overlap of the two species, general to combinations of magnetic and nonmagnetic atoms. When prepared near the ^{6}Li Feshbach resonance, bosonic Yb can act as a microscopic probe of the strongly interacting lithium Fermi gas. Other future applications of the mixture include the study of condensed matter models in an optical lattice, such as the binary-alloy model.

An interspecies Feshbach resonance between lithium and ytterbium will allow the exploration of three-body Efimov states with large mass mismatch, and potential studies of the many-body physics of mass-imbalanced pairs. While such resonances have not yet been observed, they may show up in the near future in experiments with the ground-state mixture, or by using Yb in an excited metastable state (such as $^{3}P_{2}$) [27]. An additional possibility is an interspecies optical Feshbach resonance [28]. Finally, the quantum-degenerate mixture of lithium and ytterbium provides the starting point for the production of quantum gases of paramagnetic polar molecules of YbLi. Such ultracold molecules are of general interest from the perspective of quantum simulation [5], quantum information [29], tests of fundamental symmetries [30], and probes of time variations of physical constants [31].

ACKNOWLEDGMENTS

We thank Lee Willcockson and Ryan Weh for major technical contributions during the early stages of the experiment. This work was supported by the National Science Foundation, the Air Force Office of Scientific Research, the Alfred P. Sloan Foundation, the UW Royalty Research Fund, and NIST.

---

[1] L. D. Carr, D. DeMille, R. V. Krems, and J. Ye, New J. Phys. **11**, 055049 (2009).

[2] Z. Hadzibabic, C. A. Stan, K. Dieckmann, S. Gupta, M. W. Zwierlein, A. Görlitz, and W. Ketterle, Phys. Rev. Lett. **88**, 160401 (2002).

[3] C. Kohstall, M. Zaccanti, M. Jag, A. Trenkwalder, P. Massignan, G. M. Bruun, F. Schreck, and R. Grimm, Nature (London) **485**, 615 (2012).

[4] K.-K. Ni, S. Ospelkaus, M. H. G. de Miranda, A. Peer, B. Neyenhuis, J. J. Zirbel, S. Kotochigova, P. S. Julienne, D. S. Jin, and J. Ye, Science **322**, 231 (2008).

[5] A. Micheli, G. K. Brennen, and P. Zoller, Nat. Phys. **2**, 341 (2006).

[6] E. Braaten and H. W. Hammer, Phys. Rep. **428**, 259 (2006).

[7] C. Ates and K. Ziegler, Phys. Rev. A **71**, 063610 (2005).

[8] M. M. Maska, R. Lemanski, J. K. Freericks, and C. J. Williams, Phys. Rev. Lett. **101**, 060404 (2008).

[9] M. M. Maska, R. Lemanski, C. J. Williams, and J. K. Freericks, Phys. Rev. A **83**, 063631 (2011).

[10] C. A. Stan and W. Ketterle, Rev. Sci. Instrum. **76**, 063113 (2005).

[11] H. J. Metcalf and P. Van der Straten, *Laser Cooling and Trapping* (Springer, Berlin, 1999).

[12] V. V. Ivanov, A. Khramov, A. H. Hansen, W. H. Dowd, F. Münchow, A. O. Jamison, and S. Gupta, Phys. Rev. Lett. **106**, 153201 (2011).

[13] At the highest laser powers (>50 W), however, we have observed thermal lensing effects in various optical components in the ODT path.

[14] A. H. Hansen, A. Khramov, W. H. Dowd, A. O. Jamison, V. V. Ivanov, and S. Gupta, Phys. Rev. A **84**, 011606(R) (2011).

[15] A. Mosk, S. Kraft, M. Mudrich, K. Singer, W. Wohlleben, R. Grimm, and M. Weidemüller, Appl. Phys. B: Lasers Opt. **73**, 791 (2001).

[16] Three-body losses may then be the dominant loss mechanism, as in the ^{174}Yb-^{87}Rb mixture [17].

[17] F. Baumer, F. Münchow, A. Görlitz, S. E. Maxwell, P. S. Julienne, and E. Tiesinga, Phys. Rev. A **83**, 040702(R) (2011).

[18] K. Henderson, C. Ryu, C. MacCormick, and M. Boshier, New J. Phys. **11**, 043030 (2009).

[19] A. O. Jamison, J. N. Kutz, and S. Gupta, Phys. Rev. A **84**, 043643 (2011).

[20] H. Hara, Y. Takasu, Y. Yamaoka, J. M. Doyle, and Y. Takahashi, Phys. Rev. Lett. **106**, 205304 (2011).
[21] A. Y. Khramov, A. H. Hansen, A. O. Jamison, W. H. Dowd, and S. Gupta, Phys. Rev. A **86**, 032705 (2012).
[22] D. A. Brue and J. M. Hutson, Phys. Rev. Lett. **108**, 043201 (2012).
[23] J. J. Zirbel, K.-K. Ni, S. Ospelkaus, J. P. D'Incao, C. E. Wieman, J. Ye, and D. S. Jin, Phys. Rev. Lett. **100**, 143201 (2008).
[24] S. Tassy, N. Nemitz, F. Baumer, C. Höhl, A. Batar, and A. Görlitz, J. Phys. B **43**, 205309 (2010).
[25] S. Jochim, M. Barternstein, A. Altmeyer, G. Hendl, S. Riedl, C. Chin, J. Hecker Deschlag, and R. Grimm, Science **302**, 2101 (2003).
[26] C.-L. Hung, X. Zhang, N. Gemelke, and C. Chin, Phys. Rev. A **78**, 011604(R) (2008).
[27] S. Kato, S. Sugawa, K. Shibata, R. Yamamoto, and Y. Takahashi, arXiv:1210.2483.
[28] S. Blatt, T. L. Nicholson, B. J. Bloom, J. R. Williams, J. W. Thomsen, P. S. Julienne, and J. Ye, Phys. Rev. Lett. **107**, 073202 (2011).
[29] D. DeMille, Phys. Rev. Lett. **88**, 067901 (2002).
[30] J. J. Hudson, D. M. Kara, I. J. Smallman, B. E. Sauer, M. R. Tarbutt, and E. A. Hinds, Nature (London) **473**, 493 (2011).
[31] M. Kajita, G. Gopakumar, M. Abe, and M. Hada, Phys. Rev. A **84**, 022507 (2011).

Appendix E

ULTRACOLD HETERONUCLEAR MIXTURE OF GROUND AND EXCITED STATE ATOMS

Ultracold Heteronuclear Mixture of Ground and Excited State Atoms

Alexander Khramov,[1] Anders Hansen,[1] William Dowd,[1] Richard Roy,[1] Constantinos Makrides,[2] Alexander Petrov,[2,3] Svetlana Kotochigova,[2] and Subhadeep Gupta[1]

[1]*Department of Physics, University of Washington, Seattle WA 98195, USA*
[2]*Department of Physics, Temple University, Philadelphia PA 19122, USA*
[3]*St. Petersburg Nuclear Physics Institute, Gatchina, 188300; Division of Quantum Mechanics, St. Petersburg State University, 198904, Russia*

(Dated: September 29, 2013)

We report on the realization of an ultracold mixture of lithium atoms in the ground state and ytterbium atoms in the excited metastable ($^3P_2$) state. Such a mixture can support broad magnetic Feshbach resonances which may be utilized for the production of ultracold molecules with an electronic spin degree of freedom, as well as novel Efimov trimers. We investigate the interaction properties of the mixture in the presence of an external magnetic field and find an upper limit for the background interspecies two-body inelastic decay coefficient of $K_2' < 3\times10^{-12}\text{cm}^3/\text{s}$ for the $^3P_2$ $m_J = -1$ substate. We calculate the dynamic polarizabilities of the Yb($^3P_2$) magnetic substates for a range of wavelengths, and find good agreement with our measurements at 1064 nm. Our calculations also allow the identification of magic frequencies where Yb ground and metastable states are identically trapped and the determination of the interspecies van der Waals coefficients.

Ultracold elemental mixtures provide unique opportunities to study few- and many-body physics with mass-mismatched atomic partners [1] and diatomic polar molecules [2, 3]. While the bulk of elemental mixture experiments have been performed using ground-state bi-alkali systems, the recent production of ground state mixtures of alkali and alkaline-earth-like atoms [4–7] further extend the experimental possibilities. These include powerful quantum simulation and information protocols [8] and tests of fundamental symmetries [9] with paramagnetic polar molecules. While tunable two-body interactions that are important for these advances have been proposed in such mixtures [10], they have not yet been experimentally detected.

In this work we realize a new class of heteronuclear mixtures in which one atomic component is in an electronically excited state, using lithium (^{6}Li) and ytterbium (^{174}Yb) atoms. This establishes a highly mass-mismatched atomic mixture where tunable anisotropic interactions are expected to play a strong role [11], laying a foundation for future studies of ultracold trapped paramagnetic polar molecules and Efimov trimers with very large mass imbalance [12]. We measure inelastic interactions in the mixture and observe the relative suppression of interspecies inelastic processes. Our experimental methods also demonstrate new techniques of production and coherent manipulation of spin components in the metastable $^3P_2$ state of Yb.

The study and control of anisotropic interactions is an increasingly important topic in ultracold atomic systems. In addition to their impact on many-body physics [3, 8, 13], anisotropic two-body interactions are proving to be of great interest for generating magnetically tunable interactions, as has been calculated theoretically [14] and observed experimentally in a mixture of ground and excited state Yb atoms [15]. The latter result applied in the context of the Li+Yb combination takes on added significance as the ground state Feshbach resonances are predicted to be extremely narrow [16] and experimentally difficult to access.

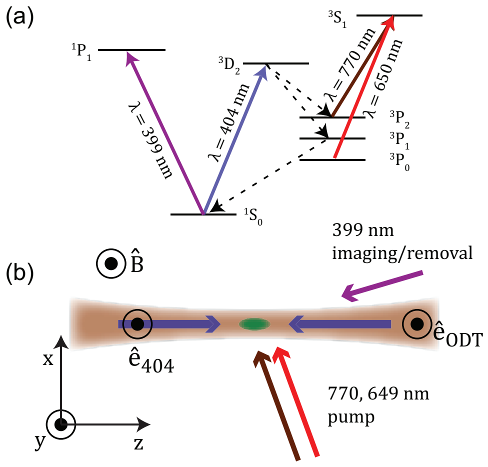

FIG. 1: (Color online). Yb* preparation and detection scheme. (a) Low-lying energy levels of ytterbium with solid (dashed) lines indicating the relevant laser excitation (spontaneous decay) processes. (b) Top-down view of experimental setup. Two counter-propagating 404 nm excitation beams (blue arrows) are overlapped with the ODT (brown). The polarizations of all three beams are vertical, parallel to the external magnetic field **B**. Laser beams at 649 and 770 nm (red, brown arrows) pump atoms back to the ground state prior to absorption imaging using the 399 nm beam (purple arrow).

An important component of the work reported here is the successful trapping of Yb atoms in the $^3P_2$ state

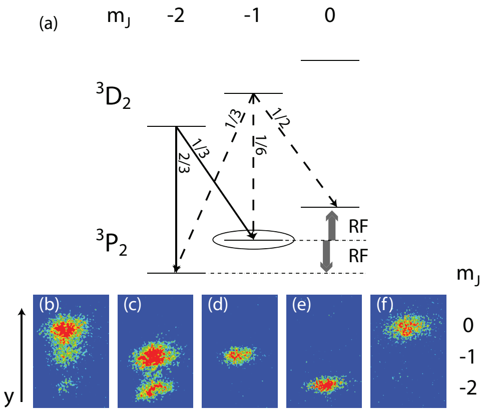

FIG. 2: (Color online). Yb* state preparation. (a) A particular magnetic substate of $^3D_2$ can be resolved via Zeeman splitting and selectively excited with 404 nm light. This state will subsequently spontaneously decay to substates in the $^3P_2$ manifold according to the indicated branching ratios. Radio frequency transitions within the $^3P_2$ manifold are spectroscopically resolved due to the state-dependent Stark shifts in the 1064 nm ODT. (b)-(f) Absorption images of different $^3P_2$ spin compositions after Stern-Gerlach separation. The images correspond to: (b) transfer via the $^3D_2$ $m_J = -1$ substate; (c) transfer via the $^3D_2$ $m_J = -2$ substate; (d) transfer via $^3D_2$ $m_J = -2$ substate with an applied in-trap gradient to obtain a pure sample of $^3P_2$ $m_J = -1$ atoms; (e) and (f) are the same as (d), followed by RF π-pulse transfer to $m_J = -2$ and $m_J = 0$, respectively, of the $^3P_2$ manifold. The RF pulses in (e,f) are 300 μs long with frequencies close to the Zeeman splitting of 26 MHz but separated by 430 kHz due to the state-dependent Stark shift.

(Yb*) in a 1064nm optical dipole trap (ODT), where Li atoms can be co-trapped. Our scheme for preparation and detection of Yb* is similar to an earlier one that was used to populate a spin mixture of Yb* in a 532 nm ODT [17] but is modified to produce pure spin states in a 1064 nm trap at an arbitrary external magnetic field. We confine ground state Yb atoms in a horizontally-oriented single-beam ODT and evaporatively cool them to the microkelvin regime. We then produce the Yb* state by optical pumping (see Fig.1) using the $^1S_0 \rightarrow {}^3D_2$ electric quadrupole transition at 404 nm [18]. With this setup [19], we can achieve a $^1S_0 \rightarrow {}^3P_2$ pumping rate of up to 50 Hz per atom. Remaining ground state atoms are removed with 399 nm light. Yb* atoms are detected by transferring them back to the ground $^1S_0$ state using light at 770/649 nm immediately prior to absorption imaging on the 399 nm transition. Further details can be found in the supplemental material.

Our method of preparing pure spin states of Yb* takes advantage of dipole selection rules and differential Stark shifts between spin states. By using an external magnetic field, we spectrally resolve magnetic substates within the $^3D_2$ manifold, from which the atoms decay into $^3P_2$ (see Fig.2(a)). The resultant population in a particular spin state of $^3P_2$ is determined by a combination of the branching ratio for spontaneous emission into that state and potential atom loss due to a trap depth reduction from the state dependent polarizability. We determine the spin composition of our trapped Yb* samples using the Stern-Gerlach technique (see Fig. 2(b-f)) to spatially separate the states during expansion from the trap. The initial composition of atoms trapped in $^3P_2$ from an excitation to the $^3D_2$ $m_J = -1\,(-2)$ state is shown in Fig.2(b(c)). For our trap, the $^3P_2$ $m_J = -2$ is very weakly trapped compared to the $^3P_2$ $m_J = -1$ state, leading to a substantial, ODT beam power-dependent loss of $m_J = -2$ atoms due to gravitational spilling. By reducing ODT power and applying a vertical magnetic gradient field during the 404 nm exposure, we can make this state un-trapped. We thus obtain a pure sample of $m_J = -1$ Yb* atoms (Fig.2(d)). By applying a transverse radiofrequency (RF) magnetic field, we can coherently drive transitions to other m_J states of Yb*. Taking advantage of the spectroscopic resolution created by the differential Stark shift of neighboring states, we obtain pure samples of either $m_J = -2$ or 0 using RF π-pulses (Fig.2(e,f)) [20].

The relevant property for controlling a particular atomic state in an optical trap is its dynamic polarizability $\alpha(\omega, \vec{\epsilon})$, a function of radiation frequency ω and polarization $\vec{\epsilon}$. The polarizability of each of the $^1S_0$ ground and $^3P_2$ metastable states of Yb is determined by the dipole couplings to all other atomic states [21]. We calculate the polarizability from a combination of experimental transition frequencies and oscillator strengths between atomic levels available from the literature [22] and additional theoretical calculations of these characteristics for other transitions using a relativistic multiconfiguration Dirac-Fock-Sturm method, described in [23]. Figure 3(a) shows the resulting polarizability as a function of laser frequency of light linearly polarized parallel to the quantization axis for ground state Yb and the five magnetic sublevels $m_J = 0, \pm 1$, and ± 2 of Yb*. The polarizability is singular at atomic transition energies and strongly depends on the absolute value of m_J. In fact, it has opposite sign for different m_J over significant ranges of frequencies. The intersections of ground and excited state curves in Fig. 3 indicate magic wavelengths for ultra-narrow optical transitions. We find good agreement with earlier measurements at 532 nm [24]. The transition frequencies and oscillator strengths used in calculating the dynamic polarizability also enable us to construct both relativistic and non-relativistic van der Waals C_6 coefficients for the Yb*+Yb* and Yb*+Li collision systems. A more detailed description of this procedure is given in the supplemental material. From these we determine the p-wave threshold for two-body collisions to be 24 μK and 2.1 mK, respectively.

We experimentally determine polarizabilities at 1064

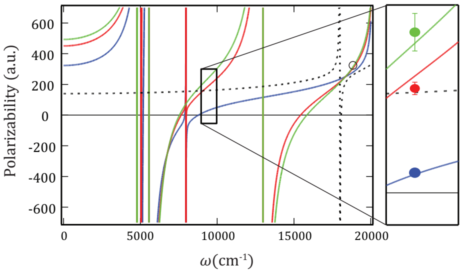

FIG. 3: (Color online). Calculated dynamic polarizability of Yb* as a function of frequency of light polarized parallel to the quantization axis. Blue, red and green solid lines correspond to the $|m_J|$ =0, 1, and 2 substates respectively and the dashed line to the ground state. Open circle indicates measurements of the ac polarizability at 532 nm [24]. Our polarizability ratio measurements at 1064 nm, scaled to the $^1S_0$ value, are shown as solid circles in inset.

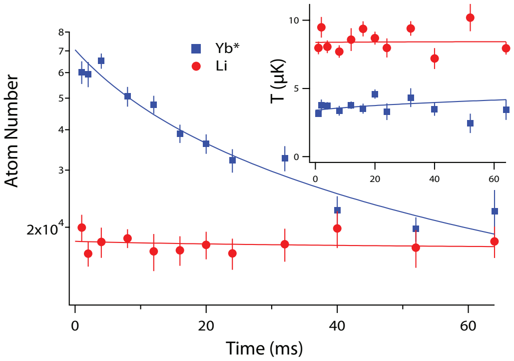

FIG. 4: (Color online). Number and temperature (inset) evolution of Yb* and Li in the ODT at an external magnetic field of 12 G. Lines show fits based on a model including two-body inelastic effects (see text).

nm to compare to our calculated values. We measure the trap frequencies of the $m_J = 0$, -1 and -2 substates and compare to an identical measurement for the ground $^1S_0$ state. The trap frequencies were measured by observing the oscillation of cloud size (breathing mode) following a diabatic increase in trap depth. These values were also verified by using the parametric excitation technique. The experimentally obtained polarizability ratios are $\alpha_{-1}/\alpha_g = 1.04(6)$, $\alpha_0/\alpha_g = 1.6(2)$, and $\alpha_{-2}/\alpha_g = 0.20(2)$. These agree well with our theoretically calculated ratios (see inset of Fig.3).

With the facility to produce, manipulate, and detect Yb* added to our Li-Yb apparatus [5, 25], we investigate the mixture of Yb* and Li. For this work, we focus on a mixture of the lowest hyperfine state of ^{6}Li (denoted $|1\rangle$) and the $m_J = -1$ state of Yb*. Starting with such an optically trapped and cooled mixture of Yb ($^1S_0$) and Li ($|1\rangle$), we change the magnetic field to a desired value and prepare the $m_J = -1$ state of Yb* as discussed above [19]. We subsequently compress the trap in order to suppress atom loss due to evaporation and to improve interspecies spatial overlap against differential gravitational sag. Further details can be found in the supplemental material.

The number and temperature evolution of an Yb*+Li mixture prepared in this way at an external magnetic field of 12 G is shown in Fig.4. The initial temperature difference between the species is due to thermal decoupling at the lowest trap depths [5, 19] and is a useful starting point to monitor elastic interspecies interactions. One-body effects from background atoms and off-resonant scattering from ODT photons are negligible on the timescale of the experiment. Since our lithium component is a single state fermion deep in the s-wave regime [26], the Li-Li interactions are negligible for our parameters. From our calculated values for the $p-$wave threshold for two-body collisions in the Yb*+Yb* and Yb*+Li systems, we infer that all two-body interactions are s-wave dominated. For the starting peak density of $n_{\mathrm{Yb^*(Li)}} = 5.3(1.2) \times 10^{12}\,\mathrm{cm}^{-3}$ and large evaporation parameter $\eta_{\mathrm{Yb^*(Li)}} = U_{\mathrm{Yb^*(Li)}}/k_B T_{\mathrm{Yb^*(Li)}} = 24(20)$, it is reasonable to expect that all number losses result from two-body inelastic processes. We observe that the system retains its initial temperature disparity throughout the timescale of the experiment. This suggests that interspecies $s-$wave elastic collisions play a negligible part in the system dynamics.

A striking feature of Fig. 4 is the stability of the Li number on the timescale of Yb* decay, suggesting a dominance of inelastic effects from Yb*+Yb* collisions over Li+Yb* collisions. We model the atomic densities with the coupled differential equations

$$\begin{aligned} \dot{n}_{\mathrm{Yb^*}} &= -K_2' n_{\mathrm{Li}} n_{\mathrm{Yb^*}} - K_2 n_{\mathrm{Yb^*}}^2 \qquad (1) \\ \dot{n}_{\mathrm{Li}} &= -K_2' n_{\mathrm{Li}} n_{\mathrm{Yb^*}} \qquad (2) \end{aligned}$$

where $n_{\mathrm{Yb^*(Li)}}$ and $K_2(K_2')$ are the densities of Yb*(Li) and the (volume-independent) two-body decay coefficients of Yb*-Yb*(Yb*-Li). The temperature evolution is given by the heating from the density-dependence of the inelastic processes which favor atom loss from near the trap center [27]. Best-fits with this model (solid lines in Fig 4(b)) yield $K_2 = 2.5 \times 10^{-11}\,\mathrm{cm}^3/\mathrm{s}$, and K_2' consistent with zero [28]. The estimated statistical error provides an upper bound of $K_2' < 3 \times 10^{-12}\mathrm{cm}^3/\mathrm{s}$. By considering the elastic cross-section needed for interspecies thermalization on the experimental timescale, we can also place an upper bound of $300\,a_0$ on the magnitude of the interspecies $s-$wave scattering length. Here a_0 is the Bohr radius.

Our study of interspecies interactions can be extended to arbitrary values of the external magnetic field and also to different magnetic substates of Yb* using the methods described above. Repeating the above experiment at 94 G we observe a similarly long lifetime of Li atoms in the presence of Yb*. These low values of background interspecies inelastic rates bode well for future searches for Feshbach resonances between spin-polarized samples of Yb* and Li, where interspecies inelastic rates should be resonantly enhanced and could be observed by monitoring the Li population as a function of magnetic field. By working in an optical lattice and/or using a fermionic Yb isotope, the inelastic effects of Yb*+Yb* collisions may be suppressed, allowing for a more precise investigation of interspecies phenomena in the mixture. We note that complementary theoretical work has already been initiated [11, 29].

In conclusion, we produced spin polarized samples of ytterbium atoms in the $^3P_2$ (Yb*) state in a 1064 nm ODT. Our demonstrated method to coherently manipulate the spin state of Yb* is extendable to production of arbitrary spin superpositions within the $^3P_2$ manifold and could be applicable towards quantum information schemes reliant on the long-range magnetic dipole-dipole interaction [30]. We measured the dynamic polarizabilities of different spin substates and found good agreement with our calculated theoretical values. These calculations also identify magic wavelength points of relevance for potential optical clock transitions between ground and long-lived metastable ($^3P_2$) states of Yb [31, 32]. We cotrapped lithium with metastable ytterbium and investigated the interaction properties of the mixture at large magnetic fields. We found a dominance of intraspecies inelastic effects over interspecies ones. Possible applications of this mixture include investigations of universal few-body physics [12] and the synthesis of ultracold paramagnetic polar molecules for quantum simulation [8] and tests of fundamental symmetries [9].

We thank J.M. Hutson, P.S. Julienne and Y. Takahashi for useful discussions. We gratefully acknowledge funding from NSF grants PHY-1308573, PHY-0847776, PHY-1306647, AFOSR grant FA9550-12-10051 and ARO MURI grant W911NF-12-1-0476.

[1] C. Kohstall, M. Zaccanti, M. Jag, A. Trenkwalder, P. Massignan, G. Bruun, F. Schreck, and R. Grimm, Nature **485**, 615 (2012).

[2] K.-K. Ni, S. Ospelkaus, D. Wang, G. Quemener, B. Neyenhuis, M. H. G. de Miranda, J. Bohn, J. Ye, and D. Jin, Nature **464**, 1324 (2010).

[3] B. Yan, S. Moses, B. Gadway, J. Covey, K. Hazzard, A. Rey, D. Jin, and J. Ye, arXiv:1305.5598 (2013).

[4] N. Nemitz, F. Baumer, F. Münchow, S. Tassy, and A. Görlitz, Phys Rev A (R) **79**, 061403 (2009).

[5] V. V. Ivanov, A. Khramov, A. H. Hansen, W. H. Dowd, F. Münchow, A. O. Jamison, and S. Gupta, Phys. Rev. Lett. **106**, 153201 (2011).

[6] H. Hara, Y. Takasu, Y. Yamaoka, J. M. Doyle, and Y. Takahashi, Phys. Rev. Lett. **106**, 205304 (2011).

[7] B. Pasquiou, A. Bayerle, S. M. Tzanova, S. Stellmer, J. Szczepkowski, M. Parigger, R. Grimm, and F. Schreck, Phys Rev A **88**, 023601 (2013).

[8] A. Micheli, G. K. Brennen, and P. Zoller, Nature Physics **2**, 341 (2006).

[9] J. J. Hudson, D. M. Kara, I. J. Smallman, B. E. Sauer, M. R. Tarbutt, and E. A. Hinds, Nature **473**, 493 (2011).

[10] P. S. Zuchowski, J. Aldegunde, and J. M. Hutson, Phys. Rev. Lett. **105**, 153201 (2010).

[11] M. L. Gonzalez-Martinez and J. M. Hutson, Phys. Rev. A **88**, 020701(R) (2013).

[12] E. Braaten and H. W. Hammer, Phys Rep **428**, 259 (2006).

[13] T. Lahaye, C. Menotti, L. Santos, M. Lewenstein, and T. Pfau, Rep. Prog. Phys. **72**, 1 (2009).

[14] A. Petrov, E. Tiesinga, and S. Kotochigova, Phys. Rev. Lett. **109**, 103002 (2012).

[15] S. Kato, S. Sugawa, K. Shibata, R. Yamamoto, and Y. Takahashi, Phys Rev Lett **110**, 173201 (2013).

[16] D. A. Brue and J. M. Hutson, Phys. Rev. Lett. **108**, 043201 (2012).

[17] A. Yamaguchi, S. Uetake, D. Hashimoto, J. M. Doyle, and Y. Takahashi, Phys. Rev. Lett. **101**, 233002 (2008).

[18] C. J. Bowers, D. Budker, S. J. Freedman, G. Gwinner, J. E. Stalnaker, and D. DeMille, Phys. Rev. A **59**, 3513 (1999).

[19] See supplemental material for this paper.

[20] Another method to achieve pure spin states in Yb* has been shown earlier [33], but relies on the availablity of an ultra-narrow laser.

[21] S. Kotochigova and E. Tiesinga, Phys. Rev. A. **73**, 041405(R) (2006).

[22] Y. Ralchenko, A. Kramida, J. Reader, and N. A. Team, NIST Atomic Spectra Database. Available: at http://physics.nist.gov/asd. (2011).

[23] S. Kotochigova, K. P. Kirby, and I. Tupitsyn, Phys. Rev. A. **76**, 052513 (2007).

[24] A. Yamaguchi, S. Uetake, S. Kato, H. Ito, and Y. Takahashi, New J. Phys. **12**, 103001 (2010).

[25] A. H. Hansen, A. Y. Khramov, W. H. Dowd, A. O. Jamison, B. Plotkin-Swing, R. J. Roy, and S. Gupta, Phys. Rev. A. **87**, 013615 (2013).

[26] Z.-C. Yan, J. F. Babb, A. Dalgarno, and G. W. F. Drake, Phys. Rev. A **54**, 2824 (1996).

[27] T. Weber, J. Herbig, M. Mark, H.-C. Nagerl, and R. Grimm, Phys. Rev. Lett. **91**, 123201 (2003).

[28] By fitting the Yb* number according to $\dot{n}_{\mathrm{Yb}^*} = -K_2 n^2_{\mathrm{Yb}^*}$ at the average temperature of $3.6\,\mu$K, we obtain the value of $K_2 = 2.6 \times 10^{-11}\,\mathrm{cm}^3/\mathrm{s}$.

[29] In progress by some of us (C.M., A.P., S.K).

[30] A. Derevianko and C. C. Cannon, Phys. Rev. A **70**, 062319 (2004).

[31] J. Hall, M. Zhu, and P. Buch, Journal of the Optical Society of America, B **6**, 2194 (1989).

[32] N. D. Lemke, A. D. Ludlow, Z. W. Barber, T. M. Fortier, S. A. Diddams, Y. Jiang, S. R. Jefferts, T. P. Heavner, T. E. Parker, and C. W. Oates, Phys. Rev. Lett. **103**, 063001 (2009).

[33] S. Uetake, R. Murakami, J. M. Doyle, and Y. Takahashi, Phys. Rev. A **86**, 032712 (2012).

BIBLIOGRAPHY

[1] E. R. I. Abraham, N. W. M. Ritchie, W. I. McAlexander, and R. G. Hulet. Photoassociative spectroscopy of long-range states of ultracold $^6\mathrm{Li}_2$ and $^7\mathrm{Li}_2$. *J. Chem. Phys.*, 103:7773, 1995.

[2] K. Aikawa, A. Frisch, M. Mark, S. Baier, A. Rietzler, R. Grimm, and F. Ferlaino. Bose-Einstein condensation of erbium. *Phys. Rev. Lett.*, 108:210401, 2012.

[3] M. H. Anderson, J. R. Ensher, M. R. Matthews, C. E. Wieman, and E. A. Cornell. Observation of Bose-Einstein condensation in a dilute atomic vapor. *Science*, 269:198, 1995.

[4] J.F. Barry, E.S. Shuman, E.B. Norrgard, and D. DeMille. Laser radiation pressure slowing of a molecular beam. *Phys. Rev. Lett*, 108:103002, 2012.

[5] M. Bartenstein, A. Altmeyer, S. Riedl, R. Geursen, S. Jochim, C. Chin, J. Hecler Denschlag, R. Grimm, A. Simoni, E. Tiesinga, C.J. Williams, and P.S. Julienne. Precise determination of ^{6}Li cold collision parameters by radio-frequency spectroscopy on weakly bound states. *Phys. Rev. Lett*, 94:103201, 2005.

[6] M. Bartenstein, A. Altmeyer, S. Riedl, S. Jochim, C. Chin, J. Hecker Denschlag, and R. Grimm. Crossover from a molecular Bose-Einstein condensate to a degenerate Fermi gas. *Phys. Rev. Lett*, 92:120401, 2004.

[7] K.P. Birch and M.J. Downs. An updated Edlén equation for the refractive index of air. *Metrologia*, 30:155, 1993.

[8] I. Bloch, J. Dalibard, and S. Nascimbène. Quantum simulations with ultracold quantum gases. *Nature Phys.*, 8:267–276, 2012.

[9] J.L. Bohn and P.S. Julienne. Semianalytic theory of laser-assisted resonant cold collisions. *Phys. Rev. A*, 60:414, 1999.

[10] C. C. Bradley, C. A. Sackett, and R. G. Hulet. Bose-Einstein condensation of lithium: Observation of limited condensate number. *Phys. Rev. Lett.*, 78:985, 1997.

[11] C. C. Bradley, C. A. Sackett, J.J. Tollett, and R. G. Hulet. Evidence of Bose-Einstein condensation in an atomic gas with attractive interactions. *Phys. Rev. Lett.*, 75:1687, 1995.

[12] J.M. Brown and A. Carrington. *Rotational spectroscopy of diatomic molecules.* Cambridge University Press, 2003.

[13] D.A. Brue and J.M. Hutson. Magnetically tunable Feshbach resonances in ultracold Li-Yb mixtures. *Phys. Rev. Lett.*, 108:043201, 2012.

[14] A. Carrington, C.H. Pyne, A.M. Shaw, S.M. Taylor, J.M. Hutson, and M.M. Law. Microwave spectroscopy and interaction potential of the long-range He-Kr^+ ion: an example of Hund's case (e). *J. Chem. Phys.*, 105:8602, 1996.

[15] Ananth Chikkatur. *Colliding and moving Bose-Einstein condensates.* PhD thesis, MIT, 2002.

[16] C. Chin and R. Grimm. Thermal equilibrium and efficient evaporation of an ultracold atom-molecule mixture. *Phys. Rev. A*, 69:033612, 2004.

[17] C. Chin, R. Grimm, P. S. Julienne, and E. Tiesinga. Feshbach resonances in ultracold gases. *Rev. Mod. Phys.*, 82:1225, 2010.

[18] R. Ciurylo, E. Tiesinga, and P. S. Julienne. Optical tuning of the scattering length of cold alkaline-earth-metal atoms. *Phys. Rev. A*, 71:030701(R), 2005.

[19] C. Cohen-Tannoudji and D. Guéry-Odelin. *Advances in Atomic Physics.* World Scientific Publishing Co., 2011.

[20] A.D. Cronin, J. Schmiedmayer, and D.E. Pritchard. Optics and interferometry with atoms and molecules. *Rev. Mod. Phys.*, 81:1051, 2009.

[21] J. Cubizolles, T. Bourdel, S. J. J. M. F. Kokkelmans, G. V. Shlyapnikov, and C. Salomon. Production of long-lived ultracold Li_2 molecules from a Fermi gas. *Phys. Rev. Lett.*, 91:240401, 2003.

[22] J. Cuevas, P.G. Keverekidis, B.A. Malomed, P. Dyke, and R.G. Hulet. Interactions of solitons with a Gaussian barrier: splitting and recombination in quasi-1Dand 3D. *New J. Phys.*, 15:063006, 2013.

[23] K. B. Davis, M.-O. Mewes, M. R. Andrews, N. J. van Druten, D. S. Durfee, D. M. Kurn, and W. Ketterle. Bose-Einstein condensation in a gas of sodium atoms. *Phys. Rev. Lett.*, 75:(22):3969, 1995.

[24] M.H.G. de Miranda, A. Chotia, B. Neyenhuis, D. Wang, G. Quéméner, S. Ospelkaus, J.L. Bohn, J. Ye, and D.S. Jin. Controlling the quantum stereodynamics of ultracold bimolecular reactions. *Nature Phys.*, 7:502, 2011.

[25] B. Deh, C. Marzok, C. Zimmermann, and Ph. W. Courteille. Feshbach resonances in mixtures of ultracold ^{6}Li and ^{87}Rb gases. *Phys Rev A*, 77:010701(R), 2008.

[26] J. Deiglmayr, A. Grochola, M. Repp, K. Mortlbauer, C. Gluck, J. Lange, O. Dulieu, R. Wester, and M. Weidemuller. Formation of ultracold polar molecules in the rovibrational ground state. *Phys. Rev. Lett.*, 101:133004, 2008.

[27] B. DeMarco and D. S. Jin. Onset of Fermi degeneracy in a trapped atomic gas. *Science*, 285:1703, 1999.

[28] D. DeMille. Quantum computation with trapped polar molecules. *Phys. Rev. Lett.*, 88:067901, 2002.

[29] K. Dieckmann, C. A. Stan, S. Gupta, Z. Hadzibabic, C. H. Schunck, and W. Ketterle. Decay of an ultracold fermionic lithium gas near a Feshbach resonance. *Phys. Rev. Lett.*, 89:203201, 2002.

[30] J. P. D'Incão and B. D. Esry. Scattering length scaling laws for ultracold three-body collisions. *Phys. Rev. Lett.*, 94:213201, 2005.

[31] J. P. D'Incão and B. D. Esry. Suppression of molecular decay in ultracold gases without Fermi statistics. *Phys. Rev. Lett.*, 100:163201, 2008.

[32] P.M. Duarte, R.A. Hart, J.M. Hitchcock, T.A. Corcovilos, T.-L. Yang, A. Reed, and R.G. Hulet. All-optical production of a lithium quantum gas using narrow-line laser cooling. *Phys. Rev. A*, 84:061406.

[33] C.J. Foot. *Atomic Physics.* Oxford University Press, 2005.

[34] M. Foss-Feig, M. Hermele, and A.M. Rey. Probing the Kondo lattice model with alkaline-earth-metal atoms. *Phys. Rev. A*, 81:051603(R), 2010.

[35] T. Fukuhara, S. Sugawa, and Y. Takahashi. Bose-Einstein condensation of an ytterbium isotope. *Phys. Rev. A*, 76:051604(R), 2007.

[36] T. Fukuhara, S. Sugawa, Y. Takasu, and Y. Takahashi. All-optical formation of quantum degenerate mixtures. *Phys. Rev. A*, 79:021601(R), 2009.

[37] T. Fukuhara, Y. Takasu, M. Kumakura, and Y. Takahashi. Degenerate Fermi gases of ytterbium. *Phys. Rev. Lett.*, 98:030401, 2007.

[38] M. E. Gehm. *Preparation of an optically trapped degenerate Fermi gas of ^{6}Li: Finding the route to degeneracy.* PhD thesis, Duke University, 2003.

[39] M.L. González-Martínez and J.M. Hutson. Magnetically tunable Feshbach resonances in Li + Yb ($^3\mathrm{P_J}$). *Phys. Rev. A*, 88:020701(R), 2013.

[40] G. Gopakumar, M. Abe, B.P. Das, M. Hada, and K. Hirao. Relativistic calculations of ground and excited statesof liyb molecule for ultracold photo association spectroscopy studies. *J. Phys. Chem.*, 133:124317, 2010.

[41] A.V. Gorshkov, M. Hermele, V. Gurarie, C. Xu, P.S. Julienne, J. Ye, P. Zoller, E. Demler, M.D. Lukin, and A.M. Rey. Two-orbital SU(N) magnetism with ultracold alkaline-earth atoms. *Nature Phys.*, 6:289, 2010.

[42] W. Greiner, L. Neise, and H. Stöcker. *Thermodynamics and Statistical Mechancis.* Springer-Verlag New York, Inc., 1995.

[43] G.F. Gribakin and V.V. Flambaum. Calculation of the scattering length in atomic collisions using the semiclassical approximation. *Phys. Rev. A*, 48:546, 1993.

[44] A.T. Grier, I. Ferrier-Barbut, B.S. Rem, M. Delahaye, L. Khaykovich, F. Chevy, and C. Salomon. Lambda-enhanced sub-Doppler cooling of lithium atoms in $\mathrm{D_1}$ gray molasses. *Phys. Rev. A*, 87:063411, 2013.

[45] J. Grünert and A. Hemmerich. A sub-Doppler magneto-optical trap for calcium. *Phys. Rev. A*, 65:041401(R), 2005.

[46] Z. Hadzibabic, C. A. Stan, K. Dieckmann, S. Gupta, M. W. Zwierlein, A. Görlitz, and W. Ketterle. Two-species mixture of quantum degenerate Bose and Fermi gases. *Phys. Rev. Lett.*, 88:160401, 2002.

[47] C. Haimberger, J. Kleinert, M. Bhattacharya, and N. P. Bigelow. Formation and detection of ultracold ground-state polar molecules. *Phys. Rev. A.*, 70:021402, 2004.

[48] P. Hamilton, G. Kim, T. Joshi, B. Mukherjee, D. Tiarks, and H. Müller. Sisyphus cooling of lithium. *arXiv:1308.1935*, 2013.

[49] A. H. Hansen, A. Khramov, W. H. Dowd, A. O. Jamison, V. V. Ivanov, and S. Gupta. Quantum degenerate mixture of ytterbium and lithium atoms. *Phys. Rev. A.*, 84:011606(R), 2011.

[50] A. H. Hansen, A. Y. Khramov, W. H. Dowd, A. O. Jamison, B. Plotkin-Swing, R. J. Roy, and S. Gupta. Production of quantum-degenerate mixtures of ytterbium and lithium with controllable interspecies overlap. *Phys. Rev. A.*, 87:013615, 2012.

[51] A.H.H. Hansen. *Interacting Quantum Gases of Lithium and Ytterbium.* PhD thesis, University of Washington, 2013.

[52] D. Hansen and A. Hemmerich. Observation of multichannel collisions of cold metastable calcium atoms. *Phys. Rev. Lett.*, 96:073003, 2006.

[53] H. Hara, Y. Takasu, Y. Yamaoka, J.M. Doyle, and Y. Takahashi. Quantum degenerate mixtures of alkali and alkaline-earth-like atoms. *Phys. Rev. Lett.*, 106:205304, 2011.

[54] J Heinze, S Götze, J.S. Krauser, B. Hundt, N. Fläschner, D.-S. Lühmann, C. Becker, and K. Sengstock. Multiband spectroscopy of ulstracold fermions: observation of reduced tunneling in attractive Bose-Fermi mixtures. *Phys. Rev. Lett.*, 107:135303, 2011.

[55] N. Hinkley, J.A. Sherman, N.B. Phillips, M. Schioppo, N.D. Lemke, K. Beloy, M. Pizzocaro, C.W. Oates, and A.D. Ludlow. An atomic clock with 10^{-18} instability. *Science*, 341:1215, 2013.

[56] K. Honda, Y. Takahashi, T. Kuwamoto, M. Fujimoto, K. Toyoda, K. Ishikawa, and T. Yabuzaki. Magneto-optical trapping of Yb atoms and a limit on the branching ratio of the $^1\mathrm{P}_1$ state. *Phys. Rev. A*, 59:R934, 1999.

[57] J. J. Hudson, B. E. Sauer, M. R. Tarbutt, and E. A. Hinds. Measurement of the electron electric dipole moment using ybf molecules. *Phys. Rev. Lett.*, 89:023003, 2002.

[58] M.T. Hummon, M. Yeo, B.K. Stuhl, A.L. Collopy, Y. Xia, and J. Ye. 2D magneto-optical trapping of diatomic molecules. *Phys. Rev. Lett.*, 110:143001, 2013.

[59] V. V. Ivanov, A. Khramov, A. H. Hansen, W. H. Dowd, F. Münchow, A. O. Jamison, and S. Gupta. Sympathetic cooling in an optically trapped mixture of alkali and spin-singlet atoms. *Phys. Rev. Lett.*, 106:153201, 2011.

[60] L.M.C. Janssen, G.C. Groenenboom, A. van der Avoird, P.S. Zuchowski, and R. Podeszwa. Ab initio potential energy surfaces for NH(3Sigma-)-NH(3Sigma-) with analytical long range. *J. Chem. Phys.*, 131:224314, 2009.

[61] T. Jeltes, J.M. McNamara, W. Hogervorst, W. Vassen, V. Krachmalnicoff, M. Schellekens, A. Perrin, H. Chang, D. Boiron, A. Aspect, and C.I. Westbrook. Comparison of the Hanbury Brown-Twiss effect for bosons and fermions. *Nature*, 445:402, 2007.

[62] S. Jochim, M. Barternstein, A. Altmeyer, G. Hendl, C. Chin, J. Hecker Deschlag, and R. Grimm. Pure gas of optically trapped molecules created from fermionic atoms. *Phys. Rev. Lett.*, 91:240402, 2003.

[63] S. Jochim, M. Barternstein, A. Altmeyer, G. Hendl, S. Riedl, C. Chin, J. Hecker Deschlag, and R. Grimm. Bose-Einstein condensation of molecules. *Science*, 302:2101, 2003.

[64] K. M. Jones, E. Tiesinga, P. D. Lett, and P. S. Julienne. Ultracold photoassociation spectroscopy: Long-range molecules and atomic scattering. *Rev. Mod. Phys.*, 78:483, 2006.

[65] P. S. Julienne. Cold binary atomic collisions in a light field. *J. Res. Natl. Inst. Stand. Technol*, 101:487, 1996.

[66] S. Kato, S. Sugawa, K. Shibata, R. Yamamoto, and Y. Takahashi. Control of resonant interaction between electronic ground and excited states. *Phys. Rev. Lett.*, 110:173201, 2013.

[67] A.J. Kerman, J.M. Sage, S. Sainis, T. Bergeman, and D. DeMille. Production of ultracold, polar RbCs* molecules via photoassociation. *Phys. Rev. Lett.*, 92:033004, 2004.

[68] A. Khramov, A. Hansen, , W. Dowd, R.J. Roy, C. Makrides, A. Petrov, S. Kotochigova, and S. Gupta. Ultracold heteronuclear mixture of ground and excited state atoms. *arXiv:1309.7926*, 2013.

[69] G.W. King and J.H. Van Vleck. Dipole-dipole resonance forces. *Phys. Rev.*, 55:1165, 1939.

[70] C. Kohstall, M. Zaccanti, M. Jag, A. Trenkwalder, P. Massignan, G. M. Bruun, F. Schreck, and R. Grimm. Metastability and coherence of repulsive polarons in a strongly interacting Fermi mixture. *Nature*, 485:615, 2012.

[71] S. Kotochigova, T. Zelevinsky, and J. Ye. Prospects for application of ultracold Sr_2 molecules in precision measurements. *Phys. Rev. A*, 79:012504, 2009.

[72] S. Kraft, F. Vogt, O. Appel, F. Riehle, and U. Sterr. Bose-Einstein condensation of alkaline earth atoms: ^{40}Ca. *Phys. Rev. Lett.*, 103:130401, 2009.

[73] R.V. Krems, G.C. Groenenboom, and A. Dalgarno. Electronic interaction anisotropy between atoms in arbitrary angular momentum states. *J. Phys. Chem.*, 108:8941, 2004.

[74] H. Lefebvre-Brion and R. W. Field. *Perturbations in the Spectra of Diatomic Molecules.* Academic Press, 1986.

[75] T.H. Maiman. Stimulated optical radiation in ruby. *Nature*, 187:493, 1960.

[76] Y. N. Martinez de Escobar, P. G. Mickelson, P. Pellegrino, S. B. Nagel, A. Travers, M. Yan, R. Cote, and T. C. Killian. Two-photon photoassociative spectroscopy of ultracold 88-Sr. *Phys. Rev.A*, 78:062708, 2008.

[77] Y. N. Martinez de Escobar, P. G. Mickelson, M. Yan, B. J. DeSalvo, S. B. Nagel, and T. C. Killian. Bose-Einstein condensation of ^{84} sr. *Phys. Rev. Lett.*, 103:200402, 2009.

[78] W.F. Meggers and J.L. Tech. The first spectrum of ytterbium (Yb I). *J. Res. Bur. Stand.*, 83:13, 1978.

[79] H. J. Metcalf and P. van der Straten. *Laser Cooling and Trapping.* Springer, 1999.

[80] A. Micheli, G. K. Brennen, and P. Zoller. A toolbox for lattice-spin models with polar molecules. *Nature Physics*, 2:341, 2006.

[81] K.W. Miller, S. Duerr, and C.E. Wieman. rf-induced Sysiphus cooling in an optical dipole trap. *Phys. Rev. A*, 66:023406, 2002.

[82] A.P. Mishra and T.K. Balasubramanian. Radiative lifetimes of the first excited $^3P_{2,0}$ metastable levels in KrI, XeI, YbI and Hg-like atoms. *J. Quant. Spectr. Radiat. Tran.*, 69:769, 2001.

[83] G. Modugno, G. Ferrari, G. Roati, R.J. Brecha, A. Simoni, and M. Inguscio. Bose-Einstein condensation of potassium atoms by sympathetic cooling. *Science*, 294:1320, 2001.

[84] A.J. Moerdijk, B.J. Verharr, and A. Axelsson. Resonances in ultracold collisions of 6-Li, 7-Li and 23-Na. *Phys. Rev. A*, 51:4852, 1995.

[85] M. Mudrich, S. Kraft, K. Singer, R. Grimm, A. Mosk, and M. Weidemüller. Sympathetic cooling with two atomic species in an optical trap. *Phys. Rev. Lett.*, 88:253001, 2002.

[86] S.B. Nagel, C.E. Simien, S. Laha, P. Gupta, V.S. Ashoka, and T.C. Killian. Magnetic trapping of metastable 3P2 atomic strontium. *Phys Rev A*, 67:011401, 2003.

[87] N. Nemitz, F. Baumer, F. Münchow, S. Tassy, and A. Görlitz. Production of heteronuclear molecules in an electronically excited state by photoassociation in a mixture of ultracold yb and rb. *Phys Rev A (R)*, 79:061403, 2009.

[88] K.-K. Ni, S. Ospelkaus, M. H. G. de Miranda, A. Peer, B. Neyenhuis, J. J. Zirbel, S. Kotochigova, P. S. Julienne, D. S. Jin, and J. Ye. A high phase-space-density gas of polar molecules. *Science*, 322:231, 2008.

[89] K. M. O'Hara, M.E. Gehm, S.R. Granade, and J. E. Thomas. Scaling laws for evaporative cooling in time-dependent optical traps. *Phys. Rev. A.*, 64:051403(R), 2001.

[90] K. M. O'Hara, S.R. Granade, M.E. Gehm, T.A. Savard, S. Bali, C. Freed, and J. E. Thomas. Ultrastable CO_2 laser trapping of lithium fermions. *Phys. Rev.Lett.*, 82:4204, 1999.

[91] K. M. O'Hara, S. L. Hemmer, M. E. Gehm, S. R. Granade, and J. E. Thomas. Observation of a strongly interacting degenerate Fermi gas of atoms. *Science*, 298:2179, 2002.

[92] M. Okano, H. Hara, M. Muramatsu, K. Doi, S. Uetake, Y. Takasu, and Y. Takahashi. Simultaneous magneto-optical trapping of lithium and ytterbium towards production of ultracold polar molecules. *Appl Phys B*, 98:691, 2010.

[93] M.L. Olsen, J.D. Perreault, T.D. Cumby, and D. S. Jin. Coherent atom-molecule oscillations in a Bose-Fermi mixture. *Phys. Rev. A*, 80:030701(R), 2009.

[94] F. Pereira dos Santos, J. Leonard, J. Wang, C.J. Barrelet, F. Perales, E. Rasel, C.S. Unnikrishnan, M. Leduc, and C. Cohen-Tannoudji. Bose-Einstein condensation of metastable helium. *Phys. Rev. Lett.*, 86:3459, 2001.

[95] A. Petrov, E. Tiesinga, and S. Kotochigova. Anisotropy-induced Feshbach resonances in a quantum dipolar gas of highly magnetic atoms. *Phys. Rev. Lett.*, 109:103002, 2012.

[96] D. S. Petrov. Three-body problem in Fermi gases with short-range interparticle interaction. *Phys. Rev. A.*, 67:010703(R), 2003.

[97] S. G. Porsev, Y. G. Rakhlina, and M. G. Kozlov. Electric-dipole amplitudes, lifetimes, and polarizabilities of the low-lying levels of atomic ytterbium. *Phys. Rev. A*, 60:2781, 1999.

[98] J.V. Porto, S. Rolston, B. Laburthe-Tolra, C.J. Williams, and W.D. Phillips. Quantum information with neutral atoms as qubits. *Phil. Trans. R. Soc. Lond. Ser. A. 361*, 1808:1417, 2003.

[99] C. A. Regal, C. Ticknor, J. L. Bohn, and D. S. Jin. Creation of ultracold molecules from a Fermi gas of atoms. *Nature*, 424:47, 2003.

[100] B.S. Rem, A.T. Grier, I. Ferrier-Barbut, U. Eismann, T. Langen, N. Navon, L. Khaykovich, F. Werner, D.S. Petrov, F. Chevy, and C. Salomon. Lifetime of the Bose gas with resonant interactions. *Phys. Rev. Lett.*, 110:163202, 2013.

[101] A. Robert, O. Sirjean, A. Browaeys, J. Poupard, S. Nowak, D. Boiron, C. I. Westbrook, and A. Aspect. A Bose-Einstein condensate of metastable atoms. *Science*, 292:461, 2001.

[102] J. M. Sage, S. Sainis, T. Bergeman, and D. DeMille. Optical production of ultracold polar molecules. *Phys. Rev. Lett.*, 94:203001, 2005.

[103] C. B. Schaffer. *Interaction of Femtosecond Laser Pulses with Transparent Materials.* PhD thesis, Harvard University, 2001.

[104] C.H. Schunck, M.W. Zwierlein, C.A. Stan, S.M.F. Raupach, W. Ketterle, A. Simoni, E. Tiesinga, and C.J. Williams. Feshbach resonances in fermionic ^{6}li. *Phys. Rev. A*, 71:045601, 2005.

[105] F.M. Spiegelhalder, A. Trenkwalder, D. Naik, G. Hendl, F. Schreck, and R. Grimm. Collisional stability of ^{40}k immersed in a strongly interacting Fermi gas of ^{6}li. *Phys. Rev. Lett.*, 103:223203, 2009.

[106] C. A. Stan and W. Ketterle. Multiple species atom source for laser-cooling experiments. *Rev. Sci. Instrum.*, 76(063113), 2005.

[107] Claudiu Stan. *Experiments with interacting Bose and Fermi gases.* PhD thesis, MIT, 2005.

[108] S. Stellmer. *Degenerate quantum gases of strontium.* PhD thesis, University of Innsbruck, 2013.

[109] S. Stellmer, B. Pasquiou, R. Grimm, and F. Schreck.

[110] S. Stellmer, B. Pasquiou, R. Grimm, and F. Schreck. Laser cooling to quantum degeneracy. *Phys. Rev. Lett.*, 110(263003), 2013.

[111] S. Stellmer, M. K. Tey, B. Huang, R. Grimm, and F. Schreck. Bose-Einstein condensation of strontium. *Phys. Rev. Lett.*, 103(200401), 2009.

[112] J.A. Stone and J.H. Zimmerman. Index of refraction of air. Technical report, NIST, 2001.

[113] K. E. Strecker, G. B. Partridge, and R. G. Hulet. Conversion of an atomic Fermi gas to a long-lived molecular Bose gas. *Phys. Rev. Lett.*, 91(080406), 2003.

[114] S. Sugawa, R. Yamazaki, S. Taie, and Y. Takahashi. Bose-Einstein condensate in gases of rare atomic species. *Phys. Rev. A*, 84:011610(R), 2011.

[115] Y. Takasu, K. Komori, K. Honda, M. Kumakura, T. Yabuzaki, and Y. Takahashi. Photoassociation spectroscopy of laser-cooled ytterbium atoms. *Phys. Rev. Lett.*, 93:123202, 2004.

[116] Y. Takasu, K. Maki, K. Komori, T. Takano, K. Honda, M. Kumakura, T. Yabuzaki, and Y. Takahashi. Spin-singlet Bose-Einstein condensation of two-electron atoms. *Phys. Rev. Lett.*, 91:040404, 2003.

[117] A.G. Truscott, K.E. strecker, W.I. McAlexander, G.B. Partridge, and R.G. Hulet. Observation of Fermi pressure in a gas of trapped atoms. *Science*, 291:2570, 2001.

[118] S. Uetake, R. Murakami, J.M. Doyle, and Y. Takahashi. Spin-dependent collision of ultracold metastable atoms. *Phys. Rev. A*, 86:032712, 2012.

[119] S. Uetake, A. Yamaguchi, D. Hashimoto, and Y. Takahashi. High-resolution laser spectroscopy of ultracold ytterbium atoms using spin-forbidden electric quadrupole transition. *Appl. Phys. B.*, 93:409, 2008.

[120] J. van Dongen. Personal communication.

[121] E. Vernier, D. Pekker, M. W. Zwierlein, and E. Demler. Bound states of a localized magnetic impurity in a superfluid of paired ultracold fermions. *arXiv:1010.6085*, 2010.

[122] T. Weber, J. Herbig, M. Mark, H.-C. Nagerl, and R. Grimm. Bose-Einstein condensation of cesium. *Science*, 299:232, 2003.

[123] M. Weissbluth. *Atoms and Molecules*. Academic Press, Inc., 1978.

[124] C.-H. Wu, J. W. Santiago, I. amd Park, P. Ahmadi, and M. W. Zwierlein. Strongly interacting isotopic Bose-Fermi mixture immersed in a Fermi sea. *Phys. Rev. A*, 84:011601(R), 2011.

[125] A. Yamaguchi. *Metastable State of Ultracold and Quantum Degenerate Ytterbium Atoms: High-Resolution Spectroscopy and Cold Collisions*. PhD thesis, Kyoto University, 2007.

[126] A. Yamaguchi, S. Uetake, D. Hashimoto, J. M. Doyle, and Y. Takahashi. Inelastic collisions in optically trapped ultracold metastable ytterbium. *Phys. Rev. Lett.*, 101:233002, 2008.

[127] A. Yamaguchi, S. Uetake, S. Kato, H. Ito, and Y. Takahashi. High-resolution laser spectroscopy of a Bose-Einstein condensate using the ultranarrow magnetic quadrupole transition. *New J. Phys.*, 12:103001, 2010.

[128] T. Yefsah, A.T. Sommer, M.J.H. Ku, L.W. Cheuk, W. Ji, W. Bakr, and M. Zwierlein. Heavy solitons in a fermionic superfluid. *Nature*, 499:426, 2013.

[129] R.N. Zare. *Angular Momentum*. John Wiley and Sons, Inc, 1988.

[130] P. Zhang, H. R. Sadeghpour, and A. Dalgarno. Structure and spectroscopy of ground and excited states of liyb. *J Chem Phys.*, 133:044306, 2010.

[131] S. Zhang and T.-L. Ho. Atom loss maximum in ultra-cold Fermi gases. *New J. Phys.*, 13:055003, 2011.

[132] P.S. Zuchowski, J. Aldegunde, and J.M. Hutson. Ultracold rbsr molecules can be formed by magnetoassociation. *Phys. Rev. Lett.*, 105:153201, 2010.

[133] M. W. Zwierlein, C. H. Schunck, A. Schirotzek, and W. Ketterle. Vortices and superfluidity in a strongly interacting Fermi gas. *Nature*, 435:1047, 2005.

[134] M. W. Zwierlein, C.A. Stan, C. H. Schunck, S.M.F. Raupach, S. Gupta, Z. Hadzibabic, and W. Ketterle. Observation of Bose-Einstein condensation of molecules. *Phys. Rev. Lett.*, 91:250401, 2003.

[135] Martin W. Zwierlein. *High temperature superfluidity in an ultracold Fermi gas.* PhD thesis, MIT, 2006.